The interior structure and geodynamics of Venus as seen by gravity and topography

Julia Maia

UNIVERSITÉ CÔTE D'AZUR

ÉCOLE DOCTORALE
SCIENCES FONDAMENTALES ET APPLIQUÉES

Structure interne et géodynamique de Vénus par analyses gravimétriques et topographiques

Julia Maia

Laboratoire J.-L. Lagrange · Observatoire de la Côte d'Azur

Présentée en vue de l'obtention du grade de docteur en
Sciences de la Planète et de l'Univers
de l'Université Côte d'Azur

Dirigée par Mark Wieczorek

Soutenue le 22 September 2023

Devant le jury composé de

Doris Breuer	*Head of department, DLR Institute of Planetary Research, Berlin, Germany*
Nicolas Coltice	*Professeur, École Normale Supérieure, Paris, France*
Caroline Dumoulin	*Maître de conférences, Nantes Université, Nantes, France*
Taras Gerya	*Professor, ETH-Zurich, Zurich, Switzerland*
Peter James	*Assistant Professor, Baylor University, Waco, USA*
Ana-Catalina Plesa	*Scientific staff member, DLR Institute of Planetary Research, Berlin, Germany*
Mark Wieczorek	*Directeur de Recherche, Institut de Physique du Globe, Paris, France*

Structure interne et géodynamique de Vénus, par analyses gravimétriques et topographiques

The interior structure and geodynamics of Venus as seen by gravity and topography

Rapporteurs

Doris Breuer
Head of department, DLR Institute of Planetary Research, Berlin, Germany

Taras Gerya
Professor, ETH-Zurich, Zurich, Switzerland

Examinateurs

Nicolas Coltice
Professeur des universités, École Normale Supérieure, Paris, France

Caroline Dumoulin
Maître de conférences, Nantes Université, Nantes, France

Peter James
Assistant Professor, Baylor University, Waco, United States of America

Ana-Catalina Plesa
Scientific staff member, DLR Institute of Planetary Research, Berlin, Germany

Mark Wieczorek
Directeur de Recherche, Institut de Physique du Globe de Paris, Paris, France

One of the reasons that planetary astronomy is such a delight these days is that it is possible to find out what's really right. In the old days, you could make any guess you liked, however improbable, about a planetary environment, and there was little chance that anyone could ever prove you wrong. Today, spacecraft hang like swords of Damocles over each hypothesis spun by planetary theoreticians, and the theoreticians can be observed in a curious amalgam of hope and fear as each new burst of spacecraft planetary information comes winging in.

— Carl Sagan, The Cosmic Connection, 1973

RESUMÉ La planète Vénus est couramment surnommée "jumelle de la Terre" du fait de leurs similarités en masse, taille, et distance au Soleil. Néanmoins, la planète est rendue inhabitable par son atmosphère écrasante, qui induit un effet de serre responsable d'une température de surface de 470°C. De plus, la tectonique des plaques, principal moteur de la géologie terrestre, n'existe pas sur Vénus. Venus et la Terre ont donc connu des histoires géologiques distinctes, pour des raisons encore incertaines. Afin de contraindre l'évolution géodynamique de Vénus et de comprendre pourquoi ces deux planètes ont évoluées différemment, il est essentiel de bien connaître leurs structure interne. Malheureusement, la structure interne de Vénus est très mal connue. Cette thèse a pour objectif de mieux estimer la structure interne de Vénus, afin d'obtenir de nouvelles perspectives sur la géodynamique et l'évolution thermique de la planète. Pour ce faire, j'ai étudié les anomalies gravitationnelles et la topographie de Vénus observées par la sonde Magellan dans les années 90, en utilisant des techniques d'analyse, des modèles géophysiques, et des méthodes d'inversion de données sophistiquées.

Durant la première partie de ma thèse, j'ai concentré mes études sur la structure interne et les mécanismes de compensation topographique d'un type de formation géologique spécifique à Vénus – les plateaux crustaux. Ces plateaux sont des régions montagneuses de milliers de kilomètres d'extension, qui présentent des anomalies gravitationnelles positives mais de magnitude discrètes. En utilisant un modèle de déformation élastique de la lithosphère, j'ai produit des données gravimétriques synthétiques qui ont été comparées avec les observations faites par Magellan. Ces modèles sont principalement sensibles aux variations d'épaisseur de la croûte, responsables de variations de densité à l'intérieur de la planète; ainsi qu'à l'épaisseur élastique, qui contrôle l'ampleur de la déformation lithosphérique lorsqu'elle est soumise à des charges à la surface et en subsurface. Mes résultats montrent que la topographie des plateaux est compensée par l'épaississement de la croûte, et qu'elle est en grande partie cohérente avec un régime de compensation isostatique d'Airy. De plus, l'épaisseur moyenne de la croûte de ces régions varie de 15 et 34 km. Cependant, à cause de la déflection lithospherique, la croûte peut atteindre plus de 40 km de profondeur dans les régions où la topographie est plus élevée. Ces valeurs sont comparables à l'épaisseur de la croûte continentale terrestre. Enfin, en supposant que les plateaux sont en isostasie d'Airy, j'ai pu déduire que l'épaisseur moyenne de la croûte de Vénus est d'environ 20 km.

Ensuite, j'ai concentré mes études sur les signaux gravimétriques et topographiques aux grandes longueurs d'onde, qui sont associées à des écoulements dans le manteau. Pour analyser ces signaux, j'ai utilisé un modèle analytique de charges dynamiques, qui suppose que la convection du manteau est déclenchée par des anomalies de densité dans le manteau et est sensible à la structure de sa viscosité. En comparant à nouveau les modèles avec les observations, j'ai pu obtenir de nouvelles informations sur les propriétés géophysiques du manteau de Vénus. Le principal résultat de cette étude a été la découverte d'une zone à faible viscosité dans le manteau supérieur. Cette zone est caractérisée par une réduction de la viscosité de 5 à 15 fois par rapport au manteau sous-jacent. Elle commence à la base de la lithosphère, à environ 80 km de profondeur, et mesure environ 325 km d'épaisseur. Cette réduction de viscosité pourrait être causée par la présence de fusion partielle dans le manteau, comme cela a été proposé pour expliquer l'origine de l'asthénosphère de la Terre. Cela soutiendrait l'interprétation selon laquelle Vénus est un monde géologiquement actif, principalement régi par des processus magmatiques en cours.

Mots clés Vénus · structure interne · gravimétrie

ABSTRACT Venus is commonly referred to as the twin planet of the Earth because of their similarities in mass, size, and distance to the Sun. However, Venus is uninhabitable due to its thick and toxic atmosphere, resulting in surface temperatures of 470°C caused by greenhouse effects. In addition, plate tectonics, the driving mechanism of Earth's geology, does not exist on Venus. These major differences show that the two planets went through distinct geological histories, for reasons that are still not well understood. To investigate Venus's geodynamic evolution and evaluate why Venus and Earth became so different, it is critical to have accurate constraints of the planet's interior structure. Yet, our knowledge of the interior of Venus is still very limited. In this context, the goal of my thesis is to provide better estimates of the interior structure of Venus and use these results to obtain insights about the geodynamics and thermal evolution of the planet. To achieve this, I revisit the gravity and topography data obtained by the Magellan spacecraft in the 1990s adopting modern analysis techniques, geophysical models, and inversion approaches.

The first project of my PhD focused on studying the interior structure of a specific type of Venusian feature – the crustal plateaus. The plateaus are thousands of kilometers wide highlands associated with positive, but low-magnitude, gravity anomalies. In this study, I systematically compare the gravity observations of these regions with the gravity signatures predicted by elastic deformation models of the lithosphere. These models are mainly sensitive to the thickness of the crust, responsible for internal density variations, and the elastic thickness, which determines the magnitude of lithospheric deformation when submitted to loads on the surface and in the subsurface. My results demonstrate that the topography of the plateaus are overall supported by thickening of the crust and that they are mostly consistent with an Airy isostasy compensation regime. Furthermore, the average crustal thickness of these highlands ranges from 15 to 34 km but, but due to lithospheric deflection, it can reach depths exceeding 40 km in areas with higher topography. These values are comparable to the crustal thickness of continental regions on Earth. In addition, by assuming that the plateaus are in Airy isostasy, I was able to infer that the average crustal thickness of Venus is about 20 km thick.

Later on, I began investigating the long-wavelength gravity and topography signatures of Venus, which are associated with flows in the mantle. To analyze these signals, I employed the dynamic loading model, an analytical approach that models mantle convection. This approach is mainly sensitive to the planet's viscosity structure and the distribution of mantle density anomalies. Once again comparing models with observations, I was able to get new insights about the geophysical properties of Venus's mantle. The main result of this study was the discovery of a low-viscosity zone in the uppermost mantle. This zone is characterized by a viscosity reduction of 5 to 15 times with respect to the underlying mantle. It starts at the base of the lithosphere, at roughly 80 km depth, and has a thickness of about 325 km. his viscosity reduction may be attributed to the presence of partial melt in the mantle, as proposed for the origin of Earth's asthenosphere, supporting the interpretation that Venus is a geologically active world predominantly governed by ongoing magmatic processes.

Keywords Venus · interior structure · gravity

ACKNOWLEDGEMENTS

About 6 years ago, finishing my bachelor and dreaming about the possibility of becoming a planetary scientist, I sent a hopeful email to Mark Wieczorek - the author of the chapter "Gravity and Topography of the Terrestrial Planets" from the Treatise of Geophysics collection - asking about the possibility of going to France and working with him. For my great surprise, he answered and encouraged me to cross the Atlantic and start the biggest adventure of my life. Since then, Mark has given me invaluable support at each step of my career. It has been an enormous privilege working with him these past years.

A heartfelt appreciation goes out to my awesome thesis committee. First, I must thank Taras Gerya and Doris Breuer for the thoughtful reviews of my thesis manuscripts. In addition, Nicolas Coltice masterfully conducted my defense, making me feel unexpectedly comfortable on a very stressful day which I deeply appreciate. I am also very grateful to Peter James and Caroline Dumoulin who were very supportive and enthusiastic about my work not only during my defense but on several occasions during my PhD.

During my PhD I had the incredible opportunity to spend 3 months at DLR's Institute of Planetary Sciences in Berlin after the invitation of Ina Plesa. I am very grateful to everyone in the Planetary Physics department who welcomed me so warmly. In particular, I must thank Ina, working with her almost doesn't feel like work - the passion that she has for planetary sciences is contagious and somehow staying at the office until 8pm discussing plots becomes the most fun thing in the world.

I doubt that there is a better place to work than in Mont Gros, not only because of the sea view and the great food, but mostly thanks to the staff of the Observatoire de la Côte d'Azur and specially of the Laboratoire Lagrange. I am also very honored for being part of the TOP team. I have learned and laughed so much during our coffee-breaks and meetings. I would like to specially thank my fellow PhD colleagues that became such an important part of my life. My thesis-twin Saburo, mutually reminding deadlines and venting to one another has made this tough road much easier. I also thank the PHC girls, Fabi, Marjo, Philou and Kate, who arrived bringing lots of life and joy to the team after a locked-down year. Last but not least I want to thank two of the greatest gifts the observatory has given me: my hermanito Nicolas and my roomie Camille.

Leaving behind family and friends was undoubtedly the most challenging aspect of this journey. Mom and dad, thanks for the unconditional love and support. Clara and Isabel you are the loves of my life

and I hope I'm making you proud. A special thanks to vovó Selce and vovó Celia who showed me that women can be anything they aspire to be, vovô Marcel who made me a slightly french brazilian, and vovô Américo who made me fall in love with maps. I cannot leave out my amazing friends that cheered for me every step of the way, especially my geophysics crew Tone, Amanda and Lorena.

Lastly, I want to thank Max for making sure I properly document my code, patiently explaining how git works at least 10 times, proof-reading my entire thesis manuscript, and calming me down in every insecurity meltdown (yes, PhD's has some of those - but it is all worth it!).

CONTENTS

LIST OF FIGURES

LIST OF TABLES

Part I

FROM GOD OF LOVE TO EVIL TWIN

1

UNVEILING VENUS

1.1 A PALE WHITE DOT: VENUS IN THE VISIBLE

As the second brightest object in the night sky, Venus's emblematic appearances during dusk or dawn turned the planet into a prominent figure throughout human civilizations. Because of its proximity to the Sun, Venus has an apparent discontinuous motion when observed from the Earth, alternating between "evening star" and "morning star" periods which led several ancient cultures to assume these were two distinct objects. For example, from the classic literary works Iliad and Odyssey it appears that Homer (~ 800 BC) was unaware that the two stars were the same object. Centuries beforehand, however, around 1600 BC, the Babylonians had created tablets listing the appearance of the first and last visible rising and setting of Venus for over 20 years (Sachs et al., 1974). The tradition of making systematic observations, and even attempting to predict the appearance of Venus in the sky, shows that the astronomy from Mesopotamia was in several aspects more advanced than in Greece, at least until the Persian invasion in 539 BC (Evans, 1998). In Babylonia, the planet was associated with Ishtar, the powerful and complex Goddess of love, fertility and war. Later, the Romans considered the planet sacred to the goddess of love and beauty Venus, which led to the naming of the planet as we know today. Venus is in fact the only planet named after a female god. In addition, Venus was of great importance for Mesoamerican civilizations, in particular the Mayans, who linked the planet to the god of War Kukulcan. The Mayans were able to predict its positions with exquisite precision and used the planet positions to guide ritual activities and harvest seasons (e. g., Nájera and Castellanos, 2020).

Passing beyond culturally focused studies of the sky, Venus became also a central figure during the emergence of modern astronomy. In late 1610, after publishing the treatise *Sidereus nuncius* – the first scientific work presenting observations made with a telescope that included the discovery of moons around Jupiter – Galileo makes yet another set of groundbreaking observations, this time of Venus. Galileo observed that Venus had phases similar to the Moon and on New Year's Day 1611 he wrote on a letter to Kepler the famous phrase "The mother of love *[Venus]* imitates the shapes of Cynthia *[Moon]*". As argued by Galileo, the findings, which were later officially published in Galilei et al. (1613) (recently translated to English in Galilei et al., 2010), were incompatible with the Ptolemaic model and could

only be explained by the heliocentric theory of Copernicus. In other words, the observations of Galileo virtually proved that the Earth was not the center of the universe. Thorough descriptions of these studies and their historical contexts can be found in Gingerich (1982), Gingerich (1984), and Palmieri (2001). Figure 1.1 presents a drawing by Galileo the phases of Venus based on his observations.

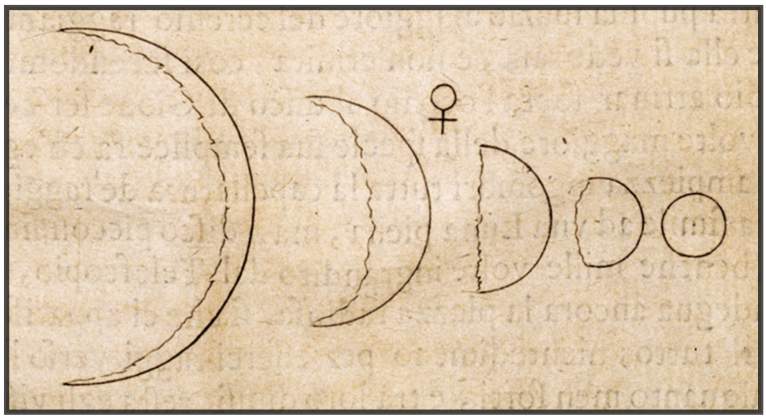

Figure 1.1: Drawings by Galileo Galilei of Venus observations showing the phases of the planet (Galilei, 1623). Retrieved from *Istituto e Museo di Storia della Scienza*.

In 1761, while observing the Venus transit at the Saint Petersburg Observatory, Mikhail Lomonosov noticed a bright ring around Venus just before the contact with the solar disk. Lomonosov rightfully interpreted the luminescence as the refraction of sunlight through a thick atmosphere (e.g., Marov, 2004). During the 18th and 19th centuries, the increase in precision of position determination of celestial objects and the advancements on the understanding of orbital dynamics allowed for the estimation of the orbits and masses of the planets of the Solar System planets (e.g., Verrier, 1872). By the end of the 19th century, scientists had recognized that Venus and the Earth had similar masses, sizes and distances to the Sun. However, because astronomy was still limited to the visible domain, these few bulk properties were essentially all that was known about Venus at the time, akin to our knowledge of exoplanets today.

The lack of data allowed for imaginative scenarios of what was happening below the thick atmosphere and global cloud layer of our mysterious sister planet. Because the similarities with the Earth, until the space age it was natural to assume that Venus was Earth-like, just slightly hotter and cloudier. The picture that scientists and popular culture had in mind was of tropical landscapes, covered by swamps, rich fauna and possibly dinosaur-like creatures (see O'Rourke et al., 2023, for a review).

1.2 THE SPACE AGE

Benefiting from the great technological advancements of the first half of the 20th century, the scenario of Venus science and exploration started to change in the 1950s. The remarkable increase in our understanding of Venus around that time happened thanks to essentially two points: the first was the establishment of radio astronomy, allowing scientists for the first time to make observations that could penetrate the Venus cloud layer and obtain data associated with the planet's surface. The second point was, of course, the start of space exploration that led to the development of interplanetary spacecrafts revolutionizing the domain of planetary sciences as a whole.

In 1956, Mayer et al. (1958) used the Naval Research Laboratory's ~15 m-diameter antenna to observe for the first time radio emissions coming from Venus. With the 3.15 cm and 9.4 cm radiation data, these workers inferred that the apparent black-body temperature of Venus should be about 600 K. Many researchers were confident that the emissions were coming from the surface and the high temperatures were cause by a very efficient greenhouse effect (e.g., Sagan, 1960; Barrett, 1961). On the other hand, part of the scientific community was reluctant to believe that the surface of Venus could be so hot. The main alternative explanation during the early 1960s was that an ionized layer in the atmosphere could be responsible for these radio emission (e.g., Jones, 1961), which would permit the surface to be cool - and maybe inhabited.

It was in the context of the radio emission discussions that the spacecraft Mariner 2 was sent to Venus by the National Aeronautics and Space Administration (NASA) to perform a flyby. The mission had seven scientific instruments and was highly interdisciplinary (Sonett, 1963). One of its instruments was a microwave radiometer, which acquired several emission measurements, covering regions both near the planet's center and limb. The observed limb darkening effect strongly supported the hot surface hypothesis (Barath et al., 1964) and in the following years the portrayal of a hellish Venus consolidated (Walker and Sagan, 1966; Sagan, 1967).

In the outreach book"Cosmic Connection" Carl Sagan, who studied Venus during his PhD, discusses how unconscious psycological biases probably influenced the propositions of a cool scenario for Venus.

Mariner 2 was humanity's first successful interplanetary mission and a key achievement of the United States during the early stages of the space race. In fact, throughout the Cold War, Venus was a primary target of exploration and staged many historical achievements. An overview of the chronology of Venus space exploration is presented in Figure 1.2, where I show the number of mission to Venus per decade and pinpoint some historical highlights. As we can see, the exploration of Venus thrived in the context of the space race. From the 1960s to the 1980s tens of missions were (tentatively) sent to the planet and 21 of them were able to successfully acquire data and send it back to Earth.

In 1967, Venera 4, the first successful Soviet mission to Venus, made the first is-situ measurements of another planet's atmosphere and estimated that the atmosphere of Venus was composed of about 95% CO_2, further supporting the greenhouse effect hypothesis to explain the observed high temperatures (Vakhnin, 1968). A few years later Venera 7 successfully landed on Venus and took direct measurements of the surface temperature, providing estimates of 747 ± 20 K (Avduevsky et al., 1971).

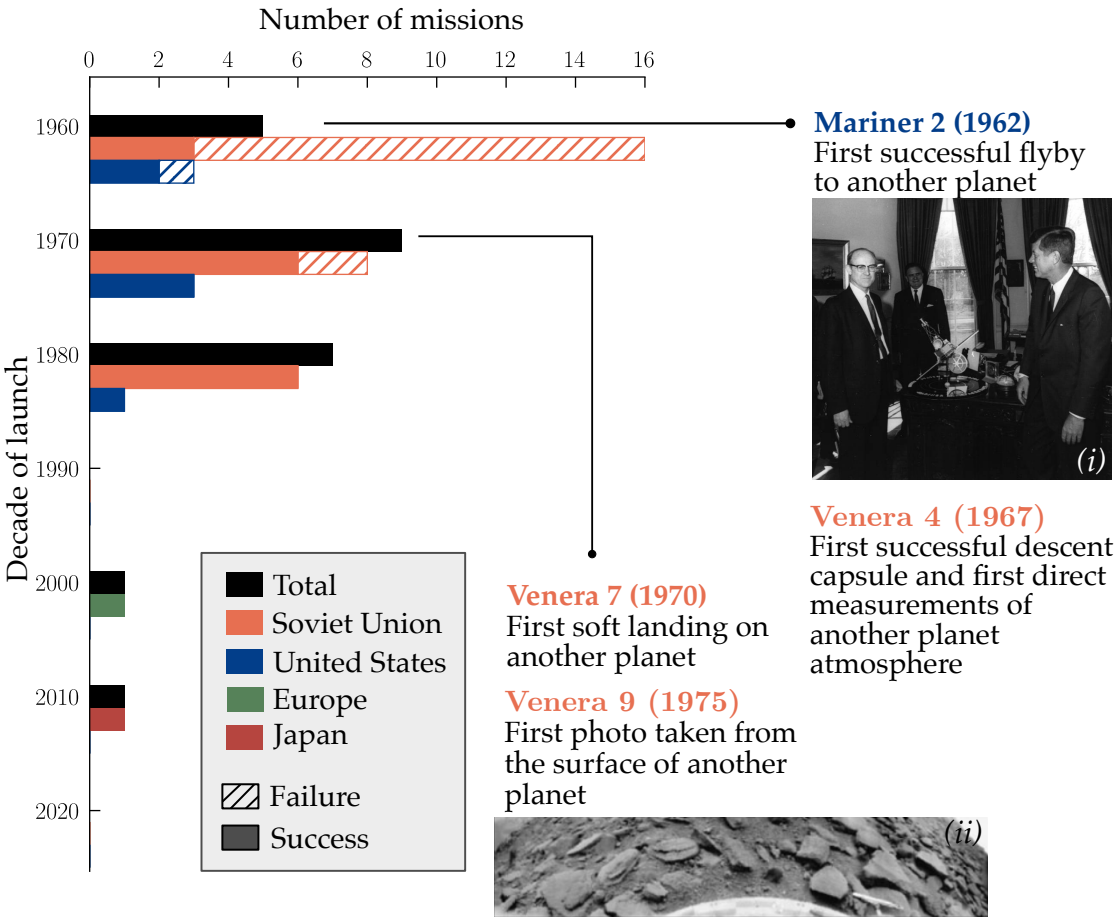

Figure 1.2: Historical overview of Venus space exploration. The bar plot shows in black the total number of successful missions per decade that had Venus as a science target. The underlying colored bars represent the contribution per country or space organization. The hashed bars are failed missions while the fully colored bars represent successes. The plot is based on the mission chronology information available at the *NASA Space Science Data Archive*. Image *(i)* is part of a photo from 1961 showing president J. Kennedy (right), Jet Propulsion Laboratory (JPL) Director Dr. W. Pickering (left), and NASA Administrator James Webb (center back) with a model of the Mariner 2 spacecraft (retrieved from the *NASA image gallery*). Image *(ii)* shows the photo taken by the Venera 9 lander, the first one taken from the surface of another planet (retrieved from Basilevsky and Head, 2003).

Venera 7 was just the beginning of a success story for the soviet landers. After that, nine other probes managed the descent through Venus's atmosphere, reach the surface and transfer data back to Earth

(see Abdrakhimov and Basilevsky, 2002, for a review). The legacy of the soviet landers is invaluable – they comprise the totality of direct surface measurements of Venus, which includes six panorama photos taken from the surface of four different landing sites (e.g., Basilevsky and Head, 2003), bulk chemical composition of three landing sites determined by X-ray fluorescence analysis (e.g., Surkov et al., 1984; Surkov et al., 1986), and radioelement composition of five landing sites obtained with gamma-ray spectroscopy (e.g., Surkov et al., 1987). Figure 1.3 shows the landing sites of all Venus landers along with the compositional constraints they obtained. The composition measurements show that Venus's surface is characterized by mafic rocks, probably basalts. In particular, the compositions found by Venera 9, 10, 14 and Vega 1, 2 are quite similar to tholeiitic (mid-ocean ridge or hotspot) basalts on Earth (e.g., Filiberto, 2014). On the other hand, the high K_2O concentration in Venera 13 indicates high-potassium alkaline basalts, while the anomalously high concentration of Th and U at Venera 8 suggests that Venus rocks can be magmatically differentiated and potentially present silicic compositions (e.g., Shellnutt, 2019).

Several important accomplishments were also carried out in the scope of remote sensing observations from orbit. In 1978, the Pioneer Venus Orbiter (PVO) was launched, corresponding to NASA's first Venusian orbiter. Performing science operations for 14 years, the spacecraft was designed as a comprehensive mission composed of 12 science instruments that aimed to study the planet's surface, atmosphere, and space environment (Colin, 1980). The spacecraft was part of the Pioneer Venus Program which also included a multiprobe mission design to perform in-situ investigations of the planet's atmosphere (Colin and Hall, 1977).

Among its many achievements, PVO mapped the entire planet with a radar altimeter providing the first global topography map of Venus, with a horizontal resolution of about 100 km (Pettengill et al., 1980). Moreover, it allowed the first gravity model of Venus to be created with a spatial resolution of roughly 2000 km (Bills et al., 1987). The datasets showed that, contrary to Earth, the long-wavelength gravity and topography of Venus are very well correlated (Sjogren et al., 1980; Bills et al., 1987) and that the planet does not present physiographic features characteristic of plate tectonics (Masursky et al., 1980; Phillips et al., 1981; Kaula and Phillips, 1981; Phillips, 1983). Even though at that time some studies argued that the data resolution was too coarse to discard the possibility of plate tectonics (Solomon and Head, 1982), it was later confirmed that Venus geology is driven by a distinct tectonic regime which is not yet well-understood, as discussed later in this chapter. In addition, joint gravity and topography investigations have shown that many Venusian high-topography features are compensated at large depths indicating that they are dy-

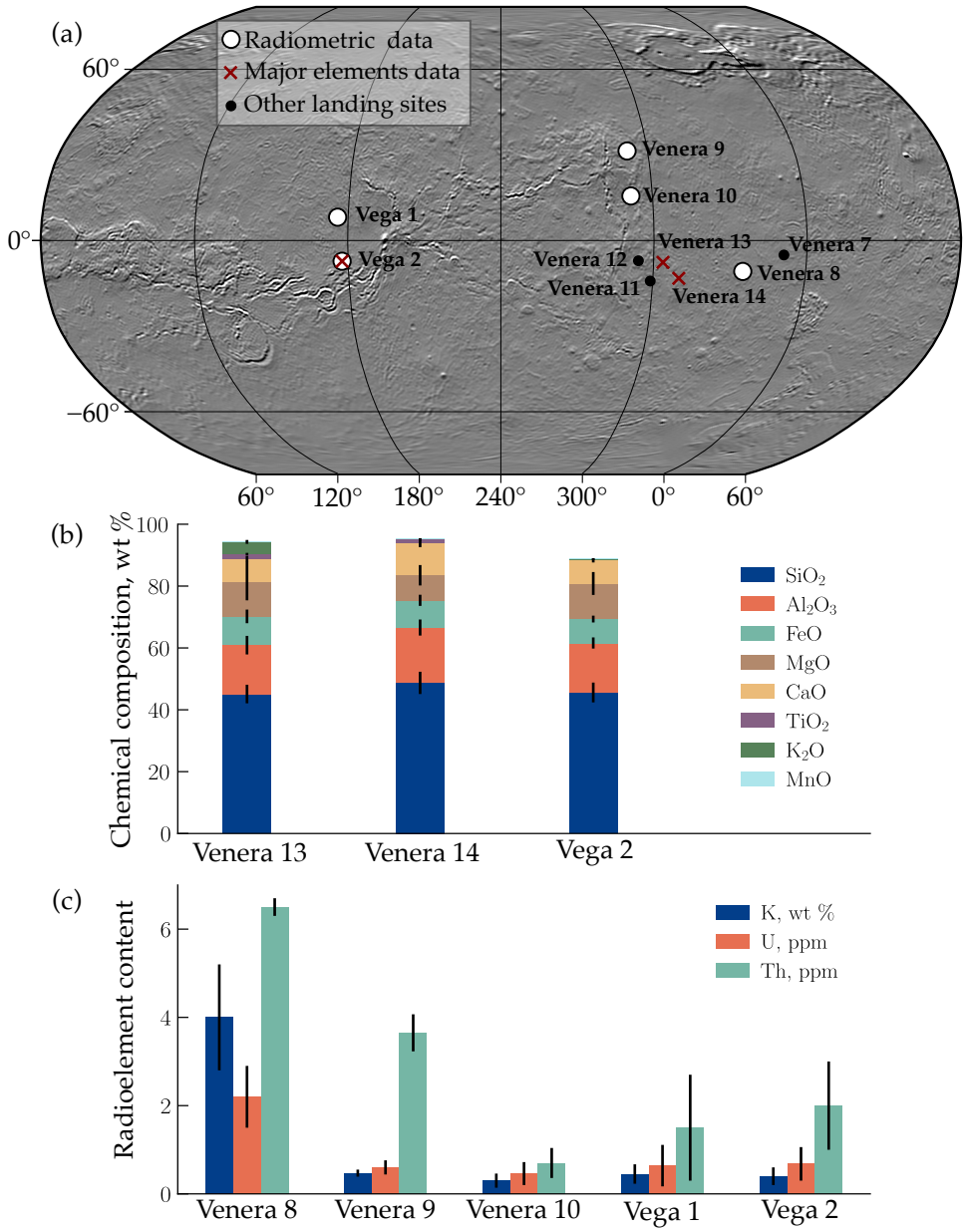

Figure 1.3: Overview of Venus missions landing sites and compositional measurements of the surface. (a) Topography shaded relief map in a Robinson projection showing all sites of successful landings were taken. The white circles indicate the sites with measurements of radioelements, the red crosses show the locations with bulk mineralogical composition measurements, and the black points indicate other landing sites. (b) Major element composition of Venusian surface rocks at three landing sites obtained via X-ray fluorescent analysis. (c) Radioelements content of the surface measured at five locations obtained via gamma-ray spectroscopy. The presented mineralogical data was retrieved from Abdrakhimov and Basilevsky (2002).

namically supported by convective flows in the mantle (Phillips et al.,

1981; Phillips and Malin, 1983; Kaula, 1984; Kiefer et al., 1986). These regions were later recognized as volcanic rises (see Section 1.3 for more details).

PVO has also searched for an intrinsic magnetic field and signs of remnant magnetization on Venus, a task that had been already attempted by several other probes such as Mariner 2 and Venera 4 (e. g. Smith et al., 1965). Once again, no indications of a present or past internal magnetic field was found (e.g., Russell et al., 1980). Nevertheless, based on the detectability limits of PVO's magnetometer, Phillips and Russell (1987) were able to constrain that if Venus have a dynamo today its magnetic moment would be at most $8.4 \times 10^{10}\,\mathrm{T\,m^3}$, i. e., 10^{-5} of Earth's magnetic moment. Because of the high surface temperatures, the possibility of remnant crustal magnetization on Venus was commonly understated. However, a recent study by O'Rourke et al. (2019) showed that at least the ~10 upper kilometers of the crust should be above the Curie temperature of magnetite and could present remnant magnetization.

The orbiter missions Venera 15 and Venera 16 were twin spacecrafts designed to map the North Hemisphere of Venus. Equipped with a synthetic aperture radar (SAR) antenna for imaging and a radar altimeter to obtain topography data, the missions operated for 8 months, mapping about 25% of the planet's surface from the north pole down to about latitude 30°N (Rzhiga, 1987). The radar images of unprecedented spatial resolution (about 1–2 km) allowed for detailed investigations of the surface geology (e.g., Barsukov et al., 1986; Alexandrov et al., 1986; Basilevsky et al., 1987). For example, Barsukov et al. (1986) observed that the volcanic plains were commonly covered by intriguing circular ring-like structures that they named coronae.

A few years later, and marking the end of a prosperous era of Venus exploration, NASA launched the Magellan spacecraft, which would be the agency's last mission to Venus for the following 40 years. Magellan orbited Venus for 4 years (1990-1994) obtaining high-resolution SAR images and topography data, covering 98% of the surface, and provided the best gravity model currently available for the planet. The mission is of uttermost significance for Venus science. For over 30 years (and counting), its datasets have continuously contributed to our understanding of the surface and interior properties of our sister planet. In fact, the studies made in the scope of this thesis have used data from the mission. The main findings from Magellan are described separately in Section 1.3.

It is important to mention that previous to the SAR imaging performed from orbit powerful Earth-based radar telescopes, such as Arecibo, Goldstone, and the Millstone Hill radars, allowed for important surface observations of Venus. The firsts surface features detected on the planet were found via the analysis of irregularities on the spec-

tral and polarization signatures of the radar waves, which were interpreted as topographic features with surface roughness larger than the radar wavelengths (Carpenter, 1966; Goldstein, 1965). In particular, Goldstein (1965) located two regions, which he named α and β (today referred to in the spelled-out forms Alpha and Beta). Using the radar facility at the Arecibo Observatory, Jurgens (1970) found a new anomalous radar feature that was named Maxwell. For these historical reasons, Alpha, Beta, and Maxwell are the only regions on Venus that are not named after female figures, which later became the official naming convention. Efforts to map Venus from Earth continued in the following decades (e.g., Rogers and Ingalls, 1969; Campbell et al., 1976; Campbell et al., 1989) and the more recent imaging campaigns from Arecibo were able to obtain images with an impressive resolution of about 1–2 km (see Campbell and Campbell, 2022, for a review).

At that point there was no convention to the naming of regions on Venus, while Goldstein used greek letters to identify features, Jurgens chose to name them after important scientists in the field of eletromagnetism.

Figure 1.4 shows observations of Venus's surface made with the Arecibo antenna via delay-Doppler imaging. The panels show approximately the same region on Venus mapped in 1976 and 2015. The bright feature is the so-called Maxwell Montes discovered by Jurgens (1970) which was later found to be the highest topographic feature on the planet, rising almost 11 km above the mean planetary radius (Pettengill et al., 1980). The radar dark and smooth region to the west of Maxwell is the Lakshmi Planum highland that seems to be covered by lava flow deposits (e. g., Masursky et al., 1980). The two features are part of Ishtar Terra, a continental-sized terrain located in the north hemisphere, spanning the latitudes 55° to 80° and longitudes 50°W to 60°E.

Precise measurements of the position of surface features through time along with analyses of Doppler shifts during the radar observations also allowed for the firsts unequivocal estimations of the planet's rotation period (e.g., Pettengill et al., 1962; Goldstein, 1964; Carpenter, 1966; Shapiro, 1967). Surprisingly, these studies showed that Venus's rotation is retrograde and extremely slow. The planet takes 243 days to turn around its axis, being longer than it's orbital period of 225 days. Different process could explain these observations. The peculiarities of Venus's spin properties in comparison to other terrestrial planets could be a result of several different processes at different stages of the planet's history. During planetary formation, the stochastic accretion of large bodies introduces substantial randomness to the spin rate and orientation (e. g., Dones and Tremaine, 1993). In addition, it has been shown that secular orbital perturbations can be responsible for large variations on the spin-axis orientation of planets (Laskar and Robutel, 1993). In any case, it is fairly accepted that Venus's atmospheric tides play an important role on the planet's spin properties (e.g., Gold and Soter, 1969; Yoder, 1997; Correia and Laskar, 2001).

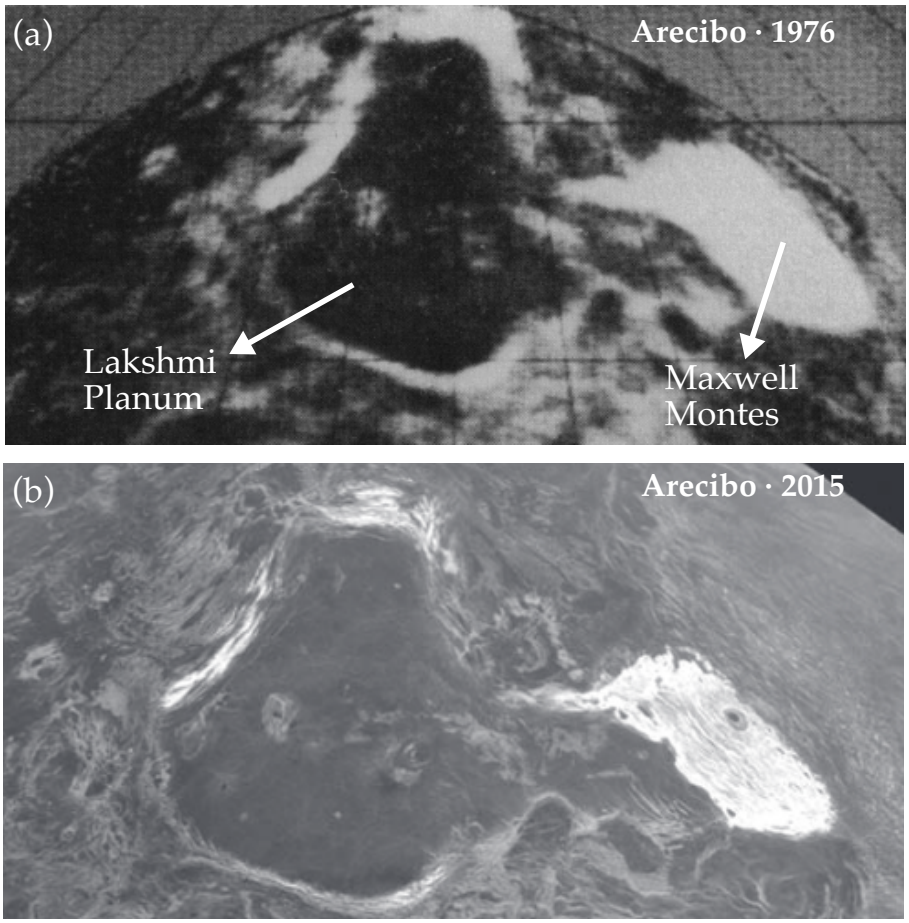

Figure 1.4: Earth-based observations of the Venus surface from the Arecibo observatory based on delay-Doppler mapping. (a) Map from Campbell et al. (1976) of relative back-scattered power with associated spatial resolution of ~ 20 km. The image shows two main features: the radar bright Maxwell Montes and the radar dark Lakshmi Planum. (b) Map of approximately the same region as (a) but with a spatial resolution of about 1–2 km (retrieved from Campbell and Campbell, 2022).

Even though this brief review mainly focused on surface and interior-related observations, these missions also had key implications in our understanding of Venus's atmosphere. For example, measurements by Pioneer Venus, Venera, and Vega provided is-situ information about the vertical structure of the Venus clouds confirming that they are mainly composed of sulfuric acid droplets (see, e. g., Titov et al., 2018, for a review). The Pioneer Venus descent probe also found that the planet's atmosphere has a very high deuterium to hydrogen ratio, about 100 times greater than Earth's, indicating that the planet once had more water (Donahue et al., 1982). The atmosphere was also the main target of the two last missions sent to the planet: Venus Express (2005-2014) by the European Space Agency (ESA) and the Japanese spacecraft Akatsuki which was launched in 2010 and is the only mis-

sion currently operating on the planet. Akatsuki's main focus is to investigate the dynamics of the atmosphere (Nakamura et al., 2011). It has already provided new insights on the superrotation of the Venusian atmosphere (e.g., Horinouchi et al., 2020) and the identification of planetary-scale gravity waves that seem to remain relatively stable over regions of high surface topography (Fukuhara et al., 2017). Venus express was a relatively quick and low-cost mission, being built around the previous Mars Express spacecraft (Svedhem et al., 2007). Yet, it was the basis of major scientific findings, including variations of SO_2 content in the atmosphere which could be an indications of volcanic outgassing (e. g., Marcq et al., 2012), transient high temperature anomalies potentially caused by volcanic eruptions (Shalygin et al., 2015), and new information about the surface composition of the planet that will be further discuss in Chapter 2.

1.3 VENUS AS SEEN BY MAGELLAN

The Magellan mission (Saunders and Pettengill, 1991; Saunders et al., 1992) orbited Venus for about 4 years and mapped 98% of the planet with a synthetic aperture radar and a radar altimeter. The radar images provided a global view of the surface with unprecedented resolution, of about about 150 m, and the altimeter was used to generate a global topography map with resolution of roughly 15 km (Rappaport et al., 1999). The final science phases of Magellan were dedicated to the radio tracking experiment that provided the best gravity model available for the planet (Konopliv et al., 1999). The Magellan topography and gravity datasets are the basis of my investigations. Hence, I chose to described them in a dedicated chapter (Chapter 4), along with an overview of the mission operations.

1.3.1 *A guided tour through Venus surface features*

From the topography data obtained by PVO, at the time of Magellan it was already known that Venus and the Earth should be tectonically different. Venus does not present an ocean/continent dichotomy, nor linear structures resembling mid-ocean ridges. Instead, the topography of Venus is quite smooth, most of the surface is covered by low-lying plains. Yet, the planet presents several highland terrains formed by intensive volcanic and/or tectonic processes. Below, I present a brief characterization of different types Venusian features. Studies by, e. g., Bindschadler et al. (1992b), Basilevsky and Head (2003), and Smrekar et al. (1997) provide further details and analyses of individual regions.

VOLCANIC PLAINS The plains (termed *planitiae*) are the predominant type of terrain on Venus, covering about 70–80% of the surface

of the planet (e.g., Price et al., 1996; Basilevsky and Head, 2003). They have relatively smooth surfaces associated with extensive flood-type volcanism probably of basaltic composition (e. g., Guest et al., 1992). In addition, they are associated with topographic lowlands and negative geoid anomalies. In fact, the lowest point on Venus, about 2 km below the mean planetary radius, occur in one of these regions, the so-called Atalanta Planitia, centered on 65°N and 165°E. Geophysical models based on gravity and topography data usually indicate that the plains correspond to the regions of thin crust and negative density anomalies in the mantle, being commonly interpreted as regions of mantle downwelling (Herrick and Phillips, 1992; Pauer et al., 2006; James et al., 2013).

Tectonic deformation in these regions are typically presented in the form of narrow, regular-spaced, and roughly linear ridges referred to as wrinkle ridges. Their formation is attributed to moderate compressional stresses likely associated with large-scale mantle convection patterns (Solomon et al., 1992; Sandwell et al., 1997; Bilotti and Suppe, 1999). These plains are also characterized by the presence of a large variety of volcanic landforms, including hundreds of tight clusters of small volcanic edifices, generally less than 10 km in diameter, denominated shield plains (Guest et al., 1992; Head et al., 1991; Head et al., 1992). Examples of wrinkle ridges and shield plains on volcanic plains are shown in Figure 1.5.

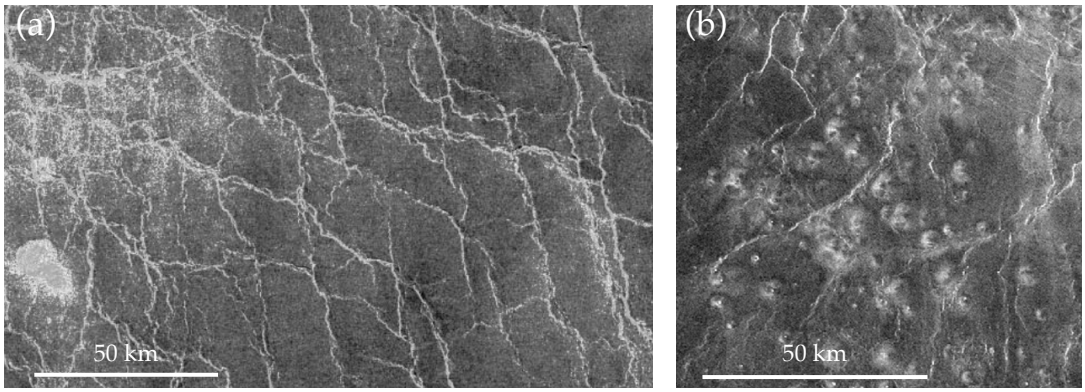

Figure 1.5: Magellan SAR images showing examples of features observed on the volcanic plains of Venus. (a) Example of wrinkle ridges (retrieved from Bilotti and Suppe, 1999). (b) Shield plains composed of tens of small volcanic edifices with diameter ranging from a few kilometers up to about 10 km (retrieved from Ivanov and Head, 2011).

VOLCANIC RISES Several highlands on Venus, the so-called volcanic rises, are characterized by broad approximately dome-shaped topographic swells with total elevation ranging from roughly 2 to 5 km altitude and diameters of about 1000 km. They also present extensive volcanism and prominent positive gravity anomalies (up to

hundreds of miligals[1].) associated with large gravity to topography ratios and deep apparent depth of compensation, as described in Senske et al. (e.g., 1992), Grimm and Phillips (1992), Phillips (1994), Stofan et al. (1995), and Smrekar et al. (1997). These studies proposed that their topography is dynamically supported by deep thermal anomalies, indicating the presence of hot, rising mantle plumes. Dynamic loading models (Herrick and Phillips, 1992; Pauer et al., 2006; James et al., 2013) and numerical simulations of whole-mantle plumes (Kiefer and Hager, 1991; Nimmo and McKenzie, 1996; Solomatov and Moresi, 1996) have been used to predicted the gravity and topography signatures of these regions, corroborating the interpretation that they are active hotspots.

The volcanic rises can present a variety of morphological features, but they usually exhibit large shield volcanoes, rift zones, and coronae. Taking the topographic, geophysical, and morphological characteristics into account, Stofan et al. (1995) argued for the existence of nine volcanic rises on Venus, which they also interpreted as being mantle hotspots. A review containing detailed descriptions of each individual rise can be found in Smrekar et al. (1997).

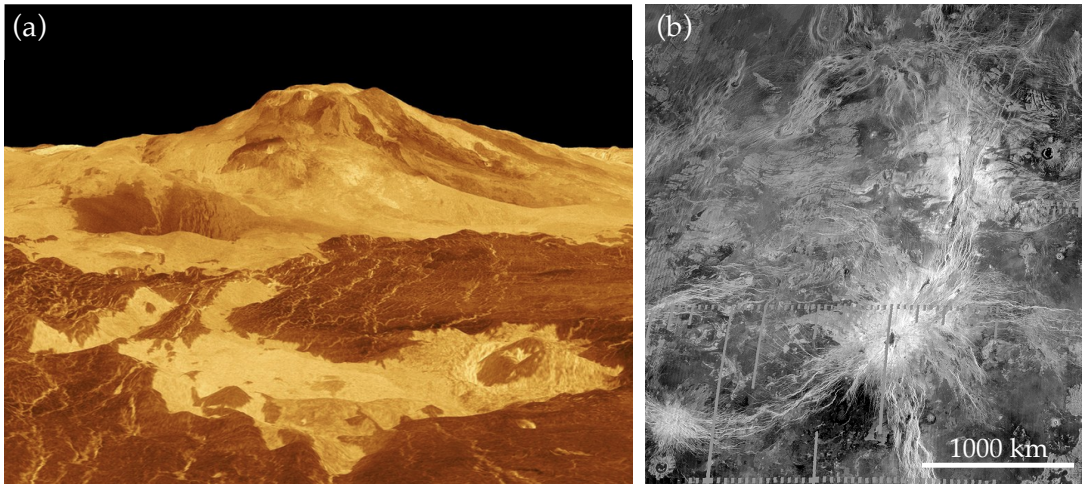

Figure 1.6: Venusian volcanic rises. (a) Perspective view of the large volcanic edifice (about 500 km diameter) Maat Mons located at 1°N and 195°E in the volcanic rise Atla Regio. The image was built using Magellan SAR false-color mosaic combined with topography data and has a vertical exaggeration of 10 times. (b) Magellan SAR image of Beta Regio, located at approximately 29°N and 281°E. This volcanic rise is crossed by a north-south rift called Devana Chasma. The two radar-bright feature represent the large shield volcanoes Theia Mons (Southern) and Rhea Mons (Northern). Images retrieved from the NASA/JPL image gallery.

CRUSTAL PLATEAUS The crustal plateaus, also referred to as highland plateaus or tessera plateaus, are Venusian highlands associated

1 miligals (mGal), named after Galileo, are commonly used units in gravity studies and correspond to 10^{-5} m s^{-2}

with relatively flat-top and steep-sided topography. They have positive moderate gravity anomalies, on the order of tens of miligals, and have been interpreted as regions of isostatic compensation by crustal thickening (e. g., Smrekar and Phillips, 1991; Grimm, 1994; Simons et al., 1997). From a morphology perspective, they are characterized by extremely complex terrains, the so-called tessera, generally presenting fractures and ridges with different intersecting trends indicating that they went through several tectonic events. Tessera morphologies also appear in the form of smaller inliers that have been commonly interpreted as remnants of collapsed plateaus (e. g., Romeo and Turcotte, 2008). Global geological mapping of Venus indicate that tessera regions are stratigraphically the oldest terrains on the planet (e.g., Price and Suppe, 1994; Basilevsky and Head, 1995; Ivanov and Head, 2011). Figure 1.7 shows a regional image of Ovda Regio plateau and a close-up look within the same region showing tessera patterns in detail.

Because of the complex geological history of the plateaus, their origin and evolution have been a topic of intense debate in the 1990s and even today their formation process is poorly understood. The images from Magellan allowed for the investigation of cross-cutting relationships in these terrains. However, there are important disagreements regarding the geological interpretation of this data. Some researchers argued that extensional structures were the first to be formed in these terrains and compression ridges were generated later (e.g., Hansen and Willis, 1996; Hansen et al., 2000). These studies concluded that the plateaus were formed by mantle upwellings, associated with the observed extensive tectonics, followed by a regional subsidence that generated the compressive patterns. Alternatively, Bindschadler et al. (1992a), Gilmore et al. (1997), and others believed that the compressional structures were the earliest to form leading to the interpretation that the plateaus are the result of mantle downwellings with associated crustal thickening. Another possibility is that the plateaus represent regions that "survived" global resurfacing events (which I will further discuss in the next section). In this case, they would correspond to Venusian counterparts of Earth's continents (Grimm, 1994; Romeo and Turcotte, 2008). The crustal plateaus are the focus of one of the studies from this thesis and, so, they will be further discussed in Chapter 6.

CORONAE As presented in Head et al. (1992) and Crumpler et al. (1997), Venus present a large variety of tectonic-volcanic features. Yet, there is one type of structure that has been of distinguished scientific interest: the coronae. Even though coronae were discovered prior to Magellan (Barsukov et al., 1986), the mission revealed over 500 of these unique features (Stofan et al., 2001) spread over the entire planet. Magellan's high-resolution images and topography data showed that

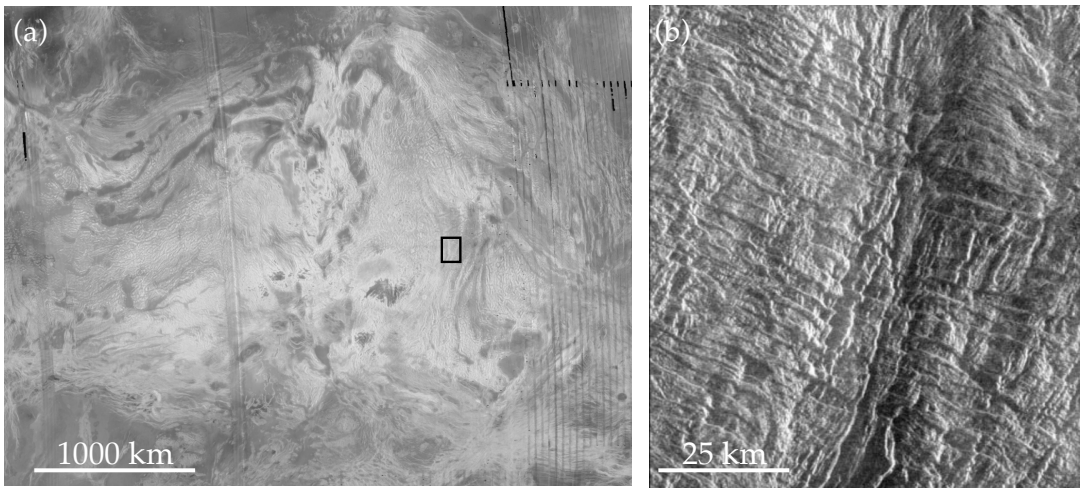

Figure 1.7: Magellan SAR images showing examples of crustal pleteaus on Venus. (a) Magellan SAR image of Ovda Regio, Venus's largest crustal plateau. It is located in the equatorial region, centered at about 5°S and 80°E. (b) Region defined by the black square in panel (a) showing in detail typical patterns found in tessera terrains (retrieved from Ghent and Hansen, 1999).

these circular structures are systematically associated with annuli of concentric fractures and ridges, while presenting a significant diversity of sizes (ranging from about 100 to over 1000 km), morphologies, and topographic shapes (see Stofan et al., 1997, for a review). Moreover, the coronae are not uniformly distributed on the surface, they are usually associated with the volcanic rises and rift zones. Yet, they can also occur as isolated features in the volcanic plains and are very rare on crustal plateaus (Stofan et al., 1992). Figure 1.8 shows examples of coronae (a) in a chain of coronae with diameters of about 200 km along the Parga Chasma rift zone and (b) the Artemis corona, the largest corona of Venus with approximately 2500 km diameter.

Based on their morphological properties, topographical shape, and common correlation with volcanism, the formation of coronae have been mostly attributed to small-scale mantle upwellings (Stofan et al., 1992; Squyres et al., 1992) with possible delamination of the crust at the rims (Smrekar and Stofan, 1997). This interpretation was further supported by recent three-dimensional numerical modeling of small-scale plumes (Gerya, 2014; Gülcher et al., 2020) and mantle convection experiments with complex rheology fluids (Davaille et al., 2017). Studies by Schubert et al. (1994), Johnson (2003), Smrekar et al. (2003), and Hoogenboom et al. (2004) have used gravity and topography data to better understand the interior structure of coronae, even though this type of analysis is challenging since the dimension of most coronae are smaller or comparable to the resolution of Magellan's gravity model. Yet, gravity-topography spectral investigations (Johnson, 2003; Smrekar et al., 2003; Hoogenboom et al., 2004) have shown that some coronae are consistent with a dynamic source of compensation, indi-

cating the presence of active mantle plumes, while others seems to be compatible with an Airy isostasy regime, probably no longer active.

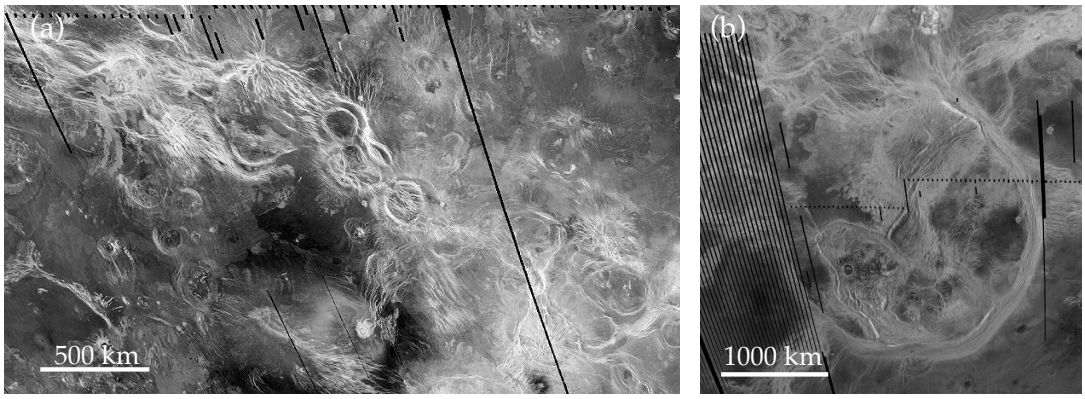

Figure 1.8: Magelan SAR images showing examples of coronae observed on Venus. (a) Chained cluster of coronae located at the Parga chasma rift. The radar-bright area in the south-east correspond to the volcanic rise Themis Regio. The image is centered at 32°S and 275°E, approximately. (b) Artemis, the largest corona on Venus with ~ 2500 km diameter, centered at 35°S and 135°E. Images retrieved from the NASA/JPL image gallery.

CRATER POPULATION AND RESURFACING SCENARIOS When studying the geology of the terrestrial planets, where radiometric dating of rocks is generally not possible, the surface ages are derived from the analysis of the impact cratering record. For a single planetary body, one can investigate relative surface chronology based on the simple but reasonable premise that the older a surface is, the more craters it will accumulate. By taking advantage of the radiometric dating of lunar rocks obtained during the Apollo missions and adopting a series of scaling laws it is possible, in principle, to obtain first-order estimates of the absolute age of any planetary surface based solely on the size-frequency distribution of craters on its surface (see Neukum et al., 2001, and references therein for details). Constraining the surface ages provides fundamental information about the temporal and spatial variations of a planet's geological activity which, in turn, allows for a better understanding of its geodynamical evolution.

With the images obtained by Magellan it was finally possible to perform a comprehensive global analysis of Venus crater population and the findings were quite surprising. Venus presents a total of just ~900 craters with diameters ranging from 1.5 to 270 km. Studies by Schaber et al. (1992), Phillips et al. (1992), and McKinnon et al. (1997) estimated that the mean surface of Venus is about 300 to 750 m.y. old. More recent analyses, that made use of refined impactor populations and scaling laws, have found moderately younger ages, ranging from 150 to 250 m.y. (Feuvre and Wieczorek, 2011; Bottke et al., 2016). These constraints show that the intensity of geological activity on Venus seems to be closer to that of the Earth than to smaller terrestrial plan-

Even though the Moon is not a planet, I will usually include it in the group of terrestrial planets for simplicity. This is commonly done from the perspective of comparative planetology, since the Moon has a complex geology and has been largely explored by planetary missions.

ets, such as Mars, Mercury and the Moon, that have average surface ages of a few billions of years.

Besides being associated with a young surface age, the Venus crater population presents other interesting properties. Investigating the morphology of the craters, Phillips et al. (1992) and Schaber et al. (1992) observed that only a small fraction of the population (less than 15%) presented clear indications of volcanic embayment or tectonic modification. In addition, statistical analyses have demonstrated that the global spatial distribution of craters on Venus are consistent with complete spatial randomness (Phillips et al., 1992; Schaber et al., 1992; Strom et al., 1994), although, as discussed in Hauck et al. (1998), this is not the only statistical model that can explain the observed crater distribution.

With the goal of explaining the observed characteristics of Venus's crater population two end-member hypotheses emerged: equilibrium and catastrophic resurfacing. Phillips et al. (1992) proposed that the Venusian crater population could be explained by the equilibrium between continuous crater production and removal. In this case, volcanic and tectonic processes happen regionally and in a stochastic fashion at a rate that is comparable to the crater production. Alternatively, Strom et al. (1994) advocated that equilibrium resurfacing was not able to satisfactorily account for the low number of lava flooded craters. Instead, they argued that the observations could only be explained by the occurrence of major global geological events that ceased somewhat abruptly around 300 m.y. ago, followed by a great reduction of volcanic and tectonic activity (Schaber et al., 1992; Strom et al., 1994). In this scenario, commonly referred to as the catastrophic resurfacing model, Venus would be in a geologically quiescent period at present day. Hypotheses about the nature of this catastrophic period include voluminous and world-wide volcanism that would have buried all pre-existing craters (Schaber et al., 1992), or a combination of volcanic and tectonic events possibly associated with global crustal recycling (Strom et al., 1994).

On one hand, it is difficult to conceive geological events that are capable of completely resurfacing Venus in a short time-scale. From this perspective, the equilibrium model seems more realistic, particularly if we make a comparison with the Earth, where the geological activity present a more steady-state character. On the other hand, many researches considered that the catastrophic model was able to better explain the observed crater population and so, this model became quite popular. This perspective led to the somewhat disappointing conclusion that Venus is currently a geologically inactive planet. However, new insights from observations and models have been indicating that Venus could be more active than previously thought – these latest views and their implications are presented in Chapter 2.

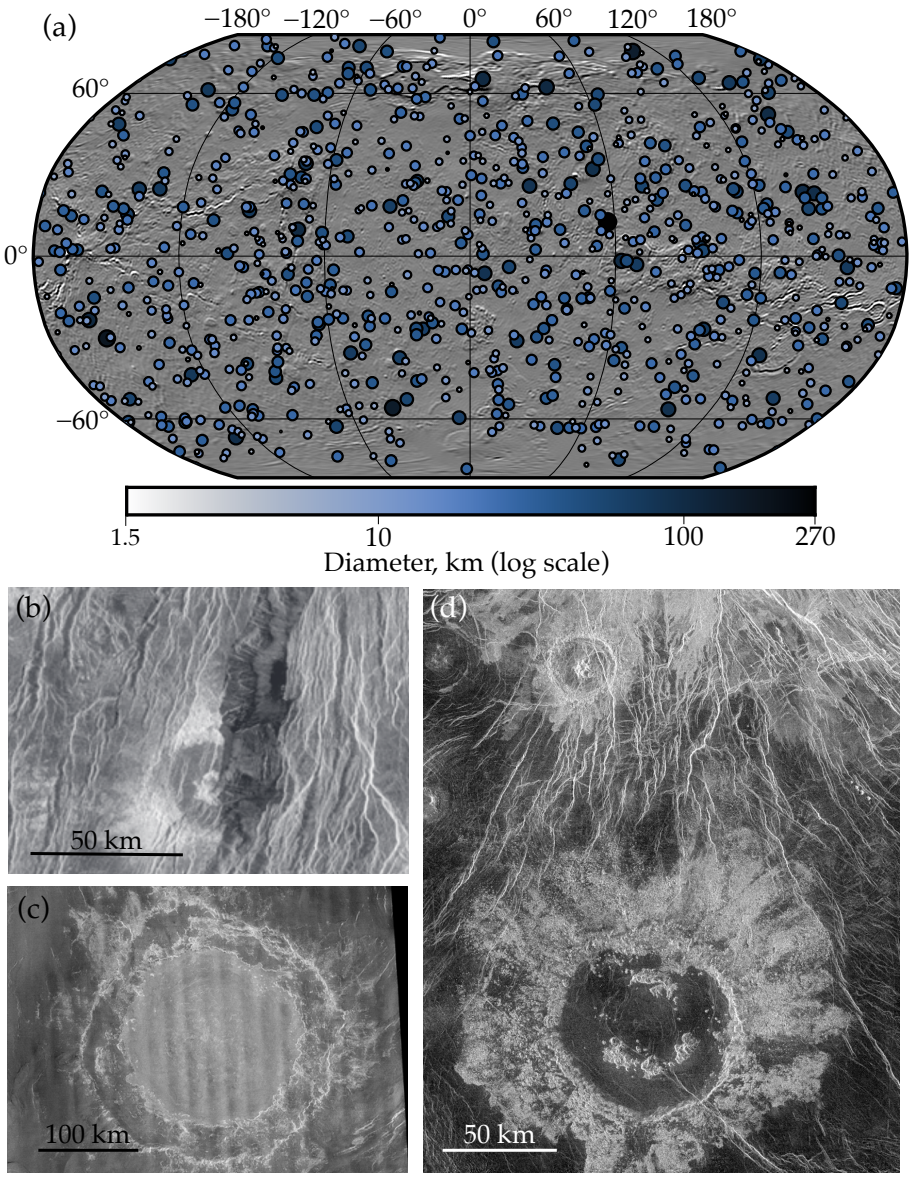

Figure 1.9: Overview of Venus crater population. (a) Topography shaded relief map showing all Venus craters from the database by Herrick et al., 1997 (Robinson projection). The color and size of the circles represent the craters diameter in log-scale. Panels (a), (c), (d) present examples of craters imaged by Magellan. (b) Partial crater located in a rift zone at Beta Regio (location: 30°N and 285°E). (c) Mead multiring impact basin - the largest crater on Venus (~ 270 km diameter), located at 12°N and 57°. (d) 73 km dark-floored crater located at 16°N and 268°E (Wheatley crater) and 26 km fractured and embayed crater located at 18°N and 268°E (Baranamtarra crater).

It is not an understatement to say that the resurfacing of Venus was one of the most polemic research topics of the Magellan era. To obtain a more comprehensive review of this debate, with discussions about the strengths and weaknesses of the two models, I recommend

the chapter by Basilevsky et al. (1997). More recently, a review paper on the resurfacing history of Venus has been put together by Herrick et al. (2023).

2

DE-STAGNATING VENUS

Our sister planet was intensely explored from the 1960s to the 1990s and, as discussed in Chapter 1, major scientific discoveries were made in that period. However, with the end of the Magellan mission in 1994, the focus of planetary exploration shifted elsewhere. Since Magellan, there has been a critical lack of new data and funding dedicated to the planet, leading to a deceleration of Venus science advances. These circumstances can be visualized if we look at the temporal evolution of research papers associated with Venus, as shown in Figure 2.1.

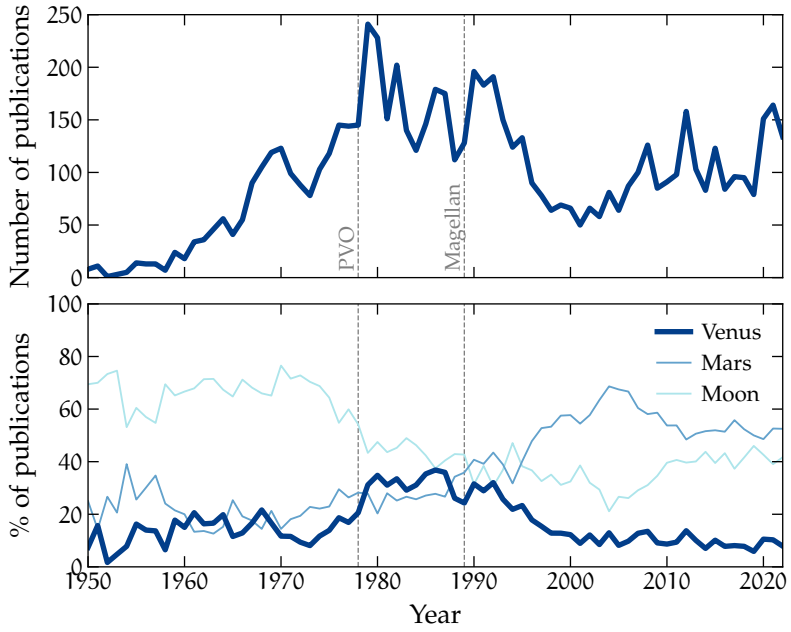

Figure 2.1: Evolution of the number of peer-reviewed publications related to Venus and other planets from 1950 to 2022. (a) Total number of peer-reviewed publications per year associated with Venus. The dashed vertical lines correspond to the launch date of the missions PVO and Magellan. (b) Percentage of peer-reviewed publications associated with Venus, Mars or the Moon with respect to total number of publication with at least one of the three bodies in the title. The data was obtained in the astrophysics data system and the query considered publications that have the planets names in the title. The query terms adopted are *Venus/Venusian*, *Mars/Martian*, or *Moon/Lunar*.

Figure 2.1 also highlights the importance of space missions in planetary science. In the years following the launch of PVO and Magellan, marked by the gray lines, the number of articles per year substantially

increased. This property can also be seen in the trends for the Moon and Mars in panel (b). During the Luna and Apollo programs, Lunar studies dominated the field and gradually drop in the late 1970s. During the 1980s and early 1990s the three planets shared approximately the same proportion of studies. From the 1990s onward, investigating extraterrestrial life and habitability became the main focus of planetary missions, particularly of NASA, which culminated in the "follow the water" program targeting Mars. Meanwhile, within a decade, from 1990 to 2000, the number of Venus-related papers dropped from roughly 200 to 50 papers per year. In the past two decades Venus had only 10% of the relative number of publications with respect to Mars and the Moon.

Even though Venus's science and exploration has stabilized at a low rate since the Magellan era, it is far from a complete stop. Along with the two successful missions Venus Express and Akatsuki that kept the planet's exploration alive (as discussed in Chapter 1), the last few decades have been associated with technological advancements that had major implications to scientific research in general. For example, it is interesting to remember that, at the time of Magellan, NASA's Planetary Data System (PDS) used to give on-demand access to the data products through the delivery of tapes and CD-ROMs (McMahon, 1996). Today, anyone in the world with internet access can get the Magellan datasets with a few clicks in the PDS website. Data analysis also became simpler and faster with the development of modern and commonly open access tools. Finally, the continuous development of powerful computers has been allowing for impressive improvements of numerical simulations, that are becoming increasingly more realistic.

In this chapter, and for the remaining of this thesis, I will show that, even with limited data, taking a fresh look at Venus with new models and analyses techniques can still lead to significant scientific results. Section 2.1 discusses the main paths for Venus geodynamic evolution that have been proposed based on models of mantle convection and thermal evolution. Then, I will present some recent observational evidence suggesting that Venus is probably more geologically active than what was previously thought (Section 2.2). Finally, Section 2.3 presents a panorama of the current state of Venus interior structure constraints.

2.1 THE GEODYNAMIC AND THERMAL EVOLUTION OF VENUS

Along with the Magellan mission, the 1990s were associated with early developments of large-scale numerical models of mantle convection (e. g., Schubert et al., 1990). The goal of these models is to understand at what rate and via which mechanisms a planet loses internal heat throughout its geological evolution. Essentially, this is

done by performing models with a range of different physical properties and evaluating how well each model predicts observations, such as gravity, topography, and surface geology. Naturally, with the new datasets acquired by Magellan, researchers got highly motivated to apply these geodynamic models to Venus and investigate the planet's possible thermal evolution paths and tectonic regimes. The investigations at that time were particularly interested in predicting the properties of Venus's intriguing crater population and testing the proposed resurfacing scenarios (see Section Section 1.3 for details). This section presents the main ideas that have been proposed to describe Venus geodynamics from the Magellan era until today. These different scenarios are illustrated in Figure 2.2 and are discussed below.

Plate tectonics, as we see on Earth, is a very efficient heat-loss mechanism. It is characterized by lithospheric recycling via the active subduction of cold oceanic lithosphere slabs and is associated with effective resurfacing at a global scale (Figure 2.2a). However, the Magellan observations have shown that Venus does not currently have Earth-like plate tectonics . Yet, until today the mechanisms responsible for the planet's heat loss are not well-understood. Throughout the Magellan era, Venus was overall considered to be in a so-called stagnant lid convection regime, where the lithosphere is a single global plate that is nearly immobile. In this framework, a few classes of heat transport mechanisms were investigated (see Schubert et al., 1997, for a review).

Plate tectonics is considered to be a particular type of the so-called mobile lid regime.

One possibility could be that Venus is a typical stagnant lid planet, as is presumed for Mars (e. g., Breuer and Moore, 2015; Tackley, 2023), where the internal heat is lost via conduction through the lithosphere (Figure 2.2b). However, Venus is expected to have a comparable internal heat production to the Earth and such a mechanism would be too inefficient, invariably leading to widespread melting and volcanism (Reese et al., 1999). Volcanism is, in fact, a considerably more efficient way to extract heat from the mantle. The convective regime where volcanism is responsible for most of the lithospheric heat transport is referred to as the "heat pipe" regime (Figure 2.2c). It is commonly interpreted that this regime occurs at Io, a Galilean moon that has hundreds of volcanoes and is extremely active due to tidal heating (e.g., Moore, 2001; Moore and Webb, 2013). However, in the case of Venus, this mechanism has some shortcomings. For example, the large amount of volcanism necessary to cool the planet would form a crust that is over 100 km thick (e. g., Armann and Tackley, 2012), which is inconsistent with the observational constraints (Grimm, 1994; Simons et al., 1997; James et al., 2013).

Another possibility could be that Venus once had some form of plate tectonics. Either as in an Earth-like regime that transitioned into a stagnant lid convection around 500 Ma (Herrick, 1994; Solomatov and Moresi, 1996) or a regime where lithospheric recycling happens episodically alternating with periods of limited geological

Throughout this thesis I consider that Ma *corresponds to 'millions of years ago',* My *to 'millions of years',* Gy *to 'billions of years', and so on.*

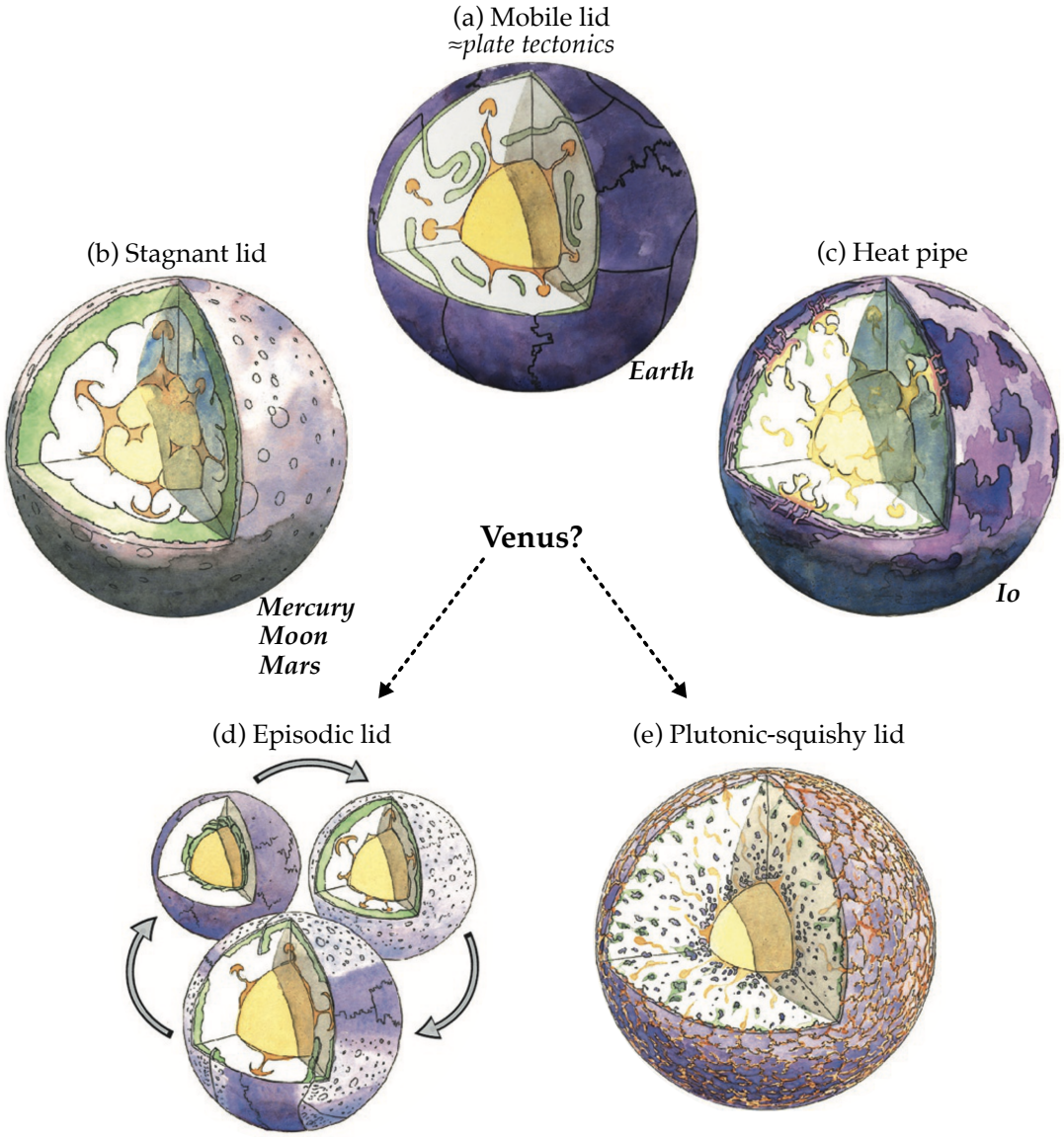

Figure 2.2: Schematic view of different tectonic regimes predicted by geodynamic thermal evolution models The yellow region in the center of the planet represents the core. As for the mantle, orange features represent upwelling plumes while green features represent downwelling. The outer purple layer represents the crust, where the darker is the tone, the younger (and less cratered) is the surface. The illustrations are from Lourenço and Rozel (2023).

activity, which is referred to as episodic-lid regime (e. g., Turcotte, 1993; Fowler and O'Brien, 1996). In this regime, the lithosphere transports heat predominantly through conduction for a certain period of time. At that stage, the lithosphere goes through a thickening process and, because the heat transport through the lid is inefficient, the mantle temperature and its convective vigor increase. At a critical moment the thick lithosphere becomes unstable triggering a global subduction event. Then, new lithosphere is formed and the process restarts. These different stages are illustrated in Figure 2.2d.

The episodic lid regime is not only consistent with the catastrophic resurfacing scenario, but recent thermal evolution simulations have shown that it also results in more reasonable crustal thicknesses in comparison to purely stagnant lid case (Armann and Tackley, 2012; Rolf et al., 2018). The view that Venus has been through major, potentially cyclic, tectonic regime variations and is currently in a quiescent period became quite popular and, even today, is considered to be a possible scenario for the geodynamic evolution of the planet. The dynamical processes that lead to the global surface mobilization events and at which rate they occur are still topics of active research (Armann and Tackley, 2012; Noack et al., 2012; Gillmann and Tackley, 2014; Rolf et al., 2018; Karlsson et al., 2020; Weller and Kiefer, 2020).

In recent studies by Rozel et al. (2017), Lourenço et al. (2018), and Lourenço et al. (2020), state-of-the-art geodynamic thermal evolution models were used to comprehensively test the role of magmatic processes in global tectonic regimes. In particular, they investigated the case where magma is mostly emplaced intrusively in the lithosphere, instead of being directly extract to the planet's surface as in the heat pipe regime. These studies have shown that the heat from magmatic intrusions makes the lithosphere warm and soft. These weakening effects lead to regional-scale, but globally-spread, lithospheric delamination which, in turn, allows for sustained crustal recycling. Surprisingly, even without large-scale subduction events, the regional delamination processes are capable of efficiently cooling down the planet Lourenço et al. (2018). This new tectonic regime is referred to as plutonic-squishy lid and is schematically represented in Figure 2.2. As shown in the illustration, in this regime the lithosphere is broken into many small plates, separated by weak boundaries that were generated by the intrusive magmatism.

In practice, it is very difficult to constrain intrusive to extrusive ratios of magmatism. Studies focused on Earth observations have found large variability for different sites. Yet, a 20% eruption efficiency could be viewed as common to most magmatic systems (White et al., 2006).

Even though it is still early to confirm that Venus is governed by squishy-lid tectonics, the model presents several attributes that are consistent with Venus's observations. Notably, the wide-spread lithospheric delamination not only allows for an efficient heat loss, but also leads to relatively thin crustal and lithospheric thicknesses, which, as already mentioned, is consistent with geophysical constraints. Moreover, the characteristics and distribution of magmatism and tectonism associated with the "squishy" plates could convincingly be responsible for efficient and randomly distributed resurfacing as predicted by the equilibrium resurfacing model. Most importantly, squishy-lid tectonics points towards a currently more active Venus than what has been suggested by episodic lid studies. As I discuss in the next section, this scenario corroborates an increasing number of studies that have been suggesting that Venus is, in fact, a geologically active planet today.

2.2 A NEW HOPE

2.2.1 *Surface sneak peeks from Venus Express*

One of the most poorly constrained geological properties of Venus is its surface composition. Even though the composition data taken from the Soviet landers are unarguably valuable, these almost 50-years old measurements are not very detailed nor precise and only investigated a few elements. More importantly, they do not provide a global knowledge of the surface composition and how it correlates with the planet's geology. In the scope of planetary sciences, this kind of investigation is typically done using orbital infrared spectroscopy (e. g., Kramer et al., 2011; Ehlmann and Edwards, 2014; Namur and Charlier, 2016) and orbital gamma ray spectroscopy citexx. However, in the case of Venus these standard spectroscopy investigations are not possible due the planet's extreme atmospheric conditions. Hence, it was a great surprise when, during a Venus flyby in 1991, the Galileo mission found small atmospheric windows in the CO_2 spectrum at around 1 µm (Carlson et al., 1991). This discovery indicated that remote sensing investigations of Venus's surface composition could be possible even if limited (e. g., Hashimoto, 2003).

Motivated by this discovery, the Venus Express spacecraft was equipped with a imaging spectrometer, named VIRTIS, that included a mid-infrared channel capable of looking through the atmospheric windows. Making use of the VIRTIS data, and with the development of a complex processing pipeline to remove a range of atmospheric effects, the first surface infrared emissivity map of Venus was created (Mueller et al., 2008). The map covers most of the southern hemisphere of Venus and has provided several interesting insights about the planet's surface composition.

The early investigations of the emissivity data by Helbert et al. (2008) and Mueller et al. (2008) were able to identify that young volcanic flows at Lada Terra, Themis Regio, and, Imdr Regio are associated with high emissivity anomalies. Notably, Imdr and Themis are two volcanic rises interpreted to be active hotspots (e. g. Stofan et al., 1995). The authors proposed that the anomalies could be either the result of differences in composition or an indication that the most recent flows are relatively unweathered. A detailed study of these emissivity anomalies was later performed by Smrekar et al. (2010) who favored the surface weathering interpretation and estimated that the high-emissivity lava flows should be younger than 2.5 My (Figure 2.3a). More recently, laboratory analyses of olivine weathering rates have shown that, under Venus's extreme atmospheric conditions, chemical weathering alterations occur extremely quickly (Filiberto et al., 2020). Their study proposed that flows associated with high emissiv-

ity anomalies should be no more than several years old, indicating that the planet is currently volcanically active.

The VIRTIS emissivity dataset also showed that the tessera regions are overall correlated with lower than average surface emissivities (Mueller et al., 2008). A similar conclusion was obtained by Hashimoto et al. (2008) from the analysis of emissivity data obtained by the Galileo spacecraft. Both Mueller et al. (2008) and Hashimoto et al. (2008) proposed that this could be an indication that tessera are composed of felsic rocks. These results support the hypothesis that tessera regions, in particular the crustal plateaus, are ancient continent-like regions that have survived resurfacing processes throughout Venus geological history. Gilmore et al. (2015) further investigated the low emissivity anomalies focusing the analysis on Alpha Regio which is the largest tessera terrain mapped by the VIRTIS instrument (Figure 2.3b). Their study confirmed that the observed anomalies are associated with intrinsic properties of the terrain and proposed a few possible explanations, including differences in grain sizes, weathering environment, and a silica-rich composition, such as granitoids or anorthosites.

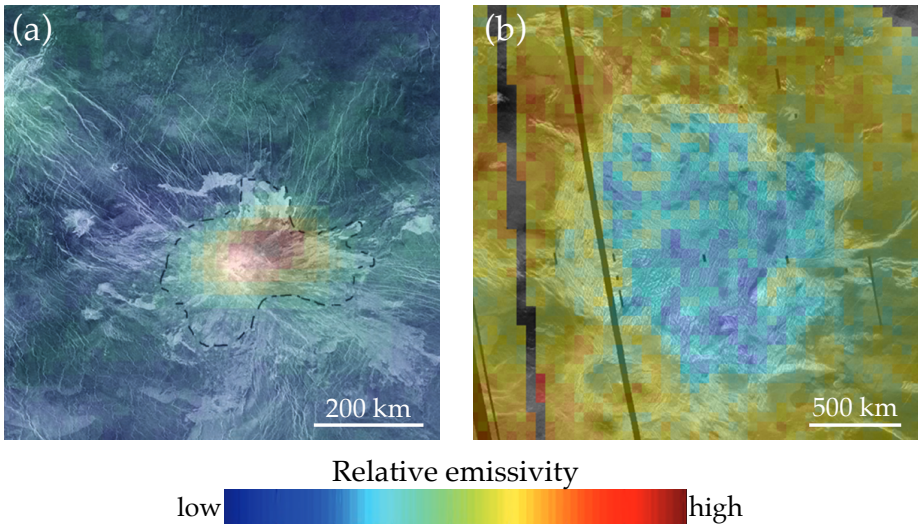

Figure 2.3: Magellan SAR images overlain by the surface emissivity obtained by the VIRTIS spectrometer onboard of Venus Express. The emissivity color scale is different for the two panels. (a) Map of the high emissivity anomalies over the volcano Idunn Mons at Imdr Regio, located at 215°E and 46°S. (b) Low emissivity anomalies associated with the crustal plateau Alpha Regio. The map is approximately centered at 25°S and 5°E. The images are reproduced from (a) Gilmore et al. (2015) and (b) Smrekar et al. (2010).

2.2.2 *Magellan data: the digging continues*

In the 1990s, the catastrophic resurfacing model gained support because it could easily explain Venus's crater population. Nevertheless, in the past decade or so, perhaps propelled by the exciting results from Venus Express, the view of a more active Venus has been getting a lot of traction. After all, the surface of Venus shows clear indications of substantial geological activity, including pervasive rift zones covering about 8% of the total surface area (Price et al., 1996), hundreds of corona structures (Stofan et al., 2001), and thousands of volcanoes of all shapes and sizes (85 thousand to be exact, based on the updated catalog by Hahn and Byrne, 2023). Therefore, it is difficult to picture that, for the last ~200 My, Venus has been a typical, quiet stagnant lid planet. A key circumstance for this change in perspective is the substantial improvements in Monte Carlo resurfacing models. In particular, studies by Bjonnes et al. (2012) and O'Rourke et al. (2014) have shown that equilibrium resurfacing models can adequately predict the Venusian crater population, including the low number of modified craters.

Another important contribution is the growing number of studies that have been presenting evidence of current geological activity on the planet. Detailed analyses of stratigraphic relations of several volcanic regions indicate that lava flows and tectonic activity are geologically recent and probably occurred at most around tens of millions of years ago (D'Incecco et al., 2017; D'Incecco et al., 2020; Brossier et al., 2020; Brossier et al., 2021). Other interesting insights have been obtained via thermomechanical modeling of coronae formation by Gülcher et al. (2020) which indicated that dozens of these features could be associated with currently active mantle plumes. In addition, the stereo topography dataset create by Herrick et al. (2012) allowed for analyses of the flexural signature of coronae and steep-sided domes (O'Rourke and Smrekar, 2018; Russell and Johnson, 2021; Borrelli et al., 2021; Smrekar et al., 2023). These studies have shown that coronae and the steep-sided domes located near coronae typically present anomalously thin lithosphere which can be associated with high surface heat flows, strengthening the arguments for present-day geological activity in these regions. Finally, earlier this year, Herrick and Hensley (2023) found, for the first time, a direct detection of volcanic activity. They observed a change in the shape of a volcanic vent and plausibly a new lava flow by comparing SAR images of the same region obtained 9 months apart by Magellan.

Steep-sided domes, or pacake domes, are circular flat-topped volcanic features commonly associated with viscous flows (e.g., Head et al., 1991)

2.3 INTERIOR STRUCTURE CONSTRAINTS

Our knowledge about the interior of Venus is extremely limited. Essentially, all available information is based on a few geophysical ob-

servations: the moment of inertia, the love number k_2, and the gravity field of the planet. The first two quantities, which are associated with the planet's precession and tidal potential, respectively, can give insights about the physical properties of the core and mantle. Alternatively, the gravity field, which is controlled by the mass distribution within the planet, can provide information about the interior structure of the crust and (mostly upper) mantle. The analysis of gravity data is particularly powerful when coupled with topography and, by making use of some reasonable assumptions, allows for the estimation of a variety geophysical quantities, including the crustal thickness, the lithosphere thickness, the distribution of density anomalies in the mantle, and the viscosity structure of the mantle.

The moment of inertia of Venus was recently determined by Margot et al. (2021) using 15 years of precise ground-based observations of the planet's precession rate. The study obtained constraints of 0.337 ± 0.024 (about 7% uncertainty) for the normalized moment of inertia and confirmed that the planet has a high density core with a radius of about 3000 to 4000 km. As for the tidal love number k_2 , the currently most precise constraints are based on radio tracking data from PVO and Magellan and were estimated by Konopliv and Yoder (1996), who found a value of 0.295 ± 0.066. k_2 indicates how a planet deforms due to gravitational forces from other celestial objects and it is mostly controlled by the rheological properties of the mantle, and the state and size of the core. The large uncertainties of these parameters have overall prevented the estimation of fundamental interior properties of Venus. Recent interior structure investigations have shown that with the current estimates it is not possible to obtain reliable constraints of Venus's core size and state (Dumoulin et al., 2017; Xiao et al., 2021; Shah et al., 2022; Saliby et al., 2023). In fact, according to these studies, the core is consistent with being fully liquid, having an inner solid core and an outer liquid core, and being completely solid. In addition, it is important to remark that the core state of terrestrial planets is intrinsically related to the presence of an internal dynamo and provides essential information about their magnetic field history.

Several studies have attempted to provide estimates of Venus's crustal thickness once the gravity and topography datasets from Magellan were available. Figure 2.4 shows, in chronological order, examples of crustal thickness estimations from eight different studies at three regions on Venus. At the time of Magellan, many investigations were made in the spatial domain by analyzing the ratio between gravity and topography of different Venusian regions (Smrekar and Phillips, 1991; Kuncinskas and Turcotte, 1994; Moore and Schubert, 1997). These studies obtained crustal thickness estimation of several highlands by considering that the regions were in a Airy isostasy regime, where the topography is compensated by crustal roots. Mean-

while, localized spectral techniques started being applied to Venus (Grimm, 1994; Phillips, 1994; Simons et al., 1997). This type of method aims to analyze wavelength-dependent signatures of gravity and topography at different regions. Spectral techniques have several advantages over spatial ones. For example, it allows for the analysis of variations in the mode of compensation with respect to wavelength. In addition, it can be used to investigate the contribution of lithospheric flexure in the support of topography allowing for the determination of both crustal thickness and the thickness of the elastic lithosphere. More recent gravity-topography investigations have focused on the construction of global maps of crustal thickness and/or elastic thickness James et al., 2013; Jimenez-Diaz et al., 2015. Although these analyses give important constraints on the crustal thickness variations throughout the entire planet, they have the drawback of depending on the choice of an average crustal thickness value which is, to some extent, arbitrary.

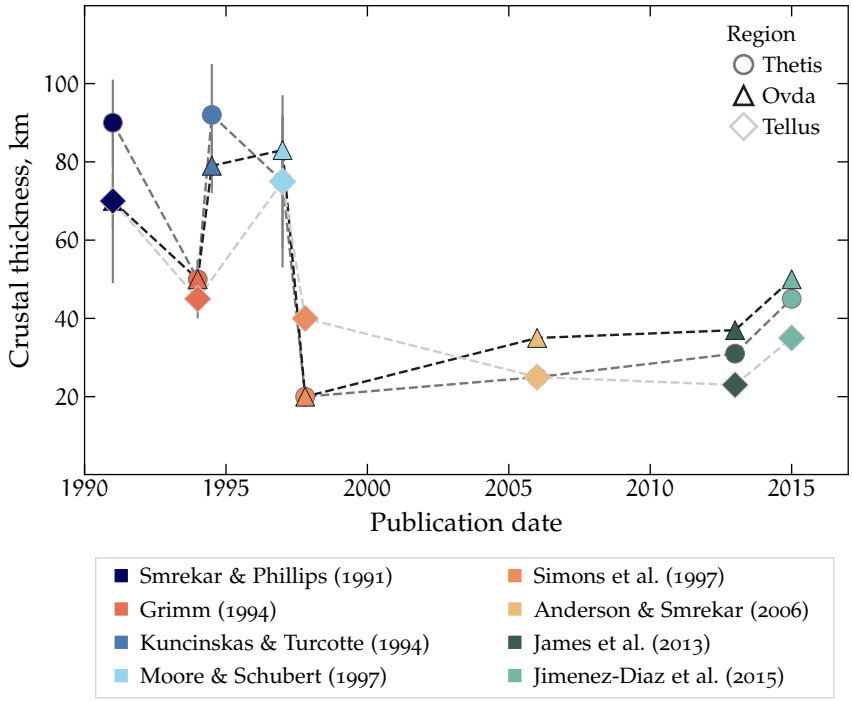

Figure 2.4: Examples of crustal thickness estimations of three crustal plateaus on Venus, Thetis, Ovda, and Tellus. The estimations are plotted in chronological order. The marker style indicates the region investigated and its color indicates the associated study. Blue shades are associated with spatial techniques, orange shades represent spectral techniques, and green shades represent global crustal thickness modeling results.

The geophysical properties of Venus's mantle have been mostly studied through the analysis of the long-wavelength ($\gtrsim$ 1000 km) gravity and topography signatures of the planet, which are believed

to predominantly associated with convective flows in mantle. Numerical and analytical modeling approaches have been adopted to investigate the mantle viscosity structure (Kiefer et al., 1986; Kiefer and Hager, 1991; Herrick and Phillips, 1992; Nimmo and McKenzie, 1996; Huang et al., 2013; Rolf et al., 2018). These studies concluded that Venus's viscosity profile was inconsistent with an "Earth-like" structure, where the upper mantle, going from the base of the lithosphere down ~700 km depth, would correspond to a low viscosity zone. Instead, they found that an isoviscous mantle could better explain the observed gravity and topography. In addition, Monte Carlo inversions by Pauer et al., 2006 showed that the mantle viscosity increases with depth. Plume modeling studies have also attempted to estimate the lithosphere thickness of the planet. Some studies suggested that the lithosphere of Venus should be 200–400 km thick potentially presenting lithospheric thinning on top of mantle plumes (Kuncinskas and Turcotte, 1994; Solomatov and Moresi, 1996). Alternatively, investigations by Smrekar and Parmentier (1996), Nimmo and McKenzie (1996), and Nimmo and McKenzie (1998) proposed that the planet has a globally thinner lithosphere, with thicknesses of about 100 to 200 km.

The "lithosphere" here correspond to the outermost layer of the planet where heat is mainly transported through conduction as opposed to the underlying convective mantle. This layer is also commonly called thermal lithosphere.

The joint analysis of gravity and topography is the main focus of the studies and will be thoroughly discussed throughout this thesis. The focus of work presented here is to reassess many of these interior structure estimations by adopting state-of-the-art geophysical models, analysis techniques and inversion methods. In these analyses, I was particularly careful in providing robust evaluations for the uncertainties of the parameters estimations, which has been somewhat of overlooked in most previous works. The second part of this manuscript, composed by chapters 3 to 5, sets the groundwork of my investigations. It includes the definition of the main equations that set the base for gravity investigations (Chapter 3), a description of the gravity and topography datasets (Chapter 4), and a description of geophysical models used Chapter 5. In Part III, I present the main studies performed during my PhD, which includes new constraints of the crustal thickness and elastic lithosphere thickness of crustal plateaus (Chapter 6) and new insights on the viscosity structure of Venus's mantle (Chapter 7). The conclusions and some considerations about ongoing and future work are presented in Part IV.

Part II

GRAVITY AND TOPOGRAPHY: DATA, MODELS, AND ANALYSIS TECHNIQUES

3

SPECTRAL ANALYSIS ON THE SPHERE

Given the approximately spherical shapes of hte planets, quantities such as gravity and topography are usually defined on the surface of a sphere. In this context, it is convenient to analyze these quantities using spherical harmonics. Their use is particularly important for smaller planets, such as Mars and the Moon, or large-scale structures on bigger planets, such as Venus and Earth, since Cartesian methods can introduce undesirable distortions and biases to the analysis (e.g., Audet, 2014). In this chapter, I present key concepts of spherical harmonics (Section 3.1) and definitions used specifically in the context of gravity field investigations (Section 3.2). In Section 3.3, I describe techniques to localize the gravity and topography data that can be used to perform regional geophysical investigations. Most of the concepts presented here further discussed in review works such as Kaula (1966), Phillips and Lambeck (1980), and Wieczorek (2015a).

3.1 SPHERICAL HARMONICS OVERVIEW

Spherical harmonics are the natural set of orthogonal basis functions on the surface of the sphere. Their linear combinations allow to express f as

$$f(\theta, \phi) = \sum_{\ell=0}^{\infty} \sum_{m=-\ell}^{\ell} f_{\ell m} Y_{\ell m}(\theta, \phi), \tag{3.1}$$

where $Y_{\ell m}$ is the spherical harmonic function of degree ℓ and order m, $f_{\ell m}$ is the corresponding spherical harmonic expansion coefficient, and θ and ϕ represent the position on the sphere in terms of planetocentric colatitude and longitude, respectively. The spherical harmonic functions are composed of the product of trigonometric function in longitude and Legendre functions in latitude. Their mathematical definition is presented in Appendix A. Note that for real datasets the infinite sum of eq. 3.1 is actually truncated based on the resolution of the data. In fact, the spherical harmonic degrees are by definition associated with an angular resolution and, given a mean planetary radius R, they can be directly associated with a Cartesian wavelength λ using

In planetocentric coordinates the colatitude is measured with respect to the polar axis. In addition, the origin of the system is at the center of the planet.

$$\lambda \approx \frac{2\pi R}{\sqrt{\ell(\ell+1)}} \tag{3.2}$$

which is known as the Jeans relation.

In order to easily visualize the spherical harmonic functions, one can make use of the property that in the longitudinal direction they have $2|m|$ zero-crossing while the latitudinal direction is characterized by $\ell - |m|$ zero-crossings. Hence, when $m = 0$ the function only has variations with respect to the latitude and when $\ell = |m|$ the variations are purely longitudinal. These two special cases are referred to as zonal and sectoral functions, respectively, while all others cases are called tesseral. In Figure 3.1(a), I present the spherical harmonic functions for $\ell \leqslant 4$ and $m \geqslant 0$ while Figure 3.1(b) shows maps of the shape of Mars built from spherical harmonic functions (eq. 3.1) for different maximum spherical harmonic degrees ℓ_{max}. We can see that $\ell_{max} = 0$ corresponds to the mean planetary radius of Mars, for $\ell_{max} = 2$ the dominating signal comes from the planet's hydrostatic flattening due to its rotation. When $\ell_{max} = 10$ one can start distinguishing major geologic features, in particular the Tharsis Province, and for $\ell_{max} = 500$ several features are clearly visible, including volcanoes, rift zones and impact basins. These maps are based on the spherical harmonic coefficients from the dataset MarsTopo2600 (Wieczorek, 2015a).

The zonal coeffcients are commonly defined as $-J_\ell$

In this work, I use real spherical harmonics and adopt the so-called 4π-normalization convention. Using the orthogonality properties of the spherical harmonic functions (eq. A.4), eq. 3.1, and a generalization of Parseval's theorem, it can be shown that the total power of a real function can be related to its spectral coefficients by

$$\frac{1}{4\pi}\int_{\theta=0}^{\pi}\int_{\phi=0}^{2\pi}[f(\theta,\phi)]^2\sin\theta\,d\theta\,d\phi = \sum_{\ell=0}^{\infty} S_{ff}(\ell), \tag{3.3}$$

where

$$S_{ff}(\ell) = \sum_{m=-\ell}^{\ell} f_{\ell m}^2 \tag{3.4}$$

is the power spectrum of the coefficients $f_{\ell m}$. In a similar fashion, we can define the cross-power spectrum of two function f and k as

$$S_{fk}(\ell) = \sum_{m=-\ell}^{\ell} f_{\ell m} k_{\ell m}. \tag{3.5}$$

3.2 GRAVITY, POTENTIAL, AND ADMITTANCE

According to Newton's universal law of gravitation, in a system with two bodies with masses m and M (where $M \gg m$) and positions $\mathbf{r}$ and $\mathbf{r}_\oplus$, the gravitational acceleration $\mathbf{g}$ of the particle of mass m reads:

$$\mathbf{g}(\mathbf{r}) = -G\,M\frac{\mathbf{r}-\mathbf{r}_\oplus}{|\mathbf{r}-\mathbf{r}_\oplus|^3} \tag{3.6}$$

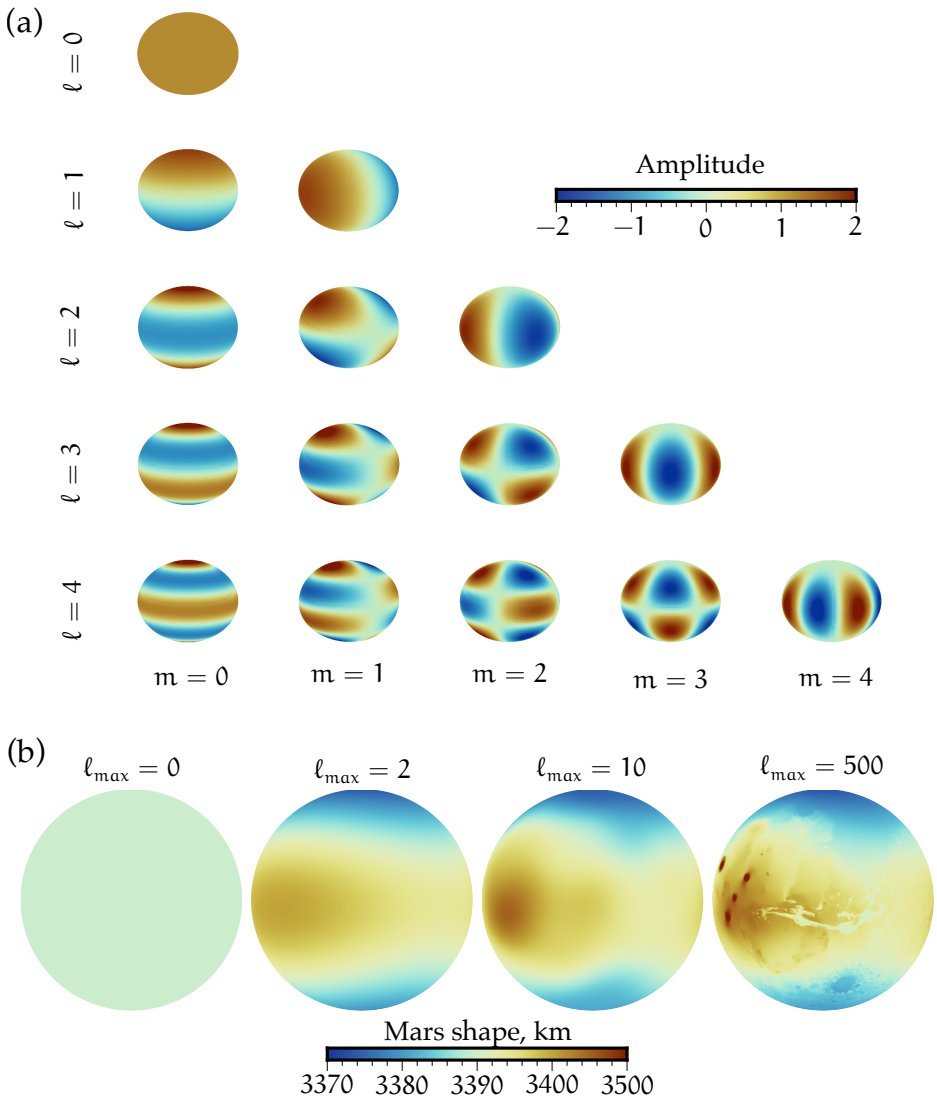

Figure 3.1: (a) Spherical harmonic functions for $\ell \leqslant 4$ and $m \geqslant 0$. The panels in the first column corresponds to zonal functions while those in the main diagonal are sectoral functions. (b) Mars's shape built from spherical harmonic functions for different maximum degres ℓ_{max} in orthographic projection centered at 300° longitude. The adopted colormap, as well as all colormaps used in this thesis, are from the scientific colomaps library by Crameri (2018). For details on the importance of perceptually uniform colormaps see Crameri et al. (2020)

where G is the gravitational constant. Given that $\mathbf{g}$ is associated with a conservative force, we can also express this acceleration as the gradient of a scalar potential:

$$\mathbf{g}(\mathbf{r}) = \nabla U. \tag{3.7}$$

The gravitational potential U associated with a body of mass distribution $M = \int_V \rho(\mathbf{r}_\oplus) dV'$ can be defined as

$$U(\mathbf{r}) = \int_V \frac{G\rho(\mathbf{r}_\oplus)}{|\mathbf{r} - \mathbf{r}_\oplus|} dV' \tag{3.8}$$

where V is the volume and $\rho(\mathbf{r}_\oplus)$ is the density distribution of the body. Exterior to the body, the gravitational potential satisfies the so-called Laplace equation

Note that the sign convention used in eqs.3.7 and 3.8 is consistent to what is used in geodesy studies and opposite to the one commonly used in physics and other disciplines.

$$\nabla^2 U = 0 \tag{3.9}$$

where ∇^2 is the Laplacian operator. In spherical coordinates eq. 3.9 has the form

$$r^2 \frac{\partial^2 U}{\partial r^2} + 2r\frac{\partial U}{\partial r} + \frac{\partial^2 U}{\partial \theta^2} + \cot\theta \frac{dU}{d\theta} + \frac{1}{\sin^2\theta}\frac{\partial^2 U}{\partial \phi^2} = 0. \tag{3.10}$$

A detailed development of the solution of this differential equation can be found in the literature such as Kaula (1966) and Hofmann-Wellenhof and Moritz (2006). In brief, the standard way of solving this equation is by separating the variables as $U(r, \theta, \phi) = F(r)\,\Theta(\theta)\,\Phi(\phi)$ in eq. 3.10 and dividing it by $F\Theta\Phi$, which yields

$$\frac{1}{F}\left(r^2\frac{\partial^2 F}{\partial r^2} + 2r\frac{\partial F}{\partial r}\right) + \frac{1}{\Theta}\left(\frac{\partial^2\Theta}{\partial\theta^2} + \cot\theta\frac{\partial\Theta}{\partial\theta}\right) + \frac{1}{\Phi}\frac{1}{\sin^2\theta}\frac{\partial^2\Phi}{\partial\phi^2} = 0. \tag{3.11}$$

The first term in eq. 3.11 is only dependent on the radial coordinate r, hence it must have a constant value. Denoting the constant as $\ell(\ell+1)$ we can write

$$r^2\frac{\partial^2 F}{\partial r^2} + 2r\frac{\partial F}{\partial r} - \ell(\ell+1)F(r) = 0 \tag{3.12}$$

which has solution of the form

$$F(r) = Ar^\ell + Br^{\ell-1} \tag{3.13}$$

where A and B are arbitrary constants. Since we are interested in the case where the potential in free space vanishes at infinity, A must be set to zero.

In a similar fashion, we can separate the angular component of eq. 3.11 into purely θ- and ϕ-dependent parts and solve them individually. Then, it can be shown that the solution of the angular portion in fact corresponds to the spherical harmonic functions $Y_{\ell m}(\theta, \phi)$ where ℓ and m must be integers for physically meaningful solutions. Hence, we can write the potential as

$$U(\mathbf{r}) = \frac{1}{r}\sum_{\ell=0}^{\infty}\sum_{m=-\ell}^{\ell}\left(\frac{1}{r}\right)^\ell u_{\ell m} Y_{\ell m}(\theta, \phi). \tag{3.14}$$

Given that the coefficient $u_{\ell m}$ have somewhat unpractical dimensions, it is a convention within the geodesy and geophysical communities to use a scaled version of eq. 3.14 in the form

$$U(\mathbf{r}) = \frac{GM}{r} \sum_{\ell=0}^{\infty} \sum_{m=-\ell}^{\ell} \left(\frac{R_0}{r}\right)^{\ell} C_{\ell m} Y_{\ell m}(\theta, \phi) \tag{3.15}$$

where $C_{\ell m}$ are dimensionless spherical harmonic coefficients of the gravitational potential at a reference radius R_0.

Taking the first partial derivative with respect to r of eq. 3.15, we obtain the radial component g of the gravitational acceleration:

$$g = \frac{GM}{r^2} \sum_{\ell=0}^{\infty} \sum_{m=-\ell}^{\ell} \left(\frac{R_0}{r}\right)^{\ell} (\ell + 1)\ C_{\ell m} Y_{\ell m}(\theta, \phi). \tag{3.16}$$

This calculation ignores the effect of the rotational potential and uses the sign convention that the gravitational acceleration is positive in the downward direction. In the context of geophysical investigations, the Galileo ($1\,\mathrm{Gal} = 10^{-2}\,\mathrm{m\,s^{-2}}$) is the standard unit used to quantify gravity perturbations. The density structure in planetary interiors usually causes gravity anomalies on the order of hundreds of miligals, therefore it is conventional to use mGal units when presenting gravity data.

The geoid is another important quantity in geodesy and geophysics. It correspond to a surface that has a constant value of the potential, i. e., an equipotential surface. The height N of an equipotential surface above a sphere with radius R_N can be obtained by approximating the potential $U(R + N)$ using a Taylor series and equating this expression to a constant value, commonly chosen to be the degree-0 term of the potential. As discussed in Wieczorek (2015a, eqs. 20-24), for planets with limited flattening such as Venus, using only up to the first-order term of the Taylor series is usually a sufficient approximation. In this scenario, we can define

$$U(R_N + N) \approx U(R_N) + \frac{dU(R_N)}{dr} N = \frac{GM}{R_N}. \tag{3.17}$$

Then, by approximating the first derivative of U to $-GM/R_N^2$, the geoid is given by

$$N \approx R_N \sum_{\ell=2}^{\infty} \sum_{m=-\ell}^{\ell} \left(\frac{R_0}{R_N}\right)^{\ell} C_{\ell m} Y_{\ell m}(\theta, \phi). \tag{3.18}$$

Note that the degree-1 term is set to zero which corresponds to the scenario where the origin of the coordinate system is defined at the center of mass of the body. Moreover, in this approximation, we neglect the pseudopotential term associated with the centrifugal force caused by the body's rotation which primarily affects the degree-2.

However, given the slow rotation of Venus, this term can generally be neglected.

An important particularity of the radial gravity in comparison with the potential and the geoid is the presence of the term $(\ell+1)$ which gives a greater importance to the higher-degree terms. This effect can be seen in the Venus maps shown in Figure 3.2. The radial gravity (a) tends to highlight the short-wavelength variations while the geoid (b) has a smooth appearance. These maps make use of the Magellan dataset MGNP180U (Konopliv et al., 1999) which are described in detail in Chapter 4.

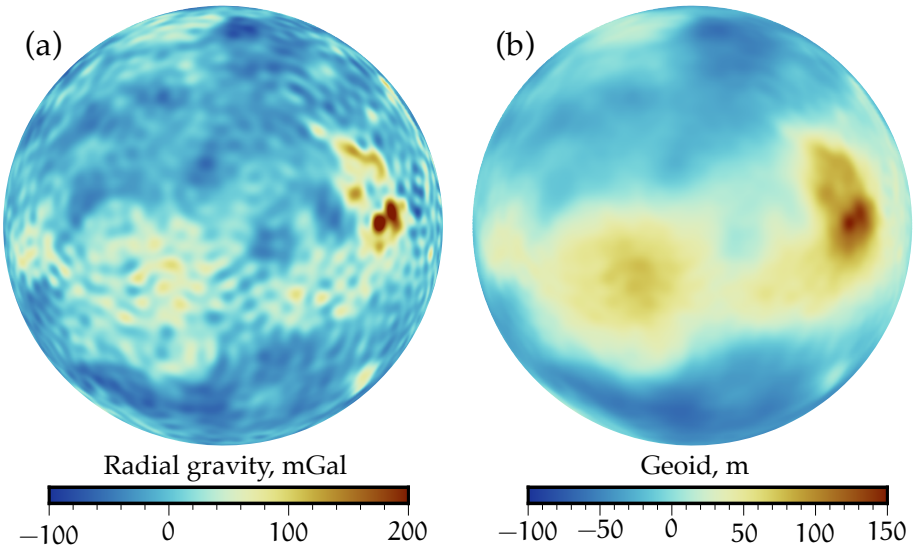

Figure 3.2: Venus maps of (a) radial gravity and (b) geoid showing Aphrodite Terra. Maps are in orthographic projection centered at 150° longitude based on the MGNP180U gravity solution (Konopliv et al., 1999).

The studies presented in this thesis aim to explore the relation between the gravity field and the topography of Venus, either assuming that the gravity signatures are associated with lithospheric deformations caused by the topography or assuming that gravity and topography are expressions of the same geophysical processes in the planet interior. These mechanisms are explored by making use of geophysical models, as detailed in chapter Chapter 5. In this context, it is useful to define quantities that allow for a quantitative evaluation of this relation, such as the spectral admittance Z and correlation γ. The admittance is defined as the amplitude ratio between gravity and topography per spherical harmonic degree

$$Z(\ell) = \frac{S_{hg}(\ell)}{S_{hh}(\ell)}, \tag{3.19}$$

while the correlation γ that characterizes the phase relation between the two quantities is defined as

$$\gamma(\ell) = \frac{S_{hg}(\ell)}{\sqrt{S_{hh}(\ell)S_{gg}(\ell)}}, \tag{3.20}$$

where S_{hh} is the power-spectrum of the topography coefficients $h_{\ell m}$, S_{gg} is the power-spectrum of the gravity coefficients, and S_{hg} is the cross-spectrum between gravity and topography. When considering the radial gravity, the admittance has units of $\mathrm{mGal\,km^{-1}}$. The correlation, which is dimensionless, has its values bounded between -1 and 1. If $\gamma = 1$, gravity and topography are perfectly correlated, while $\gamma = -1$ indicates that they are perfectly anticorrelated and $\gamma = 0$ indicates that they are uncorrelated. A third quantity that has been broadly used is the so-called coherence, defined as γ^2. I usually prefer using the correlation and not the coherence because the later loses the sign information, even though anti-correlations are not typically observed on Venus.

Note that if the geoid is used instead of the gravity, the admittance has the somewhat awkward units of $\mathrm{m\,km^{-1}}$

3.3 LOCALIZED GRAVITY-TOPOGRAPHY ANALYSIS

The mathematical foundation I presented in the previous sections allows us to investigate global properties of planets from the power spectra of gravity and topography observations. However, planets – and in this case Venus – have an important diversity of geological provinces that have unique origins and evolutionary paths. Hence, it is expected that the geophysical properties of the planet will vary according to the region under investigation. Moreover, it is possible that the dataset of interest has gaps that should be removed from the investigation. In these scenarios, it is necessary to employ an analysis technique that allows us to extract information from data that are localized to specific regions of interest. Some techniques analyze such data using purely spatial domain approaches, whereas others use more sophisticated spectral localization methods. Previous gravity investigations of geologic features on Venus have used a variety of localization methods, as discussed in Section 3.3.1. Yet, the spherical spatio-spectral windowing technique used in the scope of this thesis, summarized in Section 3.3.2, has not yet been applied to study the planet.

3.3.1 *Previous regional studies*

During the Magellan era, many gravity studies used geoid-to-tography ratios (GTRs) to investigate the interiors of various regions on Venus (e.g., Smrekar and Phillips, 1991; Kuncinskas and Turcotte, 1994; Moore and Schubert, 1997). GTRs provide, for a finite region, a single number that characterizes the best fitting linear relation between the geoid

and topography. As a purely spatial method, this technique preserves precise spatial information but loses all spectral information, making it difficult to account for and subtract long-wavelength gravity signals that are comparable to or larger in size than the analysis region. In addition, it is more difficult to validate the assumptions of the theoretical model and obtain quantitative model constraints, given that geophysical models are usually wavelength-dependent, as shown in Chapter 5.

Meanwhile, some of the first localized spectral admittance studies were performed for Venusian regions. In this type of analysis, commonly referred to as spatio-spectral localization techniques, the data are localized by employing windowing functions (also called data tapers) that have a restricted bandwidth in the spectral domain. These methods are subject to a trade-off between spatial and spectral resolution. Due to this compromise and considering the generally low resolution of planetary gravity datasets, these methods are usually restricted to large features. Particularly on Venus, localized spectral analyses are restricted to regions with diameters of the order of 1000 km or more.

The design of the window function is a key aspect to localized spectral analyses because the spectral signature of the window contaminates the data spectrum, an effect known as spectral leakage. Since this contamination is overall analogous to a convolution, as described in section 3.3.2, the larger the spectral bandwidth of the window the larger is the spectral leakage. The box-car function, which is one in the region of interest and zero elsewhere, is the end-member scenario of spectral leakage. Although being capable of perfectly suppressing the signal outside the region of interest, this window has an infinite bandwidth due to its sharp boundaries. This means that every localized spectral estimate would be influenced by every degree of the global spectrum. Therefore, for over half a century there have been many endeavors to design windows that have well-constrained spectral bandwidth (for a thorough review, see Percival and Walden, 1993). In the scope of planetary sciences, given the nearly-spherical shape of the large celestial bodies, most efforts have been towards the design of windows in spherical coordinates (e.g. Simons et al., 1997; Wieczorek and Simons, 2007; Audet, 2014).

On Venus, a variety of windowing techniques have already been applied to investigate its gravity and topography. Grimm (1994) employed Hann window functions, Cartesian half-cosine shaped windows that are able to attenuate spectral leakage, to investigate the admittance signatures of Venusian crustal plateaus. Following this, Simons et al. (1997) introduced a spherical wavelet-like analysis to perform admittance studies over various features on Venus. This wavelet technique was later used in several investigations on the planet (e.g. Smrekar et al., 2003; Hoogenboom et al., 2004; Anderson and Smrekar,

2006). In this technique, the size of the analysis region is wavelength-dependent, scaling with the size of the wavelet and the spatial-spectral trade-off of the wavelets is analogous to the Heisenberg uncertainty principle. In addition, Wavelet analysis in the Cartesian domain was employed by Jimenez-Diaz et al. (2015) to investigate the lithospheric structure of Venus. Audet (2014) used directional wavelets in both Cartesian and spherical domains for estimating elastic lithosphere thickness.

3.3.2 *Localized spectral analysis on the sphere*

In the studies undertaken in this thesis, the localization technique introduced in a series of papers by Wieczorek and Simons (2005), Simons et al. (2006), and Wieczorek and Simons (2007) is adopted. The method consists of multiplying the gravity and topography data by a fixed localization window and expanding the results in spherical harmonics in order to retrieve the localized spectral estimate for a specific region. The spatially localized version of a global function f can be written as

$$\mathcal{F}(\theta, \phi) = w(\theta, \phi) f(\theta, \phi) \tag{3.21}$$

where $\mathcal{F}$ is the localized version of f and w is the localization window. The main difference between this and the wavelet-based techniques is that the window is fixed in size and geometry for all wavelengths. This allows the analyst to ensure that all signals are from a single geologic region of interest. The power-spectrum of $\mathcal{F}$ can be estimated in the same manner as for the global function, using eq. 3.4.

The relation between the global power spectrum and the localized one is quite complex for an arbitrary function. However, it can be shown that, for the case where the spherical harmonics coefficients of $f_{\ell m}$ are zero-mean random variables, the expectation of the windowed power spectrum $\langle S_{\mathcal{F}\mathcal{F}} \rangle$ is related to the global power spectrum S_{ff} by the following relation (see appendix B of Wieczorek and Simons (2007) for the full development):

$$\langle S_{\mathcal{F}\mathcal{F}}(\ell) \rangle = \sum_{j=0}^{\ell_{win}} S_{ww}(j) \sum_{i=|\ell-j|}^{\ell+j} S_{ff}(i) \left(C^{\ell 0}_{j0i0} \right)^2 \tag{3.22}$$

where $\langle ... \rangle$ represents the expectation operator, ℓ_{win} is the spectral bandwidth of the window, and $C^{\ell 0}_{j0i0}$ is a Clebsch-Gordan coefficient.

The key outcome of eq. 3.22, for the purpose of the analyses presented here, is that $\langle S_{\mathcal{F}\mathcal{F}} \rangle$ is related to the power spectrum of the global function f and window w by an operation reminiscent of a convolution. Hence, it becomes clear that each degree ℓ of the localized power spectrum contains contributions from the global power spectrum within the range $\ell \pm \ell_{win}$ and has uncorrelated points only

every $2\ell_{win}+1$. Therefore, a large ℓ_{win} increases the smoothness of the localized spectrum while further limiting the degree range we can consider when doing the localized spectral analysis. By defining ℓ_{data} as the maximum spectral resolution of the data, the highest reliable degree becomes $\ell_{data}-\ell_{win}$ as higher degrees would be convolved with coefficients of the function f that are unknown. Moreover, $\ell<\ell_{win}$ should also be neglected as these are dominated by signals with wavelengths that are greater than the window size. Therefore, in constructing the localization windows, ℓ_{win} should be chosen small enough to have enough data points to perform robust geophysical data inversions.

In order to provide localization in both the spatial and spectral domains, the windows designed by Wieczorek and Simons (2005) and Wieczorek and Simons (2007) follow an optimization problem initially developed in the Cartesian domain as proposed in a series of papers during the 1960s by Slepian and colleagues (see Slepian, 1983, for a review), for which the solutions are known as Slepian functions. One way to present this problem is to find the windowing functions that optimally concentrate their power within a region of interest for a fixed and predefined spectral bandwidth ℓ_{win}. Hence, if we define the region of interest as a polar spherical cap with angular radius θ_0, our problem consists in finding the functions that maximize the ratio

$$\Lambda = \frac{\int_0^{\theta_0}\int_0^{2\pi} w^2(\theta,\phi)\sin\theta d\theta d\phi}{\int_0^{\pi}\int_0^{2\pi} w^2(\theta,\phi)\sin\theta d\theta d\phi} \tag{3.23}$$

where Λ is the so-called concentration factor that represents the quality of the spatial concentration. As shown in Wieczorek and Simons (2005) and Wieczorek and Simons (2007), eq. 3.23 can be reduced to an eigenvalue problem with solution consisting of a family of $(\ell_{win}+1)^2$ orthogonal windows w^i (eigenfunctions), each one associated with a concentration factor Λ^i (eigenvalue) that varies from zero to one and monotonically decreases with taper number. Although the spherical cap is originally built at the pole, standards algorithms can be used to rotate them to an arbitrary position on the sphere, allowing for the investigation of any location on a planet. In some applications it might be important to use localization windows with shapes different from a spherical cap. This problem was studied by Simons and Dahlen (2006a), who investigated the "polar gap" problem, and Simons et al. (2006), who generalized the solution to arbitrary-shaped regions.

Figure 3.3 shows the first window function w^0 (i. e., the window with highest concentration) based on a spherical cap with $\theta_0 = 16°$ for three different spectral bandwidths. Panel (a) shows the power spectra of the three windows and panel (b) a cross-section of the corresponding windows in the spatial domain. This figure allow us to clearly visualize the trade-off between the window spectral bandwidth and the spatial concentration.

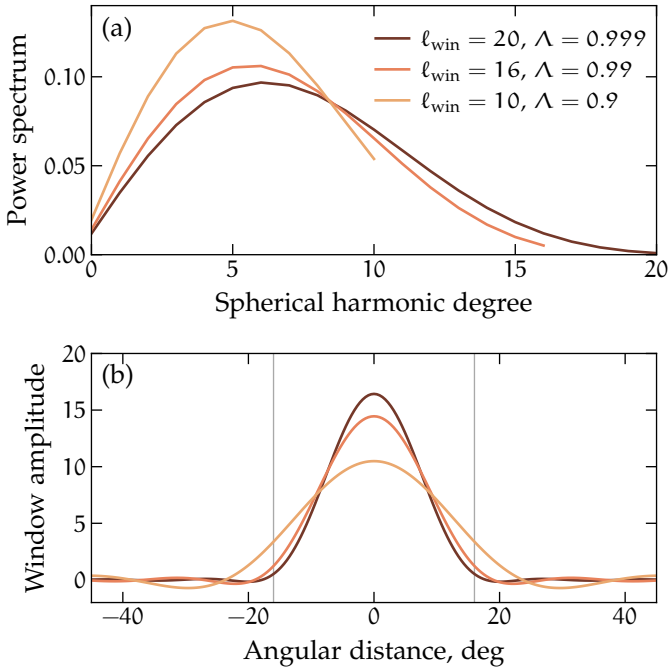

Figure 3.3: (a) Power spectrum and (b) spatial cross-section of a localization window w constructed using a spherical cap with $\theta_0 = 16°$, indicated by the gray lines, and varying spectral bandwidths. The choice of the bandwidth has a direct impact on the spacial concentration of the window, associated with the trade-off between spatial and spectral resolution.

Given that the solution is composed of multiple orthogonal windows, it is possible to combine them to perform the localization procedure, a technique commonly referred to as a multitaper spectral estimation (Thomson, 1982). There are several advantages of adopting multitapers over the use of any single window technique, such as the spherical wavelets (Wieczorek and Simons, 2005; Wieczorek and Simons, 2007). For example, the use of a single window always result in a heterogeneous coverage of the region of interest, as shown in Figure 3.3(b), leading to an unbalanced representation of the localized data in the spectral domain. Examples of localization windows associated with a multitaper approach are shown in Figure 3.4. In particular, the figure shows two-dimensional spatial renderings of the nearly perfectly concentrated ($\Lambda \geqslant 0.99$) windowing functions based on a spherical cap with $\theta_0 = 25°$, as well as the combined power of all the windows. The windows are constructed based on a spectral bandwidth $\ell_{win} = 20$ which results in a total of 8 windows with concentration above 99%.

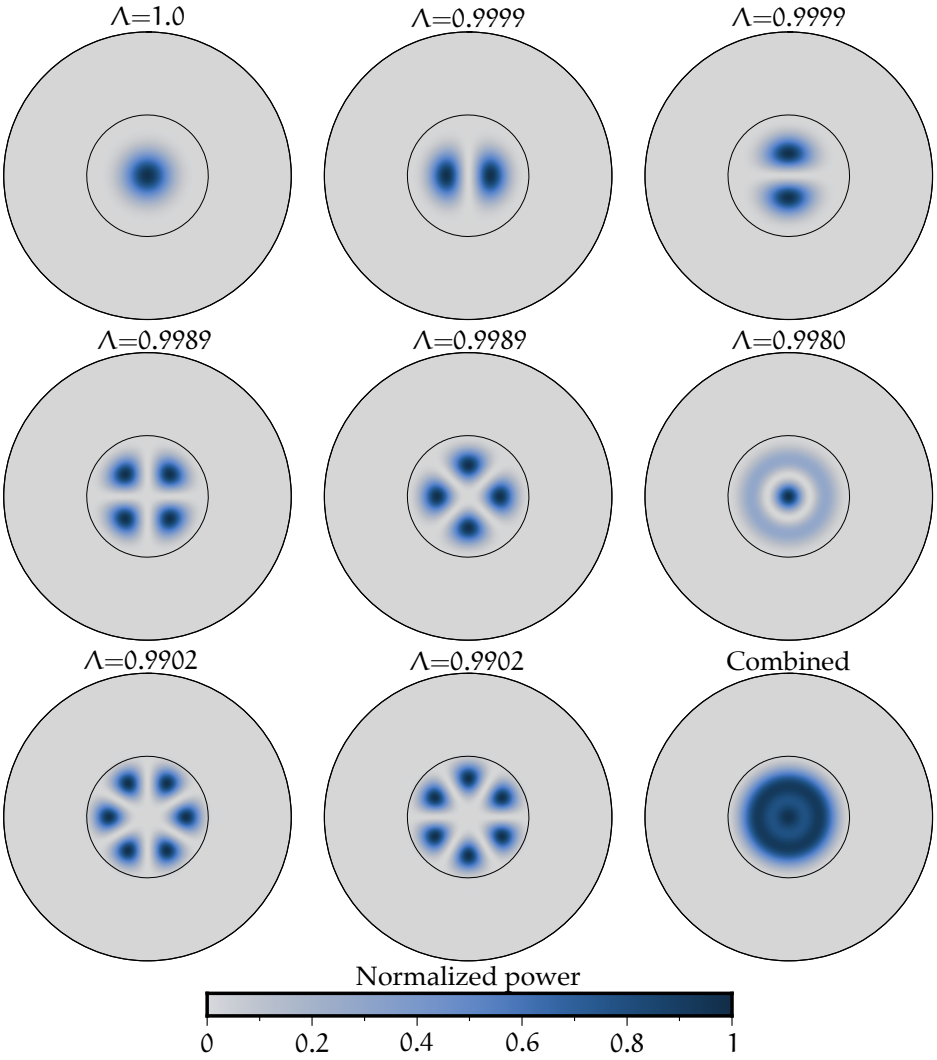

Figure 3.4: Spatial power distribution of orthogonal windowing functions localized within a spherical cap with $\theta_0 = 25°$, which is represented by the black circle in each panel, and with spectral bandwidth $\ell_{win} = 20$. The windows shown correspond to a subset of solutions with spatial concentration above 99%, which in this case is composed of 8 windows. The bottom-right panels shows the total combined power of the 8 windows.

The power-spectrum of a multitaper estimate for a number of N well-concentrated orthogonal windows can be computed as:

$$S_{\mathcal{FF}}^{(mt)}(\ell) = \sum_{n=1}^{N} a_n S_{\mathcal{FF}}^{(n)}(\ell) \tag{3.24}$$

where a_n are weights assigned to each taper. The weights are usually chosen to be uniform $(1/N)$ or proportional to Λ_n. Since in my investigations only the nearly perfectly concentrated tapers are used ($\Lambda \leqslant 0.99$), the difference between the two choices is negligible. Hence, for

simplicity, I chose to use equal weights for all tapers in my multitaper analyses.

Another useful property of the multitaper analysis is that it naturally provides the uncertainties of the localized spectral estimations, as discussed in detail by Wieczorek and Simons (2007). A rigorous estimation of the variance of a multitaper estimate relies upon the calculation of the covariance matrix between the individual window functions. Nevertheless, given that the windows are somewhat uncorrelated, Wieczorek and Simons (2007) showed that for practical applications, it is commonly sufficient to use a simplified version where the individual spectral estimates that contribute to the multitaper spectrum are statistically independent and Gaussian-distributed. In this case, the variance estimate reads:

$$\operatorname{var}\left\{S_{\mathcal{GF}}^{(mt)}(\ell)\right\} \approx \left(\frac{\sum_{n=1}^{N} a_n^2}{1-\sum_{n=1}^{N} a_n^2}\right) \sum_{n=1}^{N} a_n \left(S_{\mathcal{GF}}^{(n)}(\ell) - S_{\mathcal{GF}}^{(mt)}(\ell)\right)^2. \tag{3.25}$$

This estimate, however, has the tendency of underestimating the true uncertainty.

Finally, it is important to emphasize that the use of multitapers in the context of planetary sciences, and in particular on Venus, is quite limited due to the low resolution of the gravity data. In order to have a reasonable range of localized spectral estimates it is essential to minimize the window spectral bandwidth. Hence, for most applications, gravity analyses are limited to the first, highest concentrated, window. Nevertheless, in some specific cases, as the studied presented in Chapter 7, the use of multitapers is not only viable, but particularly useful. Other studies that adopted multitaper techniques include analyses of the lunar gravity field using the high-resolution gravity model from the GRAIL mission (Besserer et al., 2014; Gong et al., 2016; Goossens et al., 2020), and investigations of the crustal remnant magnetic anomalies from the Moon (Wieczorek, 2018) and Mars (Lewis and Simons, 2012).

4

DATASETS

There is a wide range of geophysical datasets that can be used to study planetary interiors. One of the most precise methods to obtain information about the subsurface of a planet is through seismic data. The extensive network of seismometers on Earth has allowed for the comprehensive mapping of the planet's interior, leading to the discovery of crucial features such as the crust-mantle interface (known as the Mohorovičić discontinuity), as well as the identification of the outer liquid core and inner solid core. However, the same resources are not available on other planets due to the high cost and technical challenge of deploying seismic stations throughout the Solar System. Nevertheless, seismometers deployed during the Apollo missions allowed for the detection of moonquakes (e.g., Latham et al., 1971) and from 2019 to 2022 marsquakes have been detected thanks to NASA's InSight lander (e.g., Giardini et al., 2020). These missions successfully determined the core radius and crustal thickness of the two planets (e. g., Lognonné et al., 2003; Garcia et al., 2011; Stähler et al., 2021; Knapmeyer-Endrun et al., 2021). Still, such type of data remains unavailable for most bodies, including Venus, and no planet besides Earth have a substantial network that allows for a global mapping of the interior. Hence, other geophysical measurements are essential in the scope of planetary sciences.

Gravity and topography are relatively low-cost datasets that can be acquired from orbit, providing a global view and allowing for analyses of lateral variations of the planet's internal properties. For Venus, the highest resolution gravity and topography were obtained by the Magellan spacecraft. In this chapter, I present the timeline and operations of Magellan (Section 4.1), followed by a detailed description of the topography (Section 4.2) and gravity (Section 4.3) datasets.

4.1 MAGELLAN MISSION SUMMARY

The Magellan spacecraft was a NASA mission that orbited Venus from 1990 to 1994 with the primary goal of globally mapping the surface of the planet. A schematic overview of the mission is shown in Figure 4.1. Magellan was launched from the Kennedy Space Center on May 4, 1989. After a 15-month cruise phase, it successfully entered in orbit around Venus on August 10, 1990. After arriving, some loss-of-signal incidents delayed the science operations by several weeks before commencing on September 15, 1990.

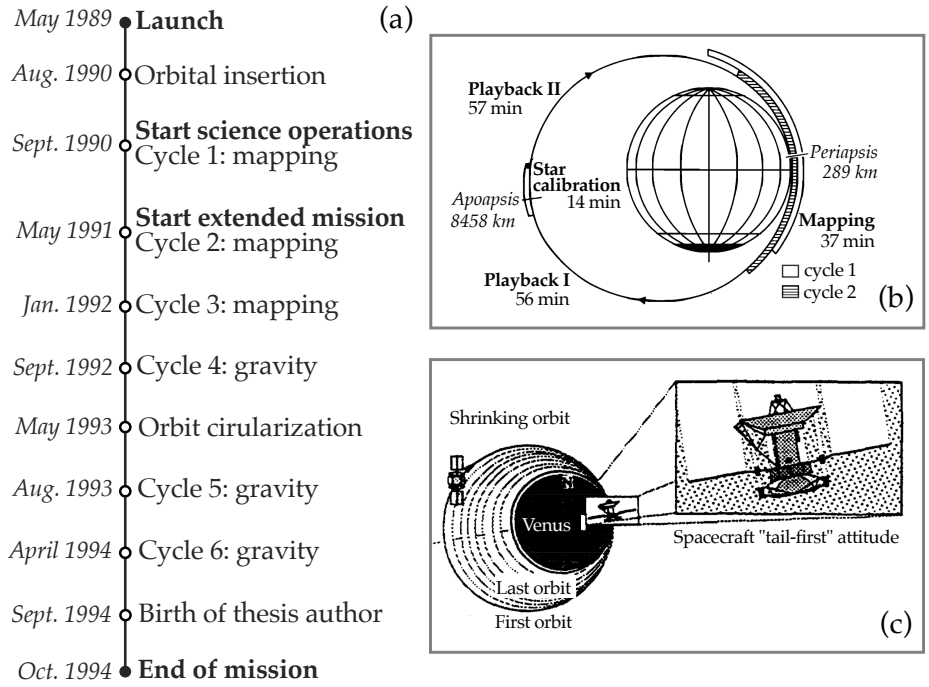

Figure 4.1: Overview of the Magellan mission operations. (a) Summary of the mission's timeline, indicating the start of the main mission phases. (b) Magellan surface mapping orbit profile. The spacecraft had an elliptical orbit and surface mapping was performed in the lower altitude portions. At higher altitudes, the spacecraft was dedicated to playback the recorded data to Earth along with a period of calibration of the spacecraft attitude with respect to reference stars (modified from Saunders et al., 1992). (c) Illustration of the aerobraking maneuver used to circularize the orbit of Magellan (modified from Lyons et al., 1995).

The Magellan payload had as its only science instrument a multimode radar sensor that includes a high-gain antenna used for both the SAR imaging and the telecommunications system, as well as a horn antenna dedicated to acquire altimetry data. The high-gain antenna was also used in a receiver-only mode to record the level of radiometric power emitted by the surface of the planet. The sensor operated in phases, cycling through the SAR, altimeter, and radiometer modes.

The mission science operations were divided into six cycles, the first half was focused on surface imaging and altimetry data acquisition, while the last half was mainly dedicated to the gravity experiment. Each cycle took 243 days, corresponding to the time that the planet takes to turn once on its axis under the spacecraft orbit. Magellan's standard operations during the mapping cycles are schematized in Figure 4.1(b). In this setting, Magellan pointed the radar sensor to Venus's surface acquiring longitudinal stripes of data during the low altitude part of the orbit and then turned the instrument towards Earth to playback the recorded data. Alternatively, during the gravity

cycles the high-gain antenna was constantly sending radio signals to the Earth in order to gather Doppler tracking data which used to produce the planet's gravity field model, as detailed later in this chapter.

Magellan's primary mission comprised only the first mapping cycle covering 84% of Venus's surface with the radar imager and altimeter, successfully achieving the mission's primary goal of mapping 70% of the planet. The main objective of the second cycle was to fill in the coverage gaps remaining from the first cycle. In particular, the mapping period was slightly delayed to get a better coverage of the south pole. After the third cycle, which focused on obtaining stereo-images to generate higher resolution topography, the mapping efforts came to an end with about 98% coverage of Venus's surface.

Still in the initial elliptical orbit, Magellan did its first cycle devoted to gravity science. However, since the altitude of the spacecraft is the primary factor controlling gravity data resolution, this orbit limited the high resolution gravity dataset to a $\pm 30^\circ$ latitude band centered on periapsis. Therefore, with the main motivation of improving the resolution of the gravity data in a global scale, Magellan went thought an orbit circularization phase. Because of insufficient propellant resources, the spacecraft shrank its orbit by performing aerobraking maneuvers, where the atmospheric drag is used to slow down the satellite, as illustrated in Figure 4.1(c). This highly delicate and risky maneuver, which, in fact, lacked normal operation safety margins, was a historic first in the scope of planetary exploration. The technical details of this endeavor can be found in Lyons et al. (1995) and Giorgini et al. (1995). Thanks to this maneuver, Magellan apoapsis lowered from 8500 km to 540 km, allowing the spacecraft to acquire gravity data in a quasi-circular orbit during cycles 5 and 6, which was a game-changer for the resolution of Venus's gravity field particularly for mid and high latitudes. Finally, on October 13, 1994 Magellan lost contact with Earth after intentionally plunging into the Venusian atmosphere.

4.2 TOPOGRAPHY

The global-scale topography mapping of Venus relied on the radar altimeter data collected in cycles 1-3 of the Magellan mission. The basic principle of this instrument is to measure the spacecraft to surface round trip time of a radar pulse which is then used to estimate the distance between the spacecraft and the surface. The first topographic map from Magellan efforts was constructed by Ford and Pettengill (1992) using data from the first cycle of the mission. Due to poor knowledge of the gravity field of Venus during the first cycles, the error of Magellan's radial orbit reached several kilometers, directly affecting the uncertainties of the topography model. Years later, Rappaport et al. (1999) reprocessed the altimetry data using the most

recent gravity model at the time, which dramatically decreased the orbital errors to a maximum radial uncertainty of 90 m and an average of 16m. The largest position error is the usual along-track, possessing an average value of 200 m and causing north-south "stripes" pattern.

The Rappaport et al. (1999) topography model is based on over 4.2 million altimeter footprints from 3971 orbits. The footprint size varies between 8×10 km at periapse and 19×30 km at the poles. The final global gridded data has a pixel size of 5×5 km covering the entire planet, with the exception of some small data gaps over 2.6% of the surface. Wieczorek (2015a) made use of this grid, supplanted by data from the Pioneer Venus and Venera 15/16 missions to fill in data gaps, to create spherical harmonic coefficients up to degree 719 of Venus topography. This data product, which is adopted in my studies, is named VenusTopo719 and is publicly available in Wieczorek (2015b). I note that a stereo-topography dataset created by Herrick et al. (2012) is also available for about 20% of Venus's surface. This dataset has a spatial resolution of 1 to 2 km, corresponding to an order of magnitude improvement with respect to the altimetry-derived topography.

Figure 4.2(a) shows the topography map of Venus based on the VenusTopo719 dataset. As we can see, on Venus the relief is reasonably smooth, over 80% of the planet's surface lies within 1 km of the mean planetary radius. The highest feature is Maxwell Montes located at the center of Ishtar Terra, reaching over 10 km altitude. All other highlands are associated with heights of about 6 km or less.

4.3 GRAVITY

While orbiting Venus, Magellan was subject to non-uniform gravitational accelerations due to internal and surface variations of the planet's mass distributions. Because of these small accelerations, the radio signals sent from Earth to the spacecraft and back to Earth (two-way travel) were subject to Doppler shifts. By measuring these Doppler shifts of Magellan, a technique called Doppler tracking, it is possible to create a gravity model of the planet.

A detailed review on the different gravity models constructed for Venus can be found in Sjogren et al. (1997). In this thesis, the MGNP180U model by Konopliv et al. (1999) is adopted, which is the most recent and highest resolution Doppler tracking gravity solution for Venus. Figure 4.2(b) shows the gridded form of this gravity solution. Comparing the topography and gravity maps, it is easy to see that the two are well correlated - topographic highlands are associated with positive gravity anomalies while the lowlands correlated with negative gravity anomalies.

The MGNP180U solution makes use of the gravity data obtained by Magellan combined with the data acquired by the Pioneer Venus

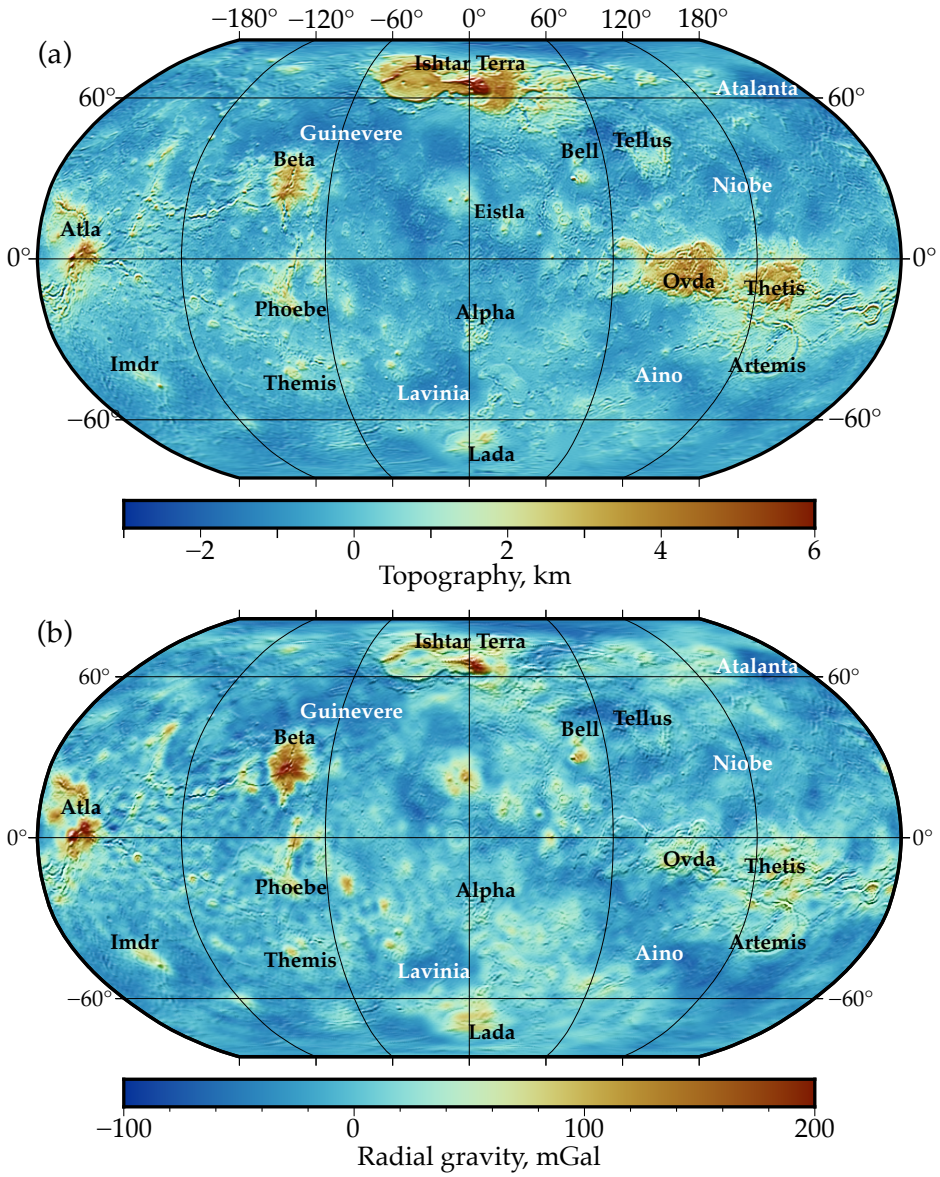

Figure 4.2: (a) Topography and (b) radial gravity disturbance maps of Venus based on the VenusTopo719 and MGNP180U spherical harmonic models, respectively. The gravity map is built from the spherical harmonic coefficients truncated at degree 75, which roughly correspond to the average global resolution of the data (see text for details). Both maps are in Robinson projection and are overlain by a gradient image derived from the topographic model. Some of the main Venusian features are labeled in the maps, the ones in black correspond to highlands while the ones in white indicate lowlands.

Orbiter and was constructed up to degree and order 180, which corresponds to a resolution of 1° by 1°. Due to computational constraints at the time, determining the gravity field up to degree 180 in a single step was a overwhelming task even for the JPL supercomputer used by Konopliv et al. To circumvent this issue, the authors decided break

up the computation of the gravity spherical harmonic coefficients into 3 successive batches. The model was built up to degree and order 120 in the first step. The second step solved for the coefficients from degree 116 to 155 only, while degrees 154 to 180 were solved in the third step.

The estimation of a gravity model based on the Doppler tracking data usually relies on the use of some a priori information which has the purpose of assuring that the inversion is well-posed. In the case of MGNP180U, the first and second steps of the model made use of a spatially varying constraint that depends on the local strength of the gravitational acceleration, while the third step is based on the standard "Kaula rule", where a power law is used to constrain the gravity model (Kaula, 1966). As for the spatially varying technique, the expected signal from the acceleration is computed globally using the Kaula rule, while the uncertainty of the acceleration is spatially mapped based on the covariance matrix and the partial derivatives of the acceleration spherical harmonic coefficients. The degree at which the amplitude of the acceleration signal crosses the estimated uncertainty is know as the degree strength. This corresponds to the spherical harmonic degree where the noise becomes more important than the signal and it is an approximate estimation of the resolution of the data.

Figure 4.3 shows the degree strength map from the MGNP180U model (adapted from Figure 3 from Konopliv et al., 1999). As we can see, there is a strong spatial variation of the gravity data resolution, which is to first order associated with variations of the spacecraft altitude. Note that the largest degree strengths correlate with the orbit's periapsis at about 9° latitude. The minimum degree strength occurs near Imdr Regio, around latitude $-50°$ and longitude 180°, and is associated with a data gap in Magellan cycles 5 and 6.

Using the spherical harmonic coefficients of the gravity and topography models, one is also able to estimate their power spectra along with the spectral admittance and correlation between them, as defined by equations 3.4, 3.19, and 3.20, respectively. These quantities are presented in Figure 4.4. Panel (a) shows the power spectra of the topography, radial gravity and gravity error. As we can see, on a global scale the model degree strength is around degree 70, which corresponds to a spatial resolution (half-wavelength) of approximately 270 km, following the Jeans relation (eq. 3.2). In addition, the error spectrum shows discontinuities at degrees 116 and 154 caused by the three step solution procedure used in to build the MGNP180U model.

The global admittance and correlation are shown in Figure4.4(b). The admittance ranges from about 20 to 50 mGal km^{-1} for $\ell < 80$, which is roughly the same range as Earths, but about 3 times lower than what has been observed for smaller bodies, such as Mars and the Moon. These differences show that on Mars and the Moon the

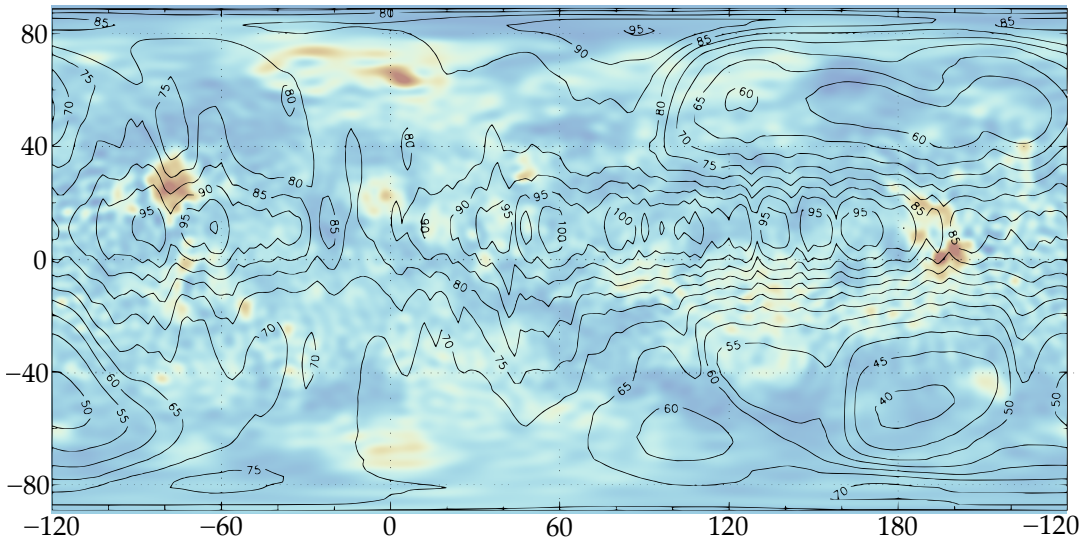

Figure 4.3: Contours of the degree strength distribution of the MGNP180U gravity solution overlaying the predicted gravity field. The contour values represent spherical harmonic degrees. Map in cylindrical equidistant projection (Plate Carrée) center at 60° longitude. Modified from Konopliv et al. (1999).

surface topographies generate larger gravity anomalies in comparison to Earth and Venus. A plausible explanation for these observations is that the larger planets have a weaker lithosphere, resulting in a larger compensation of the topography and smaller gravity anomalies (this attribute is further discussed in Section 5.1). Above degree 80, Venus's admittance decreases linearly, likely an effect from a poor determination of the gravity field in the short wavelength range. Furthermore, Venus presents a high correlation for the long wavelength range, particularly in comparison to the Earth. For $2 < \ell < 30$, Venus has an average correlation of about 0.84 while Earth's correlation is 0.54, Mars's is 0.74, and the Moon's is 0.47 on average for the same degree range. This is an indication that the long wavelength topography and gravity of Venus are coupled and result from the same processes, such as convective flows in the mantle (e. g., Phillips et al., 1981).

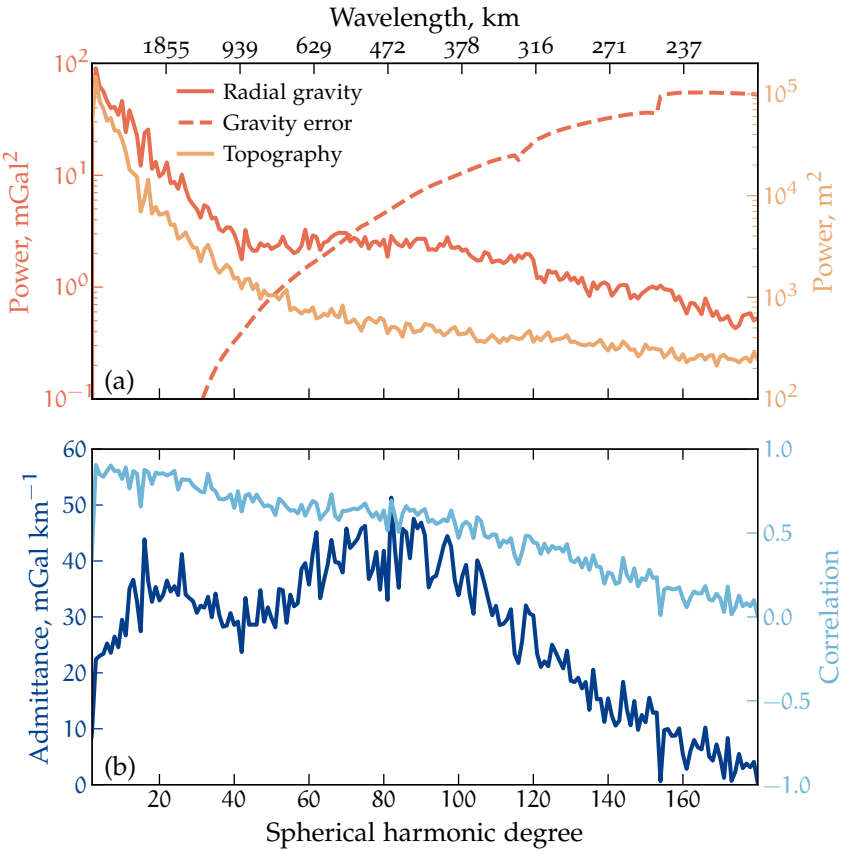

Figure 4.4: (a) Power spectra of topography based on the VenusTopo719 model, radial gravity and gravity error from the MGNP180U model. The error spectrum shows discontinuities at degrees 116 and 154 caused by the three step solution procedure. (b) Spectral admittance and correlation between gravity and topography.

5 GEOPHYSICAL MODELS

The interpretation of gravity field observations is non-unique, meaning that a variety of internal density anomaly distributions can explain equally well the observations. Yet, by making plausible geological and physical assumptions about the interior structure, the interpretation of the gravity data can become a unique problem. This set of assumptions is built in terms of a geophysical model that depends on a series of parameters, such as the crustal thickness or the viscosity of the mantle. The values of these parameters will directly affect the predicted gravity field and, by comparing the model predictions with the observations, we can estimate these interior properties. The exercise of inferring unknown model parameters based on observations involves an extensive group of techniques that compose the domain of data inversion theory.

This chapter is dedicated to detailing the geophysical models adopted in the investigations presented in this thesis. In Section 5.1, I present the elastic loading model I adopted to study the crust and lithosphere of the crustal plateaus. In Section 5.2, I introduce the dynamic loading model used to investigate Venus's mantle. Lastly, Section 5.3 briefly describes the inversion approaches relevant to my studies.

5.1 LITHOSPHERIC MODEL

The lithosphere is the outermost rheological layer of terrestrial planets. It is characterized by being a strong rigid layer in which heat is transported inductively from the thermal boundary layer, defined as the limit between the convective and conductive regimes, to the planet's surface. The strength of the lithosphere is in practice finite and can present significant variations not only from one planet to the other but also regionally and temporally within a single planet. The lithospheric strength will affect the degree of compensation of the topographic features which, in turn affects their associated gravity signature. In this section, I present an approach to model the gravity signature associated with the crust and lithospheric properties. I start by formally introducing how to estimate the gravitational potential from a surface density interface with arbitrary relief, followed by the description of the flexural loading approach used to model the lithosphere. Then, I show how this model can also help us understand the thermal conditions of the lithosphere.

5.1.1 *Gravity field from the relief of a density interface*

To compute the gravitational potential coefficients $C_{\ell m}$ (eq. 3.15) from an observer position $\mathbf{r}$ of a body located at $\mathbf{r}_\oplus$ with density distribution $\rho(\mathbf{r}_\oplus)$ we take advantage of well-knwon the identity:

$$\frac{1}{|\mathbf{r}-\mathbf{r}_\oplus|} = \frac{1}{r}\sum_{\ell=0}^{\infty}\left(\frac{r_\oplus}{r}\right)^{\ell} P_\ell(\cos\alpha), \text{ for } r \geqslant r_\oplus \tag{5.1}$$

where α is the angle subtended by the positional vectors. The Legendre polynomials $P_\ell(\cos\alpha)$ can be computed using the so-called Legendre addition theorem

$$P_\ell(\cos\alpha) = \frac{1}{2\ell+1}\sum_{m=-\ell}^{\ell} Y_{\ell m}(\theta,\phi)Y_{\ell m}(\theta_\oplus,\phi_\oplus). \tag{5.2}$$

By inserting these two identities into eq. 3.8, it can be shown that the potential coefficients may be computed as

$$C_{\ell m} = \frac{1}{MR_0^\ell(2\ell+1)}\int_V \rho(\mathbf{r}_\oplus) r_\oplus^\ell Y_{\ell m}(\theta_\oplus,\phi_\oplus)dV', \tag{5.3}$$

which is a relation valid only in cases where the observation point $\mathbf{r}$ is greater than the maximum radius of the body $\mathbf{r}_\oplus$, given the inequality from eq. 5.1 (see Wieczorek, 2015a, for details).

It is further possible – and particularly useful in the scope of geophysical studies – to compute the potential coefficients for the case of a surface with relief $\tau(\theta, \phi)$ referenced to a spherical interface of radius R_τ where the density contrast between τ and R_τ depends only on latitude and longitude. As shown in Wieczorek and Phillips (1998), in this case ,the potential coefficients can be defined as:

$$C_{\ell m} = \frac{4\pi R_\tau^3}{M(2\ell+1)}\sum_{n=1}^{\ell+3}\frac{(\rho\tau^n)_{\ell m}}{R_\tau^n n!}\frac{\prod_{j=1}^{n}(\ell+4-j)}{(\ell+3)}. \tag{5.4}$$

We can use this equation to compute the gravity signature from the observed topographic relief of a planet. Given the usual lack of prior knowledge, it is common to consider a constant value for the density contrast between the crustal rocks (for example, standard density values of basalts) and the atmosphere (usually assumed to have negligible density). The estimation of gravity from topography is a widely-used approach with many applications and is commonly referred to as the Bouguer correction.

Even though the sum in eq. 5.4 is finite, meaning it can be computed exactly, the number of terms grows linearly with the spherical harmonic degree. However, since each succeeding term is smaller than the previous, the sum can be truncated at a value n_{max}. The choice of n_{max} depends on the resolution of the gravity model as

well as on the amplitude of the relief. For Venus, when computing gravity from topography, it is usually sufficient to limit the analysis to $n_{max} = 1$ given the overall smooth topography observed on the planet. The use of higher-order terms is only necessary on Maxwell Montes, which is the highest topographic feature of the planet. In this case, an accurate gravity prediction is obtained with $n_{max} = 3$ (James et al., 2013; Wieczorek, 2015a).

The version of eq. 5.4 that uses only the first-order term is referred to as the "mass-sheet" approximation and reads:

$$C_{\ell m} = \frac{4\pi R_\tau^2 (\rho\tau)_{\ell m}}{M(2\ell+1)}. \tag{5.5}$$

The higher-order terms are commonly called the "finite-amplitude" correction terms. Yet, since my investigations are directed to relatively smooth-relief regions on Venus, it is reasonable to neglect the finite-amplitude terms. Note that, for increasing ℓ, the radial gravity predicted using the mass-sheet approximation approaches the expression $g = 2\pi\rho G h$, in the case where τ is the topographic relief h associated with a constant density. This expression is known as the Bouguer slab approximation.

when using the mass-sheet approximation to compute the radial gravity (eq. 3.16), for increasing ℓ the predicted gravity approaches the expression $g = 2\pi\rho G h$ (in the case where τ is the topographic relief h associated with a constant density) which is known as the Bouguer slab approximation.

5.1.2 *The gravity signature of topographic support*

For centuries, scientists have been investigating the possible mechanisms responsible for the support of topographic features, which correspond to non-hydrostatic deviations from the hydrostatic shapes of planets. In fact, one of the most notorious debates in the geosciences domain led to the development of two well-known models of isostatic compensation, named Pratt and and Airy isostasy (Airy, 1855; Pratt, 1855).

In an isostatic regime, the topographic loads are supported buoyantl as the light crustal loads float on top of a denser yet weaker (i.e. more viscous) mantle. In Airy's model, the weight of topography is balanced by crustal thickness variations such that crust-mantle vertical columns always have the same total mass (Airy, 1855). In this case, considering a Cartesian geometry, the relief of a crustal root h_r is related to the height of the surface h via the simple relation

$$h_r = -h\frac{\rho_c}{\rho_m - \rho_c} \tag{5.6}$$

where ρ_c is the density of the crust and ρ_m is the density of the mantle. As for Pratt isostasy, the equal-mass columns result from

lateral variations of crustal density and there is no relief within the crust-mantle interface (Pratt, 1855). I note, however, that the historical "equal-mass" definitions for isostasy tends to overestimate the crustal thickness for smaller bodies, where the crust is relatively thick with respect to the radius. Hemingway and Matsuyama (2017) have shown that, in order to accurately estimate crustal thicknesses of small bodies, it is instead necessary to consider the "equal-pressures" model.

The assumption of an isostatic regime is commonly seen to be adequate when considering broad topographic features and over long time-scales. However, it is well known that elastic stresses within the lithosphere play an important role in the support of topographic features, especially in the short-wavelength range. In fact, the analysis of the gravity signature associated with topographic relief is one of the best ways of investigating the properties of a planet's lithosphere, as I will further discuss in this section.

For any of the support mechanisms just described, we can estimate the spherical harmonic coefficients of the gravity field from the topography coefficients $h_{\ell m}$ via the general relation

$$g_{\ell m} = Q_{\ell m} h_{\ell m} + I_{\ell m}, \tag{5.7}$$

where $I_{\ell m}$ is the part of the gravity signal not predicted by the model and $Q_{\ell m}$ is the model-dependent linear transfer function that accounts for the mechanisms controlling the support of topography. When $I_{\ell m}$ is uncorrelated with topography, which would be the case if it was originated by measurement noise, the power spectrum of the observed gravity field can be defined as

$$S_{gg} = S^{Q}_{gg} + S_{II} \tag{5.8}$$

where S^{Q}_{gg} is the power spectrum resulting from the model and S_{II} is the power of the signal not predicted by the model. Note that the presence of $I_{\ell m}$ signals tends to increase the observed gravity power spectrum, causing a decrease in the gravity-topography correlation (eq. 3.20).

Even though eq. 5.7 is intrinsically a nonisotropic relation, the loading model adopted here is built in terms of a transfer function Q_ℓ that depends only on ℓ. This is a practical approach because it allows us to readily work with the power and cross-power spectra of the gravitational field and topography. In this case, by multiplying both sides of eq. 5.7 by $h_{\ell m}$, summing over all orders m, and computing the expectation, we find that Q_ℓ corresponds to the spectral admittance Z, assuming that $I_{\ell m}$ is a zero-mean random variable. Furthermore, if it is assumed that the gravity and topography should be perfectly correlated, any correlation value below unity would represent noise (either measurement noise or geologic signals not accounted for by

the model) and the admittance uncertainty σ^2 would directly be related to the correlation as follows:

$$\sigma^2 = \frac{S_{gg}(\ell)}{S_{hh}(\ell)} \frac{1-\gamma(\ell)^2}{2\ell}. \tag{5.9}$$

If we define S_{gg}/S_{II} as the "signal-to-noise ratio", one can obtain a direct relation between S_{gg}/S_{II} and the correlation by inserting eq. 5.8 into eq. 3.20. As presented in Wieczorek (2008), correlation values of 0.0707 and 0.816 correspond to signal-to-noise ratios of 1 and 2, respectively.

5.1.3 *Loading a thin elastic shell*

Here, I describe the flexural model of the lithosphere as presented in Broquet and Wieczorek (2019), which allows for the placement of loads both on the surface and in the subsurface, providing some small improvements upon previous loading models developed for Mars by McGovern et al. (2002), Belleguic et al. (2005), Beuthe et al. (2012), and Grott and Wieczorek (2012).

The model considers that the lithosphere behaves as a thin elastic shell that overlies a fluid interior. The main assumptions and theoretical development of thin elastic shells is presented in Kraus (1967) and explored in the context of topographic loads on elastic lithospheres by Turcotte et al. (1981), with further developments presented in Beuthe (2008). This formulation establishes the relation between the pressure of loads acting on the elastic lithosphere to the vertical deflection of the surface. The amount of deflection is controlled by the flexural rigidity D of the lithosphere, which depends on the Poisson's ratio ν, Young's modulus E, and the elastic thickness T_e, as follows:

$$D = \frac{ET_e^3}{12(1-\nu^2)}. \tag{5.10}$$

The equation that governs the shell deflection ω in the presence of a load q reads (Kraus, 1967):

$$\left[D(\nabla^2+2)^3 - 2D(\nabla^2+2)^2 + ET_eR_e^2(\nabla^2+2)\right]\omega(\theta,\phi) = -R_e^4(\nabla^2+1-\nu)q(\theta,\phi), \tag{5.11}$$

where R_e is the radius of the elastic shell, here taken as $R_e{=}R{-}T_e/2$. Expressing the load and deflection in spherical harmonics coefficients, $q_{\ell m}$ and $\omega_{\ell m}$, and using the identity of the Laplacian in the spectral domain for functions defined in the surface of a sphere

$$\nabla^2 Y_{\ell m} = -\ell(\ell+1)Y_{\ell m} \tag{5.12}$$

we can rewrite equation 5.11 in linear form as

$$\omega_{\ell m} = \xi_\ell q_{\ell m}, \tag{5.13}$$

where

$$\xi_\ell = -\frac{R_e^4[\ell(\ell+1)-1+\nu]}{Dn^3+2Dn^2+ET_eR_e^2n} \tag{5.14}$$

is a wavelength-dependent parameter that contains the elastic properties of the shell and $n = \ell(\ell+1)-2$. Note that the loading q is defined as positive when directed downwards while the deflection ω is positive when directed upwards

It is then necessary to compute the net load q acting on the lithosphere. q is defined as the difference between the vertical gravitational force per unit area acting on the lithosphere q_a and the hydrostatic pressure at the base of the lithosphere from the fluid mantle q_h. As shown by Belleguic et al. (2005), the gravitational force per unit area can be written as

$$q_a = -\frac{1}{R^2}\int_{U(r_1)}^{U(r_N)} \rho(r,\theta,\phi)r^2 dU, \tag{5.15}$$

where $r_N(\theta,\phi) = R+h(\theta,\phi)$ is the surface and $r_1(\theta,\phi) = R-T_x+\omega(\theta,\phi)$ represents the thickness of the lithosphere with

$$T_x = \begin{cases} T_e & \text{if } T_e \geqslant T_c \\ T_c & \text{if } T_e < T_c \end{cases} \tag{5.16}$$

with T_c indicating the thickness of the crust. Then, by numerically approximating the integral in eq. 5.15 and taking $q_h = \rho_m U(r_1)$ where ρ_m is the density of the mantle, the net load can be expressed as

$$q = q_a - q_h = -\frac{1}{R^2}\sum_{j=1}^{N} \rho(r_j)r_j^2\left[U(r_{j+1})-U(r_j)\right] - \rho_m U(r_1), \tag{5.17}$$

where N represents the total number lithospheric layers characterized by density interfaces and $\rho(r_j)$ indicates the density difference between radii r_j and r_{j+1}. Moreover, $\rho(r_j)$, r_j, $U(r_j)$, and $U(r_{j+1})$ depend implicitly on θ and ϕ.

This general relation can be interpreted and rewritten for specific scenarios of surface loading or subsurface loading. Surface loads can be the result of extrusive volcanism or topographic highs generated by tectonic processes, while subsurface loads will be modeled either as a low-density layer in the mantle, such as from a buoyant mantle plume, or a high density layer within the crust, which could correspond to dense magmatic intrusions. Below, I outline the main steps and assumptions used to derive the surface loading transfer function as presented in Broquet and Wieczorek (2019). Then, I provide the main equations used to compute subsurface loads and how the two contributions can then be combined.

SURFACES LOADS The first step is to expand the latitude- and longitude-dependent variables into spherical harmonics such that each spherical harmonic coefficient can be treated individually. Hence, q, U, h, and ω become $q_{\ell m}$, $U_{\ell m}$, $h_{\ell m}$, and $\omega_{\ell m}$. The model is built in terms of three layers: the mantle, the crust, and the loads, each one associated with a specific and constant density with values represented by ρ_m, ρ_c, and ρ_l, respectively. Meanwhile, the density of the atmosphere is set to $0\,\mathrm{kg\,m^{-3}}$. The interfaces between the rocky layers are assumed to deflect by the same amount $\omega_{\ell m}$. The model also assumes that $r_j{=}Re{=}R$. Finally, given that the lithosphere deflection ω is small with respect to the planetary radius, one can make use of the first-order Taylor series approximation $U_{\ell m}(r+\omega_{\ell m}) = U_{\ell m}(r) - g(r)\omega_{\ell m}$ and express eq. 5.17 as

$$q_{\ell m} = g_0 \Delta\rho_l \omega_{\ell m} + g_m \Delta\rho_c \omega_{\ell m} + g_0 \rho_l h_{\ell m} - \Delta\rho_c U_{\ell m}(R - T_c) - \rho_c U_{\ell m}(R), \quad (5.18)$$

where g_0 and g_m are the radial gravity acceleration at the surface $g(R)$ and at the crust-mantle boundary $g(R{-}T_c)$ respectively, $\Delta\rho_l = \rho_c - \rho_l$, and $\Delta\rho_c = \rho_m - \rho_c$. The first two terms of eq. 5.18 are associated with the deflection of the lithosphere which, in turn, deflects the crust-mantle boundary. The third term account for the "extra" weight of the load itself which is the mass that occupies the region between the mean planetary radius and the topographic relief. The two last terms are associated with "self-gravity" effects, i. e., they represent changes to the gravitational potential induced by the topography and deflection.

Considering the contributions of the three density interfaces and making use of the mass-sheet approximation (eq. 5.5), it is straightforward to compute the potential spherical harmonic coefficients of the potential $U_{\ell m}$, where $U_{\ell m} = \frac{GM}{R} C_{\ell m}$. Defining that (*i*) at the surface relief $\tau_{\ell m} = h_{\ell m}$, $R_\tau{=}R$, and $\rho_{\ell m} {=}\rho_l$, (*ii*) at the load-crust interface $\tau_{\ell m} {=}\omega_{\ell m}$, $R_\tau{=}R$, and $\rho_{\ell m} = \Delta\rho_l$, (*iii*) at the crust-mantle interface $\tau_{\ell m} {=}\omega_{\ell m}$, $R_\tau{=}\, R - T_c$, $\rho_{\ell m} = \Delta\rho_c$ and that this interface has to be downward continued to $R - T_c$, and (*iv*) making use of the identity $4\pi G = 3g_0/\bar{\rho}R$, where $\bar{\rho}$ is the planet's bulk density, one obtains

$$U(R) = \frac{3g_0}{\bar{\rho}(2\ell+1)} \left[\rho_l h_{\ell m} + \Delta\rho_l \omega_{\ell m} + \Delta\rho_c \left(\frac{R - T_c}{R} \right)^{\ell+2} \omega_{\ell m} \right]. \quad (5.19)$$

An analogous rational can be used to estimate the potential at the crust-mantle boundary, which yields

$$U(R-T_c) = \frac{3g_0}{\bar{\rho}(2\ell+1)} \times \left[(\rho_l h_{\ell m} + \Delta\rho_l \omega_{\ell m}) \left(\frac{R-Tc}{R}\right)^{\ell} + \Delta\rho_c \left(\frac{R-T_c}{R}\right) \omega_{\ell m} \right]. \tag{5.20}$$

Inserting eqs. 5.18, 5.19, and 5.20 into eq. 5.13, after some algebra, one can draw a linear relation between the deflection and the topography as follows

$$\omega_{\ell m} = -\frac{\rho_l C_\ell^s}{\Delta\rho_c} h_{\ell m}, \tag{5.21}$$

where C_ℓ^s represents the amount of compensation of the surface topography and is defined as

$$C_\ell^s = \frac{1 - \frac{3}{\bar{\rho}(2\ell+1)} \left[\rho_c + \Delta\rho_c \left(\frac{R-T_c}{R}\right)^{\ell}\right]}{\frac{g_m}{g_0} + \frac{\rho_c-\rho_l}{\Delta\rho_c} - \frac{1}{\xi_\ell g_0 \Delta\rho_c} - \frac{3}{\bar{\rho}(2\ell+1)} P} \tag{5.22}$$

and $P = \Delta\rho_l \left(\frac{R-T_c}{R}\right)^{\ell} + \Delta\rho_c \left(\frac{R-T_c}{R}\right) + \rho_c \left[\frac{\Delta\rho_l}{\Delta\rho_c} + \left(\frac{R-T_c}{R}\right)^{\ell+2}\right]$.

Finally, the relationship between the radial gravity coefficients $g_{\ell m}$ and the surface topography $h_{\ell m}$ can be expressed as

$$g_{\ell m} = \frac{Q_\ell^s(\ell+1)}{R} h_{\ell m}, \tag{5.23}$$

where Q_ℓ^s is the degree dependent transfer function given by

$$Q_\ell^s = \frac{3g_0\rho_l}{\bar{\rho}(2\ell+1)} \left[1 - C_\ell^s \frac{\Delta\rho_l}{\Delta\rho_c} - C_\ell^s \left(\frac{R-T_c}{R}\right)^{\ell+2}\right]. \tag{5.24}$$

Although this model allows for a density interface between the surface load and crust, given the lack of knowledge on the composition of the Venusian crust and to reduce the number of parameters in the model, I will assume for the remaining of the thesis that the two have the same density ρ_c. Figure 5.1 presents how the modeled spectral admittance, which corresponds to $Q_\ell^s(\ell+1)/R$, varies with respect to the elastic thickness T_e, the crustal thickness T_c, and the crustal density ρ_c. These models assume a mantle density of $\rho_m = 3300\,\mathrm{kg\,m^{-3}}$, a Young's modulus of $E = 100\,\mathrm{GPa}$, and a Poisson ratio of $\nu = 0.25$, which are constants adopted throughout this work. The chosen values are based on what has been measured for terrestrial rocks (e. g., Hyndman and Drury, 1976; Turcotte and Schubert, 2002) and are consistent with what has been used in previous studies of Venus. I

further remark that, even though other planets such as Mars are probably associated with higher upper mantle densities due to a high iron content, Venus is expected to be much more Earth-like as indicated by surface composition constraints obtained by soviet landers (Figure 1.3).

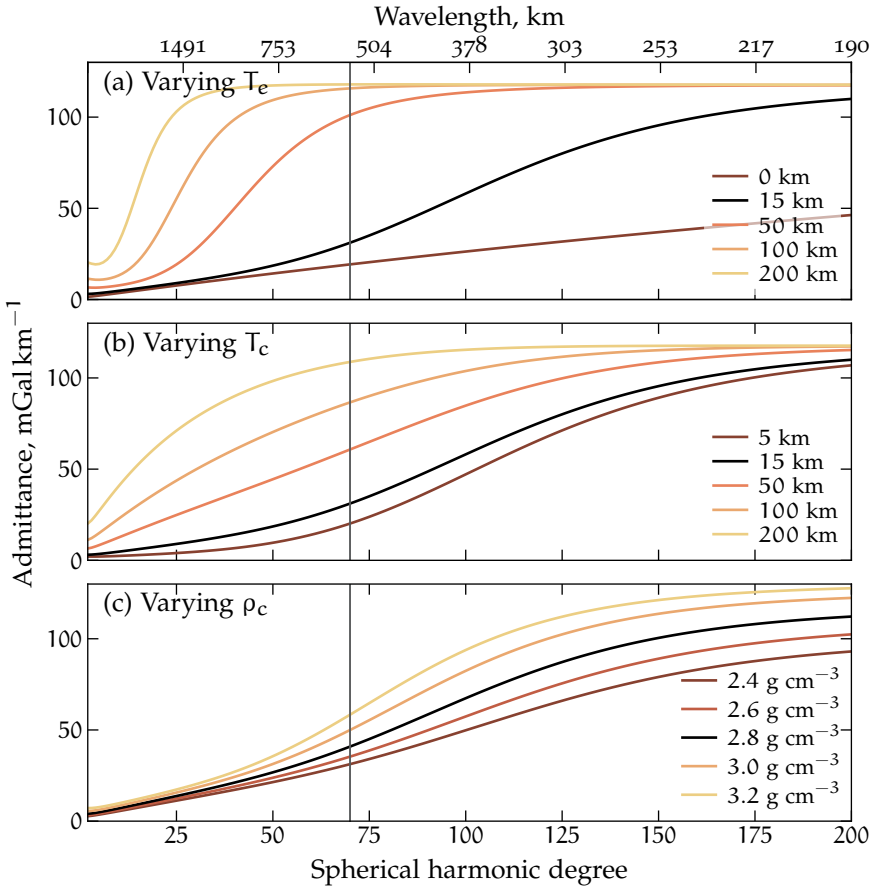

Figure 5.1: Theoretical admittances spectra for a surface loading model. The black curves in the three plots are generated using the same elastic thickness of 15km, crustal thickness of 15 km, and crustal density of 2800 kg m^{-3}. (a) Varying elastic thickness, with T_c = 15 km and ρ_c = 2800 kg m^{-3}. (b) Varying the crustal thickness, with T_e = 15 km and ρ_c = 2800kg m^{-3}. (c) Varying crustal density, with T_e = 15 km and T_c = 15 km. The dark gray vertical line indicated the global resolution of the MGNP180U gravity model based on Magellan data (Konopliv et al., 1999). Modified from Maia and Wieczorek (2022), Supplemental information (SI).

Figure 5.1 shows that, for the current gravity data resolution available for Venus ($\ell_{data} < 70$), the model is not very sensitive to the elastic thickness when it has relative small values, as expected for Venus. Moreover, in this degree range, the model is also relatively insensitive to crustal density. With higher-resolution gravity models it would

probably be possible to explore lateral variations of Venus's crustal density and better assess the contribution of lithospheric strength in the support of short-wavelength topography on the planet.

SUBSURFACE LOADS The rationale behind the development of the internal loads equations are quite similar to the one just demonstrated for the surface loads and so I chose to only present the final equations used in the model. However, for those interested in a step-by-step explanation, I recommend the thesis of Broquet (2020). The equations presented below can also be found in Grott and Wieczorek (2012) and Broquet and Wieczorek (2019).

For the internal loading scenario we assume that the loads are concentrated within a thin mass-sheet defined as $\psi^z_{\ell m} = \delta\rho_{\ell m} dr$, where $\delta\rho_{\ell m}$ is the density contrast of the loads with respect to the surroundings and dr is the thickness of the mass-sheet. The deflection caused by these loads reads

$$\omega^z_{\ell m} = -C^z_\ell \frac{\psi^z_{\ell m}}{\rho_m} \tag{5.25}$$

with

$$C^z_\ell = \frac{\frac{\rho_m}{\Delta\rho_c}\left\{\frac{g_z}{g_0} - \frac{3}{\bar{\rho}(2\ell+1)}\left[\rho_c\left(\frac{R-z_\psi}{R}\right)^{\ell+2} + \Delta\rho_c\left(\frac{R-z_\psi}{R}\right)\mathcal{Z}\right]\right\}}{\frac{\rho_c}{\Delta\rho_c} + \frac{g_m}{g_0} - \frac{1}{\xi_\ell g_0 \Delta\rho_c} - \frac{3\Delta\rho_c}{\bar{\rho}(2\ell+1)}\left(\frac{R-T_c}{R}\right) - \frac{3\rho_c}{\bar{\rho}(2\ell+1)}P'}, \tag{5.26}$$

where $P' = \left[\left(\frac{R-T_c}{R}\right)^{\ell+2} - \left(\frac{R-T_c}{R}\right)^{\ell} - \frac{\rho_c}{\Delta\rho_c}\right]$, z_ψ represents the depth of the mass-sheet, and

$$\mathcal{Z} = \begin{cases} \left(\frac{R-T_c}{R-z_\psi}\right)^{\ell} & \text{if } z_\psi \leqslant T_c \\ \left(\frac{R-z_\psi}{R-T_c}\right)^{\ell+1} & \text{if } z_\psi > T_c \end{cases}.$$

Equivalent to the surface loading scenario, the predicted radial gravity coefficients can be computed as

$$g^z_{\ell m} = \frac{Q^z_\ell(\ell+1)}{R}\frac{\psi^z_{\ell m}}{\rho_c}, \tag{5.27}$$

with Q^z_ℓ representing the transfer function defined as

$$Q^z_\ell = \frac{3g_0\rho_c}{\bar{\rho}(2\ell+2)}\left[\left(\frac{R-z_\psi}{z_\psi}\right)^{\ell+2} - C^z_\ell\frac{\rho_c}{\rho_m} - C^z_\ell\frac{\Delta\rho_c}{\rho_m}\left(\frac{R-T_c}{R}\right)^{\ell+2}\right]. \tag{5.28}$$

Figure 5.2 presents illustrations of the surface and subsurface loading scenarios and their gravitational signatures. Panels (a) and (b) show the surface loading model for elastic thicknesses of 300 and 15

km, respectively. We can see a considerable difference in the gravity for these two cases, with a more rigid lithosphere being associated with a stronger signal, while for a flexible lithosphere the longer wavelengths are nearly completely compensated and the gravity signals are related to the uncompensated shorter-wavelength relief. Note that for decreasing T_e, the load approaches an isostatic support state. In fact, if $T_e = 0\,\text{km}$, the model is equivalent to the Airy isostasy model with the "equal-pressures" formulation (Hemingway and Matsuyama, 2017). Panel (c) shows the effect of a internal load with negative (buoyant) density anomalies, while (d) illustrates the flexure caused by high-density subsurface loads at the base of the crust. In all examples we can clearly see that gravity and topography are perfectly correlated. In fact, the model is designed in such a way that the global spectral correlation is always equal to 1 or -1 (perfectly correlated or anti-correlated).

COMBINED LOADS The final step of our model is to combine the loading contributions from both surface and subsurface. Following Grott and Wieczorek (2012), the loads are assumed to be in phase, which is a valid assumption when the correlation is high. Defining the surface load as $\psi^s_{\ell m} = \rho_l(h_{\ell m} - \omega_{\ell m})$, the ratio between the two loads is $f_{\ell m} = \psi^s_{\ell m}/\psi^z_{\ell m}$. In order to have a bounded loading ratio L, the ratio $f_{\ell m}$ can be reparameterized as

$$L_{\ell m} = \frac{f_{\ell m}}{|f_{\ell m}| + 1} \tag{5.29}$$

that can vary between -1 and 1. In this parameterization, $L = 0$ represents the presence of surface loads only, while $L = -1$ and $L = 1$ correspond respectively to pure bottom-loading with low-density and high-density mass-sheets. For simplicity, the loading ratio will be assumed isotropic and independent of wavelength, i.e. $L_{\ell m} = L$.

Finally, the predicted radial gravity coefficients $g^{\text{flex}}_{\ell m}$ from the combination of the two loads can be written as

$$g^{\text{flex}}_{\ell m} = Q^{\text{flex}}_\ell (h_{\ell m} + \omega^z_{\ell m}) \tag{5.30}$$

where

$$Q^{\text{flex}}_\ell = \frac{Q^s_\ell + Q^z_\ell \frac{\rho_l}{\rho_c}\left(1 + \frac{\rho_l}{\Delta\rho_c} C^s_\ell\right) f}{1 - C^z_\ell \frac{\rho_l}{\rho_m}\left(1 + \frac{\rho_l}{\Delta\rho_c} C^s_\ell\right) f}. \tag{5.31}$$

Lastly, I remark that this loading model differs somewhat from the model of Forsyth (1985) that was previously applied to Venus (e.g., Phillips, 1994; Hoogenboom et al., 2005). The fundamental difference between the two models concerns how subsurface loads are treated. In Forsyth (1985), the subsurface loads are assumed to be on average uncorrelated with the surface loads, whereas, in the model presented here, the loads are assumed to be perfectly correlated. Though

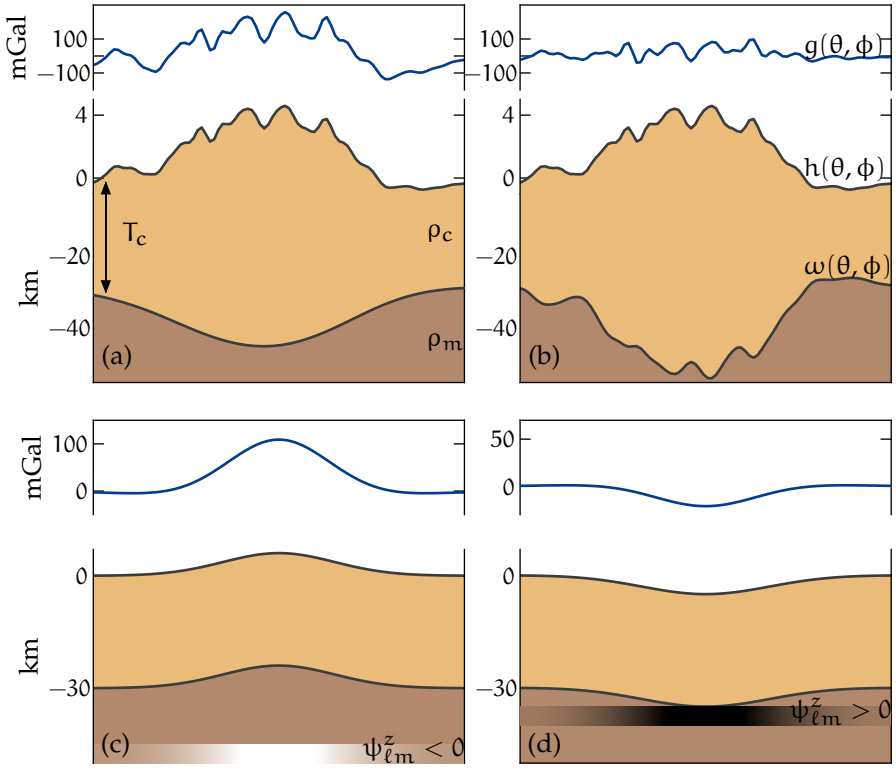

Figure 5.2: Schematic view of the adopted flexural model, showing the topography profile $h(\theta, \phi)$ and associated deflection $\omega(\theta, \phi)$. The corresponding radial gravity signal $g(\theta, \phi)$ is represented by the blue curve at the top of each subplot. Panel (a) shows the case of surface loads with T_e=300 km while (b) represents surface loading with T_e=15 km. Panel (c) displays the subsurface loading scenario in which the topography is supported by a buoyant layer in the mantle, represented by the thin layer at 150 km depth, with light colors indicating a negative density anomaly. Panel (d) exemplifies the case of a high-density layer, such as intrusions, represented by the thin layer at the base of the crust with dark colors indicating positive density anomalies. Panels (c) and (d) have a 15 km elastic thickness and the vertical scale of both surface relief and the crust-mantle interface are doubled for visual purposes. All profiles measure approximately 4000 km across. The models have a crustal thickness of 30 km, crustal and load densities of 2800 $kg\,m^{-3}$and a mantle density of 3300 $kg\,m^{-3}$. Figure from Maia and Wieczorek (2022).

Forsyth acknowledged that tectonic and volcanic processes would likely favor the formation of correlated loads, it was argued that erosion of the continental crust on Earth could act to decorrelate surface and subsurface loads. Since there is little to no erosion occurring on Venus today, the assumption of uncorrelated loads for this planet is thus questionable. Regardless, it is important to emphasize that the

differences between the two models become less prominent as the elastic thickness decreases, and that the two models are in fact identical for the case of Airy isostasy (i.e., $T_e = 0\,\mathrm{km}$). A second difference is that, in Forsyth's original approach, the subsurface load was determined from the observed gravity field. Hence, the modeled admittance function exactly fits the observed admittance. Their analysis instead focused on interpreting the correlation function.

5.1.4 *From elastic thickness to lithospheric thermal properties*

The elastic shell formulation provides a simplified mathematical representation of the lithosphere. On one hand, it enables a linear treatment of lithospheric loading, allowing for geophysical inversions. On the other hand, this formulation neglects significant modes of lithospheric deformation associated with viscous and plastic rheologies. The more realistic definition of the lithosphere, composed of a plastic-elastic-viscous rheology, is known as the mechanical lithosphere. Conveniently, it is possible to determine the mechanical lithosphere from the elastic lithosphere via a moment-matching technique, as introduced by McNutt (1984). In addition, because the mechanical thickness directly depends on the temperature with depth, it can be use to estimate the thermal gradient of the lithosphere. Hence, in the absence of direct heat flow measurements, elastic thickness estimations are one of the few quantities that can help constrain the thermal evolution of the planet through space and time. It is important to remark that these estimations are associated with thermal properties of when the lithosphere under the topographic feature was hottest and that the flexural signature "freezes" at that state. Therefore, since planets tend to cool with time, it is generally reasonable to assume that these estimations correspond to the thermal state during the formation of the region, although lithospheric reheating can trigger the process of thermal rejuvenation (McNutt, 1984; Albert and Phillips, 2000).

The main idea behind McNutt's method is that the bending moment $\mathcal{M}$ must be balanced by the stress differences within the vertical profile of the flexed lithospheric plate, independent of its rheology. I. e., an elastic plate and a more complex mechanical plate must support identical bending moments for a given curvature. In mathematical terms, this relation reads

$$\mathcal{M} = \int_0^\infty \Delta\sigma(z)(z - z_n)\,dz, \tag{5.32}$$

where $\Delta\sigma$ represents the differential stress, z is the depth, and z_n corresponds to the depth of the neutral axis where $\Delta\sigma = 0$. In practice, the integral can be stopped at the depth where $\Delta\sigma$ is equal or close to zero. This equation provides a quantitative relation between the mechanical and elastic lithosphere since both plates should have the

same bending moment. It is then possible to estimate the mechanical lithosphere thickness T_m from T_e.

The variation of the differential stress with depth, commonly referred to as yield strength envelope, is represented in Figure 5.3 for both (a) elastic lithosphere and (b) mechanical lithosphere. In the elastic plate model the differential stresses vary linearly from the surface down to the T_e reaching maxima and minima at $z = 0$ and $z = Te$ in the case where the plate bending is concave downward. In this scenario, it is straight-forward to integrate the differential stress, and the bending moment reads

$$\mathcal{M} = \frac{KET_e^3}{12(1-\nu)}, \tag{5.33}$$

which is simply the product between the plate curvature K with the rigidity eq. 5.10. Even though K can vary spatially, using the maximum curvature for the elastic to mechanical plate conversion generally yields reliable results, as shown by Mueller and Phillips (1995). In this work, the maximum curvature is computed by taking the second derivative of the modeled lithospheric deflection ω and not from actual observations. Hence, the curvature depends upon the validity of the model assumptions.

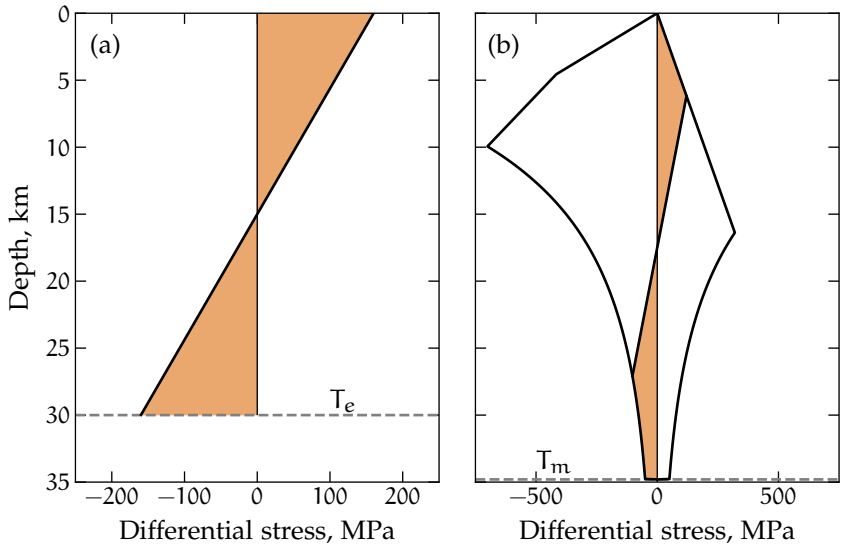

Figure 5.3: Differential stress with respect to depth for a lithosphere plate bent concave downward, i. e., with tensional stresses at the top and compressional stresses at the bottom of the plate. (a) Elastic plate model for T_e= 30 km and K= 10^{-7} m^{-1}. (b) Estimated mechanical yield stress enveloped considering brittle failure near the surface, an elastic core and, viscous flow near the base of the lithosphere, considering a strain rate of 10^{-16} s^{-1} and dry diabase rheology.

The mechanical plate is more complex and accounts for different rheological contributions. The uppermost colder lithosphere is controlled by brittle failure (i. e., faulting), the lower and hotter lithosphere is associated with viscous stresses and, in its middle, the plate behaves elastically, as shown in Figure 5.3(b). The brittle behavior was experimentally studied by Byerlee (1968), who found that the frictional resistance of rocks are mostly insensitive to temperature, strain rate, and rock composition. Based on the empirical laws from the works of Byerlee (1968) and Jaeger and Cook (1976), Mueller and Phillips (1995) derived expressions to estimate minimum differential stress necessary to cause brittle failure. For a tension regime, the differential stress is defined as

$$\Delta\sigma = \begin{cases} 0.786\bar{\sigma}_v & \text{if } \bar{\sigma}_v \leqslant 529.9\text{MPa} \\ 56.7\text{MPa} + 0.679\bar{\sigma}_v & \text{if } \bar{\sigma}_v > 529.9\text{MPa} \end{cases}, \tag{5.34}$$

while in compression it reads

$$\Delta\sigma = \begin{cases} -3.68\bar{\sigma}_v & \text{if } \bar{\sigma}_v \geqslant 113.2\text{MPa} \\ -176.6\text{MPa} - 2.12\bar{\sigma}_v & \text{if } \bar{\sigma}_v < 113.2\text{MPa} \end{cases}, \tag{5.35}$$

where $\bar{\sigma}_v$ is the effective vertical stress (i. e., lithostatic overburden).

Viscous stresses control the rheology of the bottom part of the lithosphere and depend on the mechanical properties of the rocks, strain rate $\dot{\varepsilon}$, and temperature T. The flow law that governs ductile deformation is defined as (e.g., McNutt, 1984):

$$\Delta\sigma(z) = \left(\frac{\dot{\varepsilon}}{A}\right)^{1/n} \exp\left(\frac{Q}{n\mathcal{R}T(z)}\right), \tag{5.36}$$

where the activation energy Q, the exponent n, and the pre-exponential factor A are rock-dependent rheological parameters that are experimentally defined, and $\mathcal{R}$ is the gas constant. As shown in eq. 5.36 and Figure 5.3(b), at the base of the lithosphere the yield strength drops towards zero exponentially with depth. In practice, however, the base of the plate is limited by a threshold bounding stress. The choice of the bounding stress value is somewhat arbitrary. However, for values smaller than 100 MPa, the impact is small given the exponential dependency on temperature. Following McNutt (1984), I consider a bounding stress value of 50 MPa. The depth where this bounding stress is reached defines the thickness of the mechanical lithosphere. Moreover, because of the dependence of eq. 5.36 on temperature, it is possible to compute the associated temperature at this depth. Assuming that there are no heat sources on the lithosphere, the thermal gradient within the lithosphere is linear and reads:

$$\frac{dT}{dz} = \frac{T(z = T_m) - T(z = 0)}{T_m}. \tag{5.37}$$

From dT/dz, it is straight-forward to estimate the heat flow F at the surface as

$$F = k\frac{dT}{dz}, \tag{5.38}$$

with k representing the thermal conductivity of the lithosphere.

5.2 DYNAMIC LOADING MODEL

Almost a century ago, Pekeris (1935) presented a mathematical relation between the magnitude of thermal anomalies in the mantle and the direction of convective flows for a self-gravitating sphere. This pioneering study presented estimations of gravity signals generated by mantle flow processes. It showed that high temperature anomalies cause rising currents which deform upwards the planetary surface and all interfaces down to the core-mantle boundary. Hence, gravity anomalies associated to mantle convection have two contributions of opposite directions. A high temperature perturbation is associated with thermal expansion and low density anomalies, which causes a negative gravity anomaly. Meanwhile, the upward deflections of the surface and internal boundaries produce a positive gravity anomaly. In fact, Pekeris estimated that, for an isoviscous mantle, the uplift resulting from a negative density anomaly would have a positive gravity signature. An analogous but opposite effect is generated by low temperature perturbations. This was the earliest demonstration of the importance of dynamically (or actively) maintained topography of planetary surfaces.

In the late 1970s, travel-time tomography techniques were first applied to seismic studies (e. g., Aki et al., 1977) and, in the following decade, they started being used in a global scale to determine lateral seismic velocity in Earth's mantle (e. g., Dziewonski, 1984). Seismic velocities can be used as a proxy for thermal density anomalies, enabling the estimation of the global distribution of density heterogeneities in the Earth's mantle. Motivated by the new data constraints and following the concepts presented by Pekeris (1935), a series of papers introduced a viscosity-dependent dynamic loading model to quantify the relation between density anomalies within Earth's mantle and long-wavelength gravity and topography signatures (Ricard et al., 1984; Richards and Hager, 1984; Hager et al., 1985; Hager and Clayton, 1989). This model is outlined in the next part.

5.2.1 *Governing equations, model assumptions, and the propagator matrix solution*

This modeling approach has a series of simplifications and assumptions which allow for an analytical tractability of the problem. The

mantle is modeled as as a self-gravitating, incompressible, Newtonian fluid. Moreover, it assumes spherical symmetry, i.e. it is only sensitive to radial variations of mantle viscosity. The fluid flow follows the equations of the Stokes flow which assumes that viscous forces dominates the flow dynamics and inertial forces are neglected. This is a reasonable approximation for mantle flow since mantle viscosities are large, in the order of 10^{20} Pa s. In the Stokes flow case, the equations of motion are a linearized version of the full Navier-Stokes equations and can be written as:

$$\nabla \cdot \boldsymbol{\tau} + \rho \mathbf{g} = 0 \tag{5.39}$$

where $\boldsymbol{\tau}$ is the stress tensor, ρ the density, and $\mathbf{g}$ the gravitational acceleration.

The Stokes equations include the equation for the conservation of mass, which is commonly written in the form of the continuity equation. For an incompressible fluid it reads:

$$\nabla \cdot \boldsymbol{\nu} = 0 \tag{5.40}$$

where $\boldsymbol{\nu}$ is the velocity vector.

The explicit form of these equation in spherical coordinates along with the definition of the stress tensor $\boldsymbol{\tau}$ for a Newtonian fluid can be found in eqs. 4.1 to 4.10 of Hager and Clayton (1989). Furthermore, by rewriting the equations in terms of spherical harmonics and taking advantage of the spherical symmetry of the problem, Hager and Clayton (1989) show that the radial dependence of the flow can be written as ordinary differential equation for each spherical harmonic and solved analytically using the propagator matrix technique. I reproduce here key parts of the development, following the 4×4 propagator system terminology presented in James et al. (2013) while seizing the opportunity to correct some typographical errors from that work.

By considering only radial dependency, assuming constant viscosity within a spherical shell, and defining a new variable $w = \ln(r/R)$, where R is the mean planetary radius, the Stokes flow can be written as a system of ordinary differential equations:

$$\frac{d\mathbf{u}(r)}{dw} = \mathbf{A} \cdot \mathbf{u}(r) + \mathbf{b}(r). \tag{5.41}$$

The variable vector $\mathbf{u}(r)$ includes the velocities (radial $v^r_{\ell m}(r)$ and tangential $v^\theta_{\ell m}(r)$) and stresses (radial $\tau^{rr}_{\ell m}$ and shear deviatoric stress $\tau^{r\theta}_{\ell m}$) as a function of the radial position r. It reads:

$$\mathbf{u}(r) = \begin{pmatrix} v^r_{\ell m}(r) \\ v^\theta_{\ell m}(r) \\ \left[\tau^{rr}_{\ell m}(r) + \rho(r) g(r) N_{\ell m}(r)\right] r/\eta_0 \\ \tau^{r\theta}_{\ell m}(r) r/\eta_0 \end{pmatrix} \tag{5.42}$$

where η_0 is the reference viscosity, g is the radial gravity (positive when directed downwards), ρ is the local density, N_{lm} is the gravitational potential perturbation, and the term $\rho g N_{lm}$ is an additional "gravitational pressure" to the normal stress component. Note that $\mathbf{u}(r)$ depends on spherical harmonic degree and order, but we are dropping the subscripts for simplicity. The same is true for $\mathbf{b}(r)$. The matrix $\mathbf{A}$, which is a function of the viscosity η of an isoviscous shell and spherical harmonic degree, is defined as:

$$\mathbf{A} = \begin{pmatrix} -2 & L & 0 & 0 \\ -1 & 1 & 0 & \eta_0/\eta \\ 12\eta/\eta_0 & -6L\eta/\eta_0 & 1 & L \\ -6\eta/\eta_0 & 2(2L-1)\eta/\eta_0 & -1 & -2 \end{pmatrix} \tag{5.43}$$

where $L = \ell(\ell+1)$. The matrix $\mathbf{A}$ is by definition isotropic, in that it does not depend on the spherical harmonic angular order. The density anomalies $\delta\rho_{\ell m}(r)$ responsible for driving the convective flow in the system are included in the vector $\mathbf{b}(r)$, which reads

$$\mathbf{b}(r) = \begin{pmatrix} 0 \\ 0 \\ g(r) r^2 \delta\rho_{\ell m}(r)/\eta_0 \\ 0 \end{pmatrix}. \tag{5.44}$$

Considering a single shell of constant viscosity, the solution of eq. 5.41, after reversing the variable change, is

$$\begin{aligned} \mathbf{u}(r) &= \exp[\mathbf{A}(\ln(r/R) - \ln(r_0/R))]\mathbf{u}(r_0) \\ &\qquad + \int_{r_0}^{r} \exp[\mathbf{A}(\ln(r/R) - \ln(\epsilon/R))]\mathbf{b}(\epsilon)\,d\epsilon \\ &= \mathbf{P}(r, r_0)\mathbf{u}(r_0) + \int_{r_0}^{r} \mathbf{P}(r, \epsilon)\mathbf{b}(\epsilon)\,d\epsilon, \end{aligned} \tag{5.45}$$

where $\mathbf{u}(r_0)$ represents the starting vector and $\mathbf{P}(r, r_0)$ is the so-called propagator matrix that propagates the solution from r_0 to r. A useful property of the propagator matrix formulation is that the solution vector propagated through a series of n-layers with different viscosities is simply the product of the matrices of the individual layers:

$$\mathbf{P}(r, r_0) = \mathbf{P}(r, r_{n-1}) \cdot \mathbf{P}(r_{n-1}, r_{n-2}) \cdots \mathbf{P}(r_1, r_0), \tag{5.46}$$

which allows for a straight-forward adaptation of the solution shown in eq. 5.45 to a multi-layer viscosity structure. Furthermore, like the matrix $\mathbf{A}$, the propagator matrix is also isotropic.

In addition, we can simplify our problem by discretizing the continuous mass-anomalies $\delta\rho_{\ell m}(r)$ into surface mass-sheets $\psi_{\ell m}$ of the form

$$\psi^i_{\ell m} = \int_{r_i - \epsilon/2}^{r_i + \epsilon/2} \delta\rho_{\ell m}(r)\,dr. \tag{5.47}$$

Similarly to the density anomaly mass-sheets used in the flexural model, these discretized layers have units of $\mathrm{kg\,m^{-2}}$. Then, we are able to rewrite eq. 5.45 as

$$\mathbf{u}(r) = \mathbf{P}(r, r_0)\mathbf{u}(r_0) + \sum_{i=1}^{n} \mathbf{P}(r, r_i)\mathbf{b}_i, \tag{5.48}$$

where

$$\mathbf{b}_i = \begin{pmatrix} 0 \\ 0 \\ g_{r_i} r_i \psi^i_{\ell m}/\eta_0 \\ 0 \end{pmatrix}. \tag{5.49}$$

5.2.2 *The Venusian case: boundary conditions and some simplifications*

Looking at our problem in the framework of mantle convection on Venus, the starting point v_0 becomes the core radius R_c and the solution is propagated through mantle layers of varying viscosity until the planetary surface R. The size of Venus's core is unfortunately poorly constrained due to the limited geophysical data available. Moment of inertia factor (MOI) estimations indicate a core radius within the range of 3000–4000 km (Margot et al., 2021). For this study, I picked the core radius of $R_c = 3225$ km. This value was theoretically estimated by Aitta (2012) and considers Venus's mass and size to provide a scaled-down version of Earth's interior model, known as Preliminary Reference Earth Model (PREM). The model by Aitta (2012) results in a moment of inertia factor of $\mathrm{MOI} = 0.338$ which is consistent with the Margot et al. (2021) estimations of $\mathrm{MOI} = 0.337 \pm 0.024$. The mantle and core densities adopted are also from Aitta (2012).

To compute the model solutions, it is necessary to define boundary conditions at the surface and at the core-mantle boundary (CMB). We assume a free-slip boundary between the core, considered as an inviscid fluid, and the overlying mantle, which requires a zero radial velocity and zero shear stress. At the surface, as will be discussed in Chapter 7, I explore both free-slip and no-slip scenarios. In the case of a no-slip boundary condition both radial and tangential velocities become zero at the boundary. This scenario can be interpreted as the presence of a stagnant lid that does not participate in the convective flow. As for the free-slip case, the fluid can freely flow in the tangential direction, which is a proxy for a mobile-lid type of regime where the surface is coupled and flows along with the mantle.

For Venus, it is, or course, not possible to estimate the distribution of density anomalies in the mantle using tomography models as is done for the Earth. Therefore, to not have a underdetermined problem, we assume that the density anomalies are concentrated on

a single shell at radius R_ψ. The use of a single density anomaly layer has been applied to Venus in several studies, including Herrick and Phillips (1992) and James et al. (2013). However, studies such as Kiefer et al. (1986) and Pauer et al. (2006) have chosen a different parameterization, where the density anomalies are assumed constant with depth throughout Venus mantle. A practical advantage of this approach is that the lack of depth-dependency removes the necessity of R_ψ, hence, there is one parameter less to take into account.

From a geophysical perspective, one can debate about which of these assumptions is more realistic. It is reasonable to assume for Venus that most gravity signals from dynamic loading are associated with hot mantle plumes and cold downwellings, where the anomalous hot and cold materials generate negative and positive density anomalies, respectively. Classic plume modeling studies show that most of the plume material tend to spread laterally under the lithosphere and only a thin conduit connects the plume head to the deep mantle e.g., Kiefer and Hager, 1991; Nimmo and McKenzie, 1996. This view was used by Herrick and Phillips (1992) to favor a mass-sheet scenario, since the density anomalies would be mostly concentrated in a thin depth range. On the other hand, Pauer et al. (2006) draws a comparison to Earth's mantle density patterns arguing that plumes and subducted slabs penetrate the mantle more or less vertically, indicating that a depth-independent distribution of density anomalies should be a reasonable first approximation. Yet, the presence of subducted slabs on Venus today is unlikely, even if the planet has been through a mobile-lid regime in the past. This is indicated by the difficulty to reproduce the small center of mass and center of figure offset considering recent (less than 1 Ga) surface mobilization events in thermal evolution simulations (King, 2018). Nonetheless, as discussed in Chapter 7, both scenarios are considered in my investigations.

Taking into account the assumptions just described, in the case where the surface is modeled as a no-slip boundary and the density anomalies are parameterized as a mass-sheet we can rewrite eq. 5.48 as

$$\begin{pmatrix} 0 \\ 0 \\ -\rho_m g_R (h^{dyn}_{\ell m} - N^{dyn}_{\ell m}) - q_{\ell m} \\ \tau^{\theta}_{\ell m}(R) \end{pmatrix} = \mathbf{P}(R, R_c) \begin{pmatrix} 0 \\ \frac{\eta_0}{R} \nu^{\theta}_{\ell m}(R_c) \\ \frac{R_c}{R} \Delta\rho_c g_c \mathcal{C}_{\ell m} \\ 0 \end{pmatrix} + \mathbf{P}(R, R_\psi) \begin{pmatrix} 0 \\ 0 \\ \frac{R_\psi g_\psi}{R} \psi_{\ell m} \\ 0 \end{pmatrix} \tag{5.50}$$

The four unknowns of this system of equations are the surface displacement caused by mantle flow (i. e., the dynamic topography) $h^{dyn}_{\ell m}$, the core-mantle boundary displacement $\mathcal{C}_{\ell m}$, the shear stress at the surface $\tau^{\theta}_{\ell m}(R)$, and the tangential velocity at the core-mantle boundary $v^{\theta}_{\ell m}(R_{\mathcal{C}})$. The term $N^{dyn}_{\ell m}$ representing the dynamic geoid exterior to the body is computed as combined contribution from the density anomalies and boundary displacements, as follows:

$$N^{dyn}_{\ell m} = \frac{4\pi G R}{g_R(2\ell+1)}\left(\rho_m h^{dyn}_{\ell m} + \left(\frac{R_\psi}{R}\right)^{\ell+2}\psi_{\ell m} + \Delta\rho_{\mathcal{C}}\left(\frac{Rc}{R}\right)^{\ell+2}\mathcal{C}_{\ell m}\right) \tag{5.51}$$

Along with the free variables, eqs. 5.50 and 5.51 include the density of the upper mantle ρ_m, the density contrast between the core and the mantle $\Delta\rho_{\mathcal{C}}$, and the gravitational accelerations g_R, g_ψ and $g_{\mathcal{C}}$ at radii R, R_ψ and $R_{\mathcal{C}}$, respectively. The density values are taken from the interior model of Aitta (2012), where $\rho_m = 3300\ \mathrm{kg\,m^{-3}}$(same as used for the flexural model) and $\Delta\rho_{\mathcal{C}} = 4050\ \mathrm{kg\,m^{-3}}$. The gravity within the mantle g_ψ is computed considering a sphere with linearly increasing density from surface to CMB.

Following the approach of James et al. (2013), we include to the surface boundary condition a flexural bottom loading term $q_{\ell m}$ that follows the thin elastic shell theory as presented in Section 5.1. This term adds an elastic strength to the surface boundary that opposes the displacement induced by mantle flow. Making use of eq. 5.13, $f_{\ell m}$ can be written as

$$q_{\ell m} = \frac{1}{\xi_\ell} h^{dyn}_{\ell m} \tag{5.52}$$

where ξ_ℓ is defined in eq. 5.14 and the flexural displacement is defined as the dynamic topography. However, for low elastic thickness values, as expected for Venus, the elastic lithosphere thickness have negligible impact on the model. This property will be further discussed in the next section.

Taking a closer look into eq. 5.50, one might notice that the reference viscosity η_0 only affects the estimated velocity and it does not influence the dynamic topography and geoid, which are the predicted observables. Therefore, our analyses are not sensitive to the absolute viscosity of the mantle but only to *relative variations of viscosity*, contained in the propagator matrices.

5.2.3 *Kernel functions*

A key property of eq. 5.50 is its linearity with respect to the density anomaly distribution. Exploring this attribute and following the standard use of response function to tidal loading with Love numbers,

Richards and Hager (1984) chose to built the dynamic loading problem in terms of normalized response functions, also known as kernels. Instead of focusing on particular density distribution for each solution, the final response can be computed by convolving the kernels functions with a given density distribution.

The kernel functions are computed by adopting $\psi_{\ell 0} = 1$ and solving eq. 5.50 degree by degree. We can re-arrange this isotropic version of eq. 5.50 and plug in eq.5.52 and eq. 5.51 to write the system of equations more explicitly as

$$\begin{aligned}
&\mathbf{P}^{i2}(R, R_c)\frac{\eta_0}{R}\,\bar{v}_{\ell m}(R_c) \\
&\quad + \left(\mathbf{P}^{i3}(R, R_c)\, g_c\, \frac{R_c}{R} - \delta_{i3}\frac{4\pi G}{2\ell+1}\rho_m R\left(\frac{R_c}{R}\right)^{\ell+2}\right)\Delta\rho_c\bar{c}_{\ell m} \\
&\quad + \delta_{i3}\left(\rho_m g - \frac{4\pi G}{2\ell+1}\rho_m^2 R + \frac{1}{\xi_\ell}\right)\bar{h}_{\ell m} - \delta_{i4}\bar{\tau}_{\ell m} \\
&\quad = -\mathbf{P}^{i3}(R, R_\psi)\frac{R_\psi g_\psi}{R} + \delta_{i3}\frac{4\pi G}{2\ell+1}\rho_m R\left(\frac{R_\psi}{R}\right)^{\ell+2}
\end{aligned} \tag{5.53}$$

where the superscripts on $\mathbf{P}$ indicate the appropriates row ($i = 1, 4$) and column, and δ_{ij} is the Kronecker delta ($\delta_{ij} = 1$ for $i = j$, otherwise $\delta_{ij} = 0$), and the overbar refers to the solution parameters for a unit load.

Following the terminology of previous works (e. g., James et al., 2013), one can define the geoid kernel N_ℓ, the surface displacement (i. e., topography) kernel H_ℓ and the admittance kernel $\mathcal{Z}_\ell^N$, which are purely degree-dependent, as

$$N_\ell \equiv \bar{N}_{\ell m} = \frac{N_{\ell m}^{dyn}}{\psi_{\ell m}} \tag{5.54}$$

$$H_\ell \equiv \bar{h}_{\ell m} = \frac{h_{\ell m}^{dyn}}{\psi_{\ell m}} \tag{5.55}$$

$$\mathcal{Z}_\ell^N = \frac{N_\ell}{H_\ell} = \frac{N_{\ell m}^{dyn}}{h_{\ell m}^{dyn}} \tag{5.56}$$

where $\bar{h}_{\ell m}$ is obtained by solving the four linear equations in eq. 5.53, and $\bar{N}_{\ell m}$ is obtained by substituting the solution parameters into eq. 5.51. In addition, we can compute alternative gravity-related kernels, such as the radial gravity kernel $\mathcal{G}_\ell$ and the associated admittance kernel $\mathcal{Z}_\ell$ as follows

$$\mathcal{G}_\ell = N_\ell\frac{GM(\ell+1)}{R^3} \tag{5.57}$$

$$\mathcal{Z}_\ell = \frac{\mathcal{G}_\ell}{H_\ell} \tag{5.58}$$

which will be preferably used in my investigations. I adopt radial gravity instead of the geoid because the associated admittance loses

the red-spectrum trait allowing for a more balanced visualization of the model over all spherical harmonic degrees. Nevertheless, I remark that if the data uncertainties are properly taken into account in the analysis, there should not be a significant discrepancies in the results for different gravity components.

SINGLE MASS-SHEET DENSITY ANOMALIES In this scenario, the density anomalies are assumed to be entirely concentrated within a single thin mass-sheet $\psi_{\ell m}$ (Herrick and Phillips, 1992; James et al., 2013). Then, the dynamic gravity $g^{dyn}_{\ell m}$ and topography $h^{dyn}_{\ell m}$ are estimated by simply multiplying the kernel function with the mass-sheet spherical harmonic coefficients:

$$g^{dyn}_{\ell m} = \mathcal{G}_\ell \psi_{\ell m} \tag{5.59}$$

$$h^{dyn}_{\ell m} = H_\ell \psi_{\ell m}. \tag{5.60}$$

An illustration of the dynamic loading model for the single mass-sheet case is presented in Figure 5.4. The figure shows the predicted surface displacement and gravity anomalies for three mantle viscosity structures for a mass-sheet placed at 200 km depth. On the right, I present the predicted spectral admittance for the three models. For comparison, the prediction from a subsurface flexural loading model is also shown. As we can see, the addition of viscosity jumps (i. e., upper mantle having a reduced viscosity with respect to the lower mantle) tend to damp the surface displacement reducing the associated gravity anomaly. Moving to the spectral domain, the impact of the viscosity structure is quite complex, but, overall, the presence of a low viscosity upper mantle tend to decrease the admittance. Comparing the viscous flow model with the flexural model, we see that the elastic model has a roughly similar admittance as the isoviscous model for $\ell < 10$. However, for larger degrees the flexural model predicts considerably larger admittance values, for example, for $\ell = 40$ there is a 20 mGal km^{-1} difference between the flexural and the isoviscous model.

CONSTANT DENSITY ANOMALY WITH DEPTH Another possibility is to assume that the mantle density anomalies do not vary with depth (e.g., Kiefer et al., 1986; Pauer et al., 2006). Given that the density anomalies are approximated as thin mass-sheets with units of kg m^{-2} (eq. 5.47), we approximate a uniform volumetric density anomaly with depth using a series of mass-sheets whose magnitudes are adjusted to account for geometric effects.

The mass of a spherical shell of thickness $\delta r = r_{i+1} - r_i$ and density $\delta\rho$ is given by

$$M_{\delta\rho} = \frac{4\pi}{3}\delta\rho(r^3_{i+1} - r^3_i), \tag{5.61}$$

whereas the mass of a sheet density in the middle of this shell with radius $r_\psi = (r_{i+1} + r_i)/2$ is

$$M_\psi = 4\pi\psi \left(\frac{r_{i+1} + r_i}{2} \right)^2 . \tag{5.62}$$

Equating $M_{\delta\rho}$ and M_ψ gives the following relation between ψ and $\delta\rho$:

$$\delta\rho = \frac{3(r_{i+1} + r_i)^2}{4(r_{i+1}^3 - r_i^3)}\psi. \tag{5.63}$$

The predicted gravity for a series of sheet masses that are distributed uniformly within the mantle is given by

$$g_{\ell m}^{dyn} = \sum_{i=1}^{N} G_\ell(r_i)\, \psi_{lm}^i(r_i), \tag{5.64}$$

where $i = 1$ corresponds to the core-mantle boundary and $i = N$ corresponds to the maximum radius of the uppermost mass sheet, respectively. A similar equation exists for the dynamic topography. By assuming that $\delta\rho_{\ell m}$ is constant with depth, eqs 5.63 and 5.64 yield

$$g_{\ell m}^{dyn} = \sum_{i=1}^{N} G_\ell(r_i)\, \delta\rho_{\ell m} \frac{4(r_{i+1}^3 - r_i^3)}{3\,(r_{i+1} + r_i)^2}. \tag{5.65}$$

As N increases and δr becomes smaller, the better will be the approximation of a constant density anomaly with depth. In this work, I use 18 layers, each being separated in depth by 150 km, with the uppermost mass sheet being placed at 100 km depth.

The load depth and the radial viscosity profile are the main attributes I will investigate. Nevertheless, our model also depend on other parameters, which I choose to fix in order to limit the parameter space and because they represent minor contributions to the modeled gravity and topography. To get an idea of the impact of some of these parameters, Figure 5.5 shows how sensitive the model is to the elastic thickness and the mantle density. For the elastic thickness, we see that when $T_e < 50$ km, which are values expected for Venus, this parameter has a negligible impact on the model. Hence, for simplicity I chose to use $T_e = 0$ km. Alternatively, changes in the mantle density tend to vertically shift the admittance. Increasing the density by 100 $\mathrm{kg\,m^{-3}}$ increases the admittance by about 2 $\mathrm{mGal\,km^{-1}}$ on average for the plotted degree range.

5.2.4 *The lateral variation of mantle density anomalies*

In order to compute the predicted gravity and topography from the kernel functions, it is necessary to know the spherical harmonic coefficients of the mass-sheet density anomalies, as indicated in eqs. 5.59

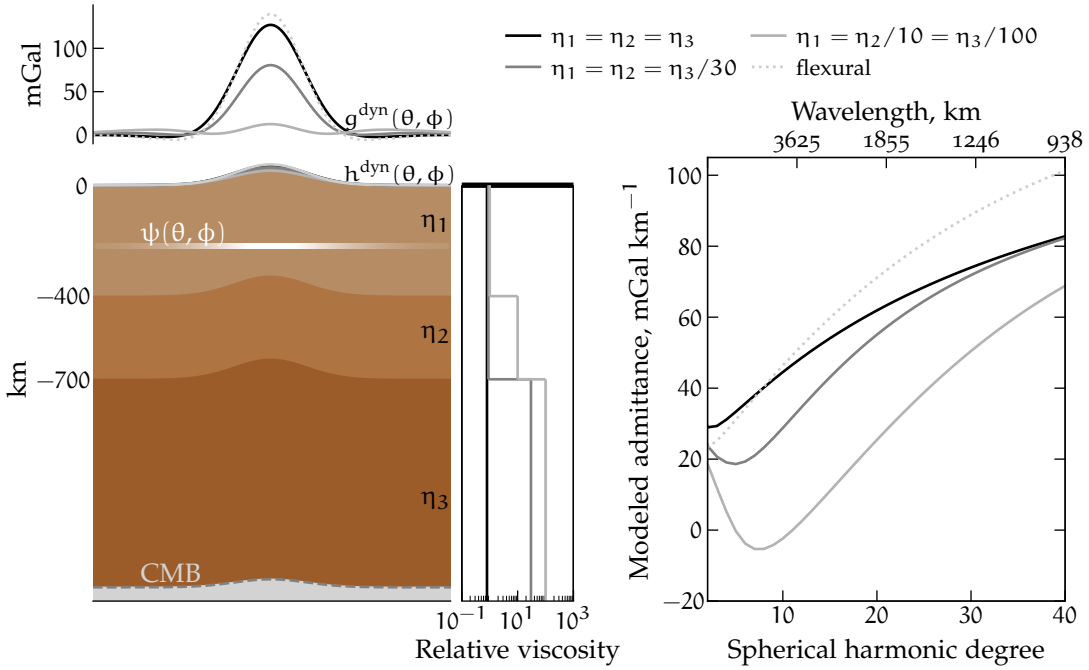

Figure 5.4: Schematic view of the dynamic loading model showing (on the left panel) the boundary displacements, including the surface topography and the associated gravity signal caused by a negative mass-sheet density anomaly. The sketch shows the gravity perturbations for three different mantle viscosity structures along with the gravity predicted by the subsurface flexural model (Section 5.1). The right panel shows the corresponding modeled admittance of the 4 model predictions.

and 5.60. However, we do not know the density anomaly distribution in Venus's mantle. Thus, we have to estimate this distribution from the data. Following the approach of Pauer et al. (2006), each coefficient $\psi_{\ell m \ell m}$ is computed such that it minimizes the difference of gravity and topography observations with respect to the predicted values. For each spherical harmonic coefficient, the misfit function is constructed as

$$M_{\ell m} = (g^{obs}_{\ell m} - g^{dyn}_{\ell m})^2 + \lambda_\ell (h^{obs}_{\ell m} - h^{dyn}_{\ell m})^2, \tag{5.66}$$

where λ_ℓ is a scaling factor that imposes equally weighted contributions from gravity and topography to the misfit. It is defined as

$$\lambda_\ell = \frac{\sum_{m=-\ell}^{\ell} \left(g^{obs}_{\ell m}\right)^2}{\sum_{m=-\ell}^{\ell} \left(h^{obs}_{\ell m}\right)^2}. \tag{5.67}$$

After plugging in eqs. 5.59 and 5.60 into eq. 5.66, we can solve $\partial M_{\ell m}/\partial \psi_{\ell m} = 0$, which yields

$$\frac{\partial M_{\ell m}}{\partial \psi_{\ell m}} = 2\mathcal{G}_\ell (g^{obs}_{\ell m} - \psi_{\ell m}\mathcal{G}_\ell) + 2\lambda_\ell H_\ell (h^{obs}_{\ell m} - \psi_{\ell m} H_\ell) = 0. \tag{5.68}$$

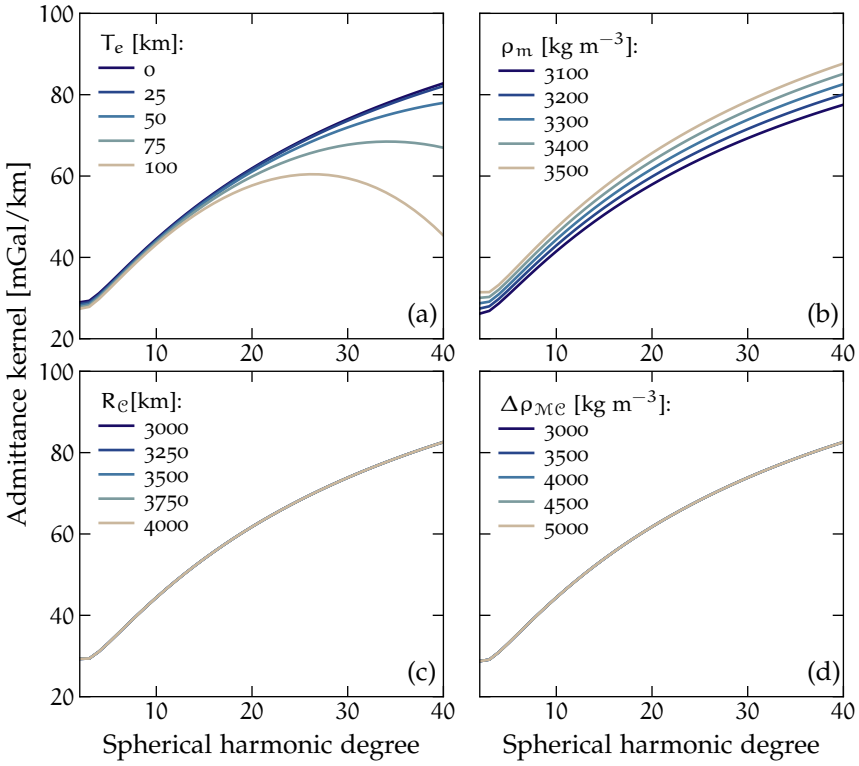

Figure 5.5: Admittance kernel sensitivity to the (a) elastic thickness T_e, (b) the mantle density ρ_m, (c) core radius R_c, and (d) core-mantle density contrast $\Delta\rho_{Mc}$. The kernels have an isoviscous mantle and the density mass-sheet is set at 200 km depth.

Re-arranging eq. 5.68, we can compute the density anomaly coefficients $\psi_{\ell m}$ associated with the minimum misfit as

$$\psi_{\ell m} = \frac{H_\ell \, h^{obs}_{\ell m} \lambda_\ell + \mathcal{G}_\ell \, g^{obs}_{\ell m}}{(H_\ell)^2 \lambda_\ell + (\mathcal{G}_\ell)^2}. \tag{5.69}$$

An analogous equation can be derived for the case of density anomalies that are continuous with depth.

5.3 DATA INVERSION

The models presented in this chapter are able to predict gravity and topography. These predictions depend on a series of geophysical parameters, such as the crustal thickness and the elastic lithosphere thickness (e.g. Figure 5.1) or the mantle viscosity e (e.g. Figure 5.4). By quantitatively comparing the modeled gravity and topography for a range of model parameters with the observations, it is possible to estimate the subset of values that can that can explain the observations well, providing constraints on the interior structure of the investigated body. Retrieving unknown physical properties from observa-

tional data, making use of a parameterized physical model is referred to as an inverse problem. This work does not provide a detailed summary of inversion problem theory, which is a vast field of research with several thorough reviews available, notably the book by Tarantola (2005). Instead, I will focus on a more practical description of the inversion approaches used in the scope of this thesis.

5.3.1 *The goodness-of-fit criteria*

A key part of an inversion problem is to provide a quantitative measurement of how well a model with a given set of parameters explains (i. e., fits) the data. Such a measurement is usually defined via a so-called misfit function (e. g. Mosegaard and Tarantola, 1995; Tarantola, 2005). The choice of the misfit function will mainly depend on properties of the data, including the probability distribution of uncertainties, the possibility of correlation between data points, and the presence of outliers.

In the majority of the geophysical problems, observations can be represented by a vector $\mathbf{d}^{obs}$ whose uncertainties follow a Gaussian distribution described by a covariance matrix C. In this case, the goodness-of-fit can be computed as:

$$S(\boldsymbol{\Theta}) = (\mathbf{d}^{obs} - \mathbf{d}^{pred}(\boldsymbol{\Theta}))^T \, C^{-1} \, (\mathbf{d}^{obs} - \mathbf{d}^{pred}(\boldsymbol{\Theta})), \tag{5.70}$$

where $\mathbf{d}^{pred}$ is the vector of model prediction for a given set of parameters $\boldsymbol{\Theta}$. If the data points are independent, the covariance matrix can be reduced to $C = \boldsymbol{\sigma}^2\mathbf{I}$, where $\boldsymbol{\sigma}^2$ is the vector of data uncertainties and $\mathbf{I}$ is the identity matrix. Then, eq. 5.70 reduces to

$$S(\boldsymbol{\Theta}) = \sum_{i=1}^{N} \frac{\left[d_i^{obs} - d_i^{pred}(\boldsymbol{\Theta})\right]^2}{\sigma_i^2} \equiv \chi^2 \tag{5.71}$$

where N represents the number of data points. Eq. 5.71 is commonly referred to as chi-square fitting.

Another simple and widely used function to assess the goodness-of-fit is the root mean square error (RMSE) which represents the standard deviation of the residuals between model predictions and observations and is mathematically defined as:

$$S(\boldsymbol{\Theta}) = \sqrt{\frac{1}{N}\sum_{i=1}^{N}\left[d_i^{obs} - d_i^{pred}(\boldsymbol{\Theta})\right]^2} \equiv \text{RMSE}. \tag{5.72}$$

Note that eqs. 5.71 and 5.72 are quite similar, with the main difference being that the chi-square weighs each data point with respect to its uncertainty while in the RMSE all points have the same contribution. Hence, the larger is the variation within data uncertainties, the larger is the difference between the misfits predicted by chi-square and RMSE.

5.3.2 *Exploring the parameter space*

Defining how the sets of model parameters to be tested by the goodness-of-fit criteria are drawn within the parameter space is another critical factor of the inversion procedure. The most simple solution is to systematically cover the parameter space with a grid search, which ensures that the entire space has been investigated. However, due to the large cost in computation time, this method can in practice only be used in problems with few free parameters. On the other hand, large-dimensional parameter spaces tend to be terribly empty, i. e., only a narrow region is able to well-explain the observations. Hence, scanning through the entire space is inefficient and commonly prohibitive for problems with a large number of dimensions, and other methods should be considered.

A popular class of sampling methods are the Monte Carlo methods, in which sample solutions are drawn randomly from a given probabilistic distribution. The most straight-forward approach would be to simply pick samples randomly from a uniform distribution, however, this would be as ineffective as the a grid search approach. Instead, the most popular Monte Carlo sampling methods are built in such way that the computational efforts focus on sampling relevant regions of the parameter space. This is usually done via probabilistic approaches, notably using Bayes's theorem, which compose the class of Bayesian inference techniques. A comparison between a grid search and a Bayesian inference sampling approach is shown in Figure 5.6. In this two-dimensional illustration, the two examples have the same number of samples. The Bayesian approach samples the high-probability region with much more detail.

In essence, when using Bayesian inference methods, one is interested in assessing the posterior probability $\mathcal{P}(\boldsymbol{\Theta}_m)$ of a vector of parameters $\boldsymbol{\Theta}$ associated with a model m given a set of observations $\mathbf{d}^{\text{obs}}$. The posterior can be computed using the Bayes rule, which, in the context of parameter inference, is commonly written as:

$$\mathcal{P}(\boldsymbol{\Theta}_m) = \frac{\mathcal{L}(\boldsymbol{\Theta}_m)\,\varpi(\boldsymbol{\Theta}_m)}{\mathcal{K}}, \tag{5.73}$$

where $\mathcal{L}(\boldsymbol{\Theta}_m)$ is the likelihood of the data given the model parameters, generally defined as

$$\mathcal{L}(\boldsymbol{\Theta}_m) = \exp\left[-\frac{1}{2}S(\boldsymbol{\Theta})\right]. \tag{5.74}$$

In addition, $\varpi(\boldsymbol{\Theta}_m)$ represents the prior probability assigned to the parameter set and contains the a priori information about the parameters. Finally, $\mathcal{K}$ is the evidence (also called marginal likelihood) and corresponds to the integral of the data likelihood over the entire parameter space $\Omega_{\boldsymbol{\Theta}}$ as follows:

$$\mathcal{K} = \int_{\Omega_{\boldsymbol{\Theta}}} \mathcal{L}(\boldsymbol{\Theta}_m)\varpi(\boldsymbol{\Theta})\,\mathrm{d}\boldsymbol{\Theta}. \tag{5.75}$$

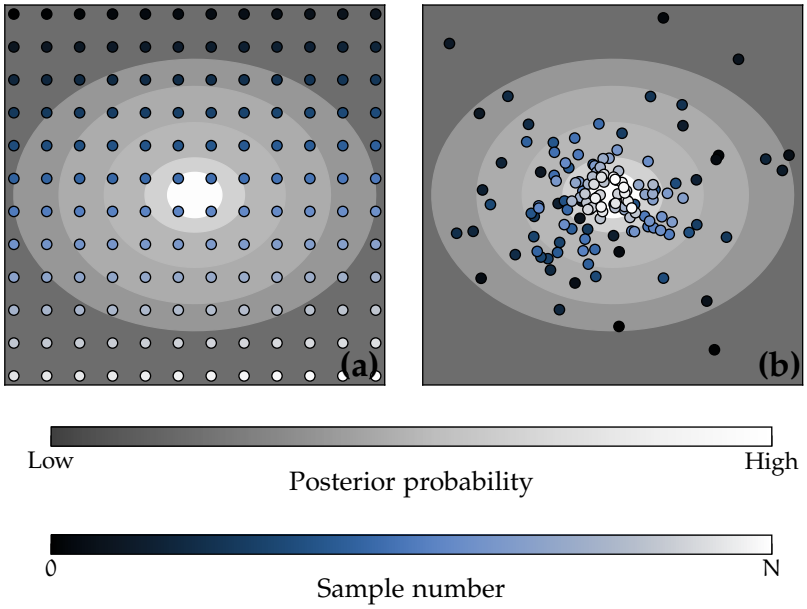

Figure 5.6: Schematic representation of different sampling approaches for a two-dimensional parameter space. (a) Simple grid search where the parameter space is systematically explored with fixed step sizes. (b) Bayesian approach where sampling is built in such way that prioritize regions of high probability. In particular, this panel illustrates the nested sampling method, where samples are randomly drawn from nested shells of increasing likelihood.

The evidence can also be thought of as a normalization constant since it normalizes the numerator part of eq. 5.73, making $\mathcal{P}$ a "proper" probability distribution that ingrates to unity. In practice, however, because this integral is difficult to compute, many techniques sample *proportionally to* the posterior distribution instead of sampling from the actual posterior distribution. This is, for example, the case of the Markov Chain Monte Carlo (MCMC), probably the most popular Bayesian inference method of the astronomy and geophysics communities (e. g. Foreman-Mackey et al., 2013).

In MCMC, the samples are drawn via a Monte Carlo (i. e., random) walk. In addition, because each step depends solely on the previous step (referred to as a memoryless sampler), it is also a Markov chain. One of the most well-known MCMC method is the Metropolis-Hastings algorithm, developed by Metropolis et al. (1953) and further improved by Hastings (1970). Detailed explanations on MCMC and the Metropolis-Hastings algorithm can be found in many reviews and text books, including Mackay (2003) and Tarantola (2005).

The basic idea of the Metropolis-Hastings method is that the acceptance of a proposed step in the random walk is evaluated based on a probabilistic rule. The proposed step taken from a position $\boldsymbol{\Theta}$ to position $\boldsymbol{\Theta}'$ is drawn from a candidate-generating distribution, named

transitional distribution q, which is commonly a multi-dimensional Gaussian centered at $\boldsymbol{\Theta}^{i}$. The acceptance of this new position is done by evaluating the ratio $\alpha = \frac{\mathcal{P}(\boldsymbol{\Theta}')q(\boldsymbol{\Theta}|\boldsymbol{\Theta}')}{\mathcal{P}(\boldsymbol{\Theta})q(\boldsymbol{\Theta}'|\boldsymbol{\Theta})}$. If $\alpha > 1$ the new position is accepted, otherwise, it randomly decides if the step is taken with a probability α. If the new position is not accepted, the walker remains at position $\boldsymbol{\Theta}$. The possibility of moving even if $\boldsymbol{\Theta}'$ has a lower probability is important because it helps avoiding the sampler to get trapped in local maxima. Over the decades, researchers worked on small modifications to the Metroplis-Hastings to improve the algorithm's performance (e.g., Goodman and Weare, 2010). Several of them have been made available via open source codes, such as the EMCEE Python package (Foreman-Mackey et al., 2013).

Although powerful and well-established, MCMC have some important shortcomings. MCMC is able to provide the posterior distribution associated with a given model and parameter space, however, it does not estimate the associated evidence $\mathcal{K}$. The evidence is a useful value as it allows for a quantitative comparison across models with different assumption and free parameters via the Bayes factor, which is the ratio between the evidences of two different models (e. g., Kass and Raftery, 1995). Another issue of MCMC is that the method has difficulties to estimate more complex posteriors, notably widely separate multimodal distributions, because the sampling procedure is characterized by subsequent steps being usually close together in the parameter space. In this context, other Bayesian inference methods have been developed with the goal of addressing these shortcomings, such as the nested sampling technique (Skilling, 2006) which is the Bayesian method adopted in this thesis. Here, I made use of the public and open-source Python package DYNESTY developed by Speagle (2020).

Instead of directly sampling from the posterior, nested sampling focuses on estimating the evidence. The evidence, however, is a complicated integral over the entire multidimensional parameter space, as defined by eq. 5.75. The idea behind nested sampling is to break down this complex problem into many simpler ones which is achieved by sampling from a uniform distribution within nested shells. These shells are defined by iso-likelihood bounds, where the bounding likelihood values must systematically increase, thus reducing the available sampling region in the parameter space over time. A schematic view of samples distribution drawn from nested sampling is shown in Figure 5.6. In addition, since the shells can easily be disjoint, the method deals very naturally with multimodal posterior distributions.

In practice, because of the difficulty of dealing with a multidimensional parameter space, the method makes use of a new variable, the prior mass X, which allows eq. 5.75 to be rewritten as a one-

dimensional integral. By defining the prior mass element as $dX = \varpi(\boldsymbol{\Theta})d\boldsymbol{\Theta}$, we have that

$$X(\beta) = \int_{\mathcal{L}(\boldsymbol{\Theta}) \geqslant \beta} \varpi(\boldsymbol{\Theta}) d(\boldsymbol{\Theta}) \tag{5.76}$$

which represents the prior fraction where the likelihood is above a given threshold β. In the case of a normalized prior, this function decreases from 1 (when $\beta = 0$) to 0 (when $\beta =$ *maximum likelihood*). Then, we can define the inverse function $\mathcal{L}(X)$, such that $\mathcal{L}(X(\beta)) = \beta$, that can be interpreted as the iso-likelihood contours determining the boundary of X, and write

$$\mathcal{K} = \int_0^1 \mathcal{L}(X) dX \tag{5.77}$$

which is the integration that is numerically performed by the nested sampling algorithm.

The basic algorithm consists in drawing N particles (usually in the order of hundreds) from the prior, called "live points". At each iteration, the likelihood of each point is computed and the sample $\boldsymbol{\Theta}_i$ with lowest likelihood becomes a "dead point", the new likelihood threshold becomes $\beta = \mathcal{L}_i$, and a new live point is drawn from within the shell where $\mathcal{L} > \beta$. In the case where the prior is a uniform distribution, statistical argumentation can be used to show that, on average, the constrained prior mass shrinks geometrically with step number and the prior mass associated with the most recently dead points reads (e.g., Skilling, 2006; Speagle, 2020)

$$\ln X_i \approx -\frac{i \pm \sqrt{i}}{N}. \tag{5.78}$$

Then, making use of a set of J dead points, the evidence can be numerically computed using

$$\mathcal{K} \approx \sum_i^J \mathcal{L}_i (X_{i-1} - X_i) \tag{5.79}$$

and the posterior probability can be directly estimated as

$$\mathcal{P}(\boldsymbol{\Theta}_i) = \frac{\mathcal{L}_i (X_{i-1} - X_i)}{\mathcal{K}}. \tag{5.80}$$

The algorithm iterates until the remaining evidence $\Delta\mathcal{K}$ to be estimated is less than a certain value, such as 1%. Even though $\Delta\mathcal{K}_i$ is virtually unknown one can consider the approximate upper bound $\Delta\mathcal{K}_i \approx \mathcal{L}_{max} X_i$, with $\mathcal{L}_{max}$ corresponding to the highest likelihood value among the live points. A last important point is that the model is constructed in a way where the prior must be always a normalized uniform distribution. This means that, in order to use a general distribution, it is necessary to apply a prior transform. In many cases, this transform is simple to derive, but increases in complexity if the different parameters are conditionally related.

Part III

NEW INSIGHTS INTO THE INTERIOR OF VENUS

6

THE LITHOSPHERE OF CRUSTAL PLATEAUS

This chapter presents the results of the first project of my PhD, which consisted in investigating the interior of some of the geologically complex and ancient highlands of Venus, the so-called crustal plateaus. This study focused on providing rigorous estimates of the crustal- and elastic lithosphere thickness and on testing the hypothesis of Airy isostasy support at these regions, assumed in many previous investigations. Most of what is presented here is reproduced from the peer-reviewed article "Lithospheric Structure of Venusian Crustal Plateaus" by Maia and Wieczorek (2022). Though I was the lead investigator in this work, I will use the first-person plural in the following chapter to highlight the contributions of my co-authors. The outline of the chapter is as follows. Section 6.1 introduces the different interpretations for the origin of the plateaus and presents a review of the previous gravity studies that investigated their interior structure. A summary of the analysis and inversion procedure along with a description of the results is presented in Section 6.2. In Section 6.3, we compare the results with previous studies and discuss the implications of my estimations regarding the compensation mechanism and the thermal evolution of plateaus. The conclusions are presented in Section 6.4.

6.1 INTRODUCTION

Crustal plateaus, also called plateau highlands, are prominent geologic features on Venus, with roughly circular planforms and diameters ranging from 1500 to 2500 km. They present a steep-sided topography reaching 2 to 4 km of altitude above the surrounding plains, with the highest elevations generally closer to the margins. The surface of the plateaus is dominated by tessera terrains, that are characterized by complex tectonic fabrics which indicate multiple stages of deformation recording both extensional and contractional events (e.g., Bindschadler et al., 1992a; Hansen and Willis, 1996). These terrains, which can also be found as low-lying patches within the plains called inliers, cover roughly 8% of the surface of Venus and are stratigraphically the oldest surfaces on the planet (Ivanov and Head, 1996). Given their relative older age, crustal plateaus have recorded a significant fraction of Venus' geologic history. Thus, investigating their structure and formation mechanism is crucial to decipher the early tectonic and geodynamic processes of the planet.

The origin of crustal plateaus is still a matter of debate. It is well established that the high topography observed is associated with thickening of the crust, however, which processes caused this thickening are not quite understood. The high-resolution full-coverage radar imagery from the Magellan mission resulted in the first detailed geological maps of these regions. Different interpretations of their tectonic evolution developed into the "hotspot-coldspot controversy" (Phillips and Hansen, 1994), a debate that carried throughout the 1990s. A first class of models considered upwelling and assumed that the crust was initially uplifted by a mantle plume and thickened by magmatic accretion due to plume-related partial melting, followed by cooling and subsidence (e.g., Phillips and Hansen, 1998; Ghent and Hansen, 1999; Hansen et al., 2000). The opposing scenario proposed that crustal plateaus are regions of downwelling related to coldspots in the mantle (e.g., Bindschadler and Head, 1991; Bindschadler et al., 1992b; Gilmore and Head, 2000). In this case, the crustal thickening is caused by horizontal shortening related to compressional stresses. However, Kidder and Phillips (1996) have shown that the formation of plateaus through subsolidus crustal thickening over downwellings would require an excessively long time scale (from 1 to 4 billion years). On the other hand, the upwelling model has difficulties to accommodate the pervasive contractional tectonics observed at these regions.

An alternative interpretation related to large asteroid impacts was later proposed by Hansen (2006) for the origin of the crustal plateaus. In this scenario, the collisions of large bolides onto the surface of Venus are able to partially melt the crust and upper mantle, generating huge lava ponds. The high relief in this model is supported by a depleted upper mantle residuum which is more buoyant and stronger than adjacent undepleted mantle. This model, however, has difficulties to explain the significant amount of shortening near the plateau margins (Romeo and Turcotte, 2008). Later, Romeo and Turcotte (2008) and Romeo and Capote (2011) suggested an alternative scenario where the crustal plateaus formed under similar conditions as the continental crust on Earth. According to this hypothesis, plateaus and tessera inliers represent buoyant areas of felsic composition with respect to the surroundings, which survived a putative global lithospheric foundering event around 500 Ma ago (e.g., Turcotte, 1993; Turcotte et al., 1999; Weller and Kiefer, 2020). The intense tectonic activity related to this event would contribute to building up the plateaus by compression. Consistent with this hypothesis, thermal emissivity data indicate that crustal plateaus could be associated with a more felsic composition, analogous to the composition of continental crust (Hashimoto et al., 2008; Gilmore et al., 2015).

The earliests investigations using gravity data on Venus showed that crustal plateaus are associated with small positive gravity anomalies and low gravity to topography ratios. The volcanic rises, such as

Atla and Beta regiones, in contrast are associated with high gravity anomalies and high gravity-topography ratios (Smrekar and Phillips, 1991; Bindschadler et al., 1992b; Grimm, 1994; Kuncinskas and Turcotte, 1994; Moore and Schubert, 1997; Simons et al., 1994; Simons et al., 1997). These studies led to the widely accepted interpretation that the topography of the crustal plateaus is isostatically compensated by thick crustal roots. Consequently, most investigations of gravity and topography in the Magellan era considered an Airy isostasy regime in order to estimate the crustal thickness of the plateaus. For this purpose, Smrekar and Phillips (1991), Kuncinskas and Turcotte (1994), and Moore and Schubert (1997) adopted spatial analysis techniques (geoid-to-topography ratios). Meanwhile, Grimm (1994) and Simons et al. (1994) and Simons et al. (1997) investigated localized spectral admittances, which are wavelength-dependent gravity-topography ratios, making use of early developed spatio-spectral localization techniques. It is important to emphasize that none of these works made use of the most recent gravity model from Konopliv et al. (1999) which is the highest-resolution model publicly available today (see Sjogren et al., 1997, for a review). Moreover, many of these studies did not try to quantify the flexural strength of the lithosphere, and instead simply assumed an isostatic regime, where the lithosphere has zero strength. Simons et al. (1997) performed preliminary tests on the elastic support of the topography of Venusian features making use of a top-loading flexural model and concluded that the crustal plateaus are generally consistent with elastic thicknesses lower than 20 km.

The few recent gravity studies on Venus have mostly focused on constructing global crustal thickness and elastic thickness maps. Anderson and Smrekar (2006) systematically computed localized spectral admittances across the planet using the wavelet technique introduced by Simons et al. (1997) and divided them into spectral classes. Crustal thickness and elastic thicknesses were estimated for each spectral class considering top, bottom and "hot-spot" loading models. James et al. (2013) investigated the crustal thickness of Venus using spatial domain geoid-to-topography ratios and created a global model considering crustal thickness variations and dynamic compensation at depth arising from the mantle. Global maps of elastic thickness variations for the Moon, Mars, and Venus were presented by Audet (2014) using a spherical wavelet analysis and a flexural loading model of the lithosphere. A crustal thickness map based on the modeling technique introduced by Wieczorek and Phillips (1998) was constructed by Jimenez-Diaz et al. (2015). These authors then used wavelet transforms to perform localized spectral analyses in order to provide elastic thickness estimations considering a lithospheric model with surface and subsurface loads and using the crustal thickness values previously estimated. In addition, several gravity studies have focused on coronae, which are circular volcano-tectonic structures

uniquely present on Venus, adopting top and bottom loading flexural models to investigate their crustal and elastic thicknesses (Smrekar et al., 2003; Hoogenboom et al., 2004; Hoogenboom et al., 2005).

Since the time of the pioneering studies of the Magellan era, several advances have been made in the techniques that are used to analyze the gravity signal arising from the lithosphere. These include improved spatio-spectral localization techniques, notably the spherical multitaper spectral estimation developed by Wieczorek and Simons (2005) and Wieczorek and Simons (2007), Simons et al. (2006), and Simons and Dahlen (2006b) that is adopted in our study. A detailed analysis comparing several methods of spectral localization can be found in Dahlen and Simons (2008). Moreover, theoretical loading models of the lithosphere that consider both surface and subsurface loads have been developed (McGovern et al., 2002; Belleguic et al., 2005; Grott and Wieczorek, 2012; Broquet and Wieczorek, 2019). Lastly, there are improved gravity and topography models (Konopliv et al., 1999; Rappaport et al., 1999; Wieczorek, 2015a) that were not available for many of the earliests studies. For these reasons, in this study, we reassess the compensation state of the highland plateaus, and attempt to place constraints on their average crustal thickness and elastic thickness. We make use of a flexural loading model and a localized spectral admittance modeling technique employed in many recent studies of Mars (Belleguic et al., 2005; Wieczorek, 2008; Grott and Wieczorek, 2012; Beuthe et al., 2012; Broquet and Wieczorek, 2019) and presented in Chapter 5 of this thesis. We investigate six Venusian crustal plateaus, namely Thetis, Ovda, Western Ovda, Alpha, Tellus and Phoebe regiones, which are indicated in Figure 4.2. We note that although Phoebe Regio was sometimes described as a crustal plateau (e.g., Phillips and Hansen, 1994; Nunes et al., 2004) it has also been defined as a transition between plateaus and volcanic rises (e.g., Phillips and Hansen, 1998; Kiefer and Peterson, 2003) since it presents some geophysical and structural features consistent with both types of features.

6.2 CONSTRAINING THE INTERIOR STRUCTURE OF THE PLATEAUS

In the first part of this section, the modeling and inversion procedures are described in detail for Alpha Regio. Following this, we summarize the inversion results for the other five investigated crustal plateaus: Ovda, Western Ovda, Thetis, Tellus and Phoebe regiones. We note that the only major tessera region that has not been included in our analysis is Fortuna Tessera, located in the eastern part of Ishtar Terra. The observed localized correlation in this region is low, mostly lower than the adopted threshold of 0.71 and always lower than 0.75. It is not obvious if this attribute is due to uncorrelated gravity signals

coming from the deep crust and mantle or poor data quality in the region.

6.2.1 *Case Study: Alpha Regio*

Alpha Regio is a ~1300 km wide radar-bright crustal plateau located at latitude 25°S and longitude 2°E. This isolated plateau is characterized by tessera terrain and steep-sized topography, standing on average 1 km above the surrounding volcanic plains. Immediately south of Alpha is located the 330 km diameter Eve Corona that marks the 0° meridian of Venus. Detailed geologic descriptions of Alpha Regio can be found in Bindschadler et al. (1992a) and Bender et al. (2000). Figure 6.1 shows the topography and radial gravity at this region where we can see positive gravity anomalies related to the high topography of the plateau. Though some of the gravity anomalies are clearly correlated with the high-standing topography, we note that there exist gravity anomalies of similar amplitude exterior to this plateau that are not strongly correlated with geologic features.

The first step in our analysis is to compute the localized observed spectral admittance and correlation, which is done by applying the windowing function as described in Section 3.3. We chose the window size to encompass the entire feature while avoiding gravitational and topographic signals exterior to the plateau. We used a window with angular radius of $\theta_0 = 16°$, corresponding to a diameter of 3380 km, which results in a spectral bandwidth of $\ell_{\text{win}} = 16$ given that a 99% concentration factor is adopted.

The windowing procedure is applied to both the data and the geophysical model that will be used to predict the observations. We adopt the surface and subsurface loading model presented in Broquet and Wieczorek (2019) and described in Section 5.1. The model can be schematically defined as

$$Q_\ell = Q_\ell(\ell, T_e, T_c, \rho_l, \rho_c, \rho_m, L, z_\psi, R_{\text{loc}}, E, \nu). \tag{6.1}$$

where Q_ℓ represents the linear transfer function between gravity and topography. The investigation will consider three free parameters: the elastic thickness T_e, the crustal thickness T_c and the load ratio between surface and subsurface loads L. When performing a localized analysis, one should use the local radius R_{loc} instead of the mean planetary radius and the observed gravity field must be downward continued to R_{loc} before computing the localized admittance and correlation. At Alpha, the average radius corresponds to 6051.86 km, which is very close to the planetary average of 6051.88 km. Although it would be useful to estimate the crustal density of the highland plateaus, the low resolution of the available gravity field data prevents the reliable determination of this parameter. Hence, we chose to use $\rho_c = 2800$ kg m^{-3}, which is representative of oceanic basalts (e. g., Hyndman

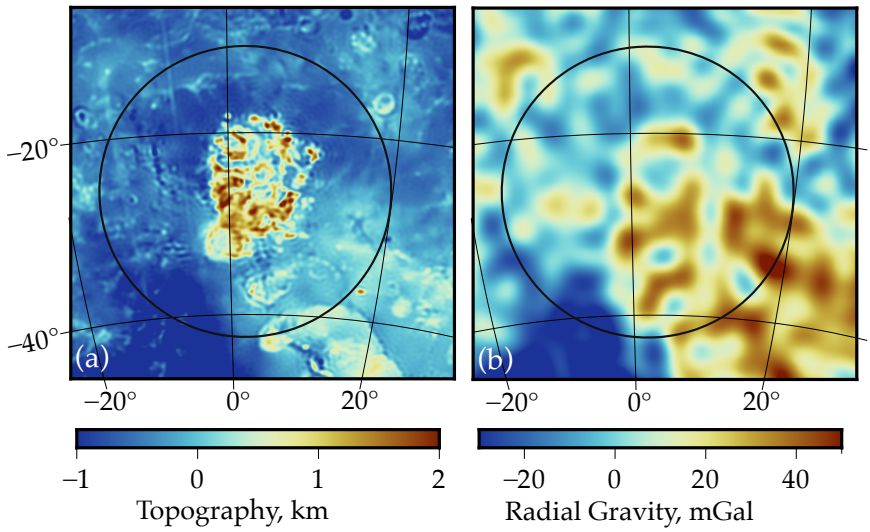

Figure 6.1: (a) Topography from VenusTopo719 and (b) radial free-air gravity anomaly from MGNP180U after truncating spherical harmonic degrees above 100 at Alpha Regio. The circles correspond to the limits of the adopted localization window, with $\theta_0 = 16°$ corresponding to a diameter of 3,380 km. The adopted projection for both maps is Lambert azimuthal equal-area. Figure from Maia and Wieczorek (2022).

and Drury, 1976). All remaining parameters are fixed in order to limit the parameter space. The adopted values are shown in Table 6.1. As discussed in Section 5.1, the choice of these values is overall based on what is known for terrestrial rocks.

We proceed by defining the range of spherical harmonic degrees that will be used to perform the model fitting. The upper limit is determined by the resolution of the data at Alpha (ℓ_{data}), which we take to be the degree strength from the map of Konopliv et al. (1999). For Alpha, the degree strength is 75. Since each degree has contributions from $\pm\ell_{\text{win}}$ we avoid the inclusion of noise-dominated data in our analysis by removing all degrees above $\ell_{\text{data}} - \ell_{\text{win}}$, resulting in a upper limit of degree 59 for the region. We also ignored all degrees in the localized spectra that were less than ℓ_{win} because these are dominated by signals with wavelengths that are greater than the window size and because these degrees typically have extremely high variances (Wieczorek and Simons, 2007). Though we never analyze data outside of this degree range, we sometimes avoid degrees where the correlation is smaller than 0.71, corresponding to a signal-to-noise ratio less than 1 (see Section 5.1.2).

The localized admittance, correlation, and the investigated degree range for Alpha Regio are shown in Figure 6.2. The correlation is high between degrees 40 to 59 with implied signal-to-noise ratios greater than 1, which was the range we initially chose to perform the inversion. The drop in correlation that starts at degrees above 60 is likely

Table 6.1: Parameter values consider in our inversions.

Parameter	Value
Elastic thickness T_e	0 to 75 km
Crustal thickness T_c	1 to 100 km
Load ratio L	-0.8 to 0.8
Mantle density ρ_m	3300 kg m^{-3}
Crustal density ρ_c	2800 kg m^{-3}
Load density ρ_l	2800 kg m^{-3}
Load depth z_ψ	150 ($L < 0$) or 15 ($L > 0$) km
Young's modulus E	100 GPa
Poisson's ratio ν	0.25

due to the strong influence of noise in the data while the mild drop around degree 30 is probably caused by true geologic signals that are not correlated with the topography. Regardless, we noticed that the degree range between 23–40 provided a very good fit to our best-fitting theoretical model. Thus, in order to increase the degrees of freedom and robustness of the inversion, we included these data points in the investigation resulting in an expanded degree range from 23 to 59, as shown in Figure 6.2. Moreover, although the degrees 17–20 have a high correlation and could in principle be used in the modelling, we found that these degrees never satisfactorily fit our best-fitting theoretical model. In all likelihood, the high admittances for $\ell < 20$ are the result of processes occurring deep in the mantle (e.g., Pauer et al., 2006).

In order to determine the best-fitting model parameters and uncertainties, we make use of an exhaustive grid-search of the parameter space. We systematically varied crustal thickness, elastic thickness and load ratio to generate modeled admittances and compared them to the observed admittance over the selected degree range. The model misfit is defined as the root mean square error:

$$\mathrm{RMSE}(T_c, T_e, L) = \sqrt{\frac{1}{N} \sum_{\ell=\ell_{min}}^{\ell_{max}} \left[Z_{obs}(\ell) - Z_{pred}(\ell, T_c, T_e, L) \right]^2} \quad (6.2)$$

where Z_{obs} is the localized observed admittance, Z_{pred} is the localized admittance predicted by the model, and N is the number of degrees adopted in the summation. The best fitting curve for Alpha is shown in Figure 6.2. Once the entire misfit function is computed, we are able to determine the accepted range of investigated parameters by the use of a maximum allowable misfit threshold. Here, we use a 1-

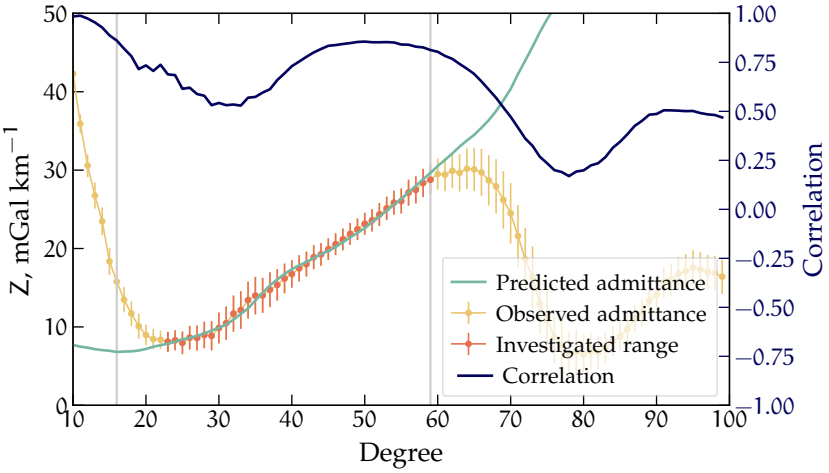

Figure 6.2: Observed localized spectral admittance (left axis) and correlation (right axis) at Alpha Regio. The points in red represent the spherical harmonic degrees used in our inversion. Gray lines show the theoretical investigation limits ℓ_{win} and $\ell_{data}-\ell_{win}$. The green curve shows the best-fitting admittance, which corresponds to $T_c = 15$ km, $T_e = 20$ km and $L = 0$. Figure from Maia and Wieczorek (2022).

standard-deviation criterion based on the average uncertainty of the observed localized admittance

$$\bar{\sigma}_{loc} = \sqrt{\frac{1}{N}\sum_{\ell=\ell_{min}}^{\ell_{max}} \sigma_{loc}^2(\ell)} \tag{6.3}$$

with $\sigma_{loc}^2(\ell)$ representing the localized version of σ^2, defined by eq. 5.9 . This criterion has been commonly used in Martian studies (Wieczorek, 2008; Grott and Wieczorek, 2012; Broquet and Wieczorek, 2019). In previous gravity studies on Venus, other workers have chosen more flexible, but arbitrary, criteria, such as 1.5 times the minimum RMSE (e.g., Smrekar et al., 2003; Hoogenboom et al., 2004). Other approaches for defining a maximum allowable misfit are discussed in Broquet and Wieczorek (2019).

In Figure 6.3, we plot various representations of the misfit functions for Alpha Regio. The three upper plots display 1-dimensional minimum misfit curves for the crustal thickness, elastic thickness, and load ratio. Looking at the dark blue curve (which is for our full inversion that includes both surface and subsurface loads), in the left plot we find that the crustal thickness is only constrained to be less than 21,km. In the center plot, we find that the elastic thickness is constrained to lie between 9 and 24 km. In the right plot, the load ratio misfits shows that this parameter is essentially constrained to the presence of surface loads only ($L = 0$) or small positive loads, indicating a potential small dense crustal intrusion, where $L = 0$ is associated with the best-fitting value.

Given that the load ratio is consistent with being zero, we decided to test two simpler scenarios: one having only surface loads (T_c and T_e as free parameters) and a second that is in an Airy isostasy regime (T_c being the only free parameter). The misfit curves for the first scenario ($L = 0$) is overplotted in the upper two figures in light blue. We find that, when subsurface loads are neglected, it does not affect the upper limit for the crustal thickness, and that we are able to obtain a firm lower bound on the crust thickness of 9 km. Similarly, for the elastic thickness, we find that this does not affect our upper bound of 24 km, but that it slightly reduces the range of the lower bound to 12 km. The case where we assume Airy isostasy is plotted in cyan in the upper left plot. Here, we find that the best fitting model has a misfit that is greater than our cutoff value. This implies that the assumption of Airy isostasy is not appropriate for this region, and that, if this was assumed, the crustal thickness would be biased towards larger values.

In the three bottom plots, we show the minimum misfit as a function of two variables, which allows us to evaluate correlations and trade-offs between parameters. The misfit plot considering crustal and elastic thicknesses (left panel) is the most complex, presenting several local minima and degeneracies. However, there is the expected trend of decreasing elastic thickness with increasing crustal thickness which is related to the attenuation of the compensating signal from the crustal roots. In the middle panel, we can see that there is a trade-off between elastic thickness and the load ratio, where the addition of positive loads decreases the elastic thickness. Regarding the relation between crustal thickness and load ratio (right panel), the addition of positive loads allows for moderately lower crustal thickness. In this situation, the addition of slightly denser material within the crust essentially counterbalances the reduction of crustal material associated to a thinner crust. On the other hand, the addition of small buoyant loads in the mantle leads to crustal thickness values lower than 10 km.

In summary, when subsurface loads are allowed, our best fitting values as well as lower and upper 1-sigma limits of the inversion parameters are the following: $L = 0 (-0.02, 0.14)$, $T_e = 20 (9, 24)$ km and $T_c = 15 (1, 21)$ km. The setting with surface loads only results in $T_e = 20 (12, 24)$ km and $T_c = 15 (9, 21)$ km. Overall, these two models result in very similar parameter estimation. The most remarkable difference is that, when subsurface loads are not considered, lower and upper bounds are obtained for the crustal thickness, whereas when subsurface loads are considered, only an upper bound is possible. Finally, for the Airy isostasy regime, there are no crustal thickness values that result in acceptable fits for Alpha Regio, the lowest RMSE value is given by $T_c = 24$ km, which is higher than the values that consider elastic support. We should remark that we do not

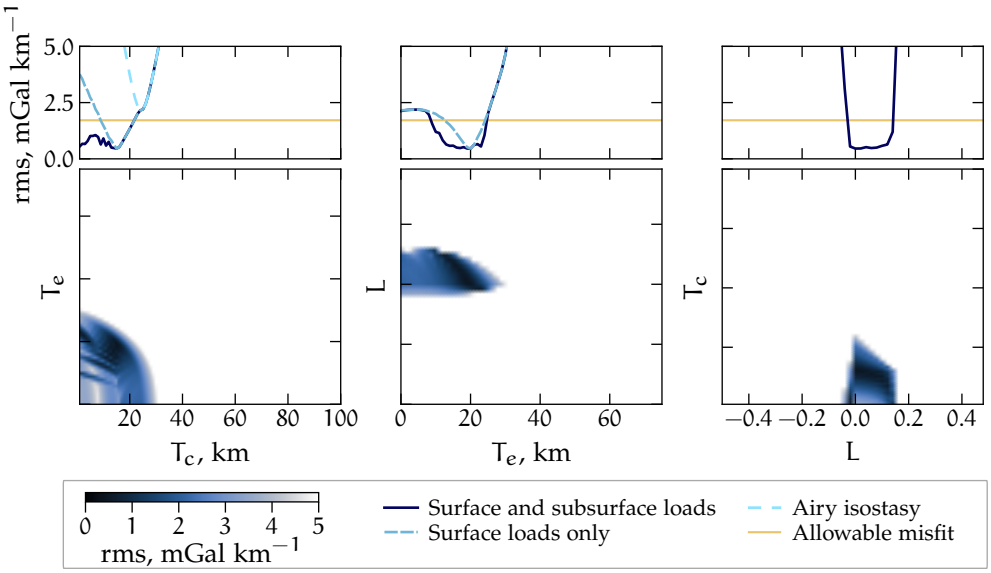

Figure 6.3: One-dimensional (upper) and two dimensional (lower) misfits between model and observation at Alpha Regio as a function of the crustal thickness, elastic thickness, and load ratio. The 1-dimensional misfit plots show the minimum misfits for three different loading scenarios, where the dark blue curves represent the case where surface and subsurface loads are allowed (3 free parameters), the lighter blue curves shows the case where only surface loads are present (i.e., $L = 0$), and the cyan curve in the upper left plot indicates an Airy isostasy regime scenario ($T_e = 0$). The 2-dimensional plots in the bottom row display the minimum misfits in terms of two free parameters for our full model with subsurface loads. All two-dimensional plots share the same color scale and the one-dimensional plots share the same x axis as the underlying two-dimensional plot. Figure from Maia and Wieczorek (2022).

investigate the possibility of topographic support by Pratt isostasy, i.e. by lateral variations of crustal density between the plateaus and the volcanic plains. In fact, our analysis approach is not well-suited to investigate this compensation regime, since the use of localization windows suppresses most of the signal coming from the plains. In any case, it is unlikely that the entirety of the plateaus are purely Pratt compensated since this would imply portions to have have extremely low densities. For example, given that the plateaus can reach up to 4 km altitude, assuming that the crustal thickness at the mean planetary radius is of 20 km and that the volcanic plains have a density of 2800 kg m^{-3}, the highest elevations of the plateaus would have a density of 2300 kg m^{-3}, which is considerably lower than the density of quartz. Moreover, previous studies that compared the two isostatic support mechanisms at crustal plateaus tended to favor Airy over Pratt isostasy (Kuncinskas and Turcotte, 1994).

In order to limit the parameter space of our inversions, several model parameters were fixed to constant values, as indicated on Table 6.1. One of these parameters is the crustal density, here assumed to be

2800 kg m^{-3} which is consistent with basaltic rocks on Earth. However, new studies of the emissivity signature of Alpha Regio suggest that the composition of this plateau could be more felsic than the surrounding plains (Gilmore et al., 2015). Therefore, we also performed inversions considering a crustal density of 2650 kg m^{-3}, which is a standard value for the density of terrestrial granites. The main effect of this modification was an overall increase of 2 km in the estimated crustal thickness values for all investigated regions. Moreover, changing the depths of the internal loads also has a minor effect on the inversion results. For example, increasing the load depths to 30 and 300 km for the positive and negative loads, respectively, had overall no impact on the elastic thickness estimations and increased the upper limit of accepted crustal thickness values by a few kilometers.

Sensitivity analyses were also performed regarding the size of the localization window and the admittance spectral range used for the inversions, since the choice of these parameters is somewhat subjective. We did inversions considering a window that was 30% larger and also changed the investigated degree range to 40–59, which corresponds to the degrees with the highest spectral correlations (Figure 6.2). The change in the degree range had only a small impact on the values of the estimated parameters. The best-fitting values and uncertainties obtained varied within a range of 15% with respect to the results presented above. Increasing the size of the localization window had a somewhat larger effect, in which the best fitting crustal thickness estimations for the top-loading model changed from 15 km to 21 km, corresponding to a 40% increase. This shift is probably caused by the large gravity signal of the surroundings of Alpha that are unrelated to the plateau itself. These sensitivity tests were performed in all studied plateaus and, as for Alpha Regio, most results varied within a range of 15% relative to the results presented in the text. In all tests we found that the results were consistent with those presented in the text within their respective uncertainties.

6.2.2 *Crustal Plateaus*

Following the same procedures as presented for Alpha Regio, we estimated the crustal thickness, elastic thickness, and load ratio values for the other five crustal plateaus of our study: Ovda, Western Ovda, Thetis, Tellus and Phoebe regiones. Information on the degree range and localization window parameters used for each region is provided in Table 6.2. In Figure 6.4, we present the topography and gravity maps for each of the five plateaus, where the circles represent the sizes of the localization windows we used. In the right column of the figure, we show the localized spectral admittance and correlation, and the best fitting theoretical model of the admittance for each region, similar as shown previously in Figure 6.2 for Alpha Regio. Because

of the geological complexity of the crustal plateaus, their admittance and correlation spectra are also complex. The correlation is generally not uniform across the entire degree range, and the best fitting model does not adequately fit the observations over the entire investigation range $\ell_{\text{win}} < \ell < \ell_{\text{data}} - \ell_{\text{win}}$ represented by the vertical lines on the plots.

Table 6.2: Position, localization window parameters (angular radius θ_0, diameter D, and spectral bandwidth ℓ_{win}), and spherical harmonic degree range used in the inversion for the six investigated regions.

Region	Coordinates		Window parameters			Degree range
	lat(°)	lon(°)	θ_0 (°)	D (km)	ℓ_{win}	
Ovda	−4.0	90.0	22	4647	11	30–39 & 60–73
Thetis	−5.0	125.0	14	2957	18	23–45
W. Ovda	−4.0	65.0	20	4225	12	33–40 & 65–71
Alpha	−26.5	2.0	16	3380	16	23–59
Tellus	38.0	81.0	17	3591	15	35–49
Phoebe	−10.0	281.0	16	3380	16	17–51

A common aspect to all five regions is a substantial drop in the localized admittance and correlation spectra around degrees 50, in the case of Ovda and Western Ovda, or 60 for Tellus, Thetis and Phoebe regiones, corresponding to wavelengths of 760 km and 630 km respectively. We systematically disregard those degrees in our analysis where the correlations fall below 0.71, which corresponds to signal-to-noise ratios less than unity. The cause of these reductions in correlation, which are also accompanied by a drop in the admittance, is not immediately obvious. One possibility is that these are a result of deficiencies in the gravity model that originate from noise and uneven radio tracking coverage. Alternatively, it is possible that these drops in correlation could be real geophysical signals that are plausibly related to processes in the upper mantle, or to processes related to crustal delamination. Lithospheric delamination related to compressive tectonics and crustal thickening was proposed by Romeo and Turcotte (2008) to explain the formation of crustal plateaus and is also predicted by numerical models of coronae formation (Gülcher et al., 2020). In addition to the degree range with low correlations near 50–60, we note that our model also can not account for the observed admittances for degrees less than about 30 for Western Ovda, Ovda and Tellus regiones. In contrast to the degrees near 50–60, these lower degrees are associated with relatively high correlations, and correspond to wavelengths greater than 1300 km, which are comparable to the size of the plateaus. We suspect that this long wavelength signal is related to processes in the upper mantle that are not adequately

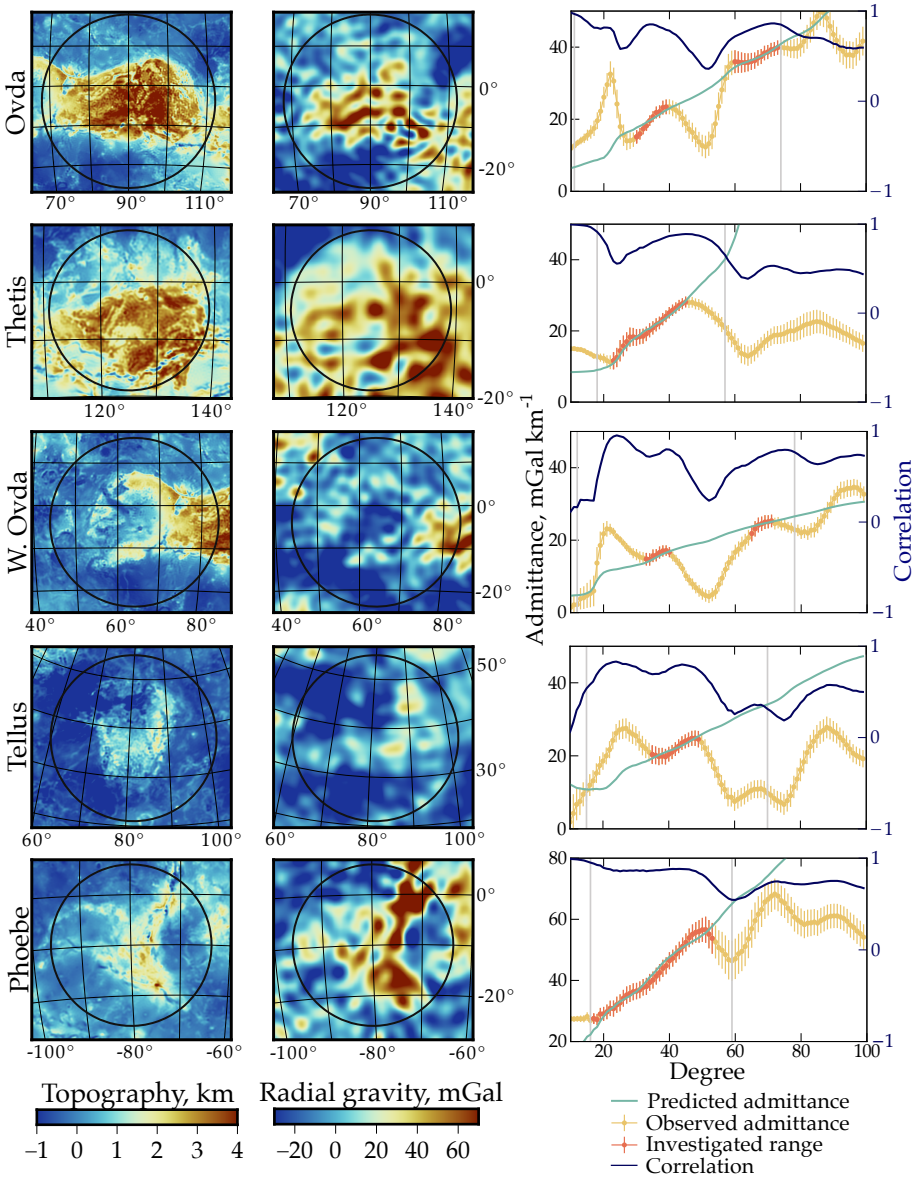

Figure 6.4: Topography (left) and free-air gravity maps (center) of the 5 investigated crustal plateaus with circles representing the localization window sizes. The adopted projection for these maps is Lambert azimuthal equal-area. (Right) observed admittance, correlation and best-fitting modeled admittance spectra. Gray lines show the maximum possible investigation limits of ℓ_{win} and $\ell_{data}-\ell_{win}$.

accounted for by our loading model that uses a single loading ratio for all spherical harmonic degrees. Since our model was unable to properly fit these components they were removed from the analysis.

In the following paragraphs, we present the crustal thickness, elastic thickness, and load ratio estimations for the five regions. Similar to our analysis of Alpha Regio, these results consider three loading scenarios: both surface and subsurface loads, surface loads only, and

a purely Airy isostasy regime. The misfit curves for each plateau are presented in Figure 6.5 and the estimated parameters are summarized in Table 6.3.

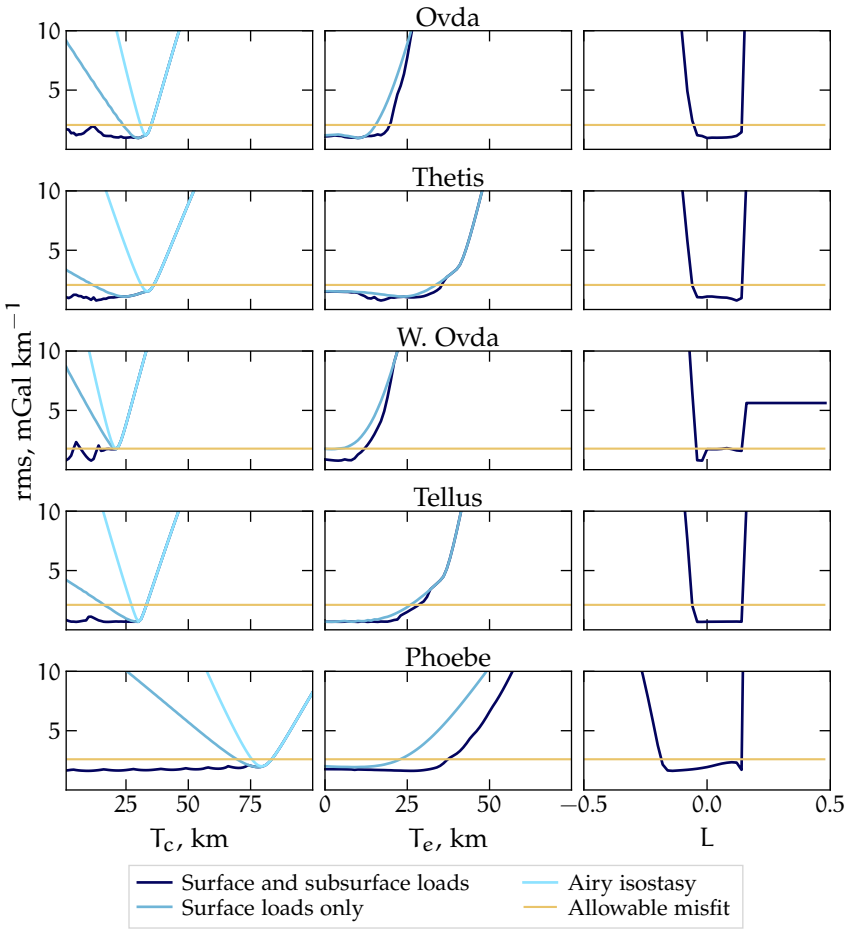

Figure 6.5: One-dimensional misfit plots for the crustal thickness (left), elastic thickness (center), and load ratio (right) for (from top to bottom) Ovda, Thetis, W. Ovda, Tellus, and Phoebe. Dark blue curves correspond to the case where both surface and subsurface loads are considered, light blue curves correspond to the scenario where only surface loads are included and the cyan curves correspond to the case of Airy isostasy. Figure from Maia and Wieczorek (2022).

THETIS AND OVDA REGIONES. Thetis, Ovda and, Western Ovda are adjacent to each other and comprise the western part of Aphrodite Terra. Thetis and Ovda are the two highest crustal plateaus, with the latter reaching over 4 km altitude with respect to the surrounding plains. For these two regions, the simple Airy isostasy model yields a satisfactory fit to the data, resulting in crustal thickness estimations of $34(32, 36)$ km and $33(31, 35)$ km, respectively (values in parentheses here represent the +-1-sigma limits). If we consider elastic support

of surface loads only, the 1-sigma upper limit of the crustal thickness does not change, but the lower limit decreases, allowing a larger range of values than the simple Airy case. For this case, the crustal thickness of Ovda is $T_c = 30(24, 35)$ km and $T_c = 24(12, 36)$ km at Thetis. Similar to what was found for Alpha Regio, when subsurface loads are included, it is only possible to obtain an upper bound for the crustal thickness. (In fact, this is the case for all analyzed regions.) For this scenario, the crustal thickness of Ovda is constrained to be less than 35 km with a best-fit of $T_c = 30$ km while for Thetis the crustal thickness is constrained to be less than 36 km with a best-fit of $T_c = 13$ km.

Regarding the elastic thickness, the scenarios of surface loads only and both surface and subsurface loads provide similar results. These two loading scenarios only allow for an upper bound of this parameter. In the case of Thetis, we find that $T_e < 33$ km for the surface loading model and $T_e < 35$ km when subsurface loads are allowed, whereas for Ovda, the upper limits are considerably smaller. In this region, the top-loading scenario results in $T_e < 15$ km and the inclusion of subsurface loads results in $T_e < 19$ km. The range of accepted load ratio values is similar for both regions, where $L = 0.00(-0.04, 0.14)$ for Ovda and $L = 0.12(-0.06, 0.14)$ for Thetis. Although the best-fitting load ratio is somewhat different for the two regions, in Figure 6.5, we can see that the range of acceptable values is similar.

WESTERN OVDA REGIO. Of the five regions discussed in this section, Western Ovda is the region that presented the most difficulties to fit the Airy isostasy and surface-loading only models. In Figure 6.5, we see that in these two cases the minimum misfit values are close to the threshold limit with both resulting in a crustal thickness of $T_c = 21$ km. When subsurface loads are allowed, we can only define an upper limit for the crustal thicknesses of 21 km. As for the elastic thickness, with the top-loading model we obtain $T_e < 4$ km, and the addition of subsurface loads increases the upper limit to 12 km. In terms of the load ratio, we estimated $L = -0.02(-0.04, 0.14)$ where we see that small amounts of buoyant material in the mantle ($-0.04 < L < -0.02$) are clearly associated with the best fitting models, which is unusual among the plateaus in this study. Nevertheless, dense crustal intrusions with loading ratios greater than zero are also possible over a limited range.

It has been suggested that Western Ovda Regio is in fact not a typical crustal plateau, and that it instead represents a transition between the plateaus and tessera inliers (e.g. Nunes et al., 2004). Its topography is characterized by a ~2 km high semicircular rim with a low relief interior that is largely embayed by volcanic plains. In particular, a 200 km diameter corona is located in the volcanic plains of its interior. In addition, W. Ovda has the lowest gravity signal among all crustal

plateaus, and even has a negative anomaly in the center. The fact that our model is parameterized in terms of the topography and W. Ovda is fully collapsed at the center could explain why our surface-loading model does not work well in this region. This is exacerbated by the fact that the localization window we use has higher amplitudes in the center, where the low elevations are located. We note that in our analysis of Ovda and W. Ovda regiones we made use of two separated degree ranges to perform the inversion. We chose to invert for both ranges simultaneously since in the case where the two ranges were investigated separately we obtained consistent results but with uncertainties that were up to two times larger.

TELLUS REGIO. Tellus Regio is an isolated crustal plateau located in the north hemisphere of Venus. The inversion results at Tellus are very similar to the estimations for Ovda and Thetis. When assuming Airy isostasy we obtain crustal thickness estimations of $T_c = 30(28, 33)$ km. When including only surface loads the 1-sigma upper limit remains unchanged but the lower limit decreases from 28 km to 17 km. Finally, in the case where subsurface loads are allowed, we were only able to obtain an upper bound on the crustal thickness of 33 km. The elastic thickness is constrained to be less than 25 km when only surface loads are considered, and less than 28 km when both surface and subsurface loads are considered. Similar to the previous analyses, load ratios ranging from -0.06 to 0.14 are accepted.

PHOEBE REGIO. Phoebe Regio presents the most distinct results in comparison to the other studied plateaus. Although the region has been previously defined as a crustal plateau (e.g. Phillips and Hansen, 1994; Nunes et al., 2004) it presents some important differences, and has been characterized as a hybrid between plateaus and volcanic rises (e.g. Phillips and Hansen, 1998; Kiefer and Peterson, 2003). In terms of tectonic features, Phoebe presents a unique structural fabric in which ribbon terrains, typical in other plateaus, are not present (Phillips and Hansen, 1998). In addition, Phoebe is connected to the volcanic rise Beta Regio by an extensive rift system called Devana Chasma. Previous geophysical studies (e.g., Simons et al., 1997; Kiefer and Peterson, 2003) have also shown that the gravity signal at Phoebe is somewhat in-between volcanic rises and crustal plateaus, probably being partially supported by a mantle plume. Of the regions in this analysis, Phoebe contains the highest values of the admittance, with values increasing from 30 mGal km^{-1} at low degrees to 60 mGal km^{-1} at high degrees. The highest admittances are about two times larger than those of the other plateaus in our study.

The three investigated scenarios provide acceptable fits for Phoebe Regio. When Airy isostasy is considered the crustal thickness is $79(75, 84)$ km, whereas when surface loads are considered, the range of values

Table 6.3: Summary of results for the six studied plateaus. $L \neq 0$ corresponds to the scenario where surface and subsurface loads are allowed, $L = 0$ has only surface loads and $T_e = 0$ represents the Airy isostasy case. The values in parentheses indicate the 1σ limits. In cases where the limits are not present, no acceptable fits were found, with the value shown corresponding to the best-fitting value.

Region	T_c (km)			T_e (km)		L
	$L \neq 0$	$L = 0$	$T_e = 0$	$L \neq 0$	$L = 0$	$L \neq 0$
Ovda	30(1–35)	30(24–35)	33(31–35)	10(0–19)	10(0–15)	0.00(-0.04–0.14)
Thetis	13(1–36)	24(12–36)	34(32–36)	17(0–35)	24(0–33)	0.12(-0.06–0.14)
W. Ovda	11(1–21)	21(20–22)	21	4(0–12)	2(0–4)	-0.02(-0.04–0.14)
Alpha	15(1–21)	15(9–21)	24	20(9–24)	20(12–24)	0.00(-0.02–0.14)
Tellus	18(1–33)	30(17–33)	30(28–33)	10(0–28)	2(0–25)	-0.02(-0.06–0.14)
Phoebe	10(1–84)	78(68–84)	79(75–84)	26(0–39)	9(0–25)	-0.14(-0.18–0.14)

increases slightly to $78(68, 84)$ km. We note that these values are about two to three times higher than the values found in other plateaus. Nevertheless, when subsurface loads are considered, all values for the crustal thickness less than 84 km are allowed. The elastic thickness is found to be less than 25 km when surface loads are considered, and less than 39 km with both surface and subsurface loads are considered. As for the loading ratio L, we note that Phoebe allows for considerable subsurface loads. Whereas the other regions in this study possess negative values down to -0.06, for Phoebe, it increases downward to -0.18. Though we cannot distinguish between surface and subsurface loads, our study corroborates the interpretation that Phoebe is potentially associated with a much more important mantle plume or buoyant layer than the other crustal plateaus.

6.3 DISCUSSION

6.3.1 *The Crustal Thickness of the Highland Plateaus*

Several studies have used gravity and topography data to investigate the Venusian crustal plateaus. Most of them, notably in the Magellan Era, studied the crustal thickness of these features, making use of spatial techniques and assuming that they were isostatically compensated (Smrekar and Phillips, 1991; Kuncinskas and Turcotte, 1994; Moore and Schubert, 1997). The crustal thickness of the highland plateaus was also investigated in some of the earliest developments of localized spectral admittance analyses (Grimm, 1994; Simons et al., 1997). Anderson and Smrekar (2006) created spectral classes from

localized spectral admittances to estimate the crustal thickness and elastic thickness across the planet. James et al. (2013) developed a global compensation model separating the effects from shallow compensation, related to crustal thickness variations, and dynamic compensation mechanisms associated with mass anomalies in the mantle. From this model, the authors were able to construct a global crustal thickness map assuming a mean crustal thickness of 15 km. Finally, Jimenez-Diaz et al. (2015) made use of the crustal thickness modeling introduced by Wieczorek and Phillips (1998) to generate a crustal thickness map of Venus assuming an average crustal thickness of 25 km. In contrast, our study made use of three loading scenarios, with different levels of complexity, to investigate the crustal and lithospheric structure and the possible compensation mechanisms of the crustal plateaus.

Our investigation showed that using an Airy isostasy regime to study the crustal plateaus, which has been done in many previous works, is in most cases a valid approximation to fit the admittance within uncertainties, with the exception of Alpha Regio, where some flexural rigidity is necessary to properly fit the data. We added a level of complexity to our model by assuming that surface loads are supported elastically by the lithosphere, i.e. the elastic thickness can be different from zero. From this, we were able to confirm that the elastic thicknesses associated with the crustal plateaus are low, with a best-fitting average of approximately 15 km among all regions. Considering the uncertainties, we found that most regions are consistent with $T_e = 0$ km, with the exception of Alpha Regio where we obtained a lower bound of $T_e = 12$ km. Moreover, we found upper bound values of no more than 35 km.

The final level of complexity in our study was to assume that the surface relief is a combination of surface loads and support from either a buoyant mantle layer or a high density intrusion within the crust. We found that the best-fitting load ratio is equal to zero or has small positive values for most regions, indicating a possibility for small amounts of dense intrusions in the crust. Considering the uncertainties, a small negative loading ratio up to about -0.05 is permitted for Ovda, Thetis and W. Ovda, and Tellus regiones. The only exception is Phoebe Regio, where L can go as low as -0.18 with a best-fitting value of -0.14. To obtain a more physically meaningful estimation we can convert L to the ratio of subsurface to surface loads, f (see eq. 5.29). We find that Phoebe may have a buoyant mantle load that is about 12% (up to 15%) of the surface load while in other regions the fraction is constrained to a maximum of 4%. Overall, our results show that the interior structure of the plateaus is well-described by the inclusion of surface loads only with a small, arguably negligible, contribution of flexural support, which is consistent with the interpre-

tation that the geological processes responsible for their formation are no longer taking place.

Considering the three loading scenarios just described, Figure 6.6 presents our crustal thickness estimations for the six studied plateaus. The figure also includes crustal thickness estimates from the previous studies mentioned above. Looking at our crustal thickness estimations, we can see that for Ovda, Thetis, W. Ovda, Tellus, and Alpha the obtained results are quite similar, with best-fitting values ranging from 15 to 30 km in the surface-loading scenario and from 11 to 30 km when internal loads are included. In addition, in these regions the different loading scenarios do not have a major impact on the results. Overall, the most important difference between the three loading scenarios is the accepted range of values. As one would expect, decreasing the number of free parameters reduces the uncertainties of the estimations. Assuming an Airy isostasy regime results in good fits for most regions with very low uncertainties of roughly ± 2 km. When only surface loads are allowed we found acceptable crustal thickness values for every region and all estimations include a lower bound. For this case, the crustal thicknesses were found to be uncertain by about ± 6 km. Lastly, when including both surface and subsurface loads, we note that we were able to obtain only an upper bound on the crustal thickness. When comparing the three scenarios, we note that the crustal thicknesses obtained when assuming Airy isostasy can be slightly larger than that of the other two techniques, with best-fitting values up to 10 km larger with respect to the surface-loading scenario.

Phoebe Regio is the only region where our crustal thickness estimates are different than the other crustal plateaus. When internal loads are not included the permitted crustal thickness values range from 68 to 84 km, which corresponds to roughly three times the thickness found for the other regions. However, when subsurface loads are present, the uncertainties are increased dramatically. Even though the upper bound in this case is comparable to the other two models, we do not find a firm lower limit for the crustal thickness. The best fitting value is 10 km, which is about 70 km lower than for the Airy and surface loading models, is more consistent with the crustal thicknesses obtained for the other plateaus.

Comparing our estimations with the previous studies, we find that, in general, the more recent investigations present a good agreement with the values we have obtained. On the other hand, many investigations done in the 1990s present considerably higher values, ranging from twice to three times what we find. This discrepancy between the earliests and latest studies probably arises from the combination of several factors, but we expect that the main contributor for the observed differences are related to differences in methodology. Many early studies assumed that the plateaus were isostatically compen-

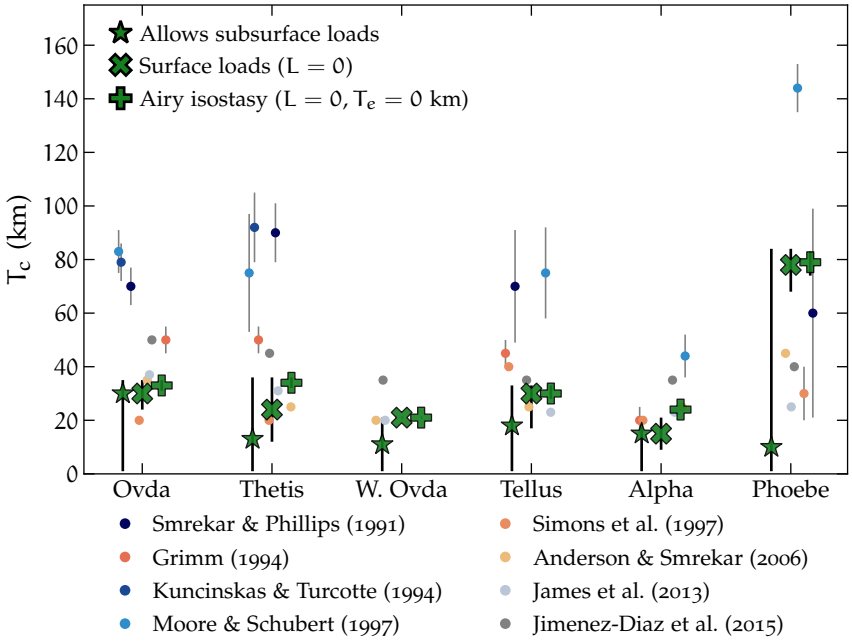

Figure 6.6: Crustal thickness estimates for the crustal plateaus of Venus. The values in green represent our results considering the three investigated compensation scenarios: Airy isostasy (+), surface loading (×), and surface-subsurface loading (⋆). The dots correspond to estimates from previous studies. Dark and light blue are associated with the use of spatial analyses methods, dark and light orange correspond to localized spectral analyses and grays represent global crustal thickness modeling. Figure from Maia and Wieczorek (2022).

sated, which can bias the crustal thickness estimations towards larger values. However, even when comparing our Airy isostasy estimation with previous ones, an important discrepancy persists, particularly for the studies that made use of spatial techniques. Therefore, it is likely that the use of different analysis techniques has a major impact on the estimations. With our approach, we were able to select only the portion of the spectrum where the correlation between gravity and topography is high. On the other hand, in space domain approaches, it is not possible to do this selection since this type of analysis collapses the wavelength-dependent gravity-topography ratio into a single value. The inclusion of gravity signals from uncorrelated sources or from long-wavelength mantle signals could be part of the cause of the bias of their crustal thickness estimations. It is also important to remark that our study presents important improvements in comparison to most previous studies regarding the uncertainty analysis. In fact, several prior studies did not provide any uncertainties for their estimations.

A second possible source for the observed discrepancy is the use of different datasets. The early gravity studies relied on gravity models with substantially lower resolutions than the MGNP180U model used in this work (which was published in 1999). Particularly, Smrekar and Phillips (1991) only had access to a gravity model from the Pioneer Venus mission, while the other studies done in the 1990s used a variety of preliminary gravity models with maximum resolutions ranging from spherical harmonic degree 60 to 120, depending on the publication year. A historical review about these early gravity models of Venus can be found in Sjogren et al. (1997).

Up until this point, we have reported crustal thickness estimations that correspond to the average crustal thickness of each region (weighted by the amplitude of the localization window). However, it is also interesting to investigate the local variations of crustal thickness within each region. In order to do so, we employ the best-fitting elastic thickness and crustal thickness estimates obtained using the surface-loading scenario (Table 6.3). With these values, we then estimate the lateral variations in deflection of the lithosphere (i.e., ω in Figure 5.2). From this global map of the crust-mantle interface, we then estimate the average crustal thickness of the analysis region (weighted by the localization window) and compare with the value T_c that we obtained from our admittance analysis. Finally, we modify the average depth of the interface ω (i.e., the degree-0 spherical harmonic term) such that the predicted value is the same value as from our analysis. The resulting crustal thickness maps, based on the best-fitting crustal thickness and elastic thickness values, are shown in Figure 6.7. These maps show that, due to the crustal roots, crustal material can reach depths much larger than the regional average. Particularly at Ovda, the highest plateau, the crustal thickness can reach up to 54 km when accounting for the uncertainties of the analysis parameters.

We emphasize two aspects concerning our crustal thickness models presented in Figure 6.7. First, even though these are computed using spherical harmonic coefficients of the deflection of the crust-mantle interface, the model is only valid locally within the analysis region. Second, our analysis differs from the more common technique where the relief of the crustal mantle interface is inverted in order to satisfy the observed gravity field (e.g. Wieczorek and Phillips, 1998; James et al., 2013; Jimenez-Diaz et al., 2015). In particular, in our model, the relief along the crust mantle interface is predicted from a flexure model that satisfies the admittance over a limited range of spherical harmonic degrees.

From the regional average crustal thickness T_c at each plateaus, we are also able to estimate the crustal thicknesses at the mean planetary

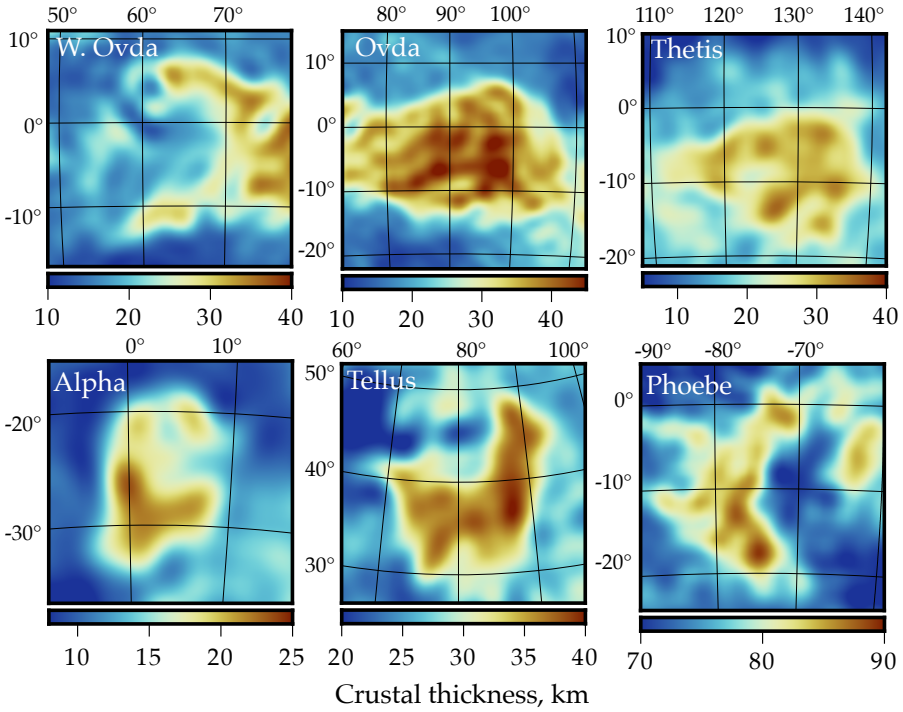

Figure 6.7: Predicted local crustal thickness variations of the six studied crustal plateaus. These maps make use of the surface topography, the best fitting crustal thickness, and the predicted flexure of the crust-mantle interface for the best-fitting elastic thickness at each region for the surface-loading model. The adopted projection for these maps is Lambert azimuthal equal-area. Figure from Maia and Wieczorek (2022).

elevation, T_0. Given that the crustal plateaus are overall consistent with being in Airy isostasy, we can use the following relation:

$$T_c = T_0 + \overline{h}_w \left(1 + \frac{\rho_c}{\rho_m - \rho_c}\right) \tag{6.4}$$

where $\overline{h}_w$ is the window-weighted average elevation of the analysis region with respect to the mean planetary radius. Disregarding the anomalous T_c estimation of Phoebe Regio, we find that the average thickness of the crust, T_0, is 22 km on average. Of course, this approach assumes that the crustal density is constant. In Table 6.4 we provide, for all studied plateaus, the regional average topography weighted by the localization window, the implied mean crustal thicknesses T_0 and the maximum depths reached by crustal materials. We note that T_0 can also be derived surface-loading scenario from the degree-0 term of each crustal thickness map (Figure 6.7). In this case, for the best-fitting crustal thicknesses and elastic thickness values, the average T_0 is 17 km.

Table 6.4: Local crustal thickness estimations. $\overline{h}_w$ is the window-weighted average topography, which is used to compute the crustal thicknesses at the mean planetary elevation T_0 (shown in the third column) assuming Airy isostasy compensation. T_0 values are estimated by applying eq. 6.4 to the fourth column of Table 6.3. T_{max} represents the maximum crustal depths reached by crustal materials under the highland plateaus. The values in parentheses indicate the estimations based on the elastic thickness and crustal thickness 1σ limits.

Region	$\overline{h}_w$ (km)	T_0 (km)	T_{max} (km)
Ovda	1.95	22	47(41–53)
Thetis	2.17	21	35(22–48)
W. Ovda	0.73	16	39(39–40)
Alpha	0.23	22	23(17–30)
Tellus	0.01	29	40(26–43)
Phoebe	0.78	74	89(77–95)

6.3.2 *Heat Flow at the Crustal Plateaus*

The elastic thickness is strongly related to the thermal state of the lithosphere and, in the absence of direct heat flow measurements, it is one of the few quantities that can help constrain the thermal evolution of the planet. It is important to remark that these estimations are associated with the lithospheric thermal properties during the formation of plateaus and do not necessarily correspond to their current, probably colder, thermal state (Albert and Phillips, 2000). The estimation of the heat flow from the elastic thickness is based on the method introduced by McNutt (1984) and comprehensively described in Section 5.1.4. In brief, the method is based on the premise that the bending moment of our modeled elastic plate, which depends on the flexural rigidity and the curvature of the plate (eq. 5.33), equates the bending moment of a more realistic rheology model, referred to as mechanical plate, where the stresses are governed by brittle failure near the surface and viscous stresses in the lower lithosphere (eqs. 5.34–5.36). Because the viscous flow law depends on the temperature, it is possible to estimate the lithosphere thermal gradient (eq. 5.37) and the associated surface heat flow by assuming a thermal conductivity k for a given mechanical lithosphere thickness T_m (eq. 5.38).

We adopt $k = 2$ W m^{-1} K^{-1} as it is a typical value for terrestrial basalts (e.g., Clifford and Fanale, 1985; Clauser and Huenges, 1995). We note, however, that the thermal conductivity of rocks strongly depends on many parameters such as porosity, fluid content, compo-

sition, and temperature. Previous studies that investigated the lithospheric heat flow on Venus considered a large variety of thermal conductivity values, ranging form 2 W m^{-1} K^{-1} (Bjonnes et al., 2021) to 4 W m^{-1} K^{-1} (O'Rourke and Korenaga, 2015), and it is important to take this into account when comparing results from different studies. Moreover, in order to compute the elastic bending moment, we adopt the maximum curvature found at each region for each set of model parameters as advocated by Mueller and Phillips (1995). The maximum curvature is computed by taking the second derivative of the modeled lithospheric deflection ω. We remark that the curvature values are derived from flexural models and not actual observations. Hence, the curvature depends upon the validity of the model assumptions.

The stress laws adopted to calculate the mechanical thickness depend on the strain rate and the mineralogical composition of the lithosphere. As discussed in Brown and Grimm (1997), during the formation of tessera terrains, craters were being destroyed faster than they were forming, indicating a high strain rate, likely around 10^{-15} s^{-1}, which is the value picked for our investigation. Concerning the composition, we consider a dry diabase rheology for the crust and a dry olivine rheology for the mantle, making use of the same flow law parameters as in Resor et al. (2021). Since new studies suggest a felsic rheology for the crustal plateaus (Gilmore et al., 2015), we also performed heat flow estimations considering an anorthite (plagioclase) rheology for the crust. We found that this change in rheology had a minor impact on the heat flow estimations, corresponding to a maximum increase of 3 mW m^{-2} with respect to the diabase rheology.

We estimate the best-fit heat flow associated with the best-fit elastic thickness for the six plateaus, and the associated uncertainties are computed using the 1-sigma uncertainties of the elastic thickness. Given that $T_e = 0$ km corresponds to an infinite thermal gradient, we were unable to compute an upper bound of the heat flow for most regions. In Table 6.5, we summarize the curvature, mechanical thickness, thermal gradient, and heat flow estimations that we obtained. As expected, the mechanical thickness estimations are always larger than the associated elastic thicknesses, ranging from 1.5 to 2 times their values. The best-fitting thermal gradients and heat flows vary considerably among the plateaus, ranging from 8 to 100°C km^{-1} and 16 to 200 mW m^{-2}. This difference is less striking when we look into the lower limits, where the thermal gradient varies from 7 to 10°C km^{-1} and the heat flow from 12 to 20 mW m^{-2}. The only exception is for W. Ovda Regio, having lower bounds of 45°C km^{-1} for the temperature gradient and 90 mW m^{-2} for the heat flow.

Overall, our heat flow estimations have very large uncertainties, mostly only being constrained to be larger than about 15 mW m^{-2}. Therefore, the interpretability of these results is quite limited. Alpha

Table 6.5: Heat flow and related quantities for the crustal plateaus of Venus. K is the maximum plate curvature, T_m is the mechanical lithosphere thickness, dT/dz is the temperature gradient, and F is the surface heat flow. The values in parentheses represent the 1σ limits of each estimation.

Region	K (10^{-7} m^{-1})	T_m (km)	dT/dz(°C km^{-1})	F (mW m^{-2})
Ovda	5.35(4.99–5.56)	16(0–30)	16(11–)	31(21–)
Thetis	3.9(3.19–5.23)	39(0–48)	8(7–)	16(13–)
W. Ovda	5.2(5.19–5.21)	3(0–6)	92(45–)	184(89–)
Alpha	2.2(2.04–2.45)	27(18–32)	12(10–19)	24(20–37)
Tellus	3.08(2.23–3.08)	3(0–35)	102(10–)	203(18–)
Phoebe	3.75(2.94–3.83)	13(0–38)	20(7–)	39(13–)

Regio, however, is an exception because it is the only region where we found a lower bound for the elastic thickness that constrains the heat flow within the range 20–37 mW m^{-2}. For the purposes of discussion, we will assume that this range is representative of the other highland plateaus, and then compare these estimations to those obtained using independent techniques. In order to perform a consistent comparison, we rescaled all heat flow estimations to use the same thermal conductivity as in this study.

Global thermal evolution models and previous elastic thickness investigations suggest that the current average or "ambient" heat flow on Venus is around 10–30 mW m^{-2} (Solomatov and Moresi, 1996; Phillips et al., 1997; O'Rourke and Korenaga, 2015). Furthermore, hydrocode modeling of the Mead impact basin formation from Bjonnes et al. (2021) constrained the temperature gradient to be 6 to 14°C km^{-1}, corresponding to a heat flow of 12–28 mW m^{-2}. This latter result was proposed to be independent of location and representative of the past 300 Myr to 1 Gyr. Gravity and topography studies of Venusian volcanic rises, including Atla, Bell and Eistla regiones, lead to heat flows estimations of 21 to 35 mW m^{-2} (Phillips et al., 1997), which are very similar to our results for Alpha Regio. In addition, flexural studies based on topography data indicate that coronae are associated with major heat flow anomalies, reaching up to ~100 mW m^{-2} (O'Rourke and Smrekar, 2018; Russell and Johnson, 2021), while steep-sided domes are associated with regional heat flows of 40 mW m^{-2} (Borrelli et al., 2021).

Our heat flow estimates generally overlap with the predicted present-day global average values. Nevertheless, our estimates are on the high end of these predictions, and are more similar to those obtained for the volcanic rises. It is possible that the plateaus were associated with higher heat flows at the time of their formation. At least for Alpha

Regio, we find that the excess heat flow with respect to the estimated global average is about 10 mW m^{-2}. For comparison, this 10 mW m^{-2} excess heat flow is consistent with estimations of excess heat flow associated with hotspots on slow moving plates on Earth (e.g., Sleep, 1990). Furthermore, orogenic belts on Earth's continental crust have also been associated with surprisingly low elastic thicknesses (lower than 20 km) and high heat flows (e.g. McNutt et al., 1988; Burov et al., 1990) which compares favorably with the values we found for the crustal plateaus. The cause of these anomalously low elastic thicknesses in continental regions is not fully understood, but data inversion and finite-element modeling studies indicate that decoupling of the strong upper crust and upper mantle probably is an important contributor (McNutt et al., 1988; Burov and Diament, 1995; Brown and Phillips, 2000). In fact, we also observed crust-mantle decoupling in the estimated yield-stress envelopes of some crustal plateaus in a few cases. The possibility of crust-mantle decoupling on Venus has been previously discussed in Buck (1992), Azuma et al. (2014), and Ghail (2015).

Regarding previous heat flow estimations of crustal plateaus, Brown and Grimm (1997) and Resor et al. (2021) were able to constrain the heat flow associated with the formation of folds in tessera terrains based on geodynamic modeling of tessera deformation. In short, they estimated the depth of the brittle-ductile transition based on the dominant wavelength of regularly spaced contractional ridges and the crustal rheology. These investigations showed that the folds observed in these regions are associated with thermal gradients of roughly 20–25°C km^{-1}, corresponding to heat flows of 40–50 mW m^{-1}, for a diabase rheology. For a felsic rheology, Resor et al. (2021) estimated that thermal gradients would be approximately twice as high, with heat flows ranging from 90 to 100 mW m^{-1}. These estimated heat flows are considerably higher than what we obtained for Alpha Regio, but are nevertheless compatible within the uncertainties of the other crustal plateaus.

6.3.3 *Insights on the Thermal and Geological Evolution of the Crustal Plateaus*

Crust-constituent minerals may undergo solid-state phase transitions or melt when they reach certain pressure-temperature conditions. These phase transitions affect the density of the host materials, and may affect the dynamics of the crust and underlying mantle. In Figure 6.8 we plot the conditions where the main phase transitions associated with a basalt system take place. Plot (a) shows the depth-temperature relationship for basalt phase transitions to granulite, eclogite, and the onset of melting. In panel (b), we plot the depths at which the eclog-

ite phase transition and melting occur for as a function of the thermal gradient, which is assume to be linear across the lithosphere

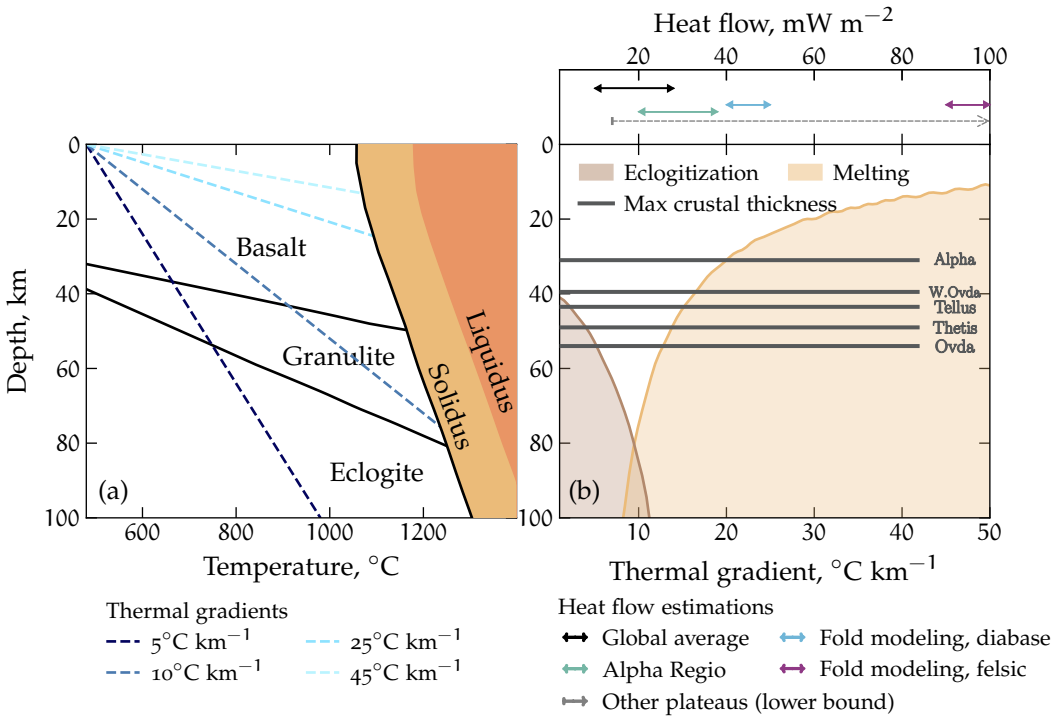

Figure 6.8: (a) Phase transitions in the basalt system as a function of depth and temperature. The phase transitions, solidus and liquidus are adapted from Hess and Head (1990) and dashed curves represent temperature profiles with constant temperature gradients from 5 to 45°C/km. (b) Depth range of eclogitization (brown) and melting (orange) as a function of the thermal gradient and corresponding heat flow. The horizontal lines correspond to the maximum depths reached by crustal materials at each plateau given the 1σ limits of average crustal thickness and elastic thickness. These maximum depths consider lithospheric flexure and are hence greater than the average values reported in the main text. The arrows above the plot correspond to different heat flow estimations associated with the crustal plateaus. The estimate we obtained for Alpha Regio is shown in green, whereas the gray arrow corresponds to the average lower bound for the other plateaus. The blue and purple arrows represent estimations from geodynamical modeling of fold formation for a diabase rheology (Brown and Grimm, 1997; Resor et al., 2021) and felsic rheology (Resor et al., 2021), respectively. The black arrow corresponds to global average estimations.Figure from Maia and Wieczorek (2022).

For low thermal gradients ($\leqslant$ 10°C km^{-1}) basaltic compositions transitions into granulite at depths ranging from 30–40 km which in turn transition into eclogite when a depth of 50–80 km is reached. These transitions are mainly driven by the production of garnet from plagioclase present in the basaltic rocks. Granulite corresponds to a phase where only part of plagioclase has been transformed into garnet, i.e., both minerals are still on the system, while in the eclogite phase all plagioclase has transformed into garnet. Meanwhile, in

an environment subject to higher thermal gradients, roughly above 10°C km^{-1} (or 20 mW m^{-1}), partial melting of the material occurs before the eclogite phase transition is reached. For reasonable depth ranges, the solidus corresponds to temperatures somewhere between 1000 to 1200°C.

Combining the local crustal thickness estimations (Figure 6.7) with the heat flow estimations (section 6.3.2), we are able to investigate whether basal melting of the crust or the formation of eclogite could have occurred at the base of the plateaus. These conditions are visualized in Figure 6.8(b) where we show the maximum crustal thickness of each region and several heat flow estimations associated with these regions. Making use of model present-day global average estimations (e.g., Solomatov and Moresi, 1996; Phillips et al., 1997; O'Rourke and Korenaga, 2015; Bjonnes et al., 2021) we adopt ~10–28 mW m^{-1} as a reasonable range of the current surface heat flow of Venus. Considering this range, represented by the black arrow, we find that the eclogite phase transition could be reached at the base of the two highest plateaus, Ovda and Thetis. In particular, we do not expect the eclogite phase transition to be reached in the other plateaus Tellus, W. Ovda, and Alpha regiones, nor for any of the plateaus if the heat flow there is greater than about 20 mW m^{-2}.

One important property of eclogite is that its density (~3500 kg m^{-3}) is considerably higher than basalt and likely higher than the underlying mantle, which would enable these materials to delaminate and sink into the mantle. Therefore, it is conceivable that delamination processes are potentially taking place in these regions, or that they occurred throughout their evolution. In fact, delamination could possibly explain the correlation and admittance decrease around spherical harmonic degrees 50–60 observed in several regions (see Figure 6.4). Moreover, as a result of delamination, the depth of the eclogite transition could potentially correspond to the maximum expected crustal thickness of the planet. Because of this, estimations of depths of the crust-mantle interface considerably greater than 70 km should be examined with suspicion, such as with the highest values (given the uncertainties) we obtain for Phoebe Regio.

The heat flows associated with the formation of the plateaus were likely higher than the present global average heat flow, as shown in Figure 6.8(b). The green arrow indicates our heat flow estimation for Alpha Regio, which corresponds to the period of load emplacement in the region. The estimations based on fold modeling (Brown and Grimm, 1997; Resor et al., 2021) are shown in blue and purple for dry diabase and dry felsic rheologies, respectively. Though the present day globally-averaged heat flow is probably not sufficient to cause melting in the crustal plateaus, the heat flows were probably substantially higher when the plateaus were forming (as obtained from our results and those of fold formation). Crustal materials that reached

40 km depth or more would have likely gone through some degree of melting. Considering the heat flow constraints from the formation of folds, the melting of crustal materials would have happened at shallow depths, of about 25 km for diabase and 15 km for more felsic compositions. We note that the heat flow estimations based on fold modeling strongly depend on the rheology law used (Brown and Grimm, 1997), appearing to be more sensitive to this parameter than the method by McNutt (1984) used in our study. Hence, in the case of the fold modeling approach, we need better constraints on the the composition and volatile content in these regions in order to estimate the inferred heat flow. We also remark that these phase transitions are based on a basaltic system and more felsic systems would tend to melt at even lower temperatures than those shown in Figure 6.8. Nevertheless, these results already indicate that magmatic processes may have played an important role in the early formation of many crustal plateaus.

The substantial difference between heat flow estimations based on fold modeling and our estimation for Alpha Regio is somewhat puzzling. Nevertheless, even if we consider that the rheological flow laws used are correct, there are several factors that could help explain this discrepancy. Since the formation of folds is associated with higher heat flows, it is plausible that these features developed early in the plateau formation history when the crust was considerably thinner than the current observations. In fact, the limited amount of volcanism in these plateaus could indicate that the crustal thickness was around 20 km or less at that time. We also remark that the heat flow estimations from fold formation are associated with a single fold wavelength that are not necessarily responsible for the entire thickening process of the plateaus.

It is also possible that some of our assumptions regarding the heat flow estimations might be oversimplified. For example, our investigation, as well as the fold wavelength modeling studies, assumed that the thermal gradient is constant across the lithosphere and neglected the presence of radiogenic heat sources in the crust. However, radiogenic elemental concentrations on the surface of Venus, as were measured by the Soviet landers (Surkov et al., 1987), are consistent with moderately radiogenic basaltic rocks found on Earth and should contribute for the surface heat flow (see Ruiz et al., 2019; Karimi and Dombard, 2020, for a discussion). Hence the heat flow near the surface, where the folds formed, should be higher than the global crustal average. Finally, several studies have also discussed the possibility that the wavelength of tectonic features may not be controlled by the depth of the brittle-ductile transition and could, for example, be associated with intracrustal layering (Montési and Zuber, 2002; Ghent et al., 2005; Romeo and Capote, 2011). Therefore, the observed wavelength might not be purely dependent on the thermal properties of

the crust. On the other hand, our simple loading model does not take into account uncorrelated loads and in-plane forces which could could impact the heat flow estimations (e.g., Mueller and Phillips, 1995) given that compressive tectonics probably played an important role in the construction of the crustal plateaus. Nevertheless, studies conducted on orogenic regions on Earth found a good agreement between admittance spectra estimates of the elastic thickness and estimations using more complex forward modeling (McNutt et al., 1988).

6.4 CONCLUSION

We have performed localized admittance modeling at six Venusian crustal plateaus using the spatio-spectral localization technique from Wieczorek and Simons (2005) and Wieczorek and Simons (2007). By testing different compensation scenarios, we were able to confirm that most of these features are consistent with being in an Airy isostasy regime. Some extent of flexural support is also accepted given that we found an average upper bound for the elastic thickness of approximately 30 km. The addition of subsurface loads does not have a major influence on the elastic thickness and crustal thickness estimations for most regions. The average crustal thickness of the plateaus is constrained between about 15 to 34 km, but because of lithospheric deflection the crustal materials can, in several cases, reach down to more than 40 km depth. These values are comparable to the crustal thickness of the continents on Earth. In addition, we were able to estimate that the average crustal thickness of the planet is 22 km when assuming an Airy isostasy, whereas for the surface-loading scenario we found a global average thickness of 17 km. The main discrepancy we found regarding crustal thickness estimations is associated with Phoebe Regio. In this region, when internal loads are not taken into account, we find anomalously high crustal thicknesses that are about 3 times larger than the other plateaus. Only when subsurface loads were added did we find crustal thicknesses that were consistent with the other regions. This indicates that Phoebe is in a different compensation regime compared to other plateaus, being partially supported by a buoyant layer in the mantle.

The elastic thickness and crustal thickness estimations provide some insights on the thermal evolution of the crustal plateaus. Adopting the method introduced by McNutt (1984), we used the elastic thickness to calculate the heat flow during the period of load emplacement. We then compared these results with other heat flow estimations, such as fold wavelength modeling studies (Brown and Grimm, 1997; Resor et al., 2021), and evaluated the possibility of phase transitions and melting at the base of plateaus during their geologic evolution. These analyses indicate that the crustal plateaus formed under higher heat flow conditions compared to the estimate current global average.

Melting of deep crustal materials may have happened during the formation of the plateaus, and in some places eclogite may have formed in the deepest crust when the heat flow was lower, potentially leading to crustal delamination and to the recycling of crustal materials into the mantle.

It is clear that a better understanding of the formation of the plateaus will be obtained with new data, including a better gravity model, composition-related measurements of the surface and higher resolution imaging. For example, if the plateaus are indeed felsic, as thermal emission data possibly indicates (Gilmore et al., 2015), it would reinforce the hypothesis that they are analogous to the continents on Earth. In this context, being able to estimate their bulk crustal density, using gravity techniques applied to the Moon and Mars (e.g., Wieczorek et al., 2013; Broquet and Wieczorek, 2019), would be extremely valuable. With the currently available gravity data, however, this is not possible. Fortunately, a better gravity model is one of the many datasets that will be obtained by the two planned Venus orbital missions VERITAS (Smrekar et al., 2021) and EnVision (Widemann et al., 2020) which should have a high enough resolution for constraining the crustal density of plateaus. Undoubtedly, these missions will play fundamental roles towards a better comprehension of the complex geological history of our twin planet.

7

THE MANTLE VISCOSITY STRUCTURE OF VENUS

This chapter presents an analysis of the long-wavelength gravity and topography of Venus which are interpreted as expressions of convective flows in the mantle. In this study, I was able to provide new insights into the geophysical properties of the Venusian mantle, particularly of its viscosity structure. The results presented here are based on the article "The Mantle Viscosity Structure of Venus" by Maia, Wieczorek and Plesa, accepted for publication at Geophysical Research Letters. The chapter structure is the following: Section 7.1 reviews previous studies that investigated the dynamic signature of Venus gravity and topography and the previous attemps to estimate the planet's mantle viscosity. Section 7.2 details the data analysis and inversion and Section 7.3 describes the estimated mantle viscosity structure. A comprehensive sensitivity analysis is presented in Section 7.4. The implications of our results are discussed in Section 7.5 and the conclusions and outlook of the study are presented in Section 7.6.

7.1 INTRODUCTION

The combined investigation of gravity and topography is one of the most powerful methods to study the interior structure of planets. Some of the earliest gravity investigations of Venus, making use of data from the Pioneer Venus Orbiter, have shown that the planet has unique geophysical characteristics. Unlike the Earth, Venus presents a strong correlation between gravity and topography at long wavelengths (Sjogren et al., 1980). In addition, Phillips et al. (1981) and Phillips and Malin (1983) showed that several Venus highlands were compensated at large depths, leading to the interpretation that these features are supported by deep sources in the mantle. Throughout the 1980s, a series of works led to the development of a well-established dynamic loading model capable of predicting the gravity and topography for a given mantle density distribution and radial viscosity profile (Richards and Hager, 1984; Ricard et al., 1984; Hager and Clayton, 1989). Using this model, Kiefer et al. (1986) quantitatively showed that the long-wavelength topography of Venus was consistent with support from mantle convection on a global scale and could not be explained by Airy or Pratt isostatic compensation models.

The advent of the Magellan mission in the 1990s, which obtained higher resolution gravity and topography data of Venus, motivated several investigations of the planet's interior. For example, Kiefer and Hager (1991), Solomatov and Moresi (1996), and Nimmo and McKen-

zie (1996) modeled the gravitational signature of plumes originating from the core-mantle boundary, corroborating the interpretation that the volcanic rises on Venus are active hotspots (e.g., Stofan et al., 1995; Smrekar et al., 2010). The model by Hager and Clayton (1989) continued to be used for constraining the distribution of density anomalies in Venus's mantle (Herrick and Phillips, 1992; Kiefer and Peterson, 2003; James et al., 2013). These investigations showed that the Venusian lowlands, referred to as volcanic plains, were associated with positive density anomalies in the mantle, while the volcanic rises corresponded to negative density anomalies, being commonly interpreted as zones of large-scale mantle downwellings and upwellings, respectively. Meanwhile, regional gravity and topography analyses showed that several Venusian highlands, mostly the plateaus associated with tessera terrains, were compensated shallowly by crustal thickness variations in contrast to the volcanic rises that have important support from mantle sources (Smrekar and Phillips, 1991; Grimm, 1994; Simons et al., 1997; Maia and Wieczorek, 2022).

Several studies have tested the impact of radial mantle viscosity variations on the predicted gravity and topography of Venus, either adopting a dynamic loading model (Kiefer et al., 1986; Herrick and Phillips, 1992; Pauer et al., 2006; Steinberger et al., 2010) or making use of 3D thermal evolution models (Huang et al., 2013; Rolf et al., 2018). The vast majority of these studies focused their investigation on the possibility of a viscosity jump at a depth analogous to the 660 km phase transition on Earth, which corresponds to about 730 km on Venus (Armann and Tackley, 2012), and found that the existence of such feature was inconsistent with the gravity and topography observations. Alternatively, Pauer et al. (2006) made use of a Monte Carlo inversion approach along with the dynamic loading model to estimate the viscosity structure of Venus. Their study showed that Venus's mantle is consistent with a viscosity profile gradually increasing with depth, and that it could have a thin low viscosity channel in the upper mantle. The moment of inertia and k_2 Love number of Venus could be used to investigate the viscosity profile as well, but they are not known with sufficiently accuracy to well-constrain relative variations with depth (see Figure 6 of Saliby et al., 2023).

In this work, we use state-of-the-art inversion methods and data analysis techniques to constrain the mantle viscosity structure of Venus. We adopt the multitaper spatio-spectral localization method by Wieczorek and Simons (2007) to remove shallowly compensated regions from the analysis. The viscosity estimations are done via a Bayesian inference approach (Speagle, 2020), allowing for an efficient exploration of the parameter space and statistical interpretation of the results. To test the robustness of our estimations, we investigate a variety of assumptions concerning boundary conditions and the density variations within the mantle. In particular, we investigate scenarios

where the density anomalies are concentrated within a single thin mass-sheet at a specific depth (e.g., Herrick and Phillips, 1992) or where they are uniformly distributed with depth in the mantle (e.g., Pauer et al., 2006). Ultimately, our study aims to contribute to a better understanding of Venus's geodynamics and tectonic regime (e.g., Rolf et al., 2022) by robustly estimating geophysical mantle properties, and to elucidate how the geologic histories of Earth and Venus diverged.

7.2 LOCALIZED BAYESIAN INVERSION

Based on the dynamical loading model described in Section 5.2 we aim to infer geophysical properties of Venus's mantle, notably its viscosity structure. To do so, we make use of the VenusTopo719 topography model (Wieczorek, 2015a) and the MGNP180U gravity solution (Konopliv et al., 1999), both derived from final Magellan mission datasets (see Chapter 4 for details).

Although mantle flows play an important role in the long wavelength gravity and topography (e.g., Phillips and Malin, 1983; Kiefer et al., 1986), the planet has major highlands, as in Ishtar Terra and Western Aphrodite Terra, that are mainly supported by crustal thickness variations (e.g., Kucinskas et al., 1996; Simons et al., 1997; Maia and Wieczorek, 2022). These shallowly compensated regions are inconsistent with the assumptions of the global dynamic loading model and, thus, should be removed from the analysis. In fact, Pauer et al. (2006) found that the worst predictions from their inversions were for the highlands of Ishtar Terra and Ovda Regio. They attempted to remove these signals by applying a binary mask to the gravity and topography followed by computing a localized power spectrum. However, binary masking procedures have well known spectral leakage problems (e.g., Wieczorek and Simons, 2005).

In order to more rigorously remove the gravity and topography signal associated with the compensated highlands, we make use of the multitaper technique as developed by Simons et al. (2006) and Wieczorek and Simons (2007), which uses optimally designed windowing functions for a specified spherical harmonic bandwidth. We chose to use windows with a spectral bandwidth of $\ell_{\text{win}} = 3$, which corresponds to a total of 9 windows with power concentration above 99%. With these parameters we obtain a reasonable spatial concentration, while keeping a small spectral bandwidth that maximizes the number of uncorrelated spherical harmonic degrees used in our analysis. The main equations related to the localization procedure are presented in Section 3.3.

The results of the multitaper localization are shown in Figure 7.1. The map in panel (a) shows the total power of the 9 localization tapers summed in the space domain with the target localization region

outlined by the white contour. In panel (b), we present the global and localized spectral admittance and correlation of gravity and topography. The localization leads to an increase in the admittance of about 30% over the entire spectrum, which is caused by the exclusion of highland regions that have high topography and low gravity. The correlation also has a significant increase in the long-wavelength range due to the data localization, for $\ell < 40$ the average correlation increases from 0.81 to 0.89.

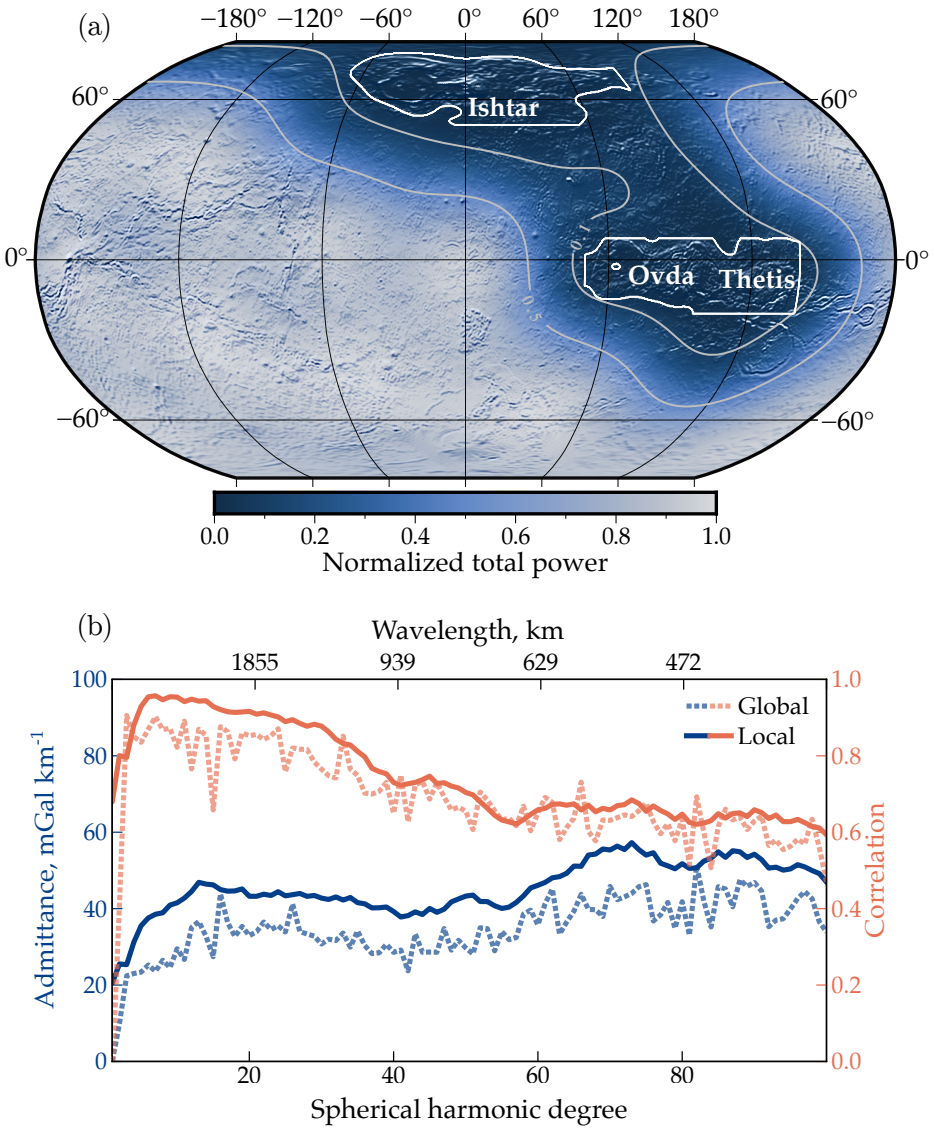

Figure 7.1: Spatio-spectral multitaper localization that excludes Ishtar Terra and Western Aphrodite Terra on Venus. (a) Total power of the 9 tapers used in the localization procedure overlain by a shaded relief map in a Robinson projection. The gray contours indicate 50% and 10% of total power from the localization tapers while the white contours outline the regions of interest to be excluded from the analysis. (b) Global and localized spectral admittances (blue curves) and correlations (orange curves).

We can then use the localized spectra of gravity and topography along with localized spectra predicted by the dynamic loading model to invert for the mantle viscosity structure, modeled in terms of constant-viscosity layers. One important aspect of the model is that the predicted gravity and topography are only sensitive to relative viscosity variations, i.e. the absolute viscosity cannot be constrained. When considering the case where the mantle density anomalies are modeled as a single mass-sheet (eqs. 5.59 and 5.60), the depth of the density anomaly is taken as a free parameter. The model further depends on other parameters such as the core radius, the core-mantle density contrast, and the average elastic lithosphere thickness, which are fixed in this study and given in Table 7.1. The core-related parameters are from Aitta (2012) and based on the Venus-scaled preliminary reference Earth model. The values adopted are consistent with moment of inertia estimates (Margot et al., 2021) and other interior modeling studies (Dumoulin et al., 2017) of Venus. In addition, the elastic thickness is set to zero. As discussed in Section 5.2 and shown in Figure 5.5 the choice of these parameters have negligible impact in our results.

Table 7.1: Values of the model parameters fixed in our inversions.

Parameter	Symbol	Value	Unit
Elastic thickness	T_e	0	km
Young's modulus	E	100	GPa
Poisson's ratio	ν	0.25	–
Upper mantle density	ρ_m	3300	$kg\,m^{-3}$
Core-mantle density contrast	$\Delta\rho_{Mc}$	4050	$kg\,m^{-3}$
Core radius	R_c	3250	km

To statistically evaluate the uncertainties of our model estimations, and considering the relatively large number of free parameters in our problem, we opted for a Bayesian sampling technique, which provides the posterior probability of each parameter. We made use of the DYNESTY package, a Python implementation of the dynamic nested sampling method (Speagle, 2020). Nested sampling estimates the marginal likelihood and the posterior distribution by sampling within nested shells of increasing likelihood. One of the main advantages of nested sampling over the popular Markov Chain Monte Carlo method is its effectiveness in sampling from complex multimodal distributions.

The posterior probability distribution calculated by the Bayesian inversion depends on the prior probability, which is based on a priori knowledge about the parameters, and the likelihood function, that

Table 7.2: Ranges and probability distributions of model priors.

Parameter	Symbol	Range	Distribution
Depth layer 1	d_1	10 to 250 km	uniform
Depth layer 2	d_2	$d_2 + 150$ to 2450 km	uniform
Depth layer 3	d_3	$d_3 + 150$ to 2600 km	uniform
Depth mass-sheet	d_ψ	$d_1 + 10$ to 700 km	uniform
Viscosity contrast layer 2	$\log_{10}(\eta_2/\eta_1)$	-4 to 0	log-uniform
Viscosity contrast layer 3	$\log_{10}(\eta_3/\eta_2)$	-3 to 3	log-uniform
Viscosity contrast layer 4	$\log_{10}(\eta_4/\eta_3)$	-3 to 3	log-uniform

represents an estimation of the misfit between the observations and model predictions (see Section 5.3 for details). Given the lack of further information about our parameters, we consider that the priors follow uniform distributions within a broad ranges of values, as specified in Table 7.2.

The (log-)likelihood function is defined as

$$\log(\mathcal{L}) = -\frac{1}{2}\sum_{\ell_u} \chi_h(\ell) + \chi_g(\ell) + \chi_Z(\ell) \tag{7.1}$$

with

$$\chi_h(\ell) = \frac{(S_{hh}^{obs}(\ell) - S_{hh}^{dyn}(\ell))^2}{\sigma_h^2(\ell)}$$
$$\chi_g(\ell) = \frac{(S_{gg}^{obs}(\ell) - S_{gg}^{dyn}(\ell))^2}{\sigma_g^2(\ell)}$$
$$\chi_z(\ell) = \frac{(Z^{obs}(\ell) - Z^{dyn}(\ell))^2}{\sigma_Z^2(\ell)},$$

where $S_{hh}(\ell)$ and $S_{gg}(\ell)$ are the localized power spectra of topography and gravity, respectively, and $Z(\ell)$ is the localized spectral admittance. The superscript "obs'" indicates quantities associated with observables while "dyn" correspond to predictions from our dynamic loading model. σ_h^2, σ_g^2, and σ_Z^2 are the data uncertainties of the localized topography, gravity, and admittance respectively, which are directly derived from the localization procedure (eq. 3.25). Our likelihood function only accounts for uncorrelated data points of the localized spectra ℓ_u, which correspond to degrees separated by $2\ell_{win} + 1$ (see Section 3.3 for details). The minimum degree considered in our inversion is $\ell_{min} = 4$ to exclude all wavelengths that are larger than the window size. As for the upper limit, we considered the maximum

degree at which dynamic loading is expected to dominate the gravity and topography, which is estimated to be between degree 27 (James et al., 2013) and 40 (Pauer et al., 2006). Considering this range and because we only use independent data points, we chose $\ell_{max} = 32$ for our nominal inversions.

The localized observed spectra of gravity, topography, and admittance along with their estimated uncertainties are presented in Figure 7.2. The figure also shows representative models predicted by the inversion, in particular the model of highest likelihood and a degree-by-degree average of 100 models randomly sampled from the posterior probability distribution.

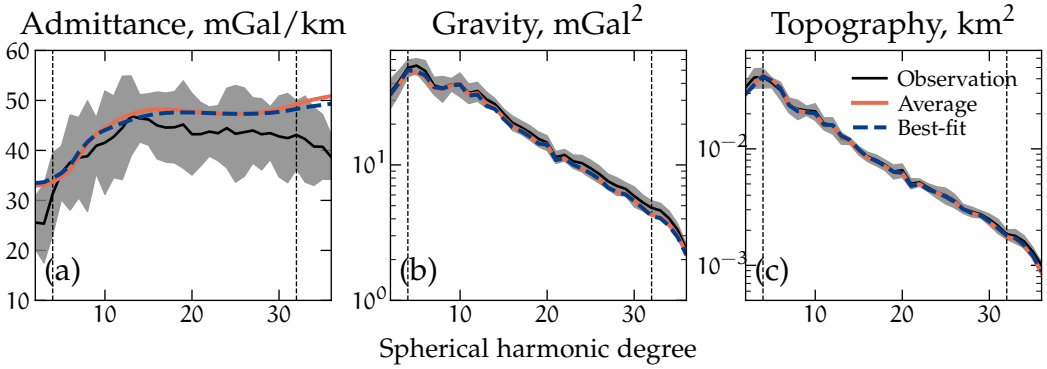

Figure 7.2: Localized observed (a) admittance Z^{obs}, (b) gravity S_{gg}^{obs}, and (c) topography S_{hh}^{obs} spectra used in the inversions are shown in black along with their uncerteinties presented in gray. The dashed blue curves correspond to the best-fit model from the so-called nominal inversion (see Section 7.3 for details). The orange curves correspond to the average of 100 models randomly sampled from the posterior distribution of the same inversion. Dashed vertical lines indicate the sherical harmonic degree range used in the inversions.

7.3 MANTLE VISCOSITY ESTIMATIONS

Even though we performed inversions for a wide range of scenarios (see Section 7.4 for a discussion), we chose to focus our analysis on the three cases that presented the largest variations in the results. The so-called *nominal* case has a no-slip boundary condition at the surface and its density anomaly distribution is parameterized as a single mass-sheet. The *free-slip* case differs from the nominal by having a free-slip boundary at the surface that allows for tangential movement of the surface, while the $\delta\rho$-*constant* case has a constant density anomaly with depth in the mantle instead of a single mass-sheet along with a no-slip boundary at the surface. For these three inversions the number of constant-viscosity layers was set to 4. Each layer was specified by its viscosity η_i and the depth to the bottom of the layer d_i. Since our model is only sensitive to the relative viscosity

Table 7.3: Summary of inversion results for three model scenarios: Nominal, Free-slip and δρ-constant (see main text for details). All models have 4 viscosity layers, where d_i corresponds to layer depths and $\log_{10}(\eta_{i+1}/\eta_i)$ corresponds to viscosity increases (positive values) or decreases (negative values) from one layer to the other. For each inversion we show the median, the 16^{th} percentile (q_{16}), and the 84^{th} percentile (q_{84}) of the posterior distributions.

Parameter	Nominal			Free-slip			δρ-constant		
	median	q_{16}	q_{84}	median	q_{16}	q_{84}	median	q_{16}	q_{84}
$\log_{10}(\eta_2/\eta_1)$	−2.1	−3.4	−0.7	−1.8	−3.4	−0.9	−2.0	−3.4	−0.6
$\log_{10}(\eta_3/\eta_2)$	0.8	0.7	1.1	0.8	0.7	1.1	1.0	0.8	1.3
$\log_{10}(\eta_4/\eta_3)$	−0.1	−2.0	1.3	−0.7	−2.3	0.4	0.8	0.8	0.9
d_1 [km]	81	34	142	67	27	142	95	39	153
d_2 [km]	322	276	406	326	245	411	385	347	423
d_3 [km]	1561	1021	2247	1725	879	2346	1409	1294	1551
d_ψ [km]	238	206	358	329	270	448	–	–	–

variations, we set $\eta_1 = 1$. Assuming that the core radius is known, the viscosity structure is therefore defined by 6 free parameters. The nominal and free-slip scenarios have the mass-sheet depth d_ψ as an additional free parameter. Given the lack of information about our parameters, we considered for our priors a uniform distribution for the depth-related parameters and a log-uniform distribution for the viscosities. The only strong prior we set was to consider that the viscosity of the uppermost lithospheric layer was greater than the underlying layer (i.e., $\log_{10}(\eta_2/\eta_1) < 0$), similar to (Pauer et al., 2006). Such an assumption is a natural feature of temperature-dependent rheological models (e.g., Breuer and Moore, 2015).

Figure 7.3 presents the posterior probability distribution of each free parameter for our three scenarios. The upper four panels show the depths of the first three viscosity layers and depth of the mass-sheet. In the bottom part, the panels correspond to the viscosity ratios of the second, third, and fourth layers with respect to the overlying layer. Positive ratios indicate an increase in viscosity with respect to the layer above while negative ratios indicate a decrease in viscosity. All parameter estimations are detailed in Table 7.3. Other inversion results are discussed in Section 7.4.

Our results show that all scenarios consistently prefer shallow depths for the thickness of the first lithospheric layer, with values less than about 200 km (Figure 7.3a). In contrast, the viscosity decrease to the second underlying layer is relatively unconstrained and reflects primarily our prior (Figure 7.3e). The difficulty to constrain the change

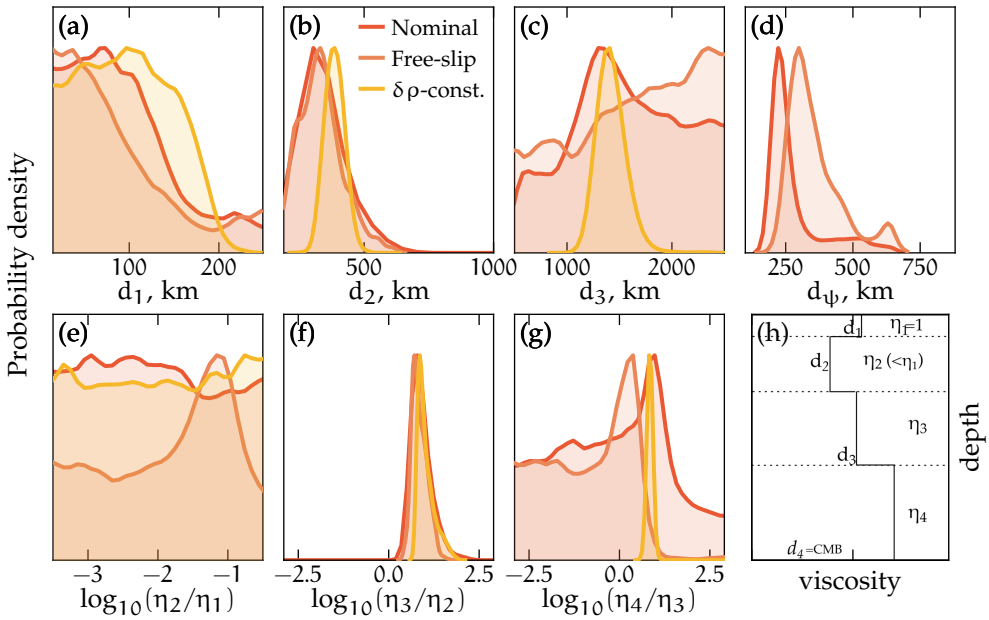

Figure 7.3: Marginalized probability densities of the model parameters for a 4-layer model with nominal, free-slip, and uniform load distribution scenarios (δρ-const.). Panels (a)–(c) correspond to the depth of the first three layers (the fourth layer corresponds to the core-mantle interface) while (d) indicates the depth of the mass-sheet density anomaly. The viscosity constraints are shown in panels (e)–(g) and are presented in terms of viscosity ratios with respect to the layer above. Panel (h) illustrates the definition of each free parameter of the model. The limits of the y-axes differ for each of the marginalized probability plots.

in viscosity between these two layers is due to the small thickness of the top layer. The viscosity interface between the second and third layer is the best constrained from our inversions (panels 7.3b and 7.3f). All three model scenarios indicate that the third layer increases in viscosity by about one order of magnitude at a depth of about 245–435 km for the three loading scenarios, with median values for the mass-sheet depth of 239 km for the nominal case and 329 km for the free-slip case. The change in viscosity between the third and fourth layers is quite variable and differs in all three loading scenarios (panels 7.3c and 7.3g). For the nominal case, both the layer depth and viscosity are poorly constrained, although the solutions prefer depths larger than 1000 km. The free-slip case tends to prefer larger depths, rejects large increases in viscosity for the last layer, and has a peak corresponding to the case where the viscosity of the two layers is the same. The δρ-constant model, on the other hand, has a well-constrained viscosity increase of about 10 times at 1300 to 1550 km depth.

In Figure 7.4 the viscosity profiles for all solutions are shown via 2-dimensional posterior distributions for our three loading scenarios. Since one of the best constrained aspect of our model is the increase in viscosity between the second and third layer, for a better visualization, we scaled our viscosity profiles such that the viscosity of the second layer was 1. The solid curves in these figures represent the logarithmic mean viscosity at each depth. The upper mantle structure is similar for the three scenarios, with a consistent viscosity increase occurring between the second and third layers. As for the lower mantle, the loading scenarios that use a single mass-sheet (Figure 7.4a and 7.4b) are consistent with an isoviscous structure, although some of the solutions suggest a basal low-viscosity layer above the core. As for the $\delta\rho$-constant model (Figure 7.4c), we see a second viscosity jump at about 1400 km depth.

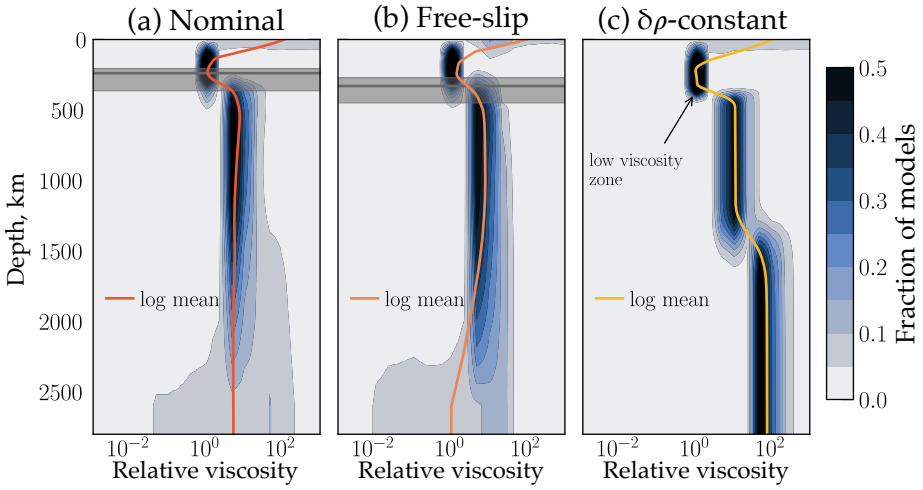

Figure 7.4: Posterior distribution of mantle viscosity structure for the (a) nominal, (b) free-slip, and (c) $\delta\rho$-constant loading scenarios. Solid curves indicate the viscosity logarithmic mean for each depth. All viscosity profiles are referenced to the viscosity of the second layer. In panels (a) and (b), the dark gray rectangles indicate the 16^{th} and 84^{th} percentiles for the d_ψ estimations, while the black horizontal lines show the median value. For clarity, the low viscosity zone is indicated only on panel (c).

7.4 MODEL SENSITIVITY ANALYSIS

The dynamic loading model used in this study depends on a large number of geophysical properties (see Table 7.1) and, from an inversion point of view, it is not possible to take all of them as free parameters. In this study, we focus on estimating the density anomaly distribution and the viscosity profile of the mantle, which are the quantities the model is most sensitive (Figure 5.4). Yet, we performed a wide range of sensitivity analyses to test the robustness of our results. As

previously discussed, parameters such as the elastic thickness, mantle density, core radius, and core density have negligible impact in the model and we chose to fix them based on values estimated by previous studies what is known for Earth.

Nevertheless, along with parameters for internal properties, our inversions are associated with several other settings that we should evaluate further. For example, our investigation is done using the radial gravity component. Yet, several previous studies have used the geoid to perform this type of analysis. In addition, as shown in eq. 7.1, we must define the degree range used to compute the model misfits – which has same level of arbitrariness. Another important aspect of our inversions is that we have to define a fixed number of viscosity layers, which is not an obvious choice. Hence, it is necessary to make sure that changing the number of layers does not affect the constrained viscosity profile.

Figure 7.5 and Figure 7.6 present results for a range of inversion scenarios, showing the main conclusions of our study – in particular the presence of a low viscosity zone – do not change. However, we can see that performing an inversion up to spherical harmonic degree 40 is associated with lower likelihood values, likely indicating that at this degree the data already have non-negligible contributions of other compensation sources. Figure 7.5 also displays the results for a global inversion (i.e., the case where the data localization is not applied). This leads to shallower mantle load depths (176 km on average) and worse fits in comparison to the localized inversions.

7.5 DISCUSSION

7.5.1 *Low Viscosity Zone in the upper Mantle*

Our inversions indicate the presence of a low viscosity zone (LVZ) beneath the lithosphere, having a viscosity of roughly 10 times lower than the underlying mantle. Its thickness is about 150 to 300 km, starting at the base of the lithosphere down to a depth of 268 to 435 km. This low viscosity zone can be interpreted as an asthenosphere-like layer. The asthenosphere of the Earth is a mechanically weak layer starting beneath the lithosphere down to the top of the transition zone at about ~400 km. It is considered to be a key ingredient for plate tectonics (e.g., Rolf et al., 2022) and its existence has been supported by several geophysical methods. On Earth, the region is characterized by high electrical conductivity, low seismic wave velocities, and strong seismic attenuation (e.g., Shankland et al., 1981). In oceanic regions, seismological observations have shown that the lithosphere-asthenosphere boundary occurs sharply at about 70 km depth, while for the continental upper mantle the seismic signature

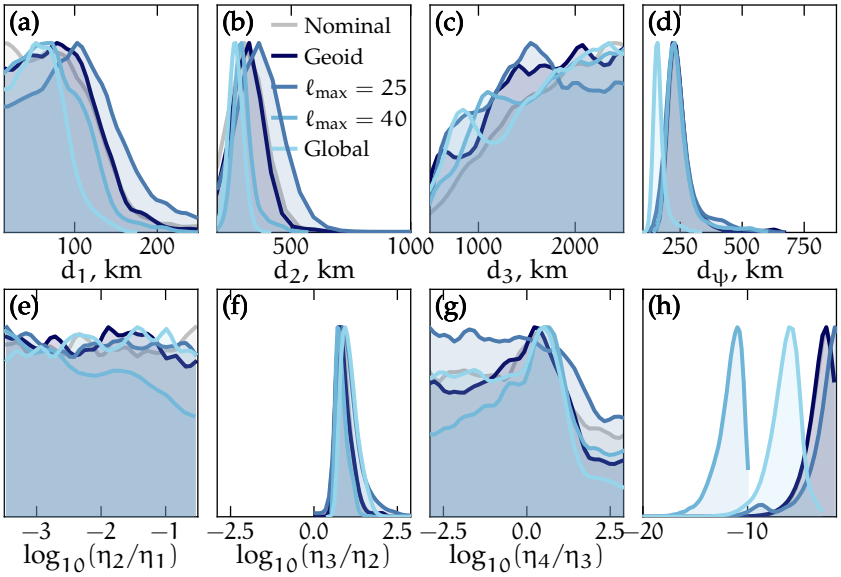

Figure 7.5: Probability density distribution of the model parameters for 5 test cases: *geoid* uses observed and modeled geoid instead of radial gravity, $\ell_{max} = 25$ and $\ell_{max} = 40$ define $\ell = 25$ and $\ell = 40$ as the maximum spherical harmonic degree used in the inversion respectively, and *global* is associated with a global inversion, i.e., it does not apply the multitaper localization to the data and model. As reference we also added the results of the nominal inversion scenario. Panels (a)-(g) are the same as displayed in Figure 2 of the main text, while panel (h) shows the log-likelihood distribution of the the different inversions, as defined in eq. 7.1.

of the lithosphere-asthenosphere boundary is weaker and deeper, at about 200 km depth (Karato, 2012).

Gravity investigations considering postglacial rebound and/or dynamic loading models commonly indicate that the asthenosphere is also characterized by low viscosities, although the published constraints present some discrepancies (King, 2016; Richards and Lenardic, 2018, see reviews by). Estimations of the LVZ are associated with reductions in viscosity of one to three orders of magnitude with respect to the underlying mantle. Moreover, some studies indicate that the LVZ is fully contained within the asthenosphere (Hager and Clayton, 1989; Forte and Mitrovica, 2001) while others suggest that the zone comprises the entire upper mantle (King and Masters, 1992; Liu and Zhong, 2016). Alternatively, Mitrovica and Forte (2004) have found a low viscosity asthenosphere along with a thin low-viscosity channel below the 660 km transition.

Many factors can be responsible for the discussed inconsistencies. For example, it is well-known that in gravity studies there is a strong trade-off between the thickness and viscosity of the LVZ (Richards and Lenardic, 2018). Another issue is that the gravity studies have difficulties in accounting for lateral viscosity variations. This is par-

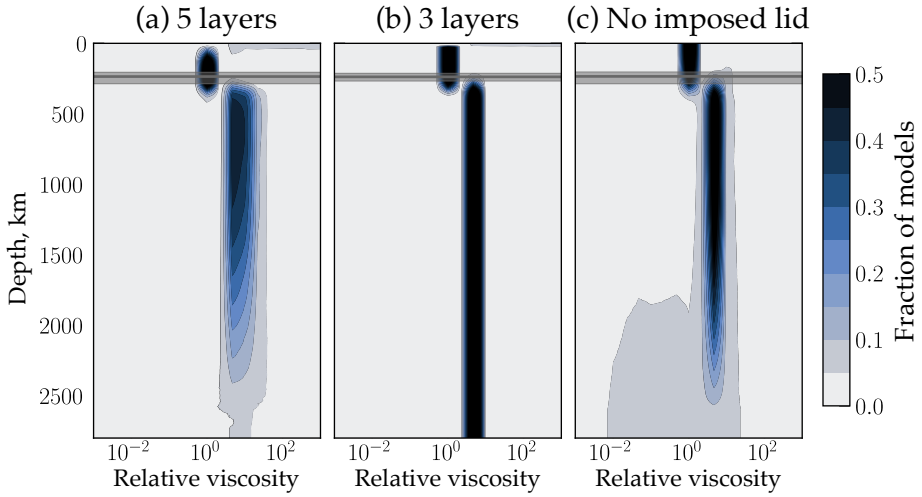

Figure 7.6: Posterior distribution of mantle viscosity structure for (a) 5-layer viscosity model, (b) 3-layer viscosity model, (c) 3-layer viscosity model without an imposed high viscosity lid. All viscosity profiles are referenced to the viscosity of the second layer. The dark gray rectangles indicate the 16^{th} and 84^{th} percentiles for the d_ψ estimations, while the black horizontal lines show the median value.

ticularly problematic for the Earth since there are fundamental differences between the upper mantle structure of continental and oceanic regions (Čadek and Fleitout, 2003) and also because cold subducted slabs often have higher viscosities than the surrounding mantle. On the other hand, it has been shown that the effects of the lateral variations in viscosity are limited for very long wavelengths, with spherical harmonic degrees lower than 10. This led several studies to restrict their analysis to this range, which has the unfortunate drawback of decreasing the model sensitivity to shallow layers. Yet, Venus does not have plate tectonics and large-scale subducted slabs are unlikely to exist. In fact, recent studies have suggested that crustal recycling on Venus occurs via regional-scale delamination scattered throughout the planet (e.g., Smrekar and Stofan, 1997; Gülcher et al., 2020; Davaille et al., 2017; Lourenço et al., 2020). Hence, we expect lateral variations in viscosity to be less important on Venus. In principle, this should allow us to analyse smaller wavelengths in comparison to terrestrial studies and yield a better vertical resolution in our inversions.

In the case of Venus, gravity and topography studies in the past have mostly argued against the existence of a LVZ in the upper mantle (e.g., Nimmo and McKenzie, 1998). However, most of those studies did not perform inversions and limited the analysis to a few models representative of Earth-like scenarios (e.g., Kiefer et al., 1986; Kiefer and Hager, 1991; Herrick and Phillips, 1992; Steinberger et al., 2010). Moreover, gravity investigations performed up to 1992 used data from the Pioneer Venus mission, whose resolution is limited to

degree 18. From a different perspective, studies by Huang et al. (2013) and Rolf et al. (2018) estimated geoid anomalies for Venus from three-dimensional mantle convection models. They showed that the presence of a thick LVZ, ranging from the base of the lithosphere down to the ringwoodite to bridgmanite phase transition at 730 km depth, was inconsistent with the observations. These results are in agreement with our study given that the inversions also disfavor such a prominent LVZ. In addition, Monte Carlo inversions performed by Pauer et al. (2006) showed that many models were consistent with the presence of a thinner LVZ with a thickness of a couple hundred of kilometers, which is in line with our results.

The origin of such a low viscosity layer on Venus is arguable. As a starting point, we may draw a parallel with the Earth and evaluate the mechanisms that have been proposed to explain the existence of its asthenosphere. However, this is a heavily debated topic with several proposed hypotheses. Some studies proposed that the asthenosphere results from the presence of small amounts of partial melts in the upper mantle (Anderson and Spetzler, 1970; Chantel et al., 2016; Debayle et al., 2020), while others consider that the region is better explained by a subsolidus regime associated with rheological weakening of mantle rocks under temperatures that are close to the solidus (Karato, 2012; Takei, 2017). For the latter hypothesis, it has been suggested that dissolved water in olivine could effectively reduce the mineral's viscosity (Hirth and Kohlstedt, 1996). Alternatively, Hua et al. (2023) have proposed that the asthenosphere is associated with partial melting, however, they argue that the melt does not primarily controls the layer's low viscosity. In addition, low viscosities in the uppermost mantle could be caused by the predominance of dislocation creep, with larger depths being dominated by diffusion creep with higher viscosities (Van Den Berg and Yuen, 1996; Semple and Lenardic, 2021). Finally, viscosity interfaces in the mantle are commonly linked to mineral phase transitions (Meade and Jeanloz, 1990).

On Venus, even though the surface and atmosphere are dry, the water content of its interior is unknown. Although Venus and the Earth should probably have accreted similar amounts of volatiles (e.g., O'Brien et al., 2018), we are still trying to quantify the abundance of these volatiles in Venus's interior (e.g., Way and Genio, 2020; Gillmann et al., 2020; Gillmann et al., 2022). On the other hand, the existence of partial melt in Venus's mantle seems plausible, given the indications that the planet is still volcanically active, particularly in regions associated with active mantle plumes (e.g., Mueller et al., 2008; Smrekar et al., 2010; Shalygin et al., 2015; Gülcher et al., 2020; Herrick and Hensley, 2023). Moreover, recent studies have shown that large amounts of magmatic intrusions could play a primary role in the lithospheric mobility and recycling on Venus, representing an efficient mechanism for heat loss (Lourenço et al., 2020; Smrekar et al.,

2023; Tian et al., 2023). Lastly, tomography investigations by Debayle et al. (2020) indicate that hotspots regions on Earth are associated with high melt content in the upper mantle. Particularly, partial melt is observed down to 250 km in Hawaii and 300 km under the east African rifts.

Following the well-established empirical relation between melt fraction φ and relative viscosity reduction η_r defined as

$$\eta_r = \exp(-\alpha\varphi), \tag{7.2}$$

with α being an experimentally defined constant, it is possible to estimate the amount of partial melt associated with the predicted LVZ (e.g., Hirth and Kohlstedt, 2003). Considering a basalt-eclogite system, α is constrained between about 25 and 30 for diffusion creep resulting in a melt fraction of about 5 to 11%, while for dislocation creep $\alpha \approx 30$ to 45 which corresponds to 3 to 9% of melt. These experimental constraints are valid for both dry and wet basalt compositions. Meanwhile, more recent experiments have shown that very small interconnected fractions of melt can have a significant impact on the viscosity (Takei and Holtzman, 2009; Holtzman, 2016), leading Holtzman (2016) to establish a new empirical law that reads

$$\eta_r = \exp\left[-\alpha\varphi - \ln(x_{\varphi_c})\,\mathrm{erf}(\varphi/\varphi_c)\right] \tag{7.3}$$

where φ_c is the critical melt fraction and x_{φ_c} is the viscosity reduction factor. These factor are associated with the geometry and connectivity of the grains and are determined experimentally. Because these experiments are still in early stages of development their values are still poorly constrained. Yet, taking $x_{\varphi_c} = 5$ and $\varphi_c = 10^{-4}$ as estimated by Takei and Holtzman (2009), the Venusian LVZ constraints would be consistent with less than 1% melt fraction. Figure 7.7 shows curves associating viscosity and melt for the two laws just described (eqs. 7.2 and 7.3). Finally, we note that the low viscosity zone and the possibly associated partial melt is not necessarily uniform throughout the planet. In fact, considering that the largest gravity and topography signatures come from the volcanic rises it is likely that their signatures dominate our analysis and that our results are mostly representative of these regions.

7.5.2 *Mantle Loads Parameterization*

Due to the lack of information regarding the density heterogeneities of the Venusian mantle we were required to make some simplifications to this regard. To assess the importance of these assumptions, we investigate further the two density anomaly parameterizations previously used in the Venus literature: a single thin mass-sheet (Figure 7.4a and 7.4b) and the depth-uniform loading (Figure 7.4c). Herrick and Phillips (1992) argued that, since plumes likely dominate the

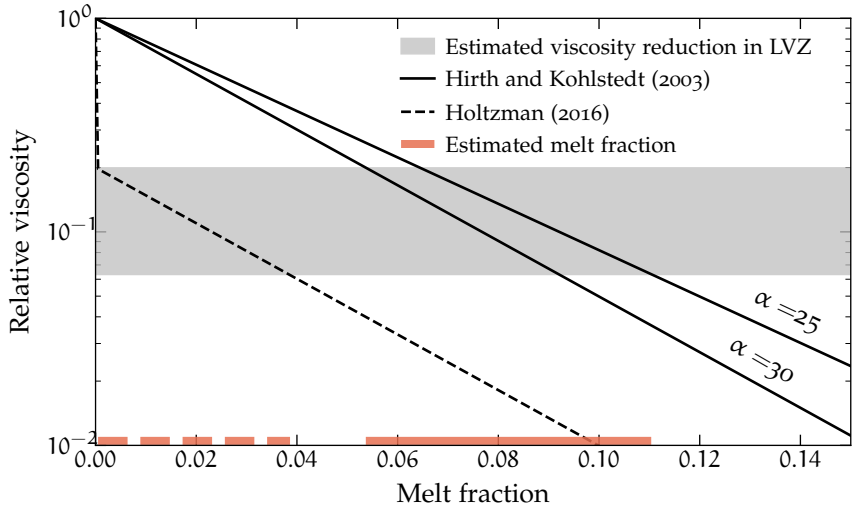

Figure 7.7: Relation between melt fraction and viscosity reduction. Solid black curves represent the melt-viscosity well-established empirical law presented in Hirth and Kohlstedt (2003) considering a basalt-eclogite diffusion creep rheology ($\alpha \approx 25$ to 30). The dashed black line represents a more recent melt-viscosity law by Holtzman (2016) that takes into account the role of very small fractions of melt in a well-connected network. For this curve, we adopt $x_{\varphi_c} = 5$ and $\varphi_c = 10^{-4}$ as estimated by Takei and Holtzman (2009). The orange horizontal lines indicate the amount of melt associated with our low viscosity zone constraints, corresponding to viscosity reduction of 5 to 16 times (represented by the gray area). The exponential law by Hirth and Kohlstedt (2003) indicates a melt fraction of 5% to 11% while the newer melt-viscosity law indicates smaller quantities, from 0.05% to 4%.

density anomaly distribution on Venus, most of the anomalies should be concentrated in a relatively thin and horizontally-spread layer associated with the plume head. In this scenario, a single mass-sheet parameterization would be more appropriate. On the other hand, Pauer et al. (2006), made a comparison to Earth's mantle density patterns, arguing that plumes and subducted slabs penetrate the mantle more or less vertically, indicating that a depth-independent distribution of density anomalies should be a reasonable first approximation.

Although the two different assumptions concerning the depth dependence of the density anomalies are opposing end-member scenarios, in practice we found that they do not substantially affect our results, in particular for the prediction of a low viscosity zone in the upper mantle. More significant differences, however, were obtained for the deep mantle. The single mass-sheet scenarios (Figure 7.4a and 7.4b) tend to accept a wide range of solutions for the fourth viscosity layer, with a large number of models consistent with an isoviscous mantle below the low viscosity zone. Moreover, about 35% of models present a viscosity decrease of over one order of magnitude from

layer 3 to 4, which would correspond to a basal low viscosity zone. If confirmed, these regions could be compared to large low-shear velocity provinces on the Earth (e.g., French and Romanowicz, 2015) or indicate partial melting (O'Rourke, 2020). In contrast, the depth-independent case (Figure 7.4c) requires an increase in viscosity in the mid mantle between the third and fourth layers. Interestingly, a comparable viscosity jump has been suggested for the Earth by several dynamic loading investigations (e.g., Forte and Peltier, 1991; Rudolph et al., 2015; Rudolph et al., 2020). These studies indicate an increase in viscosity at depths of about 800 to 1200 km, roughly corresponding to 960 to 1330 km on Venus, while we obtained a range of about 1300 to 1550 km. In any case, our results should motivate future studies to explore more realistic density anomaly distributions in Venus based on mantle convection simulations, or by using a more complex statistical distribution of mass anomalies as in Steinberger et al. (2010).

The predicted density anomaly distribution estimated for the nominal loading model with the largest likelihood is shown in Figure 7.8. As expected, at large volcanic rises, such as Atla and Beta Regiones, we observe negative density anomalies, associated with positive buoyancy and commonly interpreted as regions of mantle upwellings, hotspots and active volcanism (e.g., Kiefer and Hager, 1991; Stofan et al., 1995; Smrekar et al., 2010; James et al., 2013). These anomalies are generally also correlated with regions of high heat flow (Smrekar et al., 2023) and with regions where coronae could be still active (Gülcher et al., 2020). Alternatively, positive density anomalies correlate with volcanic plains which can interpreted as regions of mantle downwellings. These results are consistent with the density anomaly distributions found in previous studies (Herrick and Phillips, 1992; Pauer et al., 2006; James et al., 2013). Moreover, we note that the different loading scenarios investigated here have comparable density distribution patterns, although for the $\delta\rho$-constant case the shorter wavelengths present relatively higher amplitudes (Herrick and Phillips, 1992).

7.6 CONCLUSIONS

Our study used a Bayesian approach to investigate the mantle viscosity structure of Venus. We made use of a dynamic loading model to predict the planet's long-wavelength gravity and topography and compared these predictions to the observations. Using a range of model scenarios, we consistently found that Venus presents a low viscosity zone in the uppermost mantle, a layer that could be interpreted as an Earth-like asthenosphere, potentially originated from partial melt in the upper mantle. This interpretation corroborates previous studies that propose that Venus is currently an active volcanic world (e.g., Smrekar et al., 2010; Herrick and Hensley, 2023; Gülcher et al.,

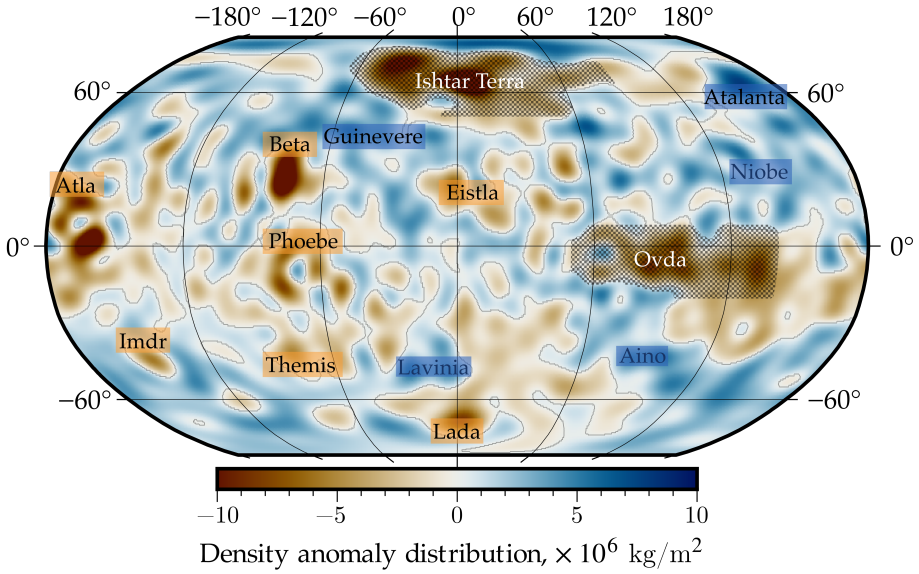

Figure 7.8: Distribution of mantle density anomalies associated with the best fitting model for the nominal loading scenario. In this model, a single mass-sheet is located at 223 km depth. Negative density anomalies correlate with volcanic rises while volcanic plains are associated with positive anomalies. For reference, some major geologic features are labeled. Text with an orange background indicates volcanic rises, while a blue text background indicates planitias. Cross-hatched regions of Ovda Regio and Ishtar Terra should be ignored as they were excluded from our localized spectral analysis.

2020; Rolf et al., 2022). Moreover, our inversions disfavor a viscosity jump associated with the phase transition at ~ 700 km depth.

One aspect that merits further investigation is how more realistic distributions of density anomalies in the mantle would affect the predicted viscosity profile. For example, one could use geodynamic simulations to estimate the density distribution based on temperature anomalies predicted by these models. Finally, improvements on deep interior constraints for Venus could be achieved by coupling dynamic loading to tidal deformation investigations. In particular, an integrated analysis would allow for an assessment of the absolute mantle viscosity profile.

Part IV

CONCLUSION

8 CONCLUSION

8.1 OVERVIEW

Over the past three years, I have investigated the gravity and topography of Venus with the goal of better understanding the planet's interior structure. By applying modern spatio-spectral localization techniques to past datasets and by performing inversions adopting analytical flexural- and dynamic-loading models, I derived important geophysical parameters of the planet. In particular, I presented robust estimates for the crustal and elastic thickness of the crustal plateaus and new insights about the viscosity structure of Venus's mantle.

Corroborating previous interpretations, my results show that the topography of most plateaus is predominantly supported by crustal thickening. The elastic thickness was constrained to be less than 35 km with a best-fitting average of 15 km, confirming that these regions are consistent with a regime close to Airy isostasy. The elastic thickness constraints were used to estimate the lithospheric thermal gradient, which suggests that the formation of plateaus probably occurred under higher temperature conditions than the current global average. The crustal thickness of the plateaus on average range from 15 to 34 km, however, the crustal roots can reach down to more than 40 km depth. These estimations indicate that the crustal thicknesses of these highlands are similar to that of Earth's continental crust. In addition, assuming that the plateaus are in Airy isostasy, the plains surrounding the plateaus are estimate to have a crustal thickness of about 20 km. Considering that the volcanic plains have a smooth topography and correspond to ~70% of the surface of Venus, this value represents a fair estimate of the planet's average crustal thickness.

By analyzing the long-wavelength gravity and topography of Venus as expressions of mantle convection, I was able to obtain new constraints on the viscosity structure of the planet. The main result from this study was the identification of a low viscosity zone in the uppermost mantle. The zone starts directly below the lithosphere at about 100 km depth and is roughly 235 km thick. It is further characterized by a viscosity reduction of 5—15 times with respect to the underlying mantle. Drawing a parallel with the Earth, the low viscosity zone was interpreted as a Venusian version of the asthenosphere. At this point, I tend to favor the hypothesis that the reduced viscosity is associated with partial melting, supporting the interpretation that Venus is a geologically active world predominantly governed by ongoing

magmatic processes. Yet, their are other possible explanations should be further investigated.

Table 8.1 presents a comparison between interior properties of the terrestrial planets. Venus, as the Earth, has a relatively thin lithosphere, indicating that the interior of the planet is still hot and conceivably active. In addition, the crusts of Venus and Earth make up a similar volume fraction of the silicate portion of the planet, suggesting that the two planets might produce and recycle crustal materials at similar rates. Hence, overall, the results presented here show that Venus's internal structure is significantly more similar to Earth's than to the other terrestrial planets of the solar system and are consistent with the increasingly more accepted interpretations that Venus is a geologically active world today (e. g. Smrekar et al., 2010; Gülcher et al., 2020; Herrick and Hensley, 2023). On the other hand, the geological evolution of Venus has been quite different from that of the Earth. This divergent evolutionary path, however, is poorly understood and several fundamental question remain unanswered. For how long has Venus been this hellish planet? Was the current crushing atmosphere emplaced by recent geological events? Or did it develop early in the planet's history? Did Venus ever have liquid water on its surface? How does Venus lose its heat and how does this influence the planet's thermal evolution?

With these questions in mind, the next areas of my research will focus on the implications of the interior structure constraints for the geodynamics and thermal evolution of Venus. In sections 8.2 and 8.3, I outline ongoing studies which represent first steps towards this goal. At the same time, groundbreaking improvements in our understanding of Venus imperatively depend on the acquisition of higher-quality data by new missions to the planet. Section 8.4 is dedicated to the future of Venus exploration and how it will help us investigate the interior structure and evolution of our twin planet.

8.2 PHASE TRANSITIONS OF THE VENUSIAN CRUST: IMPLICATIONS FOR INTERIOR STRUCTURE AND DYNAMICS

This section is a summary of the study by Collinet, Maia, et al. (in prep)

In Chapter 6, I have briefly discussed thermodynamical processes that could occur at large crustal depths under the crustal plateaus due to high pressures and temperatures. Essentially, for small lithospheric thermal gradients ($\lesssim 10\,\mathrm{K\,km^{-1}}$), basaltic crustal materials can transition into eclogite. This transition generates a negative buoyancy of the crust and can lead to crustal delamination. Alternatively, for higher thermal gradients, the crust typically starts to melt before the formation of eclogite. These processes have a significant impact on the bulk properties of Venus's crust and have major implications for the geodynamics of the planet. However, the precise conditions for their

Table 8.1: Comparison of crustal and lithospheric properties of the terrestrial planets. The table presents estimated average values of the crustal thickness, the volume of the crust with respect to the total silicate volume of the planet (crust+mantle), and the thermal lithosphere thickness. The total silicate volume was computed as the difference between the total volume and the core volume. Uncertainties can be found in the original studies listed below the table.

Planet	Crustal thick.	Crust silicate vol.	Lithosphere thick.
Earth	O: 6 km C: 40 km	1%	O: 70 km C: 200 km
Venus	20 km	1%	100 km
Mars	57 km	6%	500 km
Mercury	35 km	10%	–
Moon	38 km	6%	700 km

Earth – Crustal thickness and core radius: Turcotte and Schubert (2002), Lithosphere thickness: Karato (2012). O=oceanic, C=continental.
Venus – This thesis.
Mars – Crustal thickness: Wieczorek et al. (2022), lithosphere thickness: Khan et al. (2021), core radius: Stähler et al. (2021).
Mercury – Crustal thickness: Watters et al. (2021), core radius: Hauck et al. (2013).
Moon – Crustal thickness; Wieczorek et al. (2013), lithosphere thickness: Gagnepain-Beyneix et al. (2006), core radius: Garcia et al. (2011).

occurrence and the characteristics of the generated products still need to be comprehensively investigated.

The goal of this study is to perform a robust analysis of these thermodynamical processes under Venus conditions. The resulting mineral phases depend on several geological and geophysical properties of the system besides the crustal thickness, including the thermal gradient of the lithosphere, the presence of volatiles, and, of course, the composition of the crust. As discussed in earlier chapters, the crust of Venus is primary composed of basalts (e. g., Abdrakhimov and Basilevsky, 2002), although low emissivity anomalies indicate that tessera regions could perhaps have a felsic composition (Gilmore et al., 2015). The volatile content of the crust is poorly constrained. Yet, the high surface temperatures are probably more consistent with dry materials. In addition, according to lithospheric-scale numerical modeling, strong dry rheologies are necessary to develop rifts under Venus temperature conditions (Regorda et al., 2023). Hence, this analysis is, for now, focused on dry compositions. Temperature gradient estimates for Venus have only been obtained indirectly, mostly from elastic thickness constraints (e. g. O'Rourke and Smrekar, 2018; Borrelli et al., 2021; Maia and Wieczorek, 2022; Smrekar et al., 2023). A compilation of these results is shown in Figure 8.1.

Features such as coronae and rifts are commonly associated with high temperature gradients, with median values of 13 and 19, respectively (O'Rourke and Smrekar, 2018; Smrekar et al., 2023). According to Smrekar et al. (2023), the large values suggest that these regions are associated with anomously high heat flows linked to ongoing geologic activity. The plateaus are also associated with high temperature gradients, of about $14\,\mathrm{K\,km^{-1}}$. However, a discussed in Chapter 6, these estimates are probably not representative of present-day conditions. The steep-sided domes, investigated by Borrelli et al., 2021, typically have more moderate temperature gradients. These authors make a distinction between the domes near coronae, that tend to have high temperatures, and the more isolated ones. For the later group, the median thermal gradient is $8\,\mathrm{K\,km^{-1}}$, which is more inline with temperature gradients predicted by thermal evolution models (e. g. O'Rourke and Korenaga, 2015).

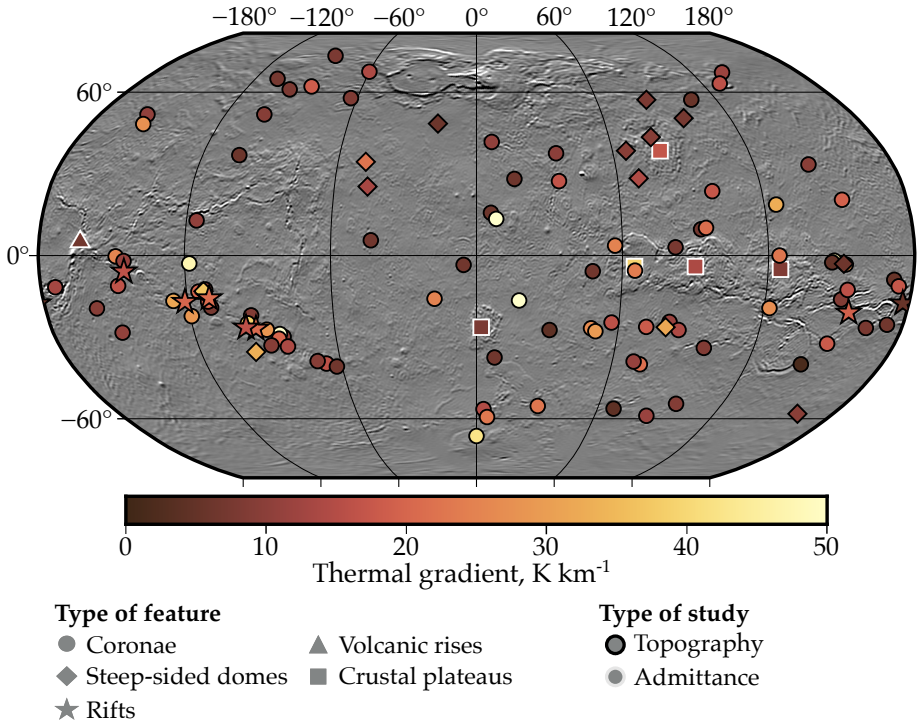

Figure 8.1: Estimations of thermal gradients from elastic thickness constraints for several features on Venus. The type of feature is indicated by the marker shape. Elastic thickness estimations based on admittance have markers with white contours while studies that analyzed topographic flexure have black contours. The map is presented in a Robinson projection. The elastic thickness estimates are from the following studies. Coronae: O'Rourke and Smrekar (2018) and Smrekar et al. (2023), steep-sided domes: Borrelli et al. (2021), Volcanic rises: Phillips (1994), and Crustal plateaus: Maia and Wieczorek (2022).

Making use of the thermodynamic calculation package Perple_X (Connolly, 2005) and the database by Holland et al. (2018), we es-

timate the phase assemblages, solidus, and density for a range of crustal compositions. We consider the basalt composition measured by the Vega 2 lander (Figure 1.3), average basaltic andesites (Schmidt and Jagoutz, 2017), andesites (Grove et al., 2004), and Earth's upper continental crust (Rudnick and Gao, 2003). Figure 8.2 shows the effect of phase transition on the density of these compositions with respect to pressure for thermal gradients of (a) $5\,\mathrm{K\,km^{-1}}$, (b) $10\,\mathrm{K\,km^{-1}}$, and (c) $15\,\mathrm{K\,km^{-1}}$.

For all compositions, the density starts increasing when feldspar starts being transformed into garnet+pyroxene, and restabilizes when there in no more feldspar in the system. The depth at which the transitions is initiated is about 20 km shallower for basalts than for the more evolved compositions, however, their dependence on temperature is minor. Alternatively, the solidus is weakly dependent on composition. For a thermal gradient of $10\,\mathrm{K\,km^{-1}}$, melting starts at about 70 km depth, while $15\,\mathrm{K\,km^{-1}}$ gradients generate melts at 40–50 km depth. In the case of even higher thermal gradients, larger than $20\,\mathrm{K\,km^{-1}}$, there would be extensive melting at about 20–30 km depth. The density strongly depends on composition, both before and after phase transitions. Interestingly, the metamorphosed crust only becomes denser than the mantle for basaltic compositions.

These results have significant impact on the possibility of crustal delamination in regions with large crustal thicknesses, such as the plateaus. In the case of low thermal gradients, negative buoyancy and possible delamination can only occur for basaltic compositions. In the case of more silicic rocks, the eclogite phase transition does not limit the thickness of the crust. If thermal gradients are in the range of about 10 to 15 $\mathrm{K\,km^{-1}}$, regions with thick crusts generate melts of felsic or intermediate compositions, depending on the original rock composition and the amount of melt produced. Hence, intermediate to felsic crust production in the deepest roots of crustal plateaus on Venus is likely, but this material would not be recycled via delamination. On the other hand, If melts are extracted, residues are denser than the mantle and can be recycled (delaminated). Finally, regions associated with very high thermal gradients, which can be the case for coronae and rifts at present day, are plausibly associated with crustal melting and should have crusts thinner than about 20 km.

8.3 COUPLING GEODYNAMIC SIMULATIONS TO GEOPHYSICAL OBSERVATIONS

This section presents early stages of a study by Maia, Plesa, and Wieczorek, started during a visiting period at the DLR, Berlin.

Global geodynamic models allow for the prediction of interior structure properties and how they evolve through time as the planet cools down. As opposed to the analytical dynamic loading approach used so far in this thesis, the numerical models can account for a lot of complexity, including melting and non-linear mantle rheologies, such as

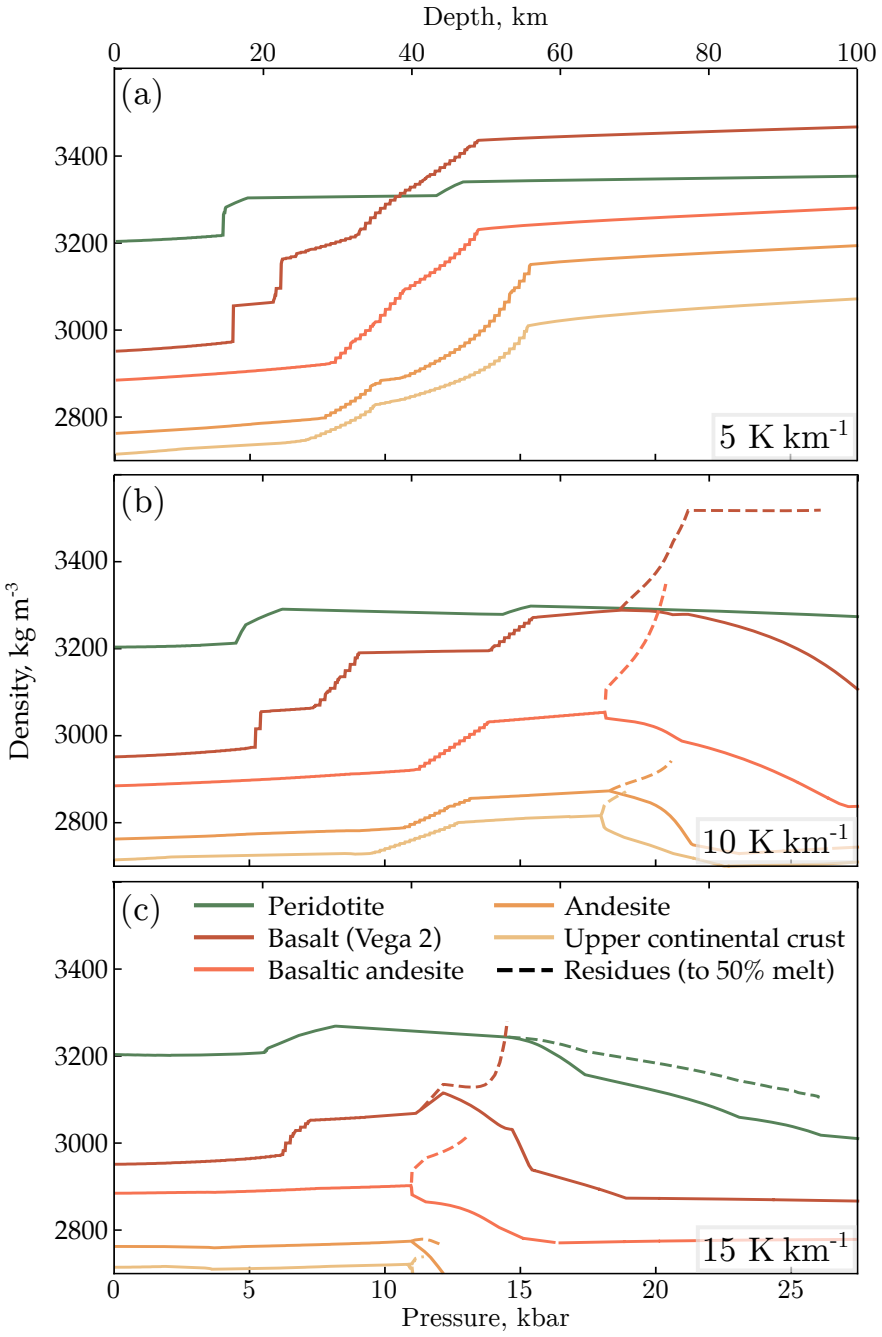

Figure 8.2: Impact of phase changes in the density for different rock compositions and different temperature gradients. The orange shades represent the composition of typical crustal rocks, either Venus basalts (measurements from Vega 2) or representative compositions of evolved terrestrial rocks. The green curve represents an Earth-like mantle composition. The dashed lines indicate that the rock is partially melted. The subplots correspond to different temperature gradient of (a) $5\,\mathrm{K\,km^{-1}}$, (b) $10\,\mathrm{K\,km^{-1}}$, and (c) $15\,\mathrm{K\,km^{-1}}$. Courtesy of M. Collinet.

diffusion and dislocation creep. My plan for this project is to pair the numerical models to the analytical ones in order to add some complexity to the problem while still being able to perform inversions.

In this scenario, I have recently started working with such geodynamic models, in particular with the mantle convection code Gaia (Hüttig and Stemmer, 2008). The first step of this study was to use the average viscosity profiles predicted by the thermal evolution models and estimate the associated gravity and topography using the dynamic loading model by Hager and Clayton (1989). Making use of two-dimensional stagnant-lid models, I have investigated different parameters that affect the viscosity profile, including the mantle reference viscosity η_0, the addition of viscosity jumps, and the activation volume V_a, a rheology parameter that controls how much the viscosity increases with depth. The viscosity dependency on pressure and temperature follows the so-called Arrhenius equation:

$$\eta = \eta_0 \exp\left(\frac{E_a + pV_a}{\mathcal{R}T_m}\right) \tag{8.1}$$

where E_a is the activation energy, p is the pressure, T_m is the temperature of the convecting fluid, and $\mathcal{R}$ is the universal gas constant. Note that I am only considering the case of diffusion creep rheology. For simplicity, in this section I focus the analysis on the activation volume and all models presented have $\eta_0 = 10^{21}$ Pa s and $E_a = 375\,\mathrm{kJ\,mol^{-1}}$. More details on mantle rheology laws and geodynamic modeling in general can be found in several review works, such as Schubert et al. (2004), Breuer and Moore (2015), and Gerya (2019).

Figure 8.3 shows the resulting viscosities and estimated spectral admittances from some of the performed models. Panel (a) presents an example of the structure of temperature anomalies in the mantle at the final state of the planet's thermal evolution (4.5 Gy), considering an activation volume of $6 \times 10^{-6}\,\mathrm{m^3/mol}$. Panel (b) shows the laterally averaged radial viscosity profile of the model presented in panel (a) in brown, as well as viscosity profiles for models with $V_a = 12 \times 10^{-6}\,\mathrm{m^3/mol}$ (orange curve) and with the addition of a viscosity jump (dark red curve). For this preliminary study, I considered only a viscosity jump of one order of magnitude placed at 300 km depth, following the constraints obtained in Chapter 7. Panel (c) shows the discretized versions of the profiles from (b), which are then used in the dynamic loading model to compute the associated gravity and topography. Panel (d) presents the modeled spectral admittance based on the three viscosity profiles. As we can see, larger activation volumes, which cause a larger increase in viscosity with depth, tend to vertically shift the admittance towards higher values, while the addition of a viscosity jump mostly impacts the shape of the curve.

Interestingly, the final radial temperature profiles of these stagnant lid models are roughly the same for a fixed reference viscosity, i. e.,

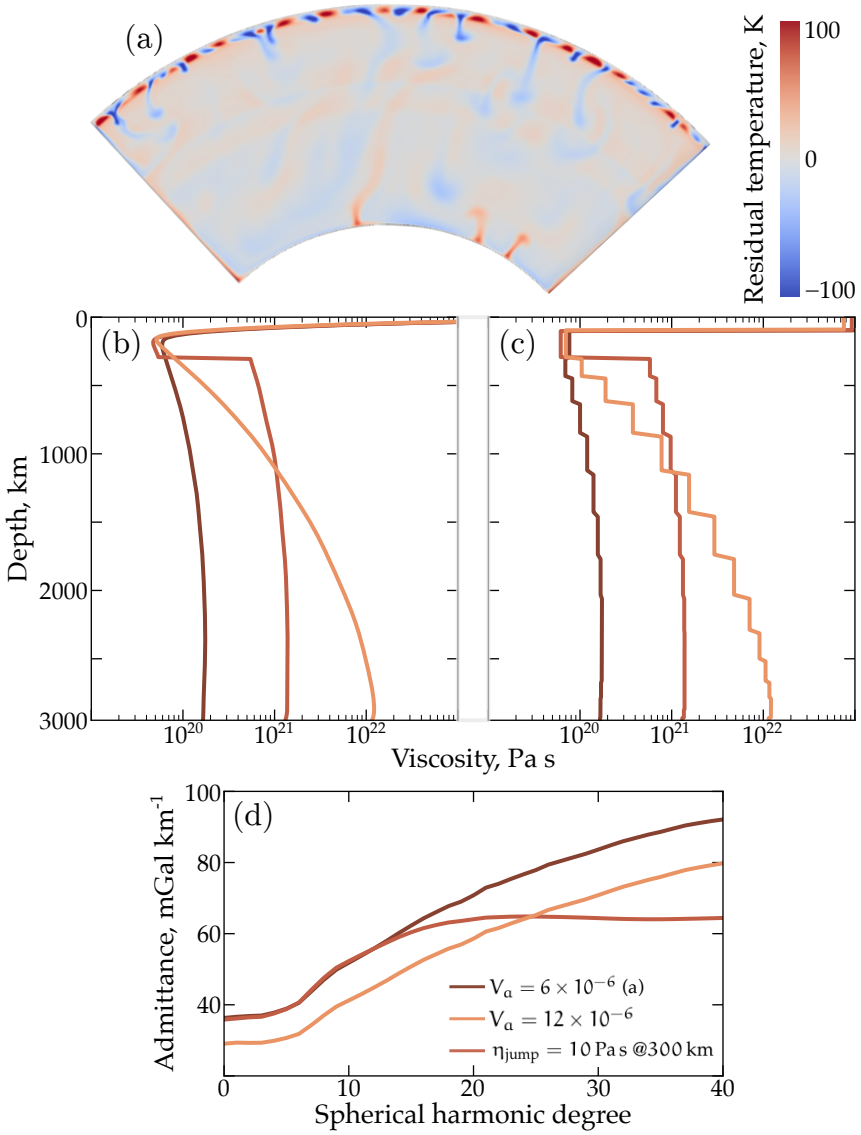

Figure 8.3: Geodynamic models of Venus. (a) Mantle temperature anomalies from a two-dimensional geodynamic model of Venus's thermal evolution at its final state (4.5 Gy). The model adopts a reference viscosity of 10^{21} Pa s and activation volume of 6×10^{-6} m^3/mol. (b) Radial profiles of horizontally averaged viscosities of the model presented in (a), along with the viscosity profiles for models with $V_a = 12 \times 10^{-6}$ m^3/mol and with the addition of a viscosity jump. (c) Discretized versions of viscosity profiles from (b) which are used to compute dynamic gravity and topography. (d) Predicted spectral admittances associated with the viscosity profiles from (c), considering that the density anomalies are concentrated in a thin mass-sheet placed at 250 km depth (see Section 5.2 for details on the dynamic loading model).

they are independent of the activation volume or the addition of viscosity jumps. This property is illustrated in Figure 8.4, where the temperature profiles (Panel a) and viscosity profiles (Panel b) are shown

for six different models with varying activation energies and with the addition of a viscosity jump at 300 km depth. Hence, as shown in Panel (c), we can apply eq. 8.1 to the temperature profiles with the appropriate rheology parameters and reproduce the viscosity profiles from the models fairly well. This attribute is very useful from the perspective of geophysical inversions, since it shows that it is not necessary to run a full thermal evolution model to estimate each viscosity profile. Instead, one is able to compute mantle viscosity structures based on a single temperature profile by simply applying eq. 8.1.

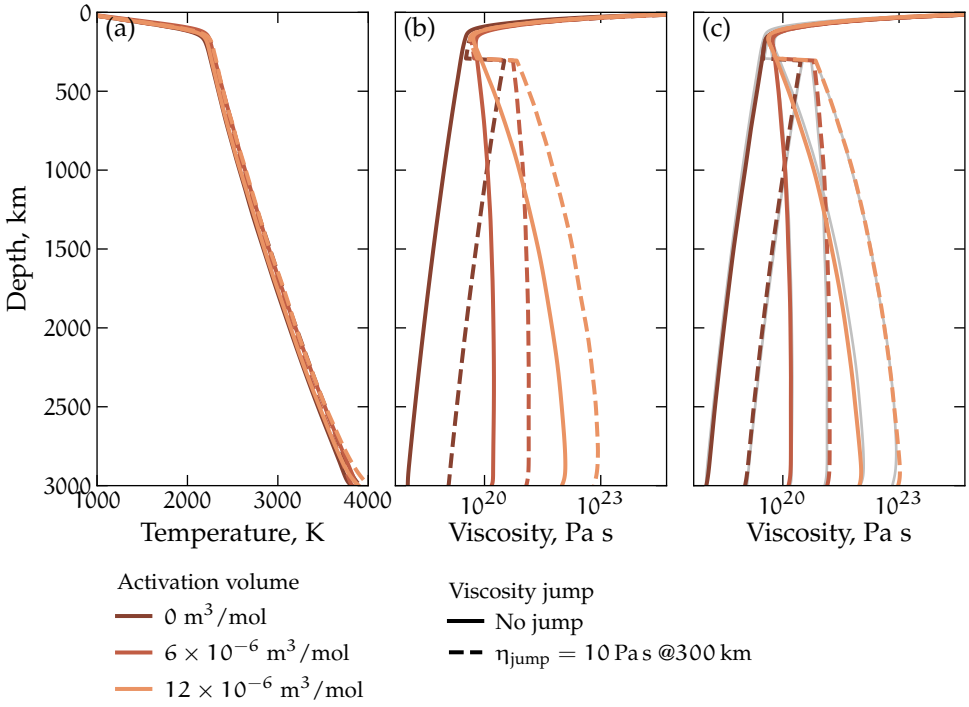

Figure 8.4: Average temperature and viscosity radial profiles from thermal evolution models at 4.5 Gy for various activation volumes and the addition of a viscosity jump at 300 km depth. (a) Horizontally-averaged temperature profiles, (b) horizontally-averaged viscosity profiles, (c) viscosity profiles estimated from the temperature profiles from panel (a) using eq. 8.1. For comparison, the original average viscosity profiles are also plotted in (c) in light gray.

Figure 8.5 shows viscosity profiles based on the temperature profile from Figure 8.4a considering a broad range of activation volume values, varying from 0 to 15×10^{-6} m^3/mol, and considering structures with (panel b) and without (panel a) viscosity jumps. Panel (c) and (d) show the estimated spectral admittances based on the viscosity profiles shown in panels (a) and (b) respectively. The activation volume and the addition of viscosity jumps have significant impact on the admittance models. Viscosity profiles that include the viscosity jump tend to better predict the observed admittance, in particular for activation volumes from about 6×10^{-6} to 8×10^{-6} m^3/mol.

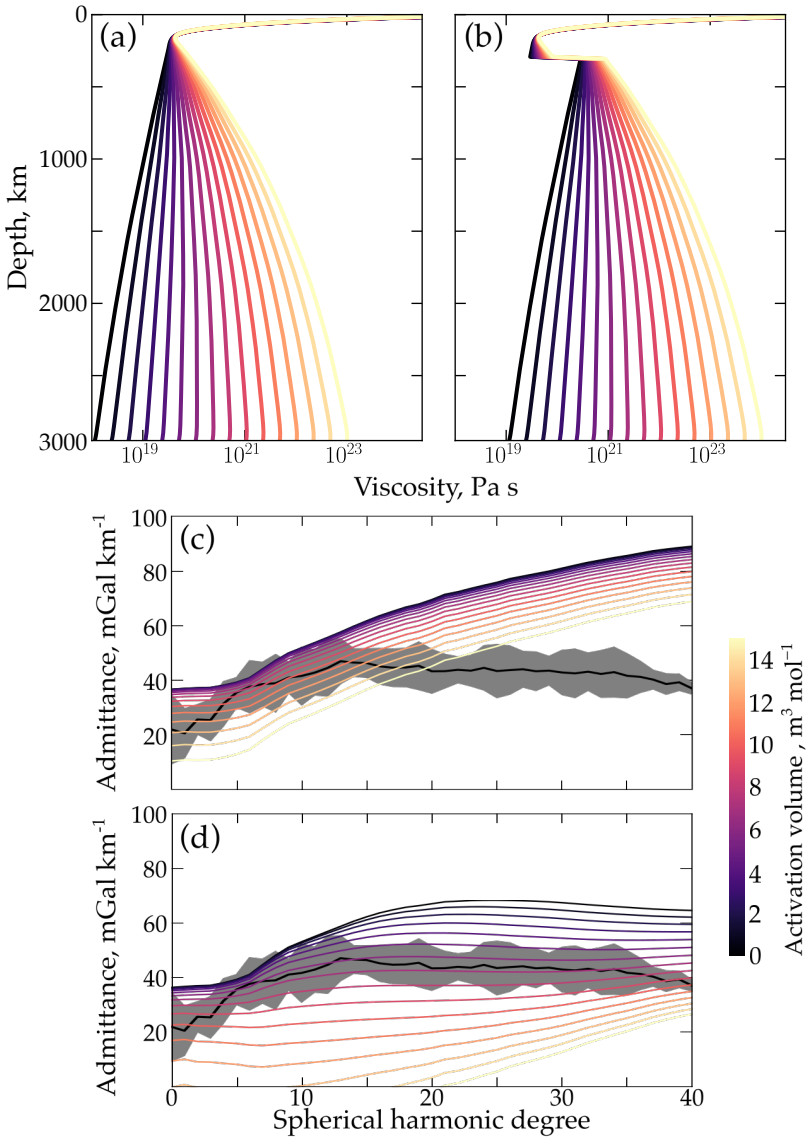

Figure 8.5: Predicted admittance based on viscosity profiles with a large range of activation volumes. (a) Temperature- and pressure-dependent radial viscosity profiles (eq. 8.1) with activation volume varying from 0 to $15 \times 10^{-6}\,\mathrm{m}^3/\mathrm{mol}$. (b) Same as (a)but after increasing the viscosity by a factor of 10 at 300 km depth. Panel (c) shows the predicted spectral admittance based on the viscosity profiles from (a) while panel (d) shows the admittances based on the profiles from (b). The black curve and the gray area correspond to the observed localized admittance and uncertainty, respectively. The admittances are modeled considering a single mass-sheet placed at 250 km depth.

These results are promising as they indicate that the gravity and topography signatures can be used to constrain rheologic properties of the mantle. Next, I plan to further test the sensitivity of the dynamical loading model to other rheologic parameters and start performing inversions using these pressure- and temperature-dependent viscos-

ity profiles. Finally, I would like to explore different approaches to parameterize the distribution of density anomalies in the mantle, beyond the mass-sheet and the continuous distribution scenarios presented in Chapter 7. In particular, I plan to test the method adopted by Steinberger (2002) and Steinberger et al. (2010), which randomly samples the spherical harmonic coefficients of the mantle density anomalies from a distribution that dependents on the power spectrum of seismic tomography constraints. However, along with testing the tomography constraints, I would also adopt the density distributions predicted by thermal evolution models.

8.4 THE DECADE OF VENUS

In June 2021, NASA made its latest discovery class mission announcement. At that time, there were four mission concepts competing for selection, two of them targeting Venus: an orbital mission called Venus Emissivity, Radio Science, InSAR, Topography And Spectroscopy (VERITAS), which will study the surface and interior of the planet, and the Deep Atmosphere Venus Investigation of Noble gases, Chemistry, and Imaging (DAVINCI) mission, focusing on in situ atmospheric investigations. Expectations were high – as we well know, NASA's last mission to Venus had been launched over 30 years before. Both VERITAS and DAVINCI had already been turned down in the discovery class selection round in 2017 and "We need better data" became a traditional motto of conference talks about Venus.

Hence, it was with great excitement and surprise that the community received the news that both Venus missions had been selected in 2021. Even more surprising was the announcement by ESA one week later confirming that its fifth medium-class mission would be the Venus orbiter EnVision. With these three missions scheduled to launch between 2029 and 2031, the 2030s are already being referred to as "the decade of Venus".

The DAVINCI mission, scheduled for launch in 2029, will perform two Venus flybys in 2030 to obtain context observations of Venus's atmosphere and cloud deck dynamics, followed by the atmospheric entry of a descent sphere in 2031, which will focus on performing in situ measurements of the atmosphere above Alpha Regio. With four atmosphere-dedicated instruments, the descent sphere will operate for about one hour, taking measurements from 70 km altitude down to the surface and providing a comprehensive dataset of chemical and isotopic composition of Venus's atmosphere. In addition, the probe is equipped with a near-infrared descent imager that will obtain images of Alpha tessera terrains with a resolution ranging from about $200\,\mathrm{m\,pixel^{-1}}$ to less than $1\,\mathrm{m\,pixel^{-1}}$ as it approaches the surface. This data set will be used to create a high-resolution digital elevation model and will provide insights into the composition of tessera. De-

tails on DAVINCI's instruments, operations, and science objectives can be found in Garvin et al. (2022).

The VERITAS mission (Smrekar et al., 2022) will obtain global coverage of SAR imaging and altimetry data with unprecedented resolution. The topography dataset will have a horizontal resolution of 250 m, up to 100 times higher than what was obtained by Magellan, and the SAR images will have a resolution of 30 m pixel^{-1}, about 10 times larger than Magellan's resolution. In addition, the instrument will perform repeat-pass interferometry in target areas with 2 cm precision, allowing for a direct detection of geological activity. The spacecraft will further carry an infrared emissivity mapper (VEM) developed over the heritage of VIRTIS (Venus Express) but with a significant increase in the signal-to-noise ratio and a total of six spectral bands instead of one. The new emissivity data, which will cover about 70% of the planet, will dramatically improve our knowledge about Venus's surface composition (Dyar et al., 2020).

EnVision is an ESA-led orbital mission designed to holistically investigate the planet using 5 scientific instruments. Three spectrometers that compose the VenSpec suite (Helbert et al., 2019): a UV spectrometer focused on studying sulfur species and cloud dynamics (VenSpec-U), an infrared spectrometer that will investigate composition anomalies in the atmosphere potentially related to the volcanic activity (VenSpec-H), and the VenSpec-M, a sibling instrument of VEM, which will focus on mapping the surface composition. The spacecraft also carries a ground penetrating radar that should be able to map the subsurface down to a few hundreds of meters (Bruzzone et al., 2020), and a synthetic aperture radar that will provide imaging and altimetry data. As opposed to VERITAS, EnVision will have a focused observation strategy, with a mapping coverage that will vary from place to place. For example, SAR imaging will cover 30% of the planet with 30 m resolution and 2% of the planet with 10 m resolution (Widemann et al., 2022).

Lastly, both VERITAS and EnVision will perform radio tracking experiments, greatly improving Venus's gravity solution. These datasets are over-due. Even though Magellan provided one of the highest, if not the highest, resolution gravity model of its time in the context of planetary sciences, today, Venus has one of the lowest-quality gravity datasets among the terrestrial planets. VERITAS and EnVision will provide models with average degree strength of about 130, corresponding to a spatial resolution of ~145 km. Yet, the spatial variation of the degree strength for the two missions is considerably different due to their distinct orbital settings. The circular orbit of VERITAS in the gravity phase helps limiting the spatial variability of the data resolution (Mazarico et al., 2023). On the other hand, EnVision has an elliptical polar orbit with altitude ranging between 220 and 515 km resulting in slightly larger degree strength variation primarily in the

latitude direction (Rosenblatt et al., 2021). Yet, EnVision should get a somewhat better resolution near the north pole. Moreover, both missions will dramatically improve the constraints of the tidal love number k_2, the tidal phase lag, and the moment of inertia factor (Cascioli et al., 2021; Rosenblatt et al., 2021).

These new datasets will be of utmost importance for our understanding of Venus geodynamic evolution and its differences from the Earth. The high-resolution gravity data will allow for more precise estimations of the crustal and elastic lithosphere thickness all over the planet at much finer scale than what is possible with Magellan data. Hence, we will be able to better characterize the spatial and potentially temporal variations of Venus's surface heat flow and heat loss mechanisms, notably by coupling the geophysical constraints to thermal evolution models. Furthermore, it will likely be possible to determine the bulk density of the crust and how it varies from place to place. This type of analysis would be remarkably useful to investigate if the crustal plateaus indeed have a felsic composition. In addition, with the precise tidal-related constraints obtained by the two missions, we will finally probe the deep interior of Venus. This data will allow for an accurate determination of the state and size of Venus's core, as well the composition and the absolute viscosity of the mantle (Dumoulin et al., 2017). In particular, it would be interesting to jointly investigate the tidal deformation and the dynamic loading signatures of gravity and topography to comprehensively characterize the geophysical properties of Venus's mantle. Undoubtedly, the new missions will play fundamental roles towards a better understanding of the complex geological history of our twin planet. "We need better data" – we will soon have it!

Part V

APPENDIX

A

REAL SPHERICAL HARMONICS AND LEGENDRE FUNCTIONS

When dealing with gravitational and geodesic applications the real spherical harmonics are generally used to represent functions on the sphere. They are defined as

$$Y_{\ell m}(\theta,\phi) = \begin{cases} \bar{P}_{\ell m}(\cos\theta)\cos m\phi, & \text{if } m \geqslant 0 \\ \bar{P}_{\ell|m|}(\cos\theta)\sin|m|\phi, & \text{if } m < 0 \end{cases} \tag{A.1}$$

where $\bar{P}_{\ell m}$ is the associated Legendre function. The normalized Legendre functions are given by

$$\bar{P}_{\ell m}(\mu) = \sqrt{(2-\delta_{0m})(2\ell+1)}\sqrt{\frac{(\ell-m)!}{(\ell+m)!}}P_{\ell m}(\mu) \tag{A.2}$$

with δ_{ij} being the Kronecker delta function and $P_{\ell m}$ the standard associated Legendre function

$$P_{\ell m}(\mu) = \frac{1}{2^\ell \ell!}\left(1-\mu^2\right)^{m/2}\left(\frac{d}{d\mu}\right)^{\ell+m}\left(\mu^2-1\right)^\ell. \tag{A.3}$$

A useful property of the spherical harmonic functions is their orthogonality over both ℓ and m. In the case of the 4π-normalization convention, it reads:

$$\int_{\theta,\phi} Y_{\ell m}(\theta,\phi)Y_{\ell' m'}(\theta,\phi)\sin\theta d\theta d\phi = 4\pi\delta_{\ell\ell'}\delta_{mm'}. \tag{A.4}$$

Then, the spherical harmonic coefficients $f_{\ell m}$ of an arbitrary function f can be computed as

$$f_{\ell m} = \frac{1}{4\pi}\int_{\theta,\phi} f(\theta,\phi)Y_{\ell m}(\theta,\phi)\sin\theta d\theta d\phi. \tag{A.5}$$

This equation can be obtained by multiplying equation 3.1 by $Y_{\ell' m'}$ and integrating over all space. A similar relation can be found in the case of the spatially localized function $\mathcal{F}$ (see Section 3.3 for details):

$$\mathcal{F}_{\ell m} = \frac{1}{4\pi}\int_{\theta,\phi} f(\theta,\phi)w(\theta,\phi)Y_{\ell m}(\theta,\phi)\sin\theta d\theta d\phi. \tag{A.6}$$

BIBLIOGRAPHY

Abdrakhimov, A. M. and A. T. Basilevsky (2002). In: *Solar System Research* 36.2, pp. 136–159. URL: https://doi.org/10.1023/a:1015222316518.

Airy, G. (1855). "III. On the computation of the effect of the attraction of mountain-masses, as disturbing the apparent astronomical latitude of stations in geodetic surveys." In: *Philosophical Transactions of the Royal Society of London* 145, pp. 101–104. URL: https://doi.org/10.1098/rstl.1855.0003.

Aitta, A. (2012). "Venus' internal structure, temperature and core composition." In: *Icarus* 218.2, pp. 967–974. URL: https://doi.org/10.1016/j.icarus.2012.01.007.

Aki, Keiiti, Anders Christoffersson, and Eystein S. Husebye (1977). "Determination of the three-dimensional seismic structure of the lithosphere." In: *Journal of Geophysical Research* 82.2, pp. 277–296. URL: https://doi.org/10.1029/jb082i002p00277.

Albert, Richard A. and Roger J. Phillips (2000). "Paleoflexure." In: *Geophysical Research Letters* 27.16, pp. 2385–2388. URL: https://doi.org/10.1029/2000GL011816.

Alexandrov, Yu. N. et al. (1986). "Venus: Detailed Mapping of Maxwell Montes Region." In: *Science* 231.4743, pp. 1271–1273. URL: https://doi.org/10.1126/science.231.4743.1271.

Anderson, Don L. and Hartmut Spetzler (1970). "Partial melting and the low-velocity zone." In: *Physics of the Earth and Planetary Interiors* 4.1, pp. 62–64. URL: https://doi.org/10.1016/0031-9201(70)90030-0.

Anderson, F. Scott and Suzanne E. Smrekar (2006). "Global mapping of crustal and lithospheric thickness on Venus." In: *Journal of Geophysical Research* 111.E8, E08006. URL: https://doi.org10.1029/2004JE002395.

Armann, Marina and Paul J. Tackley (2012). "Simulating the thermochemical magmatic and tectonic evolution of Venus's mantle and lithosphere: Two-dimensional models." In: *Journal of Geophysical Research: Planets* 117.E12, n/a–n/a. URL: https://doi.org/10.1029/2012je004231.

Audet, Pascal (2014). "Toward mapping the effective elastic thickness of planetary lithospheres from a spherical wavelet analysis of gravity and topography." In: *Physics of the Earth and Planetary Interiors* 226, pp. 48–82. URL: https://doi.org/10.1016/j.pepi.2013.09.011.

Avduevsky, V. S., M. Ya Marov, M. K. Rozhdestvensky, N. F. Borodin, and V. V. Kerzhanovich (1971). "Soft Landing of Venera 7 on the

Venus Surface and Preliminary Results of Investigations of the Venus Atmosphere." In: *Journal of the Atmospheric Sciences* 28.2, pp. 263–269. URL: https://doi.org/10.1175/1520-0469(1971)028<0263:slovot>2.0.co;2.

Azuma, Shintaro, Ikuo Katayama, and Tomoeki Nakakuki (2014). "Rheological decoupling at the Moho and implication to Venusian tectonics." In: 4.1. DOI: 10.1038/srep04403. URL: https://doi.org/10.1038/srep04403.

Barath, F. T., A. H. Barrett, J. Copeland, D. E. Jones, and A. E. Lilley (1964). "Symposium on Radar and Radiometric Observations of Venus during the 1962 Conjunction: Mariner 2 microwave radiometer experiment and results." In: *The Astronomical Journal* 69, p. 49. URL: https://doi.org/10.1086/109227.

Barrett, Alan H. (1961). "Microwave Absorption and Emission in the Atmosphere of Venus." In: *The Astrophysical Journal* 133, p. 281. URL: https://doi.org/10.1086/147024.

Barsukov, V. L. et al. (1986). "The geology and geomorphology of the Venus surface as revealed by the radar images obtained by Veneras 15 and 16." In: *Journal of Geophysical Research: Solid Earth* 91.B4, pp. 378–398. URL: https://doi.org/10.1029/jb091ib04p0d378.

Basilevsky, A. T., J. W. Head, G. G. Schaber, and R. G. Strom (1997). "The Resurfacing History of Venus." In: *Venus II*. Ed. by Stephen W. Bougher, D. M. Hunten, and R. J. Phillips, p. 1047.

Basilevsky, A. T., B. A. Ivanov, G. A. Burba, I. M. Chernaya, V. P. Kryuchkov, O. V. Nikolaeva, D. B. Campbell, and L. B. Ronca (1987). "Impact craters of Venus: A continuation of the analysis of data from the Venera 15 and 16 spacecraft." In: *Journal of Geophysical Research* 92.B12, p. 12869. DOI: 10.1029/jb092ib12p12869. URL: https://doi.org/10.1029/jb092ib12p12869.

Basilevsky, Alexander T. and James W. Head (1995). "Regional and global stratigraphy of Venus: a preliminary assessment and implications for the geological history of Venus." In: *Planetary and Space Science* 43.12, pp. 1523–1553. URL: https://doi.org/10.1016/0032-0633(95)00070-4.

Basilevsky, Alexander T and James W Head (2003). "The surface of Venus." In: *Reports on Progress in Physics* 66.10, pp. 1699–1734. URL: https://doi.org/10.1088/0034-4885/66/10/r04.

Belleguic, V., P. Lognonné, and M. Wieczorek (2005). "Constraints on the Martian lithosphere from gravity and topography data." In: *Journal of Geophysical Research* 110.E11. URL: https://doi.org/10.1029/2005je002437.

Bender, Kelly C., Kevin K. Williams, and Kimberly S. Homan (2000). "Tectonic Evaluation of Alpha Regio Highland and Environs, Venus." In: *Icarus* 148.1, pp. 153–159. URL: https://doi.org/10.1006/icar.2000.6479.

Besserer, Jonathan, Francis Nimmo, Mark A. Wieczorek, Renee C. Weber, Walter S. Kiefer, Patrick J. McGovern, Jeffrey C. Andrews-Hanna, David E. Smith, and Maria T. Zuber (2014). "GRAIL gravity constraints on the vertical and lateral density structure of the lunar crust." In: *Geophysical Research Letters* 41.16, pp. 5771–5777. URL: https://doi.org/10.1002/2014gl060240.

Beuthe, M., S. Le stre, P. Rosenblatt, M. Pätzold, and V. Dehant (2012). "Density and lithospheric thickness of the Tharsis Province from MEX MaRS and MRO gravity data." In: *Journal of Geophysical Research: Planets* 117.E4. URL: https://doi.org/10.1029/2011JE003976.

Beuthe, Mikael (2008). "Thin elastic shells with variable thickness for lithospheric flexure of one-plate planets." In: *Geophysical Journal International* 172.2, pp. 817–841. URL: https://doi.org/10.1111/j.1365-246x.2007.03671.x.

Bills, Bruce G., Walter S. Kiefer, and Robert L. Jones (1987). "Venus gravity: A harmonic analysis." In: *Journal of Geophysical Research: Solid Earth* 92.B10, pp. 10335–10351. URL: https://doi.org/10.1029/jb092ib10p10335.

Bilotti, Frank and John Suppe (1999). "The Global Distribution of Wrinkle Ridges on Venus." In: *Icarus* 139.1, pp. 137–157. URL: https://doi.org/10.1006/icar.1999.6092.

Bindschadler, D. L. and J. W. Head (1991). "Tessera terrain, Venus: characterization and models for origin and evolution." In: *Journal of Geophysical Research: Solid Earth* 96.B4, pp. 5889–5907. URL: https://doi.org/10.1029/90JB02742.

Bindschadler, Duane L., Annette DeCharon, Kathi K. Beratan, Suzanne E. Smrekar, and James W. Head (1992a). "Magellan observations of Alpha Regio: Implications for formation of complex ridged terrains on Venus." In: *Journal of Geophysical Research: Planets* 97.E8, pp. 13563–13577. URL: https://doi.org/10.1029/92je01332.

Bindschadler, Duane, Gerald Schubert, and William Kaula (1992b). "Coldspots and hotspots: Global tectonics and mantle dynamics of Venus." In: *Journal of Geophysical Research* 97.E8, pp. 13495–13532. URL: https://doi.org/10.1029/92je01165.

Bjonnes, E., B. C. Johnson, and A. J. Evans (2021). "Estimating Venusian thermal conditions using multiring basin morphology." In: *Nature Astronomy* 5.5, pp. 498–502. URL: https://doi.org/10.1038/s41550-020-01289-6.

Bjonnes, E.E., V.L. Hansen, B. James, and J.B. Swenson (2012). "Equilibrium resurfacing of Venus: Results from new Monte Carlo modeling and implications for Venus surface histories." In: *Icarus* 217.2, pp. 451–461. URL: https://doi.org/10.1016/j.icarus.2011.03.033.

Borrelli, M. E., J. G. O'Rourke, S. E. Smrekar, and C. M. Ostberg (July 2021). "A Global Survey of Lithospheric Flexure at Steep-Sided Domical Volcanoes on Venus Reveals Intermediate Elas-

tic Thicknesses." In: *Journal of Geophysical Research: Planets* 126.7. DOI: 10.1029/2020je006756. URL: https://doi.org/10.1029/2020je006756.

Bottke, W. F., D. Vokrouhlicky, B. Ghent, S. Mazrouei, S. Robbins, and S. Marchi (2016). "On Asteroid Impacts, Crater Scaling Laws, and a Proposed Younger Surface Age for Venus." In: *47th Annual Lunar and Planetary Science Conference*. Lunar and Planetary Science Conference, p. 2036.

Breuer, D. and W.B. Moore (2015). "Dynamics and Thermal History of the Terrestrial Planets, the Moon, and Io." In: *Treatise on Geophysics*. Elsevier, pp. 255–305. URL: https://doi.org/10.1016/b978-0-444-53802-4.00173-1.

Broquet, A. and M. A. Wieczorek (2019). "The Gravitational Signature of Martian Volcanoes." In: *Journal of Geophysical Research: Planets* 124.8, pp. 2054–2086. URL: https://doi.org/10.1029/2019je005959.

Broquet, Adrien (2020). "The lithosphere of Mars." PhD thesis. Université Côte d'Azur.

Brossier, J., M. S. Gilmore, K. Toner, and A. J. Stein (2021). "Distinct Mineralogy and Age of Individual Lava Flows in Atla Regio, Venus Derived From Magellan Radar Emissivity." In: *Journal of Geophysical Research: Planets* 126.3. URL: https://doi.org/10.1029/2020je006722.

Brossier, J.F., M.S. Gilmore, and K. Toner (2020). "Low radar emissivity signatures on Venus volcanoes and coronae: New insights on relative composition and age." In: *Icarus* 343, p. 113693. URL: https://doi.org/10.1016/j.icarus.2020.113693.

Brown, C. David and Robert E. Grimm (1997). "Tessera deformation and the contemporaneous thermal state of the plateau highlands, Venus." In: *Earth and Planetary Science Letters* 147.1, pp. 1–10. URL: https://doi.org/10.1016/S0012-821X(97)00007-1.

Brown, C. David and Roger J. Phillips (June 2000). "Crust-mantle decoupling by flexure of continental lithosphere." In: 105.B6, pp. 13221–13237. DOI: 10.1029/2000jb900069. URL: https://doi.org/10.1029/2000jb900069.

Bruzzone, L. et al. (2020). "Subsurface Radar Sounder On-board EnVision Mission to Venus." In: *AGU Fall Meeting Abstracts*. Vol. 2020, P026–0004.

Buck, W. Roger (1992). "Global decoupling of crust and mantle: Implications for topography, geoid and mantle viscosity on Venus." In: *Geophysical Research Letters* 19.21, pp. 2111–2114. URL: https://doi.org/10.1029/92GL02462.

Burov, E.V., M.G. Kogan, Hélène Lyon-Caen, and Peter Molnar (Jan. 1990). "Gravity anomalies, the deep structure, and dynamic processes beneath the Tien Shan." In: 96.3-4, pp. 367–383. DOI: 10.

1016/0012-821x(90)90013-n. URL: https://doi.org/10.1016/0012-821x(90)90013-n.

Burov, Evgene and Michel Diament (Mar. 1995). "The effective elastic thickness (Te) of continental lithosphere: What does it really mean?" In: 100.B3, pp. 3905–3927. DOI: 10.1029/94jb02770. URL: https://doi.org/10.1029/94jb02770.

Byerlee, James D. (1968). "Brittle-ductile transition in rocks." In: *Journal of Geophysical Research* 73.14, pp. 4741–4750. URL: https://agupubs.onlinelibrary.wiley.com/doi/abs/10.1029/JB073i014p04741.

Campbell, Bruce A. and Donald B. Campbell (2022). "Arecibo Radar Maps of Venus from 1988 to 2020." In: *The Planetary Science Journal* 3.3, p. 55. DOI: 10.3847/psj/ac4f43. URL: https://doi.org/10.3847/psj/ac4f43.

Campbell, D. B., R. B. Dyce, and G. H. Pettengill (1976). "New Radar Image of Venus." In: *Science* 193.4258, pp. 1123–1124. DOI: 10.1126/science.193.4258.1123. URL: https://doi.org/10.1126/science.193.4258.1123.

Campbell, Donald B., James W. Head, David A. Senske, Paul C. Fisher, Alice A. Hine, and John K. Harmon (1989). "Styles of Volcanism on Venus: New Arecibo High Resolution Radar Data." In: *Science* 246.4928, pp. 373–377. URL: https://doi.org/10.1126/science.246.4928.373.

Carlson, R. W. et al. (1991). "Galileo Infrared Imaging Spectroscopy Measurements at Venus." In: *Science* 253.5027, pp. 1541–1548. URL: https://doi.org/10.1126/science.253.5027.1541.

Carpenter, I. R. L. (1966). "Study of Venus by CW radar-1964 results." In: *The Astronomical Journal* 71, p. 142. URL: https://doi.org/10.1086/109872.

Cascioli, G., S. Hensley, F. De Marchi, D. Breuer, D. Durante, P. Racioppa, L. Iess, E. Mazarico, and S. E. Smrekar (Nov. 2021). "The Determination of the Rotational State and Interior Structure of Venus with VERITAS." In: *The Planetary Science Journal* 2.6, p. 220. DOI: 10.3847/psj/ac26c0. URL: https://doi.org/10.3847/psj/ac26c0.

Chantel, Julien, Geeth Manthilake, Denis Andrault, Davide Novella, Tony Yu, and Yanbin Wang (2016). "Experimental evidence supports mantle partial melting in the asthenosphere." In: *Science Advances* 2.5. URL: https://doi.org/10.1126/sciadv.1600246.

Clauser, Christoph and Ernst Huenges (1995). "Thermal Conductivity of Rocks and Minerals." In: *Rock Physics & Phase Relations*. American Geophysical Union (AGU), pp. 105–126. ISBN: 9781118668108. URL: https://doi.org/10.1029/RF003p0105.

Clifford, S. M. and F. P. Fanale (1985). "The Thermal Conductivity of the Martian Crust." In: *Lunar and Planetary Science Conference*. Lunar and Planetary Science Conference, pp. 144–145.

Colin, Lawrence (1980). "The Pioneer Venus Program." In: *Journal of Geophysical Research* 85.A13, p. 7575. DOI: 10.1029/ja085ia13p07575. URL: https://doi.org/10.1029/ja085ia13p07575.

Colin, Lawrence and Charles F. Hall (1977). "The Pioneer Venus Program." In: *Space Science Reviews* 20.3, pp. 283–306. DOI: 10.1007/bf02186467. URL: https://doi.org/10.1007/bf02186467.

Connolly, J.A.D. (2005). "Computation of phase equilibria by linear programming: A tool for geodynamic modeling and its application to subduction zone decarbonation." In: *Earth and Planetary Science Letters* 236.1-2, pp. 524–541. URL: https://doi.org/10.1016/j.epsl.2005.04.033.

Correia, Alexandre C. M. and Jacques Laskar (June 2001). "The four final rotation states of Venus." In: *Nature* 411.6839, pp. 767–770. URL: https://doi.org/10.1038/35081000.

Crameri, Fabio (2018). *Scientific colour maps (4.0.0)*. URL: https://zenodo.org/record/2649252.

Crameri, Fabio, Grace E. Shephard, and Philip J. Heron (Oct. 2020). "The misuse of colour in science communication." In: *Nature Communications* 11.1. DOI: 10.1038/s41467-020-19160-7. URL: https://doi.org/10.1038/s41467-020-19160-7.

Crumpler, L. S., J. C. Aubele, D. A. Senske, S. T. Keddie, K. P. Magee, and J. W. Head (1997). "Volcanoes and Centers of Volcanism on Venus." In: *Venus II*. Ed. by Stephen W. Bougher, D. M. Hunten, and R. J. Phillips, p. 697.

D'Incecco, Piero, Iván López, Goro Komatsu, Gian Gabriele Ori, and Marko Aittola (2020). "Local stratigraphic relations at Sandel crater, Venus: Possible evidence for recent volcano-tectonic activity in Imdr Regio." In: *Earth and Planetary Science Letters* 546, p. 116410. URL: https://doi.org/10.1016/j.epsl.2020.116410.

D'Incecco, Piero, Nils Müller, Jörn Helbert, and Mario D'Amore (2017). "Idunn Mons on Venus: Location and extent of recently active lava flows." In: *Planetary and Space Science* 136, pp. 25–33. URL: https://doi.org/10.1016/j.pss.2016.12.002.

Dahlen, F. A. and Frederik J. Simons (Sept. 2008). "Spectral estimation on a sphere in geophysics and cosmology." In: *Geophysical Journal International* 174.3, pp. 774–807. DOI: 10.1111/j.1365-246x.2008.03854.x. URL: https://doi.org/10.1111/j.1365-246x.2008.03854.x.

Davaille, A., S. E. Smrekar, and S. Tomlinson (2017). "Experimental and observational evidence for plume-induced subduction on Venus." In: *Nature Geoscience* 10.5, pp. 349–355. URL: https://doi.org/10.1038/ngeo2928.

Debayle, Eric, Thomas Bodin, Stéphanie Durand, and Yanick Ricard (2020). "Seismic evidence for partial melt below tectonic plates." In: *Nature* 586.7830, pp. 555–559. URL: https://doi.org/10.1038/s41586-020-2809-4.

Donahue, T. M., J. H. Hoffman, R. R. Hodges, and A. J. Watson (1982). "Venus Was Wet: A Measurement of the Ratio of Deuterium to Hydrogen." In: *Science* 216.4546, pp. 630–633. URL: https://doi.org/10.1126/science.216.4546.630.

Dones, Luke and Scott Tremaine (1993). "Why Does the Earth Spin Forward?" In: *Science* 259.5093, pp. 350–354. URL: https://doi.org/10.1126/science.259.5093.350.

Dumoulin, C., G. Tobie, O. Verhoeven, P. Rosenblatt, and N. Rambaux (2017). "Tidal constraints on the interior of Venus." In: *Journal of Geophysical Research: Planets* 122.6, pp. 1338–1352. URL: https://doi.org/10.1002/2016je005249.

Dyar, M. D., J. Helbert, A. Maturilli, N. T. Müller, and D. Kappel (2020). "Probing Venus Surface Iron Contents With Six-Band Visible Near-Infrared Spectroscopy From Orbit." In: *Geophysical Research Letters* 47.23. URL: https://doi.org/10.1029/2020gl090497.

Dziewonski, Adam M. (1984). "Mapping the lower mantle: Determination of lateral heterogeneity in P velocity up to degree and order 6." In: *Journal of Geophysical Research: Solid Earth* 89.B7, pp. 5929–5952. URL: https://agupubs.onlinelibrary.wiley.com/doi/abs/10.1029/JB089iB07p05929.

Ehlmann, Bethany L. and Christopher S. Edwards (2014). "Mineralogy of the Martian Surface." In: *Annual Review of Earth and Planetary Sciences* 42.1, pp. 291–315. URL: https://doi.org/10.1146/annurev-earth-060313-055024.

Evans, James (1998). *The history and practice of Ancient Astronomy*. Oxford University Press.

Feuvre, Mathieu Le and Mark A. Wieczorek (2011). "Nonuniform cratering of the Moon and a revised crater chronology of the inner Solar System." In: *Icarus* 214.1, pp. 1–20. URL: https://doi.org/10.1016/j.icarus.2011.03.010.

Filiberto, Justin (2014). "Magmatic diversity on Venus: Constraints from terrestrial analog crystallization experiments." In: *Icarus* 231, pp. 131–136. URL: https://doi.org/10.1016/j.icarus.2013.12.003.

Filiberto, Justin, David Trang, Allan H. Treiman, and Martha S. Gilmore (2020). "Present-day volcanism on Venus as evidenced from weathering rates of olivine." In: *Science Advances* 6.1. URL: https://doi.org/10.1126/sciadv.aax7445.

Ford, Peter G. and Gordon H. Pettengill (1992). "Venus topography and kilometer-scale slopes." In: *Journal of Geophysical Research* 97.E8, p. 13103. URL: https://doi.org/10.1029/92je01085.

Foreman-Mackey, Daniel, David Hogg, Dustin Lang, and Jonathan Goodman (2013). "emcee: The MCMC Hammer." In: *Publications of the Astronomical Society of the Pacific* 125.925, pp. 306–312. DOI: 10.1086/670067. URL: https://doi.org/10.1086/670067.

Forsyth, D. W. (1985). "Subsurface loading and estimates of the flexural rigidity of continental lithosphere." In: *Journal of Geophysical Research* 90, pp. 12623–12632. URL: https://doi.org/10.1029/JB090iB14p12623.

Forte, Alessandro M. and Jerry X. Mitrovica (2001). "Deep-mantle high-viscosity flow and thermochemical structure inferred from seismic and geodynamic data." In: *Nature* 410.6832, pp. 1049–1056. URL: https://doi.org/10.1038/35074000.

Forte, Alessandro M. and Richard Peltier (1991). "Viscous flow models of global geophysical observables: 1. Forward problems." In: *Journal of Geophysical Research: Solid Earth* 96.B12, pp. 20131–20159. URL: https://doi.org/10.1029/91jb01709.

Fowler, A. C. and S. B. G. O'Brien (1996). "A mechanism for episodic subduction on Venus." In: *Journal of Geophysical Research: Planets* 101.E2, pp. 4755–4763. URL: https://doi.org/10.1029/95je03261.

French, Scott W. and Barbara Romanowicz (2015). "Broad plumes rooted at the base of the Earth's mantle beneath major hotspots." In: *Nature* 525.7567, pp. 95–99. URL: https://doi.org/10.1038/nature14876.

Fukuhara, Tetsuya et al. (2017). "Large stationary gravity wave in the atmosphere of Venus." In: *Nature Geoscience* 10.2, pp. 85–88. URL: https://doi.org/10.1038/ngeo2873.

Gagnepain-Beyneix, Jeannine, Philippe Lognonné, Hugues Chenet, Denis Lombardi, and Tilman Spohn (2006). "A seismic model of the lunar mantle and constraints on temperature and mineralogy." In: *Physics of the Earth and Planetary Interiors* 159.3-4, pp. 140–166. URL: https://doi.org/10.1016/j.pepi.2006.05.009.

Galilei, Galileo (1610). *Sidereus nuncius*.

Galilei, Galileo (1623). *Il Saggiatore*.

Galilei, Galileo, Christoph Scheiner, Eileen Reeves, Albert van Helden, Eileen Reeves, and Albert van Helden (2010). *On Sunspots*. University of Chicago Press. DOI: 10.7208/chicago/9780226707174.001.0001. URL: https://doi.org/10.7208/chicago/9780226707174.001.0001.

Galilei, Galileo, Marcus Welser, and Angelo de Filiis (1613). *Istoria E dimostrazioni intorno alle macchie solari E loro accidenti comprese in tre lettere scritte all'illvstrissimo signor Marco Velseri ...*

Garcia, Raphaël F., Jeannine Gagnepain-Beyneix, Sébastien Chevrot, and Philippe Lognonné (2011). "Very preliminary reference Moon model." In: *Physics of the Earth and Planetary Interiors* 188.1-2, pp. 96–113. URL: https://doi.org/10.1016/j.pepi.2011.06.015.

Garvin, James B. et al. (2022). "Revealing the Mysteries of Venus: The DAVINCI Mission." In: *The Planetary Science Journal* 3.5, p. 117. URL: https://doi.org/10.3847/psj/ac63c2.

Gerya, T.V. (2014). "Plume-induced crustal convection: 3D thermomechanical model and implications for the origin of novae and coronae on Venus." In: *Earth and Planetary Science Letters* 391, pp. 183–192. URL: https://doi.org/10.1016/j.epsl.2014.02.005.

Gerya, Taras (2019). *Introduction to Numerical Geodynamic Modelling*. 2nd ed. Cambridge University Press. DOI: 10.1017/9781316534243.

Ghail, Richard (2015). "Rheological and petrological implications for a stagnant lid regime on Venus." In: 113-114, pp. 2–9. DOI: 10.1016/j.pss.2015.02.005. URL: https://doi.org/10.1016/j.pss.2015.02.005.

Ghent, Rebecca R., Roger J. Phillips, Vicki L. Hansen, and Daniel C. Nunes (2005). "Finite element modeling of short-wavelength folding on Venus: Implications for the plume hypothesis for crustal plateau formation." In: *Journal of Geophysical Research* 110.E11. URL: https://doi.org/10.1029/2005je002522.

Ghent, Rebecca and Vicki Hansen (1999). "Structural and Kinematic Analysis of Eastern Ovda Regio, Venus: Implications for Crustal Plateau Formation." In: *Icarus* 139.1, pp. 116–136. ISSN: 0019-1035. URL: https://doi.org/10.1006/icar.1999.6085.

Giardini, D. et al. (2020). "The seismicity of Mars." In: *Nature Geoscience* 13.3, pp. 205–212. URL: https://doi.org/10.1038/s41561-020-0539-8.

Gillmann, C., G. J. Golabek, S. N. Raymond, M. Schönbächler, P. J. Tackley, V. Dehant, and V. Debaille (2020). "Dry late accretion inferred from Venus's coupled atmosphere and internal evolution." In: *Nature Geoscience* 13.4, pp. 265–269. URL: https://doi.org/10.1038/s41561-020-0561-x.

Gillmann, Cedric and Paul Tackley (2014). "Atmosphere/mantle coupling and feedbacks on Venus." In: *Journal of Geophysical Research: Planets* 119.6, pp. 1189–1217. URL: https://doi.org/10.1002/2013je004505.

Gillmann, Cedric et al. (2022). "The Long-Term Evolution of the Atmosphere of Venus: Processes and Feedback Mechanisms." In: *Space Science Reviews* 218.7. DOI: 10.1007/s11214-022-00924-0. URL: https://doi.org/10.1007/s11214-022-00924-0.

Gilmore, Martha S. and James W. Head (2000). "Sequential deformation of plains at the margins of Alpha Regio, Venus: Implications for tessera formation." In: *Meteoritics & Planetary Science* 35.4, pp. 667–687. URL: https://doi.org/10.1111/j.1945-5100.2000.tb01451.x.

Gilmore, Martha S., Mikhail A. Ivanov, James W. Head, and Alexander T. Basilevsky (1997). "Duration of tessera deformation on Venus." In: *Journal of Geophysical Research: Planets* 102.E6, pp. 13357–13368. URL: https://doi.org/10.1029/97je00965.

Gilmore, Martha S., Nils Mueller, and Jörn Helbert (2015). "VIRTIS emissivity of Alpha Regio, Venus, with implications for tessera

composition." In: *Icarus* 254, pp. 350–361. URL: https://doi.org/10.1016/j.icarus.2015.04.008.

Gingerich, Owen (1982). "The Galileo Affair." In: *Scientific American* 247.2, pp. 132–143. ISSN: 00368733, 19467087. URL: http://www.jstor.org/stable/24966665 (visited on 05/30/2023).

Gingerich, Owen (1984). "Phases of Venus in 1610." In: *Journal for the History of Astronomy* 15.3, pp. 209–210. URL: https://doi.org/10.1177/002182868401500305.

Giorgini, Jon, Kuen Wong, Tung-Han You, Pam Chadbourne, and Lily Lim (1995). "Magellan Aerobrake Navigation." In: *Journal of The British Interplanetary Society* 48, pp. 111–122. URL: https://ssd.jpl.nasa.gov/x/jdg/papers/magellan.pdf.

Gold, Thomas and Steven Soter (1969). "Atmospheric tides and the resonant rotation of Venus." In: *Icarus* 11.3, pp. 356–366. URL: https://doi.org/10.1016/0019-1035(69)90068-2.

Goldstein, R. M. (1964). "Symposium on Radar and Radiometric Observations of Venus during the 1962 Conjunction: Venus characteristics by earth-based radar." In: *The Astronomical Journal* 69, p. 12. URL: https://doi.org/10.1086/109221.

Goldstein, Richard M. (1965). "Preliminary Venus radar results." In: *Journal of Research of the National Bureau of Standards, Section D: Radio Science* 69D.12, p. 1623. URL: https://doi.org/10.6028/jres.069d.187.

Gong, Shengxia, Mark A. Wieczorek, Francis Nimmo, Walter S. Kiefer, James W. Head, Chengli Huang, David E. Smith, and Maria T. Zuber (2016). "Thicknesses of mare basalts on the Moon from gravity and topography." In: *Journal of Geophysical Research: Planets* 121.5, pp. 854–870. URL: https://doi.org/10.1002/2016je005008.

Goodman, Jonathan and Jonathan Weare (2010). "Ensemble samplers with affine invariance." In: *Communications in Applied Mathematics and Computational Science* 5.1, pp. 65–80. URL: https://doi.org/10.2140/camcos.2010.5.65.

Goossens, S., T. J. Sabaka, M. A. Wieczorek, G. A. Neumann, E. Mazarico, F. G. Lemoine, J. B. Nicholas, D. E. Smith, and M. T. Zuber (2020). "High-Resolution Gravity Field Models from GRAIL Data and Implications for Models of the Density Structure of the Moon's Crust." In: *Journal of Geophysical Research: Planets* 125.2. URL: https://doi.org/10.1029/2019je006086.

Grimm, Robert E. (1994). "The Deep Structure of Venusian Plateau Highlands." In: *Icarus* 112. URL: https://doi.org/10.1006/icar.1994.1171.

Grimm, Robert E. and Roger J. Phillips (1992). "Anatomy of a Venusian hot spot: Geology, gravity, and mantle dynamics of Eistla Regio." In: *Journal of Geophysical Research* 97.E10, p. 16035. URL: https://doi.org/10.1029/92je01500.

Grott, M. and M.A. Wieczorek (2012). "Density and lithospheric structure at Tyrrhena Patera, Mars, from gravity and topography data." In: *Icarus* 221.1, pp. 43–52. URL: https://doi.org/10.1016/j.icarus.2012.07.008.

Grove, Timothy L., Michael B. Baker, Richard C. Price, Stephen W. Parman, Linda T. Elkins-Tanton, Nilanjan Chatterjee, and Othmar Muntener (2004). "Magnesian andesite and dacite lavas from Mt. Shasta, northern California: products of fractional crystallization of H2O-rich mantle melts." In: *Contributions to Mineralogy and Petrology* 148.5, pp. 542–565. URL: https://doi.org/10.1007/s00410-004-0619-6.

Guest, John E., Mark H. Bulmer, Jayne Aubele, Kathi Beratan, Ronald Greeley, James W. Head, Gregory Michaels, Catherine Weitz, and Charles Wiles (1992). "Small volcanic edifices and volcanism in the plains of Venus." In: *Journal of Geophysical Research* 97.E10, p. 15949. URL: https://doi.org/10.1029/92je01438.

Gülcher, Anna J. P., Taras V. Gerya, Laurent G. J. Montési, and Jessica Munch (2020). "Corona structures driven by plume–lithosphere interactions and evidence for ongoing plume activity on Venus." In: *Nature Geoscience* 13.8, pp. 547–554. URL: https://doi.org/10.1038/s41561-020-0606-1.

Hager, Bradford H. and Robert W. Clayton (1989). "Constraints on the Structure of Mantle Convection Using Seismic Observations, Flow Models, and the Geoid." In: *Mantle Convection; plate tectonics and global dynamics*. Ed. by W.R. Peltier. New York: Gordon and Breach Science Publishers, pp. 657–763.

Hager, Bradford H., Robert W. Clayton, Mark A. Richards, Robert P. Comer, and Adam M. Dziewonski (1985). "Lower mantle heterogeneity, dynamic topography and the geoid." In: *Nature* 313.6003, pp. 541–545. URL: https://doi.org/10.1038/313541a0.

Hahn, Rebecca M. and Paul K. Byrne (2023). "A Morphological and Spatial Analysis of Volcanoes on Venus." In: *Journal of Geophysical Research: Planets* 128.4. URL: https://doi.org/10.1029/2023je007753.

Hansen, Vicki L. (2006). "Geologic constraints on crustal plateau surface histories, Venus: The lava pond and bolide impact hypotheses." In: *Journal of Geophysical Research: Planets* 111.E11. URL: https://doi.org/10.1029/2006je002714.

Hansen, Vicki L., Roger J. Phillips, James J. Willis, and Rebecca R. Ghent (2000). "Structures in tessera terrain, Venus: Issues and answers." In: *Journal of Geophysical Research: Planets* 105.E2, pp. 4135–4152. URL: https://doi.org/10.1029/1999JE001137.

Hansen, Vicki L. and James A. Willis (1996). "Structural Analysis of a Sampling of Tesserae: Implications for Venus Geodynamics." In: *Icarus* 123.2, pp. 296–312. URL: https://doi.org/10.1006/icar.1996.0159.

Hashimoto, George L. (2003). "On observing the compositional variability of the surface of Venus using nightside near-infrared thermal radiation." In: *Journal of Geophysical Research* 108.E9. URL: https://doi.org/10.1029/2003je002082.

Hashimoto, George L., Maarten Roos-Serote, Seiji Sugita, Martha S. Gilmore, Lucas W. Kamp, Robert W. Carlson, and Kevin H. Baines (2008). "Felsic highland crust on Venus suggested by Galileo Near-Infrared Mapping Spectrometer data." In: *Journal of Geophysical Research: Planets* 113.E5. URL: https://doi.org/10.1029/2008JE003134.

Hastings, W. K. (1970). "Monte Carlo sampling methods using Markov chains and their applications." In: *Biometrika* 57.1, pp. 97–109. URL: https://doi.org/10.1093/biomet/57.1.97.

Hauck, Steven A., Roger J. Phillips, and Maribeth H. Price (1998). "Venus: Crater distribution and plains resurfacing models." In: *Journal of Geophysical Research: Planets* 103.E6, pp. 13635–13642. URL: https://doi.org/10.1029/98je00400.

Hauck, Steven A. et al. (2013). "The curious case of Mercury's internal structure." In: *Journal of Geophysical Research: Planets* 118.6, pp. 1204–1220. URL: https://doi.org/10.1002/jgre.20091.

Head, James W., Donald B. Campbell, Charles Elachi, John E. Guest, Dan P. McKenzie, R. Stephen Saunders, Gerald G. Schaber, and Gerald Schubert (1991). "Venus Volcanism: Initial Analysis from Magellan Data." In: *Science* 252.5003, pp. 276–288. URL: https://doi.org/10.1126/science.252.5003.276.

Head, James W., L. S. Crumpler, Jayne C. Aubele, John E. Guest, and R. Stephen Saunders (1992). "Venus volcanism: Classification of volcanic features and structures, associations, and global distribution from Magellan data." In: *Journal of Geophysical Research* 97.E8, p. 13153. URL: https://doi.org/10.1029/92je01273.

Helbert, Jörn, Nils Müller, Petri Kostama, Lucia Marinangeli, Giuseppe Piccioni, and Pierre Drossart (2008). "Surface brightness variations seen by VIRTIS on Venus Express and implications for the evolution of the Lada Terra region, Venus." In: *Geophysical Research Letters* 35.11. URL: https://doi.org/10.1029/2008gl033609.

Helbert, Jörn et al. (2019). "The VenSpec suite on the ESA EnVision mission to Venus." In: *Infrared Remote Sensing and Instrumentation XXVII*. Ed. by Marija Strojnik and Gabriele E. Arnold. SPIE. DOI: 10.1117/12.2529248. URL: https://doi.org/10.1117/12.2529248.

Hemingway, Douglas J. and Isamu Matsuyama (2017). "Isostatic equilibrium in spherical coordinates and implications for crustal thickness on the Moon, Mars, Enceladus, and elsewhere." In: *Geophysical Research Letters* 44.15, pp. 7695–7705. URL: https://doi.org/10.1002/2017gl073334.

Herrick, R. R., V. L. Sharpton, M. C. Malin, S. N. Lyons, and K. Feely (1997). "Morphology and Morphometry of Impact Craters." In:

Venus II. Ed. by Stephen W. Bougher, D. M. Hunten, and R. J. Phillips, p. 1015.

Herrick, Robert R. (1994). "Resurfacing history of Venus." In: *Geology* 22.8, p. 703. URL: https://doi.org/10.1130/0091-7613(1994)022<0703:rhov>2.3.co;2.

Herrick, Robert R. and Roger J. Phillips (1992). "Geological correlations with the interior density structure of Venus." In: *Journal of Geophysical Research: Planets* 97.E10, pp. 16017–16034. URL: https://agupubs.onlinelibrary.wiley.com/doi/abs/10.1029/92JE01498.

Herrick, Robert R., Daniel L. Stahlke, and Virgil L. Sharpton (2012). "Fine-scale Venusian topography from Magellan stereo data." In: *Eos, Transactions American Geophysical Union* 93.12, pp. 125–126. URL: https://doi.org/10.1029/2012eo120002.

Herrick, Robert R. et al. (2023). "Resurfacing History and Volcanic Activity of Venus." In: *Space Science Reviews* 219.4. URL: https://doi.org/10.1007/s11214-023-00966-y.

Herrick, Robert and Scott Hensley (2023). "Surface changes observed on a Venusian volcano during the Magellan mission." In: *Science*. URL: https://doi.org/10.1126/science.abm7735.

Hess, Paul C. and James W. Head (1990). "Derivation of Primary Magmas and Melting of Crustal Materials on Venus: Some Preliminary Petrogenetic Considerations." In: *Earth Moon and Planets* 50-51, p. 57. URL: https://doi.org/10.1007/BF00142389.

Hirth, Greg and David L. Kohlstedt (1996). "Water in the oceanic upper mantle: implications for rheology, melt extraction and the evolution of the lithosphere." In: *Earth and Planetary Science Letters* 144.1-2, pp. 93–108. URL: https://doi.org/10.1016/0012-821x(96)00154-9.

Hirth, Greg and David Kohlstedt (2003). "Rheology of the upper mantle and the mantle wedge: A view from the experimentalists." In: *Inside the Subduction Factory*. American Geophysical Union, pp. 83–105. URL: https://doi.org/10.1029/138gm06.

Hofmann-Wellenhof, Bernhard and Helmut Moritz (2006). *Physical Geodesy*. Springer Vienna. URL: https://doi.org/10.1007/978-3-211-33545-1.

Holland, Tim J B, Eleanor C R Green, and Roger Powell (2018). "Melting of Peridotites through to Granites: A Simple Thermodynamic Model in the System KNCFMASHTOCr." In: *Journal of Petrology* 59.5, pp. 881–900. URL: https://doi.org/10.1093/petrology/egy048.

Holtzman, Benjamin K. (2016). "Questions on the existence, persistence, and mechanical effects of a very small melt fraction in the asthenosphere." In: *Geochemistry, Geophysics, Geosystems* 17.2, pp. 470–484. URL: https://doi.org/10.1002/2015gc006102.

Hoogenboom, Trudi, Greg Houseman, and Paula Martin (2005). "Elastic thickness estimates for coronae associated with chasmata on Venus." In: *Journal of Geophysical Research* 110.E9. URL: https://doi.org/10.1029/2004je002394.

Hoogenboom, Trudi, Suzanne E. Smrekar, F. Scott Anderson, and Greg Houseman (2004). "Admittance survey of type 1 coronae on Venus." In: *Journal of Geophysical Research: Planets* 109.E3. URL: https://doi.org/10.1029/2003JE002171.

Horinouchi, Takeshi et al. (2020). "How waves and turbulence maintain the super-rotation of Venus' atmosphere." In: *Science* 368.6489, pp. 405–409. URL: https://doi.org/10.1126/science.aaz4439.

Hua, Junlin, Karen M. Fischer, Thorsten W. Becker, Esteban Gazel, and Greg Hirth (2023). "Asthenospheric low-velocity zone consistent with globally prevalent partial melting." In: *Nature Geoscience* 16.2, pp. 175–181. URL: https://doi.org/10.1038/s41561-022-01116-9.

Huang, Jinshui, An Yang, and Shijie Zhong (2013). "Constraints of the topography, gravity and volcanism on Venusian mantle dynamics and generation of plate tectonics." In: *Earth and Planetary Science Letters* 362, pp. 207–214. URL: https://doi.org/10.1016/j.epsl.2012.11.051.

Hüttig, Christian and Kai Stemmer (2008). "Finite volume discretization for dynamic viscosities on Voronoi grids." In: *Physics of the Earth and Planetary Interiors* 171.1-4, pp. 137–146. URL: https://doi.org/10.1016/j.pepi.2008.07.007.

Hyndman, R. D. and M. J. Drury (1976). "The physical properties of oceanic basement rocks from deep drilling on the Mid-Atlantic Ridge." In: *Journal of Geophysical Research* 81.23, pp. 4042–4052. URL: https://doi.org/10.1029/jb081i023p04042.

Ivanov, Mikhail A. and James W. Head (1996). "Tessera terrain on Venus: A survey of the global distribution, characteristics, and relation to surrounding units from Magellan data." In: *Journal of Geophysical Research: Planets* 101.E6, pp. 14861–14908. URL: https://doi.org/10.1029/96JE01245.

Ivanov, Mikhail A. and James W. Head (2011). "Global geological map of Venus." In: *Planetary and Space Science* 59.13, pp. 1559–1600. URL: https://doi.org/10.1016/j.pss.2011.07.008.

Jaeger, John and Neville Cook (1976). *Fundamentals of rock mechanics*. John Wiley & Sons.

James, Peter B., Maria T. Zuber, and Roger J. Phillips (2013). "Crustal thickness and support of topography on Venus." In: *Journal of Geophysical Research: Planets* 118.4, pp. 859–875. URL: https://doi.org/10.1029/2012je004237.

Jimenez-Diaz, Alberto, Javier Ruiz, Jon F. Kirby, Ignacio Romeo, Rosa Tejero, and Ramón Capote (2015). "Lithospheric structure of Venus

from gravity and topography." In: *Icarus* 260, pp. 215–231. URL: https://doi.org10.1016/j.icarus.2015.07.020.

Johnson, Catherine L. (2003). "A conceptual model for the relationship between coronae and large-scale mantle dynamics on Venus." In: *Journal of Geophysical Research* 108.E6. URL: https://doi.org/10.1029/2002je001962.

Jones, D.E. (1961). "The microwave temperature of Venus." In: *Planetary and Space Science* 5.2, pp. 166–167. URL: https://doi.org/10.1016/0032-0633(61)90094-0.

Jurgens, Raymond F. (1970). "Some Preliminary Results of the 70-cm Radar Studies of Venus." In: *Radio Science* 5.2, pp. 435–442. URL: https://doi.org/10.1029/rs005i002p00435.

Karato, Shun-ichiro (2012). "On the origin of the asthenosphere." In: *Earth and Planetary Science Letters* 321-322, pp. 95–103. URL: https://doi.org/10.1016/j.epsl.2012.01.001.

Karimi, Saman and Andrew J. Dombard (2020). "Reply." In: *Icarus* 336, p. 113360. URL: https://doi.org/10.1016/j.icarus.2019.06.021.

Karlsson, R. V. M. K., K. W. Cheng, F. Crameri, T. Rolf, S. Uppalapati, and S. C. Werner (2020). "Implications of Anomalous Crustal Provinces for Venus' Resurfacing History." In: *Journal of Geophysical Research: Planets* 125.10. URL: https://doi.org/10.1029/2019je006340.

Kass, Robert E. and Adrian E. Raftery (1995). "Bayes Factors." In: *Journal of the American Statistical Association* 90.430, pp. 773–795. URL: https://doi.org/10.1080/01621459.1995.10476572.

Kaula, W. M. and R. J. Phillips (1981). "Quantitative tests for plate tectonics on Venus." In: *Geophysical Research Letters* 8.12, pp. 1187–1190. URL: https://doi.org/10.1029/gl008i012p01187.

Kaula, William M. (1966). *Theory of satellite geodesy. Applications of satellites to geodesy*. Blaisdell Publishing Company.

Kaula, William M. (1984). "Tectonic contrasts between Venus and the Earth." In: *Geophysical Research Letters* 11.1, pp. 35–37. URL: https://doi.org/10.1029/gl011i001p00035.

Khan, Amir et al. (2021). "Upper mantle structure of Mars from InSight seismic data." In: *Science* 373.6553, pp. 434–438. URL: https://doi.org/10.1126/science.abf2966.

Kidder, Jennifer G. and Roger J. Phillips (1996). "Convection-driven subsolidus crustal thickening on Venus." In: *Journal of Geophysical Research: Planets* 101.E10, pp. 23181–23194. DOI: https://doi.org/10.1029/96JE02530.

Kiefer, Walter S. and Bradford H. Hager (1991). "A mantle plume model for the equatorial highlands of Venus." In: *Journal of Geophysical Research* 96.E4, p. 20947. URL: https://doi.org/10.1029/91je02221.

Kiefer, Walter S. and Kelly Peterson (2003). "Mantle and crustal structure in Phoebe Regio and Devana Chasma, Venus." In: *Geophysical Research Letters* 30.1, pp. 5–1–5–4. URL: https://agupubs.onlinelibrary.wiley.com/doi/abs/10.1029/2002GL015762.

Kiefer, Walter S., Mark A. Richards, Bradford H. Hager, and Bruce G. Bills (1986). "A dynamic model of Venus's gravity field." In: *Geophysical Research Letters* 13.1, pp. 14–17. URL: https://agupubs.onlinelibrary.wiley.com/doi/abs/10.1029/GL013i001p00014.

King, Scott D. (2016). "An evolving view of transition zone and midmantle viscosity." In: *Geochemistry, Geophysics, Geosystems* 17.3, pp. 1234–1237. DOI: 10.1002/2016gc006279. URL: https://doi.org/10.1002/2016gc006279.

King, Scott D. (2018). "Venus Resurfacing Constrained by Geoid and Topography." In: *Journal of Geophysical Research: Planets* 123.5, pp. 1041–1060. URL: https://doi.org/10.1002/2017je005475.

King, Scott D. and Guy Masters (1992). "An inversion for radial viscosity structure using seismic tomography." In: *Geophysical Research Letters* 19.15, pp. 1551–1554. URL: https://doi.org/10.1029/92gl01700.

Knapmeyer-Endrun, Brigitte et al. (2021). "Thickness and structure of the martian crust from InSight seismic data." In: *Science* 373.6553, pp. 438–443. URL: https://doi.org/10.1126/science.abf8966.

Konopliv, A. S. and C. F. Yoder (1996). "Venusian k2 tidal Love number from Magellan and PVO tracking data." In: *Geophysical Research Letters* 23.14, pp. 1857–1860. URL: https://doi.org/10.1029/96gl01589.

Konopliv, A.S., W.B. Banerdt, and W.L. Sjogren (1999). "Venus Gravity: 180th Degree and Order Model." In: *Icarus* 139.1, pp. 3–18. URL: https://doi.org/10.1006/icar.1999.6086.

Kramer, Georgiana Y. et al. (2011). "Newer views of the Moon: Comparing spectra from Clementine and the Moon Mineralogy Mapper." In: *Journal of Geophysical Research* 116. URL: https://doi.org/10.1029/2010je003728.

Kraus, Henry (1967). *Thin Elastic Shells: : An introduction to the theoretical foundations and the analysis of their static and dynamic behavior*. New York: John Wiley. ISBN: 9780471507208.

Kucinskas, Algis B., Donald L. Turcotte, and Jafar Arkani-Hamed (1996). "Isostatic compensation of Ishtar Terra, Venus." In: *Journal of Geophysical Research: Planets* 101.E2, pp. 4725–4736. URL: https://doi.org/10.1029/95je02979.

Kuncinskas, A.B. and D.L. Turcotte (1994). "Isostatic compensation of Equatorial highlands on Venus." In: *Icarus* 112, pp. 104–116. URL: https://doi.org/10.1006/icar.1994.1172.

Laskar, J. and P. Robutel (1993). "The chaotic obliquity of the planets." In: *Nature* 361.6413, pp. 608–612. URL: https://doi.org/10.1038/361608a0.

Latham, G., M. Ewing, J. Dorman, D. Lammlein, F. Press, N. Toksoz, G. Sutton, F. Duennebier, and Y. Nakamura (1971). "Moonquakes." In: *Science* 174.4010, pp. 687–692. DOI: 10.1126/science.174.4010.687. URL: https://doi.org/10.1126/science.174.4010.687.

Lewis, Kevin W. and Frederik J. Simons (2012). "Local spectral variability and the origin of the Martian crustal magnetic field." In: *Geophysical Research Letters* 39.18. URL: https://doi.org/10.1029/2012gl052708.

Liu, Xi and Shijie Zhong (2016). "Constraining mantle viscosity structure for a thermochemical mantle using the geoid observation." In: *Geochemistry, Geophysics, Geosystems* 17.3, pp. 895–913. URL: https://doi.org/10.1002/2015gc006161.

Lognonné, Philippe, Jeannine Gagnepain-Beyneix, and Hugues Chenet (2003). "A new seismic model of the Moon: implications for structure, thermal evolution and formation of the Moon." In: *Earth and Planetary Science Letters* 211.1-2, pp. 27–44. URL: https://doi.org/10.1016/s0012-821x(03)00172-9.

Lourenço, Diogo L. and Antoine B. Rozel (2023). "The Past and the Future of Plate Tectonics and Other Tectonic Regimes." In: *Dynamics of Plate Tectonics and Mantle Convection*. Elsevier, pp. 181–196. URL: https://doi.org/10.1016/b978-0-323-85733-8.00004-4.

Lourenço, Diogo L., Antoine B. Rozel, Maxim D. Ballmer, and Paul J. Tackley (2020). "Plutonic-Squishy Lid: A New Global Tectonic Regime Generated by Intrusive Magmatism on Earth-Like Planets." In: *Geochemistry, Geophysics, Geosystems* 21.4. URL: https://doi.org/10.1029/2019gc008756.

Lourenço, Diogo L., Antoine B. Rozel, Taras Gerya, and Paul J. Tackley (2018). "Efficient cooling of rocky planets by intrusive magmatism." In: *Nature Geoscience* 11.5, pp. 322–327. URL: https://doi.org/10.1038/s41561-018-0094-8.

Lyons, Daniel T., R.Stephen Saunders, and Douglas G. Griffith (1995). "The Magellan Venus mapping mission: Aerobraking operations." In: *Acta Astronautica* 35.9-11, pp. 669–676. URL: https://doi.org/10.1016/0094-5765(95)00032-u.

Mackay, David (2003). *Information Theory, Inference, and Learning Algorithms*. Cambridge University Press. URL: https://www.inference.org.uk/mackay/itprnn/book.html.

Maia, J. S. and M. A. Wieczorek (2022). "Lithospheric Structure of Venusian Crustal Plateaus." In: *Journal of Geophysical Research: Planets* 127.2. URL: https://doi.org/10.1029/2021je007004.

Marcq, Emmanuel, Jean-Loup Bertaux, Franck Montmessin, and Denis Belyaev (2012). "Variations of sulphur dioxide at the cloud top of Venus's dynamic atmosphere." In: *Nature Geoscience* 6.1, pp. 25–28. URL: https://doi.org/10.1038/ngeo1650.

Margot, Jean-Luc, Donald B. Campbell, Jon D. Giorgini, Joseph S. Jao, Lawrence G. Snedeker, Frank D. Ghigo, and Amber Bonsall (2021). "Spin state and moment of inertia of Venus." In: *Nature Astronomy* 5.7, pp. 676–683. URL: https://doi.org/10.1038/s41550-021-01339-7.

Marov, Mikhail Ya. (2004). "Mikhail Lomonosov and the discovery of the atmosphere of Venus during the 1761 transit." In: *Proceedings of the International Astronomical Union* 2004.IAUC196, pp. 209–219. URL: https://doi.org/10.1017/s1743921305001390.

Masursky, Harold, Eric Eliason, Peter G. Ford, George E. McGill, Gordon H. Pettengill, Gerald G. Schaber, and Gerald Schubert (1980). "Pioneer Venus Radar results: Geology from images and altimetry." In: *Journal of Geophysical Research* 85.A13, p. 8232. URL: https://doi.org/10.1029/ja085ia13p08232.

Mayer, C. H., T. P. McCullough, and R. M. Sloanaker (1958). "Observations of Venus at 3.15-cm Wavelength." In: *The Astrophysical Journal* 127, p. 1. URL: https://doi.org/10.1086/146433.

Mazarico, Erwan, Luciano Iess, Gael Cascioli, Daniele Durante, Fabrizio De Marchi, Scott Hensley, and Suzanne Smrekar (2023). "EXPLORING THE VENUS CRUST AND LITHOSPHERE WITH THE VERITAS GRAVITY SCIENCE INVESTIGATION." In: *54rd Lunar and Planetary Science Conference*. Vol. 2678. LPI Contributions, p. 2153.

McGovern, Patrick J., Sean C. Solomon, David E. Smith, Maria T. Zuber, Mark Simons, Mark A. Wieczorek, Roger J. Phillips, Gregory A. Neumann, Oded Aharonson, and James W. Head (2002). "Localized gravity/topography admittance and correlation spectra on Mars: Implications for regional and global evolution." In: *Journal of Geophysical Research: Planets* 107.E12, pp. 19–1–19–25. URL: https://doi.org/10.1029/2002JE001854.

McKinnon, W. B., K. J. Zahnle, B. A. Ivanov, and H. J. Melosh (1997). "Cratering on Venus: Models and Observations." In: *Venus II*. Ed. by Stephen W. Bougher, D. M. Hunten, and R. J. Phillips, p. 969.

McMahon, Susan K. (1996). "Overview of the Planetary Data System." In: *Planetary and Space Science* 44.1, pp. 3–12. URL: https://doi.org/10.1016/0032-0633(95)00101-8.

McNutt, M., M. Diament, and M. Kogan (1988). "Variations of elastic plate thickness at continental thrust belts." In: 93.B8, p. 8825. DOI: 10.1029/jb093ib08p08825. URL: https://doi.org/10.1029/jb093ib08p08825.

McNutt, Marcia K. (1984). "Lithospheric flexure and thermal anomalies." In: *Journal of Geophysical Research: Solid Earth* 89.B13, pp. 11180–11194. URL: https://doi.org/10.1029/jb089ib13p11180.

Meade, Charles and Raymond Jeanloz (1990). "The strength of mantle silicates at high pressures and room temperature: implications for the viscosity of the mantle." In: *Nature* 348, pp. 533–535.

Metropolis, Nicholas, Arianna W. Rosenbluth, Marshall N. Rosenbluth, Augusta H. Teller, and Edward Teller (1953). "Equation of State Calculations by Fast Computing Machines." In: *The Journal of Chemical Physics* 21.6, pp. 1087–1092. DOI: 10.1063/1.1699114. URL: https://doi.org/10.1063/1.1699114.

Mitrovica, J.X. and A.M. Forte (2004). "A new inference of mantle viscosity based upon joint inversion of convection and glacial isostatic adjustment data." In: *Earth and Planetary Science Letters* 225.1-2, pp. 177–189. URL: https://doi.org/10.1016/j.epsl.2004.06.005.

Montési, L. G. and M. T. Zuber (2002). "Revisiting the Origin of Tectonic Spacing on Venus: Importance of Localizationand Surface Temperature." In: *Lunar and Planetary Science Conference*. Lunar and Planetary Science Conference, p. 1618.

Moore, William B. and Gerald Schubert (1997). "Venusian Crustal and Lithospheric Properties from Nonlinear Regressions of Highland Geoid and Topography." en. In: *Icarus* 128.2, pp. 415–428. URL: https://doi.org/10.1006/icar.1997.5750.

Moore, William B. and A. Alexander G. Webb (2013). "Heat-pipe Earth." In: *Nature* 501.7468, pp. 501–505. URL: https://doi.org/10.1038/nature12473.

Moore, William (2001). "The Thermal State of Io." In: *Icarus* 154.2, pp. 548–550. URL: https://doi.org/10.1006/icar.2001.6739.

Mosegaard, Klaus and Albert Tarantola (1995). "Monte Carlo sampling of solutions to inverse problems." In: *Journal of Geophysical Research: Solid Earth* 100.B7, pp. 12431–12447. URL: https://doi.org/10.1029/94jb03097.

Mueller, N., J. Helbert, G. L. Hashimoto, C. C. C. Tsang, S. Erard, G. Piccioni, and P. Drossart (2008). "Venus surface thermal emission at 1μm in VIRTIS imaging observations: Evidence for variation of crust and mantle differentiation conditions." In: *Journal of Geophysical Research* 113. URL: https://doi.org/10.1029/2008je003118.

Mueller, Steve and Roger J. Phillips (1995). "On the reliability of lithospheric constraints derived from models of outer-rise flexure." In: *Geophysical Journal International* 123.3, pp. 887–902. URL: https://doi.org/10.1111/j.1365-246X.1995.tb06896.x.

Nájera, Margarita Juárez and Mariana Castellanos (2020). "Elucidating the Visual Language of the Venus Table in the Dresden Codex: A Visual Semiotics Approach." In: *Estudios de Cultura Maya* 56.2, pp. 95–126. URL: https://doi.org/10.19130/iifl.ecm.2020.56.2.0004.

Nakamura, M. et al. (2011). "Overview of Venus orbiter, Akatsuki." In: *Earth, Planets and Space* 63.5, pp. 443–457. URL: https://doi.org/10.5047/eps.2011.02.009.

Namur, Olivier and Bernard Charlier (2016). "Silicate mineralogy at the surface of Mercury." In: *Nature Geoscience* 10.1, pp. 9–13. URL: https://doi.org/10.1038/ngeo2860.

Neukum, G., B.A. Ivanov, and W.K. Hartmann (2001). In: *Space Science Reviews* 96.1/4, pp. 55–86. URL: https://doi.org/10.1023/a:1011989004263.

Nimmo, F. and D. McKenzie (1998). "Volcanism and tectonics on Venus." In: *Annual Review of Earth and Planetary Sciences* 26.1, pp. 23–51. URL: https://doi.org/10.1146/annurev.{E}arth.26.1.23.

Nimmo, Francis and Dan McKenzie (1996). "Modelling plume-related uplift, gravity and melting on Venus." In: *Earth and Planetary Science Letters* 145.1-4, pp. 109–123. URL: https://doi.org/10.1016/s0012-821x(96)00200-2.

Noack, L., D. Breuer, and T. Spohn (2012). "Coupling the atmosphere with interior dynamics: Implications for the resurfacing of Venus." In: *Icarus* 217.2, pp. 484–498. URL: https://doi.org/10.1016/j.icarus.2011.08.026.

Nunes, Daniel Cahn, Roger J. Phillips, C. David Brown, and Andrew J. Dombard (2004). "Relaxation of compensated topography and the evolution of crustal plateaus on Venus." In: *Journal of Geophysical Research: Planets* 109.E1. DOI: https://doi.org/10.1029/2003JE002119. URL: https://agupubs.onlinelibrary.wiley.com/doi/abs/10.1029/2003JE002119.

O'Brien, David P., Andre Izidoro, Seth A. Jacobson, Sean N. Raymond, and David C. Rubie (2018). "The Delivery of Water During Terrestrial Planet Formation." In: *Space Science Reviews* 214.1. DOI: 10.1007/s11214-018-0475-8. URL: https://doi.org/10.1007/s11214-018-0475-8.

O'Rourke, J. G. (2020). "Venus: A Thick Basal Magma Ocean May Exist Today." In: *Geophysical Research Letters* 47.4. URL: https://doi.org/10.1029/2019gl086126.

O'Rourke, J. G., J. Buz, R. R. Fu, and R. J. Lillis (2019). "Detectability of Remanent Magnetism in the Crust of Venus." In: *Geophysical Research Letters* 46.11, pp. 5768–5777. URL: https://doi.org/10.1029/2019gl082725.

O'Rourke, Joseph G. and Suzanne E. Smrekar (2018). "Signatures of Lithospheric Flexure and Elevated Heat Flow in Stereo Topography at Coronae on Venus." In: *Journal of Geophysical Research: Planets* 123.2, pp. 369–389. URL: https://doi.org/10.1002/2017je005358.

O'Rourke, Joseph G., Aaron S. Wolf, and Bethany L. Ehlmann (2014). "Venus: Interpreting the spatial distribution of volcanically modified craters." In: *Geophysical Research Letters* 41.23, pp. 8252–8260. DOI: 10.1002/2014gl062121. URL: https://doi.org/10.1002/2014gl062121.

O'Rourke, Joseph G. et al. (2023). "Venus, the Planet: Introduction to the Evolution of Earth's Sister Planet." In: *Space Science Reviews* 219.1. URL: https://doi.org/10.1007/s11214-023-00956-0.

O'Rourke, Joseph and Jun Korenaga (2015). "Thermal evolution of Venus with argon degassing." In: *Icarus* 260, pp. 128–140. URL: https://doi.org/10.1016/j.icarus.2015.07.009.

Palmieri, Paolo (2001). "Galileo and the Discovery of the Phases of Venus." In: *Journal for the History of Astronomy* 32.2, pp. 109–129. URL: https://doi.org/10.1177/002182860103200202.

Pauer, M., K. Fleming, and O. Čadek (2006). "Modeling the dynamic component of the geoid and topography of Venus." In: *Journal of Geophysical Research* 111.E11. URL: https://doi.org/10.1029/2005je002511.

Pekeris, Chaim L. (1935). "Thermal Convection in the Interior of the Earth." In: *Geophysical Supplements to the Monthly Notices of the Royal Astronomical Society* 3.8, pp. 343–367. ISSN: 2051-1965. URL: https://doi.org/10.1111/j.1365-246X.1935.tb01742.x.

Percival, Donald B. and Andrew T. Walden (1993). *Spectral Analysis for Physical Applications: Multitaper and Conventional*. Cambridge University Press. URL: https://www.cambridge.org/us/catalogue/catalogue.asp?isbn=9780521355322.

Pettengill, G. H., H. W. Briscoe, J. V. Evans, E. Gehrels, G. M. Hyde, L. G. Kraft, R. Price, and W. B. Smith (1962). "A radar investigation of Venus." In: *The Astronomical Journal* 67, p. 181. URL: https://doi.org/10.1086/108692.

Pettengill, Gordon H., Eric Eliason, Peter G. Ford, George B. Loriot, Harold Masursky, and George E. McGill (1980). "Pioneer Venus Radar results altimetry and surface properties." In: *Journal of Geophysical Research* 85.A13, p. 8261. DOI: 10.1029/ja085ia13p08261. URL: https://doi.org/10.1029/ja085ia13p08261.

Phillips, J. L. and C. T. Russell (1987). "Upper limit on the intrinsic magnetic field of Venus." In: *Journal of Geophysical Research* 92.A3, p. 2253. DOI: 10.1029/ja092ia03p02253. URL: https://doi.org/10.1029/ja092ia03p02253.

Phillips, R. J. (1983). "Geophysics: Plate tectonics on Venus?" In: *Nature* 302.5910, pp. 655–656. URL: https://doi.org/10.1038/302655a0.

Phillips, R. J., C. L. Johnson, S. L. Mackwell, P. Morgan, D. T. Sandwell, and M. T. Zuber (1997). "Lithospheric Mechanics and Dynamics of Venus." In: *Venus II*. Ed. by Stephen W. Bougher, D. M. Hunten, and R. J. Phillips. Tucson: University of Arizona Press, pp. 1163–1204.

Phillips, R. J., W. M. Kaula, G. E. McGill, and M. C. Malin (1981). "Tectonics and Evolution of Venus." In: *Science* 212.4497, pp. 879–887. URL: https://doi.org/10.1126/science.212.4497.879.

Phillips, R. J. and M. C. Malin (1983). "The interior of Venus and tectonic implications." In: *Venus*, pp. 159–214.

Phillips, Roger J. (1994). "Estimating Lithospheric Properties at Atla Regio, Venus." In: *Icarus* 112.1, pp. 147–170. URL: https://doi.org/10.1006/icar.1994.1175.

Phillips, Roger J. and Vicki L. Hansen (1994). "TECTONIC AND MAGMATIC EVOLUTION OF VENUS." In: *Annual Review of Earth and Planetary Sciences* 22.1, pp. 597–656. URL: https://doi.org/10.1146/annurev.ea.22.050194.003121.

Phillips, Roger J. and Vicki L. Hansen (1998). "Geological Evolution of Venus: Rises, Plains, Plumes, and Plateaus." In: *Science* 279.5356, pp. 1492–1497. URL: https://doi.org/10.1126/science.279.5356.1492.

Phillips, Roger J. and Kurt Lambeck (1980). "Gravity fields of the terrestrial planets: Long-wavelength anomalies and tectonics." In: *Reviews of Geophysics* 18.1, p. 27. URL: https://doi.org/10.1029/rg018i001p00027.

Phillips, Roger J., Richard F. Raubertas, Raymond E. Arvidson, Ila C. Sarkar, Robert R. Herrick, Noam Izenberg, and Robert E. Grimm (1992). "Impact craters and Venus resurfacing history." In: *Journal of Geophysical Research* 97.E10, p. 15923. DOI: 10.1029/92je01696. URL: https://doi.org/10.1029/92je01696.

Pratt, John Henry (1855). "I. On the attraction of the Himalaya Mountains, and of the elevated regions beyond them, upon the plumb-line in India." In: *Philosophical Transactions of the Royal Society of London* 145, pp. 53–100. URL: https://royalsocietypublishing.org/doi/abs/10.1098/rstl.1855.0002.

Price, Maribeth H., Geoffrey Watson, John Suppe, and Charles Brankman (1996). "Dating volcanism and rifting on Venus using impact crater densities." In: *Journal of Geophysical Research: Planets* 101.E2, pp. 4657–4671. URL: https://doi.org/10.1029/95je03017.

Price, Maribeth and John Suppe (1994). "Mean age of rifting and volcanism on Venus deduced from impact crater densities." In: *Nature* 372.6508, pp. 756–759. URL: https://doi.org/10.1038/372756a0.

Rappaport, Nicole J., Alex S. Konopliv, Algis B. Kucinskas, and Peter G. Ford (1999). "An Improved 360 Degree and Order Model of Venus Topography." In: *Icarus* 139.1, pp. 19–31. URL: https://doi.org/10.1006/icar.1999.6081.

Reese, C.C., V.S. Solomatov, and L.-N. Moresi (1999). "Non-Newtonian Stagnant Lid Convection and Magmatic Resur facing on Venus." In: *Icarus* 139.1, pp. 67–80. URL: https://doi.org/10.1006/icar.1999.6088.

Regorda, Alessandro, Cedric Thieulot, Iris van Zelst, Zoltán Erdős, Julia Maia, and Susanne Buiter (2023). "Rifting Venus: Insights

From Numerical Modeling." In: *Journal of Geophysical Research: Planets* 128.3. URL: https://doi.org/10.1029/2022je007588.

Resor, P., M. Gilmore, B. Straley, D. Senske, and R. Herrick (2021). "Felsic Tesserae on Venus Permitted by Lithospheric Deformation Models." In: *Journal of Geophysical Research: Planets* 126.4. URL: https://doi.org/10.1029/2020je006642.

Ricard, Y., L. Fleitout, and C. Froidevaux (1984). "Geoid heights and lithospheric stresses for a dynamic Earth." In: *Annales Geophysicae* 2, pp. 267–285. URL: https://hal.archives-ouvertes.fr/hal-02013128.

Richards, Mark A. and Bradford H. Hager (1984). "Geoid anomalies in a dynamic Earth." In: *Journal of Geophysical Research: Solid Earth* 89.B7, pp. 5987–6002. URL: https://doi.org/10.1029/jb089ib07p05987.

Richards, Mark A. and Adrian Lenardic (2018). "The Cathles Parameter: A Geodynamic Definition of the Asthenosphere and Implications for the Nature of Plate Tectonics." In: *Geochemistry, Geophysics, Geosystems*. URL: https://doi.org/10.1029/2018gc007664.

Rogers, A. E. E. and R. P. Ingalls (1969). "Venus: Mapping the Surface Reflectivity by Radar Interferometry." In: *Science* 165.3895, pp. 797–799. URL: https://doi.org/10.1126/science.165.3895.797.

Rolf, T., B. Steinberger, U. Sruthi, and S.C. Werner (2018). "Inferences on the mantle viscosity structure and the post-overturn evolutionary state of Venus." In: *Icarus* 313, pp. 107–123. URL: https://doi.org/10.1016/j.icarus.2018.05.014.

Rolf, Tobias et al. (2022). "Dynamics and Evolution of Venus' Mantle Through Time." In: *Space Science Reviews* 218.8. URL: https://doi.org/10.1007/s11214-022-00937-9.

Romeo, I. and R. Capote (2011). "Tectonic evolution of Ovda Regio: An example of highly deformed continental crust on Venus?" In: *Planetary and Space Science* 59.13, pp. 1428–1445. URL: https://doi.org/10.1016/j.pss.2011.05.013.

Romeo, I. and D.L. Turcotte (2008). "Pulsating continents on Venus: An explanation for crustal plateaus and tessera terrains." In: *Earth and Planetary Science Letters* 276.1-2, pp. 85–97. URL: https://doi.org/10.1016/j.epsl.2008.09.009.

Rosenblatt, Pascal, Caroline Dumoulin, Jean-Charles Marty, and Antonio Genova (2021). "Determination of Venus' Interior Structure with EnVision." In: *Remote Sensing* 13.9, p. 1624. DOI: 10.3390/rs13091624. URL: https://doi.org/10.3390/rs13091624.

Rozel, A. B., G. J. Golabek, C. Jain, P. J. Tackley, and T. Gerya (2017). "Continental crust formation on early Earth controlled by intrusive magmatism." In: *Nature* 545.7654, pp. 332–335. URL: https://doi.org/10.1038/nature22042.

Rudnick, R. and S. Gao (2003). "Composition of the Continental Crust." In: *Treatise on Geochemistry*. Elsevier, pp. 1–64. URL: https://doi.org/10.1016/b0-08-043751-6/03016-4.

Rudolph, M. L., V. Leki, and C. Lithgow-Bertelloni (2015). "Viscosity jump in Earth's mid-mantle." In: *Science* 350.6266, pp. 1349–1352. URL: https://doi.org/10.1126/science.aad1929.

Rudolph, M. L., P. Moulik, and V. Lekić (2020). "Bayesian Inference of Mantle Viscosity From Whole-Mantle Density Models." In: *Geochemistry, Geophysics, Geosystems* 21.11. URL: https://doi.org/10.1029/2020gc009335.

Ruiz, Javier, Alberto Jiménez-Díaz, Isabel Egea-González, Laura M. Parro, and Federico Mansilla (2019). "Comments on "Using the viscoelastic relaxation of large impact craters to study the thermal history of Mars" (Karimi et al., 2016, Icarus 272, 102–113) and "Studying lower crustal flow beneath mead basin: Implications for the thermal history and rheology of Venus" (Karimi and Dombard, 2017, Icarus 282, 34–39)." In: *Icarus* 322, pp. 221–226. URL: https://doi.org/10.1016/j.icarus.2018.10.009.

Russell, C. T., R. C. Elphic, J. G. Luhmann, and J. A. Slavin (1980). "On the search for an intrinsic magnetic field at Venus." In: *Lunar and Planetary Science Conference Proceedings* 3, pp. 1897–1906.

Russell, M. B. and C. L. Johnson (2021). "Evidence for a Locally Thinned Lithosphere Associated With Recent Volcanism at Aramaiti Corona, Venus." In: *Journal of Geophysical Research: Planets* 126.8. DOI: 10.1029/2020je006783. URL: https://doi.org/10.1029/2020je006783.

Rzhiga, O.N. (1987). "Venera-15 and -16 spacecraft: Images and maps of Venus." In: *Advances in Space Research* 7.12, pp. 269–278. DOI: 10.1016/0273-1177(87)90229-8. URL: https://doi.org/10.1016/0273-1177(87)90229-8.

Sachs, A., David George Kendall, S. Piggott, Desmond George King-Hele, I. E. S. Edwards, and F. R. Hodson (1974). "Babylonian observational astronomy." In: *Philosophical Transactions of the Royal Society of London. Series A, Mathematical and Physical Sciences* 276.1257, pp. 43–50. URL: https://royalsocietypublishing.org/doi/abs/10.1098/rsta.1974.0008.

Sagan, Carl (1960). "The Surface Temperature of Venus." In: *The Astronomical Journal* 65, p. 352. URL: https://doi.org/10.1086/108265.

Sagan, Carl (1967). "An Estimate of the Surface Temperature of Venus Independent of Passive Microwave Radiometry." In: *The Astrophysical Journal* 149, p. 731. URL: https://doi.org/10.1086/149306.

Saliby, Christelle, Agnès Fienga, Arthur Briaud, Anthony Mémin, and Carianna Herrera (2023). "Viscosity contrasts in the Venus mantle from tidal deformations." en. In: *Planetary and Space Science* 231,

p. 105677. ISSN: 0032-0633. URL: https://www.sciencedirect.com/science/article/pii/S0032063323000466.

Sandwell, David T., Catherine L. Johnson, Frank Bilotti, and John Suppe (1997). "Driving Forces for Limited Tectonics on Venus." In: *Icarus* 129.1, pp. 232–244. URL: https://doi.org/10.1006/icar.1997.5721.

Saunders, R. S. et al. (1992). "Magellan mission summary." In: *Journal of Geophysical Research* 97.E8, p. 13067. URL: https://doi.org/10.1029/92je01397.

Saunders, R. Stephen and Gordon H. Pettengill (1991). "Magellan: Mission Summary." In: *Science* 252.5003, pp. 247–249. URL: https://doi.org/10.1126/science.252.5003.247.

Schaber, G. G., R. G. Strom, H. J. Moore, L. A. Soderblom, R. L. Kirk, D. J. Chadwick, D. D. Dawson, L. R. Gaddis, J. M. Boyce, and Joel Russell (1992). "Geology and distribution of impact craters on Venus: What are they telling us?" In: *Journal of Geophysical Research* 97.E8, p. 13257. URL: https://doi.org/10.1029/92je01246.

Schmidt, M. and O. Jagoutz (2017). "The global systematics of primitive arc melts." In: *Geochemistry, Geophysics, Geosystems* 18.8, pp. 2817–2854. URL: https://doi.org/10.1002/2016gc006699.

Schubert, G., D. Bercovici, and G. A. Glatzmaier (1990). "Mantle dynamics in Mars and Venus: Influence of an immobile lithosphere on three-dimensional mantle convection." In: *Journal of Geophysical Research* 95.B9, p. 14105. URL: https://doi.org/10.1029/jb095ib09p14105.

Schubert, G., V. S. Solomatov, P. J. Tackley, and D. L. Turcotte (1997). "Mantle Convection and the Thermal Evolution of Venus." In: *Venus II*. Ed. by Stephen W. Bougher, D. M. Hunten, and R. J. Phillips, p. 1245.

Schubert, Gerald, William B. Moore, and David T. Sandwell (1994). "Gravity over Coronae and Chasmata on Venus." In: *Icarus* 112.1, pp. 130–146. URL: https://doi.org/10.1006/icar.1994.1174.

Schubert, Gerald, Donald Turcotte, and Peter Olson (2004). *Mantle Convection in the Earth and Planets*. Cambridge University Press. URL: https://doi.org/10.1017/cbo9780511612879.

Semple, AG and A Lenardic (2021). "Feedbacks between a non-Newtonian upper mantle, mantle viscosity structure and mantle dynamics." In: *Geophysical Journal International* 224.2, pp. 961–972.

Senske, D. A., G. G. Schaber, and E. R. Stofan (1992). "Regional topographic rises on Venus: Geology of Western Eistla Regio and comparison to Beta Regio and Atla Regio." In: *Journal of Geophysical Research* 97.E8, p. 13395. URL: https://doi.org/10.1029/92je01167.

Shah, Oliver, Ravit Helled, Yann Alibert, and Klaus Mezger (2022). "Possible Chemical Composition And Interior Structure Models Of Venus Inferred From Numerical Modelling." In: *The Astrophys-*

ical Journal 926.2, p. 217. URL: https://doi.org/10.3847/1538-4357/ac410d.

Shalygin, E. V., W. J. Markiewicz, A. T. Basilevsky, D. V. Titov, N. I. Ignatiev, and J. W. Head (2015). "Active volcanism on Venus in the Ganiki Chasma rift zone." In: *Geophysical Research Letters* 42.12, pp. 4762–4769. URL: https://doi.org/10.1002/2015gl064088.

Shankland, T. J., R. J. O'Connell, and H. S. Waff (1981). "Geophysical constraints on partial melt in the upper mantle." In: *Reviews of Geophysics* 19.3, p. 394. URL: https://doi.org/10.1029/rg019i003p00394.

Shapiro, Irwin I. (1967). "Resonance Rotation of Venus." In: *Science* 157.3787, pp. 423–425. URL: https://doi.org/10.1126/science.157.3787.423.

Shellnutt, J. Gregory (2019). "The curious case of the rock at Venera 8." In: *Icarus* 321, pp. 50–61. URL: https://doi.org/10.1016/j.icarus.2018.11.001.

Simons, Frederik J. and F. A. Dahlen (2006a). "Spherical Slepian functions and the polar gap in geodesy." In: *Geophysical Journal International* 166.3, pp. 1039–1061. URL: https://doi.org/10.1111/j.1365-246x.2006.03065.x.

Simons, Frederik J. and F. A. Dahlen (2006b). "Spherical Slepian functions and the polar gap in geodesy." In: *Geophysical Journal International* 166.3, pp. 1039–1061. URL: https://doi.org/10.1111/j.1365-246x.2006.03065.x.

Simons, Frederik J., F. A. Dahlen, and Mark A. Wieczorek (2006). "Spatiospectral Concentration on a Sphere." In: *SIAM Review* 48.3, pp. 504–536. URL: https://doi.org/10.1137/s0036144504445765.

Simons, Mark, Bradford Hager, and Sean Solomon (1994). "Global Variations in the Geoid/Topography Admittance of Venus." In: *Science* 264.5160, pp. 798–803. DOI: https://doi.org10.1126/science.264.5160.798.

Simons, Mark, Sean Solomon, and Bradford Hager (1997). "Localization of gravity and topography: constraints on the tectonics and mantle dynamics of Venus." In: *Geophysical Journal International* 131.1, pp. 24–44. URL: https://doi.org/10.1111/j.1365-246X.1997.tb00593.x (visited on 07/22/2020).

Sjogren, W. L., W. B. Banerdt, P. W. Chodas, A. S. Konopliv, G. Balmino, J. P. Barriot, J. Arkani-Hamed, T. R. Colvin, and M. E. Davies (1997). "The Venus Gravity Field and Other Geodetic Parameters." In: *Venus II: Geology, Geophysics, Atmosphere, and Solar Wind Environment*. Ed. by Stephen W. Bougher, D. M. Hunten, and R. J. Phillips, p. 1125.

Sjogren, W. L., R. J. Phillips, P. W. Birkeland, and R. N. Wimberly (1980). "Gravity anomalies on Venus." In: *Journal of Geophysical Research* 85.A13, p. 8295. URL: https://doi.org/10.1029/ja085ia13p08295.

Skilling, John (2006). "Nested sampling for general Bayesian computation." In: *Bayesian Analysis* 1.4. URL: https://doi.org/10.1214/06-ba127.

Sleep, Norman H. (1990). "Hotspots and mantle plumes: Some phenomenology." In: *Journal of Geophysical Research* 95.B5, pp. 6715–6736. URL: https://doi.org/10.1029/JB095iB05p06715.

Slepian, David (1983). "Some Comments on Fourier Analysis, Uncertainty and Modeling." In: *SIAM Review* 25.3, pp. 379–393. ISSN: 00361445. URL: http://www.jstor.org/stable/2029386 (visited on 04/06/2023).

Smith, Edward J., Leverett Davis, Paul J. Coleman, and Charles P. Sonett (1965). "Magnetic measurements near Venus." In: *Journal of Geophysical Research* 70.7, pp. 1571–1586. URL: https://doi.org/10.1029/jz070i007p01571.

Smrekar, S. E., W. S. Kiefer, and E. R. Stofan (1997). "Large Volcanic Rises on Venus." In: *Venus II*. Ed. by Stephen W. Bougher, D. M. Hunten, and R. J. Phillips, p. 845.

Smrekar, S. E. et al. (2021). "VERITAS (Venus Emissivity, Radio Science, In-SAR, Topography, and Spectroscopy): A Proposed Discovery Mission." In: *Lunar and Planetary Science Conference*. Lunar and Planetary Science Conference, p. 2211.

Smrekar, Sue et al. (2022). "VERITAS (Venus Emissivity, Radio Science, InSAR, Topography, and Spectroscopy): A Discovery Mission." In: *2022 IEEE Aerospace Conference (AERO)*. IEEE. URL: https://doi.org/10.1109/aero53065.2022.9843269.

Smrekar, Suzanne E., Robert Comstock, and F. Scott Anderson (2003). "A gravity survey of Type 2 coronae on Venus." In: *Journal of Geophysical Research: Planets* 108.E8. URL: https://doi.org/10.1029/2002JE001935.

Smrekar, Suzanne E., Colby Ostberg, and Joseph G. O'Rourke (2023). "Earth-like lithospheric thickness and heat flow on Venus consistent with active rifting." In: *Nature Geoscience* 16.1, pp. 13–18. URL: https://doi.org/10.1038/s41561-022-01068-0.

Smrekar, Suzanne E. and E. Marc Parmentier (1996). "The interaction of mantle plumes with surface thermal and chemical boundary layers: Applications to hotspots on Venus." In: *Journal of Geophysical Research: Solid Earth* 101.B3, pp. 5397–5410. URL: https://doi.org/10.1029/95jb02877.

Smrekar, Suzanne E. and Roger J. Phillips (1991). "Venusian highlands: geoid to topography ratios and their implications." In: *Earth and Planetary Science Letters* 107.3-4, pp. 582–597. URL: https://doi.org/10.1016/0012-821X(91)90103-O.

Smrekar, Suzanne E. and Ellen R. Stofan (1997). "Corona Formation and Heat Loss on Venus by Coupled Upwelling and Delamination." In: *Science* 277.5330, pp. 1289–1294. DOI: 10.1126/science.

277.5330.1289. URL: https://doi.org/10.1126/science.277.5330.1289.

Smrekar, Suzanne E., Ellen R. Stofan, Nils Mueller, Allan Treiman, Linda Elkins-Tanton, Joern Helbert, Giuseppe Piccioni, and Pierre Drossart (2010). "Recent Hotspot Volcanism on Venus from VIRTIS Emissivity Data." In: *Science* 328.5978, pp. 605–608. URL: https://doi.org/10.1126/science.1186785.

Solomatov, V. S. and L.-N. Moresi (1996). "Stagnant lid convection on Venus." In: *Journal of Geophysical Research: Planets* 101.E2, pp. 4737–4753. URL: https://doi.org/10.1029/95JE03361.

Solomon, Sean C. and James W. Head (1982). "Mechanisms for lithospheric heat transport on Venus: Implications for tectonic style and volcanism." In: *Journal of Geophysical Research* 87.B11, p. 9236. DOI: 10.1029/jb087ib11p09236. URL: https://doi.org/10.1029/jb087ib11p09236.

Solomon, Sean C. et al. (1992). "Venus tectonics: An overview of Magellan observations." In: *Journal of Geophysical Research* 97.E8, p. 13199. URL: https://doi.org/10.1029/92je01418.

Sonett, CharlesP. (1963). "A summary review of the scientific findings of the Mariner Venus mission." In: *Space Science Reviews* 2.6. URL: https://doi.org/10.1007/bf00208814.

Speagle, Joshua S. (2020). "DYNESTY: a dynamic nested sampling package for estimating Bayesian posteriors and evidences." In: *Monthly Notices of the Royal Astronomical Society* 493.3, pp. 3132–3158. URL: https://doi.org/10.1093/mnras/staa278.

Squyres, Steven W., D. M. Janes, Gidon Baer, Duane L. Bindschadler, Gerald Schubert, Virgil L. Sharpton, and Ellen R. Stofan (1992). "The morphology and evolution of coronae on Venus." In: *Journal of Geophysical Research* 97.E8, p. 13611. URL: https://doi.org/10.1029/92je01213.

Stähler, Simon C. et al. (2021). "Seismic detection of the martian core." In: *Science* 373.6553, pp. 443–448. URL: https://doi.org/10.1126/science.abi7730.

Steinberger, Bernhard (2002). "An explanation for the shape of Earth's gravity spectrum based on viscous mantle flow models." In: *Geophysical Research Letters* 29.21. URL: https://doi.org/10.1029/2002gl015476.

Steinberger, Bernhard, Stephanie C. Werner, and Trond H. Torsvik (2010). "Deep versus shallow origin of gravity anomalies, topography and volcanism on Earth, Venus and Mars." In: *Icarus* 207.2, pp. 564–577. URL: https://doi.org/10.1016/j.icarus.2009.12.025.

Stofan, E. R., V. E. Hamilton, D. M. Janes, and S. E. Smrekar (1997). "Coronae on Venus: Morphology and Origin." In: *Venus II*. Ed. by Stephen W. Bougher, D. M. Hunten, and R. J. Phillips, p. 931.

Stofan, Ellen R., Virgil L. Sharpton, Gerald Schubert, Gidon Baer, Duane L. Bindschadler, Daniel M. Janes, and Steven W. Squyres (1992). "Global distribution and characteristics of coronae and related features on Venus: Implications for origin and relation to mantle processes." In: *Journal of Geophysical Research* 97.E8, p. 13347. URL: https://doi.org/10.1029/92je01314.

Stofan, Ellen R., Suzanne E. Smrekar, Duane L. Bindschadler, and David A. Senske (1995). "Large topographic rises on Venus: Implications for mantle upwelling." In: *Journal of Geophysical Research* 100.E11, p. 23317. URL: https://doi.org/10.1029/95je01834.

Stofan, Ellen R., Suzanne E. Smrekar, Simon W. Tapper, John E. Guest, and Peter M. Grindrod (2001). "Preliminary analysis of an expanded corona database for Venus." In: *Geophysical Research Letters* 28.22, pp. 4267–4270. URL: https://doi.org/10.1029/2001gl013307.

Strom, Robert G., Gerald G. Schaber, and Douglas D. Dawson (1994). "The global resurfacing of Venus." In: *Journal of Geophysical Research* 99.E5, p. 10899. URL: https://doi.org/10.1029/94je00388.

Surkov, Yu. A., V. L. Barsukov, L. P. Moskalyeva, V. P. Kharyukova, and A. L. Kemurdzhian (1984). "New data on the composition, structure, and properties of Venus rock obtained by Venera 13 and Venera 14." In: *Journal of Geophysical Research* 89.S02, B393. URL: https://doi.org/10.1029/jb089is02p0b393.

Surkov, Yu. A., F. F. Kirnozov, V. N. Glazov, A. G. Dunchenko, L. P. Tatsy, and O. P. Sobornov (1987). "Uranium, thorium, and potassium in the Venusian rocks at the landing sites of Vega 1 and 2." In: *Journal of Geophysical Research: Solid Earth* 92.B4, E537–E540. URL: https://doi.org/10.1029/JB092iB04p0E537.

Surkov, Yu. A., L. P. Moskalyova, V. P. Kharyukova, A. D. Dudin, G. G. Smirnov, and S. Ye. Zaitseva (1986). "Venus rock composition at the Vega 2 Landing Site." In: *Journal of Geophysical Research* 91.B13, E215. DOI: 10.1029/jb091ib13p0e215. URL: https://doi.org/10.1029/jb091ib13p0e215.

Svedhem, H. et al. (2007). "Venus Express—The first European mission to Venus." In: *Planetary and Space Science* 55.12, pp. 1636–1652. URL: https://doi.org/10.1016/j.pss.2007.01.013.

Tackley, Paul J. (2023). "Tectono-Convective Modes on Earth and Other Terrestrial Bodies." In: *Dynamics of Plate Tectonics and Mantle Convection*. Elsevier, pp. 159–180. URL: https://doi.org/10.1016/b978-0-323-85733-8.00006-8.

Takei, Yasuko (2017). "Effects of Partial Melting on Seismic Velocity and Attenuation: A New Insight from Experiments." In: *Annual Review of Earth and Planetary Sciences* 45.1, pp. 447–470. URL: https://doi.org/10.1146/annurev-{E}arth-063016-015820.

Takei, Yasuko and Benjamin K. Holtzman (2009). "Viscous constitutive relations of solid-liquid composites in terms of grain bound-

ary contiguity: 1. Grain boundary diffusion control model." In: *Journal of Geophysical Research* 114.B6. URL: https://doi.org/10.1029/2008jb005850.

Tarantola, Albert (2005). *Inverse Problem Theory and Methods for Model Parameter Estimation*. Society for Industrial and Applied Mathematics. URL: https://doi.org/10.1137/1.9780898717921.

Thomson, D.J. (1982). "Spectrum estimation and harmonic analysis." In: *Proceedings of the IEEE* 70.9, pp. 1055–1096. URL: https://doi.org/10.1109/proc.1982.12433.

Tian, Jiacheng, Paul J. Tackley, and Diogo L. Lourenço (2023). "The tectonics and volcanism of Venus: New modes facilitated by realistic crustal rheology and intrusive magmatism." In: *Icarus* 399, p. 115539. DOI: 10.1016/j.icarus.2023.115539. URL: https://doi.org/10.1016/j.icarus.2023.115539.

Titov, Dmitrij V., Nikolay I. Ignatiev, Kevin McGouldrick, Valérie Wilquet, and Colin F. Wilson (2018). "Clouds and Hazes of Venus." In: *Space Science Reviews* 214.8. URL: https://doi.org/10.1007/s11214-018-0552-z.

Turcotte, D. L., R. J. Willemann, W. F. Haxby, and John Norberry (1981). "Role of membrane stresses in the support of planetary topography." In: *Journal of Geophysical Research* 86.B5, pp. 3951–3959. URL: https://doi.org/10.1029/jb086ib05p03951.

Turcotte, D.L. (1993). "An episodic hypothesis for Venusian tectonics." In: *Journal of Geophysical Research* 98.E9, pp. 17061–17068. URL: https://doi.org/10.1029/93je01775.

Turcotte, D.L., G. Morein, D. Roberts, and B.D. Malamud (1999). "Catastrophic Resurfacing and Episodic Subduction on Venus." In: *Icarus* 139.1, pp. 49–54. URL: https://doi.org/10.1006/icar.1999.6084.

Turcotte, Donald L. and Gerald Schubert (2002). *Geodynamics - 2nd Edition*. Cambridge University Press. DOI: 10.2277/0521661862.

Vakhnin, V. M. (1968). "A Review of the Venera 4 Flight and Its Scientific Program." In: *Journal of the Atmospheric Sciences* 25.4, pp. 533–534. URL: https://doi.org/10.1175/1520-0469(1968)025<0533:arotvf>2.0.co;2.

Van Den Berg, Arie P and David A Yuen (1996). "Is the lower-mantle rheology Newtonian today?" In: *Geophysical research letters* 23.16, pp. 2033–2036.

Verrier, M. Le (1872). "On the Masses of the Planets and the Parallax of the Sun." In: *Monthly Notices of the Royal Astronomical Society* 32.9, pp. 322–328. URL: https://doi.org/10.1093/mnras/32.9.322.

Walker, Russell G. and Carl Sagan (1966). "The ionospheric model of the Venus microwave emission: An obituary." In: *Icarus* 5.1-6, pp. 105–123. URL: https://doi.org/10.1016/0019-1035(66)90014-5.

Watters, Thomas R., Peter B. James, and Michelle M. Selvans (2021). "Mercury's Crustal Thickness and Contractional Strain." In: *Geophysical Research Letters* 48.17. URL: https://doi.org/10.1029/2021gl093528.

Way, M. J. and Anthony D. Del Genio (2020). "Venusian Habitable Climate Scenarios: Modeling Venus Through Time and Applications to Slowly Rotating Venus-Like Exoplanets." In: *Journal of Geophysical Research: Planets* 125.5. URL: https://doi.org/10.1029/2019je006276.

Weller, Matthew B. and Walter S. Kiefer (2020). "The Physics of Changing Tectonic Regimes: Implications for the Temporal Evolution of Mantle Convection and the Thermal History of Venus." In: *Journal of Geophysical Research: Planets* 125.1. URL: https://doi.org/10.1029/2019je005960.

White, Scott M., Joy A. Crisp, and Frank J. Spera (2006). "Long-term volumetric eruption rates and magma budgets." In: *Geochemistry, Geophysics, Geosystems* 7.3. URL: https://doi.org/10.1029/2005gc001002.

Widemann, T., R. Ghail, C. F. Wilson, and D. V. Titov (2020). "EnVision: Europe's Proposed Mission to Venus." In: *AGU Fall Meeting Abstracts*. Vol. 2020, P022–02.

Widemann, Thomas et al. (2022). "EnVision: a Nominal Science Phase Spanning Six Venus Sidereal Days (Four Earth Years)." In: *AGU Fall Meeting Abstracts*. Vol. 2022, P55B–05.

Wieczorek, M. A. et al. (2013). "The Crust of the Moon as Seen by GRAIL." In: *Science* 339.6120, pp. 671–675. URL: https://doi.org/10.1126/science.1231530.

Wieczorek, M. (2008). "Constraints on the composition of the martian south polar cap from gravity and topography." In: *Icarus* 196.2, pp. 506–517. URL: https://doi.org/10.1016/j.icarus.2007.10.026.

Wieczorek, Mark A. (2015a). "Gravity and Topography of the Terrestrial Planets." In: *Treatise on Geophysics (Second Edition)*. Ed. by Gerald Schubert. Second Edition. Oxford: Elsevier, pp. 153–193. URL: https://doi.org/10.1016/B978-0-444-53802-4.00169-X.

Wieczorek, Mark A. (2015b). *Spherical harmonic model of the planet Venus: VenusTopo719*. DOI: 10.5281/zenodo.3870926. URL: https://zenodo.org/record/3870926.

Wieczorek, Mark A. (2018). "Strength, Depth, and Geometry of Magnetic Sources in the Crust of the Moon From Localized Power Spectrum Analysis." In: *Journal of Geophysical Research: Planets* 123.1, pp. 291–316. URL: https://doi.org/10.1002/2017je005418.

Wieczorek, Mark A. and Roger J. Phillips (1998). "Potential anomalies on a sphere: Applications to the thickness of the lunar crust." In: *Journal of Geophysical Research: Planets* 103.E1, pp. 1715–1724. URL: http://doi.wiley.com/10.1029/97JE03136.

Wieczorek, Mark A. and Frederik J. Simons (2005). "Localized spectral analysis on the sphere." In: *Geophysical Journal International* 162.3, pp. 655–675. URL: https://doi.org/10.1111/j.1365-246X.2005.02687.x.

Wieczorek, Mark A. and Frederik J. Simons (2007). "Minimum-Variance Multitaper Spectral Estimation on the Sphere." In: *Journal of Fourier Analysis and Applications* 13.6, pp. 665–692. URL: https://doi.org/10.1007/s00041-006-6904-1.

Wieczorek, Mark A. et al. (2022). "InSight Constraints on the Global Character of the Martian Crust." In: *Journal of Geophysical Research: Planets* 127.5. URL: https://doi.org/10.1029/2022je007298.

Xiao, Chi, Fei Li, Jianguo Yan, Michel Gregoire, Weifeng Hao, Yuji Harada, Mao Ye, and Jean-Pierre Barriot (2021). "Possible Deep Structure and Composition of Venus With Respect to the Current Knowledge From Geodetic Data." In: *Journal of Geophysical Research: Planets* 126.7. URL: https://doi.org/10.1029/2019je006243.

Yoder, C. F. (1997). "Venusian Spin Dynamics." In: *Venus II*. Ed. by Stephen W. Bougher, D. M. Hunten, and R. J. Phillips, p. 1087.

Čadek, O. and L. Fleitout (2003). "Effect of lateral viscosity variations in the top 300 km on the geoid and dynamic topography." In: *Geophysical Journal International* 152.3, pp. 566–580. URL: https://doi.org/10.1046/j.1365-246x.2003.01859.x.

ACRONYMS

CMB core-mantle boundary.
DAVINCI Deep Atmosphere Venus Investigation of Noble gases, Chemistry, and Imaging.
ESA European Space Agency.
GTR geoid-to-tography ratio.
JPL Jet Propulsion Laboratory.
LVZ low viscosity zone.
MCMC Markov Chain Monte Carlo.
NASA National Aeronautics and Space Administration.
PDS Planetary Data System.
PVO Pioneer Venus Orbiter.
RMSE root mean square error.
SAR synthetic aperture radar.
SI Supplemental information.
VERITAS Venus Emissivity, Radio Science, InSAR, Topography And Spectroscopy.

f Arbitrary square-integrable function.
$Y_{\ell m}$ Spherical harminc function.
ℓ Spherical harmonic degree.
m Spherical harmonic order.
$f_{\ell m}$ Spherical harmonics coefficents of an arbitrary function f.
θ Colatitude on the sphere.
ϕ Longitude on the sphere.
R Mean planetary radius.
λ Wavelength in Cartesian domain.
$\ell_{\mathbf{max}}$ Maximum spherical harmonic degree.
S Power-spectrum of a function (if indices are repeated) or cross-spectrum between two functions (if indices are different).
m Mass of secondary body.
M Mass of primary body / planet's mass.
$\mathbf{r}$ Position vector of the secondary body or "observer".
$\mathbf{r}_\oplus$ Position vector of the primary body or "observation target".
$\mathbf{g}$ Gravitational acceleration vector.
G Gravitational constant $= 6.6743 \cdot 10^{-11}\ \mathrm{m^3 kg^{-1} s^{-2}}$.
U Gravitational potential.
V Volume.
$\rho(\mathbf{r}_\oplus)$ Density distribution of a a body.
∇^2 Laplacian operator.
r Radial coordinate.
$C_{\ell m}$ Gravity spherical harmonic coefficents.
R_0 Reference radius of the gravitational potential coefficients.
g Radial component of the gravitational acceleration.
N Geoid.
Z Spectral admittance.
γ Spectral correlation.
h Topography.
$\mathcal{F}$ Localized version of an arbitrary function f.
w Localizarion window.
$\ell_{\mathbf{win}}$ Spectral bandwidth of localization window.
$\ell_{\mathbf{data}}$ Maximum spectral resolution of the data.
θ_0 Angular radius of spherical cap localization window.
Λ Spatial concentration factor of a spatio-spectral localization window.
τ Arbitrary relief associated with a density interface.
R_τ Radius of an interface with arbitrary relief τ.
$h_{\ell m}$ Topography spherical harmonic coefficients.
$I_{\ell m}$ Part of the gravity signal not predicted by the model.

Q_ℓ Transfer fuction betwdeen gravity and topography (model-dependent).
σ^2 Data uncertainty or variance.
D Flexural rigidity of the lithosphere.
ν Poisson's ratio.
E Young's modulus.
T_e Elastic lithosphere thickness.
ω Lithospheric deflection.
q Lithospheric load (placed on the surface or in the subsurface).
R_e Radius of the elastic lithosphere.
T_c Crustal thickness.
ρ_m Mantle density near the crust-mantle boundary.
ρ_c Crust density.
ρ_l Surface load density.
g_0 Gravity at the surface.
g_m Gravity at the crust-mantle boundary.
$\bar{\rho}$ Bulk planetary density.
z_ψ Depth of thz mass-sheet density anomaly.
L Bounded ratio between surface and subsurface loads.
$g_{\ell m}^{\mathbf{flex}}$ Radial gravity predicted from the surface and subsurface loading model.
T_m Mechanical lithosphere thickness.
K Lithospheic plate curvature.
$\dot{\varepsilon}$ Strain rate.
$\boldsymbol{T}$ Temperature.
$\mathcal{R}$ Gas constant.
$d\boldsymbol{T}/dz$ Lithosphere thermal gradient.
F Surface heat flow.
k Thermal conductivity.
η_0 Reference mantle viscosity.
η Viscosity.
$\psi_{\ell m}$ Mass-sheet density anomaly.
H_ℓ Topography dynamic kernel.
$\mathcal{G}_\ell$ Radial gravity dynamic kernel.
$\mathcal{Z}_\ell$ Admittance dynamic kernel.
$g_{\ell m}^{\mathbf{dyn}}$ Radial gravity predicted from the dynamic loading model.
$h_{\ell m}^{\mathbf{dyn}}$ Topography predicted from the dynamic loading model.
$\mathbf{d}^{\mathbf{obs}}$ Observations vector.
$\mathbf{d}^{\mathbf{pred}}$ Model prediction vector.
$\boldsymbol{\Theta}$ Set of model parameters.
$\mathcal{P}$ Posterior probability.
$\mathcal{L}$ Likelihood function.
ϖ Prior probability.
$\mathcal{K}$ Model evidence / marginal probability.